Workshop on
ICES, OCEANS, AND FIRE:
SATELLITES OF THE OUTER SOLAR SYSTEM

AUGUST 13–15, 2007
BOULDER, COLORADO

WORKSHOP PROGRAM
AND ABSTRACTS

Workshop on

Ices, Oceans, and Fire:
Satellites of the Outer Solar System

August 13–15, 2007
Boulder, Colorado

Abstracts in this volume may be cited as

Author A. B. (2007) Title of abstract. In *Workshop on Ices, Oceans, and Fire: Satellites of the Outer Solar System,* p. XX. LPI Contribution No. 1357, Lunar and Planetary Institute, Houston.

Preface

This volume contains abstracts that have been accepted for presentation at the Workshop on Ices, Oceans, and Fire: Satellites of the Outer Solar System, August 13–15, 2007, Boulder, Colorado.

Contents

Program

Monday, August 13, 2007
WELCOME AND OPENING REMARKS
8:30 a.m.   Boulderado Ballroom

8:30 a.m.   Johnson T. *
              Welcome

THE EARLY YEARS: ORIGINS AND EARLY EVOLUTION
9:00 a.m.   Boulderado Ballroom

Chair: A. Barr

9:00 a.m.   Barr A. C. *   Canup R. M.
              Formation of the Saturnian Satellites: Constraints from Rhea's Undifferentiated State **[#6059]**

9:20 a.m.   Castillo-Rogez J. C. *   Matson D. L.   Johnson T. V.   Lunine J. I.
              *Searching for Constraints on the Chronology of the Outer Solar System from
              Satellite Geophysics* **[#6053]**

9:32 a.m.   Matson D. L. *   Castillo-Rogez J. C.   Vance S. D.   Davies A. G.   Johnson T. V.
              The Early History of Enceladus: Setting the Scene for Today's Activity **[#6052]**

9:44 a.m.   Zolotov M. Yu. *   Mironenko M. V.   Glein C. R.   Shock E. L.
              The Formation and Nature of Early Oceans on Icy Satellites: Geochemical Constraints **[#6047]**

9:56 a.m.   DISCUSSION

10:16 a.m.   COFFEE BREAK

Monday, August 13, 2007
WHAT LIES BELOW: OCEANS AND INTERIORS
10:30 a.m.   Boulderado Ballroom

Chair: R. Pappalardo

10:30 a.m.   Showman A. *
The Convective Dynamics of Icy Stellites and Implications for Surface Evolution **[#6091]**

10:50 a.m.   Hand K. P. * Chyba C. F.
Magnetometer Constraints on the Ocean Salinity and Ice Shell Thickness of Europa **[#6078]**

11:02 a.m.   Bland M. T. * Showman A. P.
Coupled Orbital and Thermal Evolution of Ganymede: Implications for Resurfacing and Magnetic Field Generation **[#6019]**

11:14 a.m.   Hussmann H. * Grott M.   Sohl F.
Enceladus: Internal Dynamics and Heat Production by Tidal Friction **[#6038]**

11:26 a.m.   Roberts J. H. * Nimmo F.
Long-Term Stability of a Subsurface Ocean on Enceladus **[#6022]**

11:38 a.m.   Mitri G. * Showman A. P.
Thermal Convection in the Ice-I Shells of Titan and Enceladus **[#6013]**

11:50 a.m.   DISCUSSION

12:10 p.m.   LUNCH BREAK

Monday, August 13, 2007
HEAVENS ON EARTH: TERRESTRIAL ANALOGS
1:30 p.m.   Boulderado Ballroom

Chair: **D. D. Blankenship**

1:30 p.m.   Lopes R. M. C. * Stofan E. R.   Mitri G.   Robshaw L. E.   Mitchell K. L.   Wood C. A.
Radebaugh J.   Kirk R. L.   Wall S. D.   Lorenz R.   Lunine J. I.   Craig J.   Paganelli F.
Soderblom L.   Cassini RADAR Team
*Much Like Earth: Distribution and Interplay of Geologic Processes on Titan from
Cassini RADAR Data* **[#6003]**

1:42 p.m.   Blankenship D. D. * Peters M. E.   Young D. A.
Terrestrial Analogs for Radar Sounding of Europa's Icy Shell: The View from Antarctica **[#6058]**

1:54 p.m.   Gleeson D. G.   Pappalardo R. T.   Grasby S. E.   Templeton A. S.   Spear J. R.
*Biochemical and Spectral Characterization of a Sulfur-rich Glacial Ecosystem and Potential Analog
to Europa* **[#6001]**

2:06 p.m.   Hays C. C. * Castillo-Rogez J. C.   Mitchell K. L.   Barmatz M. B.   Zhong F.   Engelhardt H.
Smythe W.   Matson D. L.   Pappalardo R. T.   Lopes R. M. C.   Gudipati S. M.   Robshaw L. E.
Neish C.   Lunine J. I.   Kargel J. S.
Cryogenic Property Measurements on Icy Compositions with Application to Solar System Ices **[#6072]**

2:18 p.m.   DISCUSSION

PLENARY SESSION: NEW HORIZONS AT JUPITER
2:30 p.m.   Boulderado Ballroom

Chair: **J. Green**

2:30 p.m.   Spencer J. *
New Horizons at Jupiter

Monday, August 13, 2007
POSTER SESSION AND RECEPTION
3:30 p.m.   Mezzanine

Hansen G. B.
Progress on Rectifying and Recalibrating Galileo/NIMS Observations of the Icy Galilean Satellites **[#6024]**

Cooper P. D.   Moore M. H.   Hudson R. L.
Vapor Pressures and Heats of Vaporization of Some Organic Acid Ices **[#6040]**

Wye L. C.   Zebker H. A.   Janssen M. A.   Lorenz R. D.   West R. D.   Cassini RADAR Team
Composition of Titan's Surface Features Constrained Through Backscatter Modeling **[#6050]**

Verbiscer A. J.   Peterson D. E.   Skrutskie M. F.   Cushing M.   Nelson M. J.   Smith J. D.   Wilson J. C.
Solid Nitrogen and Simple Hydrocarbons on Charon **[#6070]**

Zolotov M. Yu.   Mironenko M. V.
Chemical Evolution on an Early Ocean on Europa: A Kinetic-Thermodynamic Modeling **[#6065]**

Strange N. J.   Russell R. P.   Landau D. F.   Yen C. L.   Sims J. A.
Trajectory Design for Jupiter System Observer **[#6044]**

Bauer J. M.   Buratti B. J.
HST Photometry of Triton: Evidence for a Changing Surface in the Outer Solar System **[#6020]**

Miller D. J.   Barnash A. N.   Bray V. J.   Turtle E. P.   Helfenstein P.   Squyres S. W.   Rathbun J. A.
Interactions Between Impact Craters and Tectonic Fractures on Enceladus and Dione **[#6007]**

Michaud R. L.   Pappalardo R. T.   Collins G. C.
Measuring Tectonic Strain: From Ganymede to Enceladus and Dione **[#6060]**

Sims D. W.   Wyrick D. Y.   Pappalardo R. T.
Tectonic Resurfacing Processes on Ganymede, Insights from Physical Models **[#6071]**

Spencer C.   Radebaugh J.   Lorenz R.   Wall S.   Lunine J.   Cassini RADAR Team
Comparative Analysis of Longutidunal Dunes on Saturn's Moon Titan and the Namib Desert, Namibia **[#6006]**

Dougherty A. J.   Hogenboom D. L.   Kargel J. S.
Volumetric and Optical Studies of High Pressure Phases of $MgSO_4 \bullet H_2O$ with Applications to Europa **[#6068]**

Papapietro N. A.   Rathbun J. A.   Spencer J. R.
Loki, Io: Model and Observations **[#6008]**

Strange N. J.   Russell R. P.   Bufington B. B.   Sims J. A.
Trajectory Design for Europa Explorer **[#6046]**

Vertucci V.   Rash K.   Hickman R.   Homolac C.   Krupp J.   Love H.   Ligon K.   Paulson A.
Vehicle for Icy Terrain Locomotion: A Rover Prototype for Europa by a University of Colorado Aerospace Engineering Senior Projects Team **[#6055]**

Cook J. C.   Desch S. J.   Roush T. L.
Near-Infrared Spectra of Kuiper Belt Objects: More than Just Water Ice **[#6061]**

Denk T.   Neukum G.   Roatsch Th.   Hendrix A. R.   Pelletier F. J.   Strange N. J.
The Cassini Targeted Iapetus Flyby Will Take Place in September, 2007 **[#6049]**

Williams D. A.   Keszthelyi L. P.   Geissler P. E.   Jaeger W. L.   Becker T. L.   Crown D. A.
Schenk P. M.   Rathbun J. A.
The Global Geologic Map of Io: Approach and Mapping Status **[#6010]**

Hurford T. A.   Helfenstein P.   Hoppa G. V.   Greenberg R.   Bills B. G.
Tidal Control of Eruptions on Enceladus **[#6031]**

Wood C. A.   Stofan E. R.   Lorenz R. D.   Kirk R. L.   Lopes R. M.   Callahan P.
Xanadu — Disaggregation of Titan's Bright Terrains **[#6082]**

Pappalardo R. T.   Davis D. M.
Where's the Compression? Explaining the Lack of Contractional Structures on Icy Satellites **[#6080]**

Dalton J. B. III   Cruikshank D. P.
Distribution of Volatile Ices in Hyperion **[#6079]**

FLAGSHIP STUDY BRIEFINGS
6:00 p.m.   Boulderado Ballroom

Chair: **C. Niebur**

6:00 p.m.   Niebur C. *
             Flagship Studies Overview

6:15 p.m.   Pappalardo R. *
             Europa Study

6:45 p.m.   Lorenz R. *
             Titan Study

7:15 p.m.   Senske D. *
             Jupiter System Observer Study

7:45 p.m.   Spencer J. *
             Enceladus Study

Tuesday, August 14, 2007
COMPOSITION: THE TOP FEW MICRONS
8:30 a.m.   Boulderado Ballroom

Chairs: **D. Cruikshank**
            J. Kargel

8:30 a.m.   Dalton J. B. *
             Surface Compositions of the Icy Satellites **[#6086]**

8:50 a.m.   Mastrapa R. M. E. *   Bernstein M. P.   Sandford S. A.
             Near Infrared Spectra of Pure Ices and Mixtures Relevant to Icy Satellites **[#6048]**

9:02 a.m.   Cruikshank D. P. *
             Carbon Dioxide on the Satellites of Saturn **[#6011]**

9:14 a.m.   Hendrix A. R. *   Hansen C. J.
             Ultraviolet Measurements of the Surfaces of the Icy Saturnian Satellites **[#6069]**

9:26 a.m.   Hansen G. B. *
             Widespread CO_2 and Other Non-Ice Compounds on the Anti-Jovian and Trailing Sides of Europa from Galileo/NIMS Observations **[#6023]**

9:38 a.m.   Hudson R. L. *   Moore M. H.
             Laboratory Studies of the Formation and Stability of Hydrates Relevant to Icy Surfaces **[#6032]**

9:50 a.m.   Dalton J. B. III *
             Modeling Europa's Surface Composition with Cryogenic Sulfate Hydrates **[#6057]**

10:02 a.m.   DISCUSSION

10:22 a.m.   COFFEE BREAK

10:34 a.m.   Gerakines P. A. *   Richey C. R.
             Near-Infrared Spectra of UV-Photolyzed Laboratory Analogs of Planetary Ices **[#6034]**

10:46 a.m.   Hendrix A. R. *   Johnson R. E.
             The Icy Galilean Satellites as Measured by the Galileo UVS **[#6077]**

10:58 a.m.   Hibbitts C. A. *   Szanyi J.
             Physisorption: Trapping Volatiles in the Surfaces of Icy Satellites **[#6036]**

11:10 a.m.   Kargel J. S. *
             Theory of Geochemical/Geological Homology Applied to Hydrocarbon and Organic Substances on Icy Satellites and Other Solid Planetary Objects **[#6084]**

11:22 a.m.   McCarthy C. *   Goldsby D. L.   Cooper R. F.   Durham W. B.   Kirby S. H.
             Steady-State Creep Respose of Ice-I/Magnesium Sulfate Hydrate **[#6075]**

11:34 a.m.   DISCUSSION

11:54 a.m.   LUNCH BREAK

Tuesday, August 14, 2007
LANDSCAPES
1:30 p.m.   Boulderado Ballroom

Chairs: **L. Prockter**
            J. Radebaugh

1:30 p.m.   Moore J. *
            Erosion and Regolith on Outer Solar System Satellites **[#6087]**

1:50 p.m.   Radebaugh J. * Lorenz R. Lunine J. Wall S. Boubin G. Reffet E. Kirk R. Lopes R.
            Stofan E. Soderblom L. Allison M. Callahan P. Cassini RADAR Team
            Longitudinal Dunes on Titan as Indicators of Global Climate **[#6005]**

2:02 p.m.   Burr D. *
            Fluvial Flow on Titan: Context for Geomorphic Interpretation **[#6088]**

2:14 p.m.   Turtle E. P. * Perry J. E. McEwen A. S. West R. A. Dawson D. D. Porco C. C. Fussner S.
            Cassini Imaging Science Subsystem Observations of Titan's High-Latitude Lakes **[#6063]**

2:26 p.m.   Mitchell K. L. * Wall S. D. Stofan E. R. Lopes R. M. C. Janssen M. Stiles B. Paillou P.
            Mitri G. Lunine J. Ostro S. Lorenz R. D. Farr T. G. Kirk R. L. Radebaugh J.
            Cassini RADAR Science Team
            Titan's North Polar Lakes as Observed by Cassini Radar: An Update **[#6042]**

2:38 p.m.   Perry J. E. * Turtle E. P. McEwen A. S. Dawson D. D. Porco C. C.
            Cassini ISS Observations of Titan's Trailing Hemisphere **[#6064]**

2:50 p.m.   Johnson W. T. K. * Callahan P. S. Gim Y. Alberti G. Flamini E. Hensley S. Lorenz R. D.
            Orosei R. Zebker H. A.
            Cassini RADAR Altimeter Observations of Titan **[#6033]**

3:02 p.m.   DISCUSSION

3:22 p.m.   COFFEE BREAK

3:34 p.m.   Wood S. E. * Moore J. M. Schenk P. M. Howard A. D. Spencer J. R.
            3D Modeling of Landscape-Modifying Processes on the Galilean Satellites **[#6035]**

3:46 p.m.   Buratti B. J. * Bauer J. Hicks M. D.
            Opposition Surges on Icy and Rocky Moons **[#6026]**

3:58 p.m.   Denk T. * Cassini ISS Team
            The Surface of Iapetus **[#6092]**

4:10 p.m.   Schenk P. M. *
            The Impact of Cratering in the Outer Solar System **[#6025]**

4:30 p.m.   Zahnle K. J. * Alvarellos J. L. Dobrovolskis A. Hamill P.
            Primary, Secondary, and Sesquinary Craters on Europa (Io Attacks) **[#6021]**

4:42 p.m.   Lorenz R. D. * Wood C. A. Lunine J. I. Wall S. D. Lopes R. M. Mitchell K. L. Paganelli F.
            Anderson Y. Z. Wye L. Zebker H. Stofan E. R. Cassini RADAR Team
            Impact Cratering on Titan — Cassini RADAR Results **[#6012]**

4:54 p.m.   Smith D. E. *   Bray V. J.   Turtle E. P.   Melosh H. J.   Perry J. E.
             Studies of Viscous Relaxation of Craters on Enceladus **[#6051]**

5:06 p.m.   Matsuyama I.   Nimmo F. *
             Reorientation of Icy Satellites Due to Impact Basins **[#6017]**

5:18 p.m.   DISCUSSION

SCIENCE ON A SPHERE
6:30 p.m.   NOAA's David Skaggs Research Center

Science On a Sphere (SOS) presentation by Steve Albers at the "Planet Theater" of NOAA's David Skaggs Research Center (DSRC). After starting from planet Earth, we will be touring the solar system with a special emphasis on planetary satellites. See spectacular recent high-resolution imagery of the satellites projected onto a 6-foot sphere seeming to float in outer space.

Wednesday, August 15, 2007
THE VIOLENT MOONS: ERUPTIONS, PLUMES, AND TECTONICS
8:30 a.m. Boulderado Ballroom

Chairs: **J. Rathbun**
S. Kattenhorn

8:30 a.m. Hurford T. *
The Role of Tides in Tectonic Formation and Eruption Activity on Satellites in the
Outer Solar System **[#6089]**

8:50 a.m. Kattenhorn S. A. * Groenleer J. M. Marshall S. T. Vetter J. C.
Shearing-induced Tectonic Deformation on Icy Satellites: Europa as a Case Study **[#6014]**

9:02 a.m. Patterson G. W. * Head J.
Kinematic Analysis of Triple Junctions on Europa **[#6018]**

9:14 a.m. Schenk P. * Matsuyama I. Nimmo F.
Global Scale Small Circle Depressions and Polar Wander on Europa **[#6090]**

9:26 a.m. Collins G. C. *
Bright Terrain Tectonics and the Evolution of Ganymede **[#6041]**

9:38 a.m. Nimmo F. * Roberts J. H. Spencer J. R. Pappalardo R. T. Prockter L. M. Mullen M. E.
Shear Heating in the Outer Solar System **[#6015]**

9:50 a.m. Smith-Konter B. R. * Crawford Z. Pappalardo R. T.
Tidally Driven Fault Deformation and Stress Accumulation at Enceladus's Tiger Stripes **[#6062]**

10:02 a.m. McKinnon W. B. * Barr A. C.
The Mimas Paradox Revisited Plus Crustal Spreading on Enceladus? **[#6083]**

10:14 a.m. DISCUSSION

10:34 a.m. COFFEE BREAK

10:46 a.m. Gregg T. K. P. * Lopes R. M.
Volcanic Depressions and Lava Lakes on Earth, Mars, Venus, Io and Titan **[#6054]**

11:06 a.m. Spitale J. N. * Porco C. C.
The Jets of Enceladus Erupt from the Warmest Regions on Its South Polar Fractures **[#6085]**

11:18 a.m. Schneider N. M. * Burger M. E. Johnson R. E. Kargel J. S. Schaller E. L. Brown M. E.
Constraints on the Salinity of Enceladus' Plumes **[#6028]**

11:30 a.m. Barnes J. W. * Brown R. H. Soderblom L. Sotin C. LeMouelic S. Rodriguez S. LeCorre L.
Buratti Bonnie J. Pitman K. M. Clark R. N. Jaumann R. Hayne P.
Titan as an Icy Moon: Evidence for Cryovolcanism and Tectonics from Cassini/VIMS **[#6066]**

11:42 a.m. Spencer J. R. * Stern S. A. Moore J. Lopes R. M. C. Retherford K. Abramov O.
Showalter M. Cheng A. F. Weaver H. A. Reuter D. C. Lunsford A. Olkin C. Throop H.
Jessup K. L.
New Horizons Observations of Io's Volcanism **[#6030]**

11:54 a.m.   Rathbun J. A. *   Spencer J. R.
              Groundbased Observations of Io in Support of the New Horizons Flyby **[#6009]**

12:06 p.m.   DISCUSSION

12:26 p.m.   LUNCH BREAK

Wednesday, August 15, 2007
WHAT LIES ABOVE: ATMOSPHERES, MAGNETOSPHERES, AND THEIR INTERACTIONS
1:30 p.m.   Boulderado Ballroom

Chairs: **M. Burger**
                M. McGrath

1:30 p.m.   Khurana K. K. * Burger M. H.   Leisner J. S.   Dougherty M. K.   Russell C. T.
              The Interaction of Enceladus' Plume with Saturn's Magnetosphere **[#6027]**

1:50 p.m.   Snowden D. * Winglee R.
              3-D Multi-Fluid Model of the Plasma Interaction at Titan Highlighting the Importance of
              Ion Gyroradus Effects **[#6016]**

2:02 p.m.   Cooper J. F. * Sturner S. J.
              Hemispheric and Topographic Asymmetry of Magnetospheric Particle Irradiation for
              Icy Moon Surfaces **[#6037]**

2:14 p.m.   Burger M. H. * Paty C.   Sittler E. C. Jr.   Johnson R. E.
              The Enceladus Water Plume and Its Interactions with the Saturnian Plasma **[#6067]**

2:26 p.m.   DISCUSSION

2:46 p.m.   COFFEE BREAK

2:58 p.m.   Smyth W. H. * Marconi M. L.
              Processes Shaping Galilean Satellite Atmospheres from the Surface to the Magnetosphere **[#6039]**

3:10 p.m.   McGrath M. A. *
              Aurora on Ganymede **[#6081]**

3:22 p.m.   Hansen C. J. * Hendrix A. R.
              Far UltraViolet Observations of Icy Satellite Atmospheres and Plumes **[#6056]**

3:34 p.m.   Moullet A. * Lellouch E.   Moreno R.   Gurwell M.   Moore C.
              Io's Surface and SO$_2$ Atmosphere: First Disk-resolved Millimetric Observations **[#6029]**

3:46 p.m.   DISCUSSION

CLOSING REMARKS
4:00 p.m.   Boulderado Ballroom

4:00 p.m.   McKinnon W. *   Nimmo F.
              Closing Remarks

TITAN AS AN ICY MOON: EVIDENCE FOR CRYOVOLCANISM AND TECTONICS FROM CASSINI/VIMS. Jason W. Barnes, *NASA Ames Research Center, M/S 244-30, Moffett Field, CA 94034-1000, USA, (Jason.W.Barnes@nasa.gov)*, Robert H. Brown, *LPL*, Laurence Soderblom, *USGS/Flagstaff*, Christophe Sotin, Stephane Le Mouélic, Sebastien Rodriguez, Lucille LeCorre, *Université Nantes*, Bonnie J. Buratti, Karly M. Pitman, *JPL*, Roger N. Clark, *USGS/Denver*, Ralf Jaumann, *DLR*, Paul Hayne, *SSI*.

Abstract:

Like the other large icy moons, Titan is predicted on theoretical grounds to posess a liquid water mantle beneath its icy crust [1]. There is as yet no more definitive empirical evidence for this subsurface ocean, unlike for Europa [2, 3], Ganymede [4], Callisto [3], and Enceladus [5]. Titan's extended atmosphere limits *Cassini* passes to be at least 1000 kilometers above the surface, reducing the sensitivity of gravitational and magnetic experiments to subsurface conditions.

The atmosphere inhibits surface imaging as well, by atmospheric absorption, haze scattering, and the closest-approach-altitude limitation. The best imaging resolution of Titan obtained to date was 400 meters/pixel by VIMS during the T20 (2006 October 20) flyby, and that only in a small footprint. Typical global resolutions are more like 10-20 km/pixel. The resolution discrepancy between available data covering Titan and that covering its sister water-mantle moons makes intercomparison challenging. Geological processes driven by Titan's atmosphere and hydrosphere (methanosphere) like aeolean burial and exhumation as well as fluvial erosion and deposition dominate on Titan, and hence conceal possible similarities between Titan and other icy moons.

Nevertheless, in this talk we identify a set of Titanian features present in the Visual and Infrared Mapping Spectrometer (VIMS) dataset that may share similar origins to those seen on other icy moons. The processes that drive these features are likely extrusive and/or tectonic.
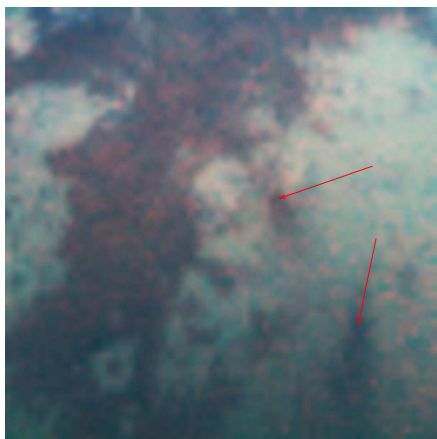
Figure 1: Omacatl (top) and Elpis (bottom) Maculae on Titan as seen from VIMS during T5 (2005 April 16).

Possible cryovolcanic features have been identified on several other icy moons, including Europa [6], Ganymede [7], Triton, Miranda, and Ariel [8]. We will discuss Titan's cryovolcanic candidates Tortola Facula [9], Tui Regio [10], and the possible flow feature seen by both VIMS and RADAR in northern Fensal [11, 12], comparing them to those on other icy moons.

Though other explanations remain viable (I prefer an impact origin myself – JWB), Titan's Omacatl and Elpis Maculae may represent plume-deposits downwind of a surface source [13] (Figure 1), reminiscent of those on Triton [14] though they would likely be heated from below, and not from above as on Triton [15].

Large-scale tectonic fractures cover the surface of Europa (e.g., [16]). VIMS T20 observations revealed what is possibly a linear mountain range on Titan, identified based on topographic shading (Figure 2. Though the processes that drive mountain formation on Titan have not yet been established, the T20 mountains may result from teconism similar to that seen on other icy moons. Titan also sports several sets of dark regions with polygonal boundaries that are preferentially oriented in the ordinal directions. The virgae seem only to exist between 20 and 30 degrees of the equator in both the northern and southern hemispheres. Though we really don't know what they are or what made them, we are investigating possible tectonic processes. As a complete speculation, the confinement of these features within a narrow latitudinal zone may be the result of a changing tidal stress field like that seen on Europa [17], but operating on a much slower timescale.

References

[1] Tobie G., Lunine J.I., and Sotin C. (2006) *Nature*, *440* 61–64.

[2] Carr M.H., Belton M.J.S., Chapman C.R., Davies M.E., et al. (1998) *Nature*, *391* 363–+.

[3] Khurana K.K., Kivelson M.G., Stevenson D.J., Schubert G., et al. (1998) *Nature*, *395* 777–+.

[4] Anderson J.D., Lau E.L., Sjogren W.L., Schubert G., et al. (1997) *Nature*, *387* 264–266.

[5] Brown R.H., Clark R.N., Buratti B.J., Cruikshank D.P., et al. (2006) *Science*, *311* 1425–1428.

[6] Figueredo P.H., Chuang F.C., Kirk R.L., and Greeley R. (2000) in Lunar and Planetary Institute Conference Abstracts, vol. 31 of *Lunar and Planetary Institute Conference Abstracts*, 1026–+.

[7] Head J.W., Pappalardo R.T., Kay J., Collins G., et al. (1998) in Lunar and Planetary Institute Conference Abstracts, vol. 29 of *Lunar and Planetary Institute Conference Abstracts*, 1666–+.
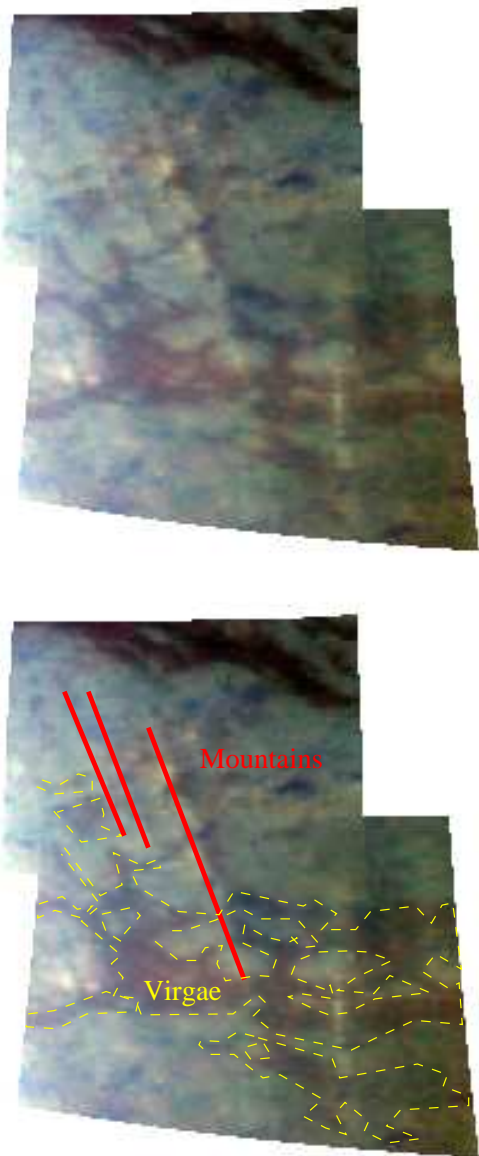
Figure 2: Mountains and the possibly tectonic Virgae on Titan, as seen by the Visual and Infrared Mapping Spectrometer onboard Cassini during the T20 flyby on 2006 October 20.

[8]   Kargel J.S. (1995) *Earth Moon and Planets*, *67* 101–113.

[9]   Sotin C., Jaumann R., Buratti B.J., Brown R.H., et al. (2005) *Nature*, *435* 786–789.

[10] Barnes J.W., Brown R.H., Radebaugh J., Buratti B.J., et al. (2006) *Geophys. Res. Lett.*, *33* 16,204–+.

[11] Le Corre L., Le Mouélic S., Sotin C., Rodriguez S., et al. (2007) in Lunar and Planetary Institute Conference Abstracts, vol. 38 of *Lunar and Planetary Institute Conference Abstracts*, 1828–+.

[12] Lopes R.M.C., Mitchell K.L., Stofan E.R., Lunine J.I., et al. (2007) *Icarus*, *186* 395–412.

[13] Hayne P., Combe J., and McCord T.B. (2006) *AGU Fall Meeting Abstracts* A166+.

[14] Soderblom L.A., Becker T.L., Kieffer S.W., Brown R.H., et al. (1990) *Science*, *250* 410–415.

[15] Brown R.H., Johnson T.V., Kirk R.L., and Soderblom L.A. (1990) *Science*, *250* 431–435.

[16] Pappalardo R.T. and Sullivan R.J. (1996) *Icarus*, *123* 557–567.

[17] Hurford T.A., Sarid A.R., and Greenberg R. (2007) *Icarus*, *186* 218–233.

FORMATION OF THE SATURNIAN SATELLITES: CONSTRAINTS FROM RHEA'S UNDIFFERENTIATED STATE. Amy C. Barr and Robin M. Canup, Department of Space Studies, Southwest Research Institute, 1050 Walnut St. Suite 300, Boulder CO 80302 (amy@boulder.swri.edu).

Introduction: *Cassini* flybys of Saturn's satellite Rhea (R_s=765 km, ρ_s=1233 kg/m^3 (Anderson & Schubert 2007)) have constrained its moment of inertia factor in independent analyses, C/MR^2=0.3721±0.0036 (Iess *et al.,* 2007) or 0.3911±0.0045 (Anderson & Schubert 2007). Both analyses suggest that Rhea is in hydrostatic equilibrium.

For Rhea to remain undifferentiated at present, it must have avoided widespread melting during its formation, when accretional energy and possibly decay of ^{26}Al delivered an initial burst of heat to its interior. We use estimates of the temperature rise associated with ^{26}Al and accretional heating to constrain the timing of Rhea's formation relative to the origin of CAI's as a function of Rhea's accretion time scale and the protosatellite disk temperature.

Our study has three goals: 1) To begin to assess whether Rhea's current state is consistent with its formation in a "gas-starved" disk as described by Canup & Ward (2002, 2006); 2) To constrain the age of Saturn's satellites, and by extension, the Saturn system; 3) To place an upper limit on the amount of ^{26}Al present to drive early geologic activity in the Saturn system.

Satellite Formation: Physically motivated models of Jupiter's growth (*e.g.,* Lubow *et al.,* 1999, Papaloizou & Nelson 2005), Ganymede and Callisto's ice-rich compositions, and of Callisto's interior state led Canup & Ward (2002) to suggest that the Galilean satellites, and by extension, the Saturnian regular satellites (Canup & Ward 2006) formed in a "gas-starved" disk supplied by a slow inflow of solid rock and ice from solar orbit.

In this scenario, gas from the solar nebula and rock-ice particles < 1 m in radius entrained in the gas inflow to the protosatellite disk. Gas flowing onto the disk achieves circumplanetary orbit and spreads viscously both outward and inward onto the growing planet. Rock-ice particles delivered to the disk also achieve circumplanetary orbit where they quickly accumulate into objects large enough to become decoupled from the gas, ultimately accreting into satellites. As the disk is continuously supplied with new material from solar orbit, the gas density in the disk achieves a quasi-steady state, but solids become concentrated in the disk over time.

In the Canup & Ward model, satellite growth rates are controlled by the rate of delivery of solids to planetary orbit. Estimates for Rhea's accretion time scale are 10^5 to 10^6 yr (Canup & Ward 2002; Barr & Canup 2007), perhaps more consistent with the partially dif-

ferentiated state of Rhea than prior work (Squyres et al., 1988) where Rhea accreted 10^3 yr in a minimum-mass subnebula (MMSN) around Saturn. Although the slow formation of Rhea predicted by Canup & Ward hypothesis strongly suggests it can remain unmelted during formation, this has yet to be shown explicitly.

^{26}Al & The Timing of Satellite Formation: It has recently been suggested that heating from short-lived radioisotopes (SLRI's) is required to "kick start" activity in the interiors of Iapetus and Enceladus (*e.g.,* Castillo *et al.,* 2005, 2006, Castillo-Rogez *et al.,* 2007, Matson *et al.,* 2007). If these materials were present in Iapetus and Enceladus, they would have been present in Rhea's interior as well because all three satellites presumably formed at the same time. However, combined accretional and ^{26}Al heating may provide enough energy to melt Rhea, which limits the amount of radiogenic heating that could have occurred. Because the ^{26}Al heat source is strongly time-dependent, avoiding ^{26}Al meltdown requires that Rhea form relatively late after CAI condensation (*cf.* similar arguments for Callisto by McKinnon 2006). It is not clear that the presence of SLRI's in Enceladus and Iapetus is consistent with Rhea's state.

Accretional Temperature Profiles: Accretional temperature profiles for a growing Rhea are calculated by balancing radiation from its surface, heating of impacted material from its initial temperature (which we assume has the same temperature as the disk, T_d) to the surface temperature (T), accretional heating, and radiogenic heating,

$$\sigma_{SB}(T^4 - T_d^4) + \rho_s C_p (T - T_d)\frac{dr}{dt} = \frac{1}{2}\frac{\dot{M}u_i^2}{4\pi r^2} + \frac{rq_r(t_f)m_r}{3}, \quad (1)$$

with Stefan-Boltzmann constant σ_{SB}, specific heat C_p=1700 J/kg, radial coordinate within Rhea r, mass accretion rate $\dot{M}=M_{s,f}/\tau_{acc}$ where $M_{s,f}$ is the final satellite mass and τ_{acc} is the accretion time scale, chondritic heating rate q_r, and satellite rock mass fraction $m_r=(\rho_r(\rho_s-\rho_i))/(\rho_s(\rho_r-\rho_i))$ where ρ_i=1000 kg/m^3 and ρ_r=3000 kg/m^3 is a representative rock density. After material at a radius r is accreted, radiogenic heating increases its temperature by ΔT_r,

$$\Delta T_r = \frac{1}{\rho_s C_p}\int_{t_f}^{\infty} q_{26}(t)dt = \frac{q_{26}(0)}{\lambda_{26}}\exp(-\lambda_{26}t_f), \quad (2)$$

where $q_{26}(0)\sim 1.63\times10^{-7}$ W/kg (using ^{26}Al/^{27}Al= 5.25x10^{-5} from Bizzarro *et al.,* (2004) and total Al abundance from Lodders (2003)) is the radiogenic heating rate from ^{26}Al at t=0, the time of CAI condensation, and λ_{26}=9.68x10^{-7} yr^{-1} is the decay constant. By using eq. (1) we have implicitly assumed that all

accretional energy is delivered by small impactors and thus deposited close to the surface where it is radiatively cooled. If more heat was deposited at depth, it would make melting more likely. By making this assumption we search for the coldest possible proto-rheas, which are more likely to be consistent with its C/MR^2 than cases involving accretion from large objects. We ignore solid-state heat transfer by conduction and convection.

The time at which a layer accretes (t_f) is,

$$t_f = t_{start} + \frac{4}{3}\frac{1}{F_g}\left(\frac{\rho_s r}{\sigma}\right)\Omega^{-1}, \tag{3}$$

where t_{start} is the time at which Rhea starts accreting relative to CAI's, σ is the surface mass density of disk solids, Ω is Rhea's orbital frequency, and $F_g = 1 + (v_{esc}/v_\infty)^2$ is the gravitational focusing factor, a function of the characteristic relative velocity of accreting material, v_∞, and satellite escape velocity $v_{esc} = (2GM/R)^{1/2}$. We assume $F_g = 5$.

To avoid melting during formation, we adopt the simple criterion that Rhea's temperature must be less than the pressure-dependent melting temperature of water ice, which ranges from 273 K at its surface to 260 K at its central pressure of 124 MPa.

Results: Key controls on Rhea's accretional temperature profiles are t_{start}, τ_{acc}, and the disk temperature T_d. We consider the disk temperature to be a free parameter, within limits based on the requirement that solid ice be present at the orbit of Rhea during its accretion ($T_d < 273$ K), and $T_d \geq 90$ K, which is the predicted solar nebula temperature at Saturn's location (Garaud and Lin 2007)).

If Rhea accretes too early in solar system history, its interior will be melted by [26]Al decay while it forms. If Rhea forms too quickly, accretional energy will melt its outermost layers. For a given nebular environment (described by T_d and τ_{acc}), there exists a critical value of t_{start}, t_{crit}, where for $t_{start} < t_{crit}$, Rhea experiences melting during accretion, and for $t_{start} > t_{crit}$, Rhea remains unmelted during accretion. Rhea then finishes accreting at time $t_{end,c} = t_{crit} + \tau_{acc}$. Figure 1 summarizes how $t_{end,c}$ varies as a function of T_d and τ_{acc}.

Conclusions: Our model assumes maximally efficient radiative cooling of the satellite; as a result, our calculations provide an upper limit on the age of the Saturnian inner satellites as a function of satellite origin conditions.

1) Is Rhea's Interior State Consistent With Its Formation In a Gas-Starved Disk? Rhea can remain unmelted during accretion if it formed in conditions consistent with the satellite formation hypothesis of Canup & Ward (2002), where $10^5 < \tau_{acc} < 10^6$ yr, provided it finished forming more than $t_{end,c} > 2$ Myr after CAI's. Solutions in which Rhea avoids melting exist

across the entire range 90 K $< T_d <$ 273 K for $\tau_{acc} > 10^5$ yr. In the context of the Canup & Ward model, the implied ages suggest that gas inflow to Saturn ceased *no earlier* than times comparable to the average nebular lifetimes inferred from circumstellar disks.

2) What is the Upper Limit on the Age of the Saturn System? Rhea must have finished accreting no earlier than 2 Myr after CAI's to avoid early melting. In the case of rapid formation, ($\tau_{acc} \leq 10^3$ yr) Rhea's formation must have been delayed until at least 3.25 Myr after CAI's for $T_d = 90$ K, and for at least 4.5 Myr for $T_d = 120$ K. For $\tau_{acc} \leq 10^3$ yr and $T_d > 130$ K, melting is predicted for all formation times.

3) Can [26]Al Kick-Start Activity in Saturn's Satellites? To avoid [26]Al meltdown in Rhea, it is necessary for it to finish accretion *no earlier* than 2 Myr after CAI's, at which point the [26]Al heating rate has decreased to $1/10^{th}$ its initial value. This places an upper limit on the role of [26]Al in the early Saturn system.

References: Barr, A. C. & R. M. Canup. *GRL* submitted (2007); Bizzarro, M. J. *et al., Nature* 431 275-278 (2004); Canup, R. M. & W. R. Ward. *AJ* 124, 3404-3423 (2000); Canup, R. M. & W. R. Ward. *Nature* 441, 834-839 (2006); Castillo, J. C., *et al., AGU Fall Abs.* no. 32.05 (2005); Castillo, J. C. *et al., Astrobiology* 6, 158 (2006); Castillo-Rogez, J. C. *et al., Icarus* in press (2007); Lodders, K. *Ap.J.* 591 1220-1247 (2003); Lubow, S. H. *et al., Ap.J.* 526 1001-1012 (1999); Matson, D. L. *et al., Icarus* 187 569-573 (2007); McKinnon, W. B. *LPSC* XXXVII abs. no. 2444 (2006); Papaloizou, J. C. & R. P. Nelson. *Astron. Astrophys.* 433 247-265 (2005).
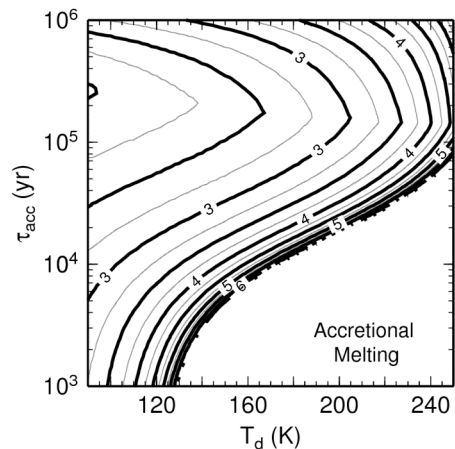
Figure 1. Contours of $t_{end,c}$ required to prevent Rhea from melting during its formation as a function of τ_{acc} and T_d. Rhea must finish accreting between 2.1 and 7 Myr for the range of τ_{acc} and T_d we consider. Fast accretion and high T_d (as suggested foor a MMSN) leads to near-surface melting due to impact energy. Slow growth (0.1 to 1 Myr) that ends > 2 Myr after CAI's is consistent with its present interior state.

HST Photometry of Triton: Evidence for a Changing Surface in the Outer Solar System. J. M. Bauer[1] and B. J. Buratti[1], [1] Jet Propulsion Laboratory, Californian Institute of Technology (4800 Oak Grove Dr., MS183-501, Pasadena, CA 91109, email contact: bauer@scn.jpl.nasa.gov).

Introduction: Triton is one of the few bodies in the solar system with observed cryo-volcanic activity, in the form of plumes [1](Soderblom et al. 1990). Prompted by evidence from previous observations at ground and space-based telescopes of possible seasonal surface changes on Triton [2],[3](Herbert et al. 2004 and Young & Stern 1999), we proposed to confirm and characterize these changes using the HST ACS instrument to image Triton at UV, B, V, I and Methane-band wavelengths over as much of its surface as visible from near Earth in 2005.

Observations: With Triton's angular diameter of nearly 0.13 arcsec in size, ACS's HRC mode afforded an approximately 5X5 pixel image of Triton's surface. The images were taken with Neptune off-frame, to avoid potential bleeding, charge transfer inefficiency, and scattered light problems. With HST's resolution, four regions could be resolved at a time, and particular surface features were restricted to a certain quadrant of Triton's surface. Our request for 6 observing longitudes has allowed us to resolve the longitude of surface features to within 60 degrees (see Figure 1).

Preliminary analysis indicates a rotation light curve amplitude in excess of that predicted by static models [4],[5](Hillier et al. 1994 & Hillier 1999) for visual wavelengths, and significant departures from observations taken 12 years earlier in the UV. We will attempt to determine the resurfacing rates and set model constraints on activity and surface temperature as well as composition. Such constraints have profound implications for our understanding of Triton's evolution as well as the history of other outer solar system bodies that may undergo similar geophysical processes or have similar composition, such as Pluto (Buratti et al. 2003, Young et al. 2001).

References: [1] Soderblom, L.A., Becker, T.L., Kieffer, S.W., Brown, R.H., Hansen, C.J., & Johnson, T.V. 1990, Science, 250, 410. [2] Herbert, B.D., Buratti, B., Schmidt, B., & Bauer, J. 2003, AGU Fall Meeting Abstracts, 443. [3] Young, L.A., & Stern, A.S. 1999, AJ, 122, 449. [4] Hillier, J., Veverka, J., Helfenstein, P., & Lee, P. 1994, Icarus, 109, 296. [5] Hillier, J.K. 1999, Icarus, 139, 202. [6] Buratti, B.J., Hillier, J.K., Heinze, A.,Hicks, M.D., Tryka, K.A., Mosher, J.A., Ward, J., Garske, M., Young, J., & Atienza-Rosel, J. Icarus, 162, 171. [7] Young, E. F.; Binzel, R. P.; Crane, K. 2001, AJ, 121, 552.
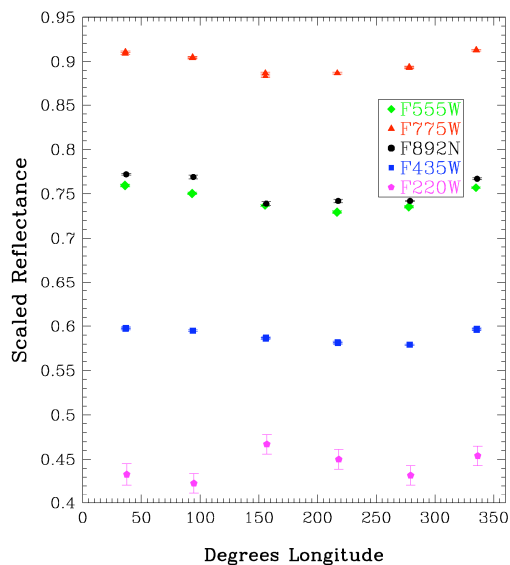
Figure 1: The light curve of Triton's rotation taken by the HST ACS camera in June of 2005. The light curves from the exposures with band passes in the visual (F435W, F555W, F775W equivalent to B, V, and R filter wavelengths respectively, and a 890nm methane, F892N, band pass) are shown along with that of the UV (220nm) band pass.

COUPLED ORBITAL AND THERMAL EVOLUTION OF GANYMEDE: IMPLICATIONS FOR RESURFACING AND MAGNETIC FIELD GENERATION. M. T. Bland[1] and A. P. Showman[2], [1]University of Arizona (mbland@lpl.arizona.edu), [2]University of Arizona (showman@lpl.arizona.edu).

Overview: Two of Ganymede's most distinctive features, its young, disrupted surface and its intrinsic magnetic field may have resulted from the Galilean satellites' passage through a Laplace-like resonance before they evolved into the current Laplace resonance. Passage through such a resonance could have increased Ganymede's eccentricity, generating tidal heating within the ice shell and silicate mantle. Heating the ice produces the melt and global expansion necessary for resurfacing the satellite, while heating the silicates thermodynamically buffers cooling of the metallic core, delaying onset of magnetic field generation until the current epoch.

To test this hypothesis we numerically model the coupled thermal and orbital evolution of Ganymede as the Galilean system progresses through one or more Laplace-like resonances.

Background: One of Ganymede's most striking features is the dichotomy of its surface terrains, with one-third of the surface consisting of ancient, heavily cratered terrain and the rest consisting of young, tectonically deformed terrain [1, 2]. These observations indicate that Ganymede has had a tumultuous history wherein large swaths of heavily cratered terrain were resurfaced. Such resurfacing requires significant internal heating of the satellite to produce both near surface melt and global expansion. However, the source of the required heating remains unclear.

One possible source is tidal heating. Ganymede is currently in a Laplace resonance with Europa and Io. However, this resonance does not pump Ganymede's eccentricity and the current rate of tidal heating is negligible. Malhotra 1991 [3] and Showman and Malhotra 1997 [4] showed, however, that the Galilean satellites may have passed through one or more Laplace-like resonances before evolving into the current Laplace resonance. These Laplace-like resonance do force Ganymede's eccentricity and can therefore lead to internal heating of the satellite as tidal dissipation attempts to circularize the orbit. Showman et al. 1997 [5] explored the effects of tidal heating on the ice mantle of Ganymede and found that, under certain conditions, it can lead to thermal runaway and melting, helping to explain the extensive resurfacing of the satellite. While this work indicated that the likelihood of thermal runaway was small, improved understanding of the internal structure of Ganymede and the nature of convection in variable-viscosity materials (e.g. ice and rock) warrants a reassessment of the applicability of the tidal heating mechanism to Ganymede's resurfacing.

Ancient tidal heating of Ganymede's silicate mantle may also allow the formation of a modern-day intrinsic magnetic field. In contrast to other large satellites (e.g. Europa and Callisto [6], or Titan [7] that show no evidence of an intrinsic magnetic field, a strong (~750 nT) intrinsic field has been observed at Ganymede [8]. Ganymede therefore joins a short list of solid bodies (Mercury and Earth) with detectable magnetic fields.

The simplest explanation for Ganymede's magnetic field is dynamo action within its metallic core, requiring vigorous motions within the conducting fluid [9]. However, because the metallic core is highly conductive, core heat can be rapidly removed without thermal convection occurring. Thus a thermally driven magnetic field cannot be produced by a core cooling slowly over the age of the solar system.

The addition of tidal heating, however, provides an alternative cooling scenario. Because the rate of core cooling is slave to the mantle temperature, tidal heating of the silicate mantle can thermodynamically buffer the core. In such a scenario, core cooling would be delayed until the rate of tidal dissipation is reduced. The silicate mantle and metallic core would then cool rapidly, triggering thermal and compositional convection within the metallic core and magnetic field production.

In light of these considerations we suggest that Ganymede may have undergone the following series of events. Passage through a Laplace-like resonance pumped the satellite's eccentricity causing tidal heating that was dissipated in Ganymede's ice shell and silicate mantle. Dissipation in the ice shell led to thermal runaway and melting [5], ultimately causing the cryovolcanic and tectonic resurfacing that produced the grooved terrain. Simultaneously, tidal heating of the silicate mantle effectively insulated the core, preventing it from cooling. As the Galilean satellites evolved out of the Laplace-like resonance the period in which Ganymede was tidally heated ended. The removal of tidal dissipation in the silicate mantle triggered the onset of core cooling via thermal and compositional convection, and the generation of Ganymede's observed magnetic field.

The Model: We follow the basic conceptual approach of Showman et al. 1997 [5] who coupled the orbital model of Malhotra 1991 [3] to a thermal model for Ganymede's interior. The orbital model is a gener-

alization of the Yoder and Peale 1981 [10] scenario for evolution into the Laplace resonance that allows a more complete dynamical investigation of the orbital histories of the Galilean satellites. This includes capture into one or more Laplace-like resonances that cannot be rigorously explored analytically. The model includes perturbations from Jupiter's gravity field, the mutual perturbations amongst Io, Europa, and Ganymede, and secular perturbations due to Callisto. Forward integration allows determination of the eccentricity, semi-major axis, mean longitude, and longitude of periapse of each satellite.

The thermal model simultaneously solves the energy balance in Ganymede's ice shell, silicate mantle, and liquid Fe/FeS core. Heat transport within the ice and silicate layers occurs via stagnant lid convection, while in the core heat transport is by conduction. Both radiogenic heating of the mantle and latent heating of the liquid core due to inner core growth are included. Ocean formation can also occur if temperatures exceed 251 K in the ice shell.

Coupling between the orbital and thermal models occurs via tidal dissipation, which depends upon both the orbital eccentricities of the satellites and their physical and thermal structure. We use the model of Tobie et al. 2005 [11] to determine how tidal heating is radially distributed throughout the satellite interior. This model provides a more robust calculation of dissipation in a multi-layered viscoelastic body than many previous studies (e.g. [5]).

Preliminary Results: Simulations both with and without tidal heating have been performed. These simulations were initialized with a range of temperatures in the ice shell, silicate mantle, and metallic core that correspond to a cold, intermediate, and hot initial Ganymede. The silicate rheology is controlled by dislocation creep appropriate to wet olivine. The rheology of the ice shell is allowed to transition between diffusion and GBS creep depending on the temperature and convective stresses (cf. [12]). We use the convective scaling of Solomatov and Moresi 2000 [13] to parameterize the convection in each layer.

The Absence of Tidal Heating. Simulations of Ganymede's evolution without tidal heating provide an essential baseline for modeling that includes tidal heating. In these simulations silicate mantle temperatures rise until convective heat transport reaches equilibrium with radiogenic heat production at a temperature of 1700 K. Mantle temperatures then steadily decline with the fall off of radiogenic heating.

Temperatures in the ice shell initially rise rapidly until a temperature of 251 K is reached. At this point an ocean forms at a depth of ~150 km and further heating of the ice shell is buffered. At its maximum extent the ocean remains 50 km below the surface. Subsequent cooling of the ice shell leads to closure of the ocean well before the present epoch.

With a relatively cool mantle above it Ganymede's metallic core initially cools rapidly. As mantle temperatures increase, however, the cooling rate of the core decreases. Once core temperatures become cool enough for iron condensation an inner core begins to form. The rate of inner core formation is initially rapid, but begins to decrease as the sulfur content of the remaining outer core increases and the release of latent heat and gravitational energy reduces the rate of core cooling. Assuming an initial sulfur mass fraction of 10%, approximately 50% of Ganymede's core remains liquid after 4.5 Ga. Cooling rates throughout Ganymede's history are significantly lower than is required for thermal convection.

We note that the timing of these events depends weakly upon the initial thermal structure assumed for the satellite.

The Addition of Tidal Heating. The inclusion of tidal heating profoundly affects Ganymede's thermal history. Preliminary modeling suggests that if passage through a Laplace-like resonance increased Ganymede's eccentricity to at least .01 (~7 times its current value) tidal heating in the ice shell would be strong enough to allow melt to exist within a few kilometers of Ganymede's surface. Such melting would accommodate resurfacing of the satellite. Furthermore, core cooling is prevented while the eccentricity is high, delaying the onset of magnetic field generation. Passage through such a resonance therefore remains a strong candidate for explaining many of Ganymede's unique features.

References: [1] Smith, B.A. et al. (1979) *Science, 206,* 927-950. [2] Pappalardo R.T. et al. (1999) *Icarus, 135,* 276-302. [3] Malhotra, R (1991) *Icarus, 94,* 399-412. [4] Showman, A.P. and R. Malhotra, (1997) *Icarus, 127,* 93-111. [5] Showman, A.P. et al. (1997) *Icarus, 129,* 367-383. [6] Kivelson M.G. et al. (1999) *JGR, 104,* 4609-4625. [7] Backes, H. et al. (2005) *Science, 308,* 992-995. [8] Kivelson, M.G. et al. (1996) *Nature, 384,* 537-541. [9] Schubert, G. et al. (1996) *Nature, 384,* 544-545. [10] Yoder, C.F. and S.J. Peale (1981) *Icarus, 47,* 1-35. [11] Tobie, G. et al. (2005) *Icarus, 177,* 534-549. [12] Barr, A.C. and R.T. Pappalardo (2005) *JGR, 110,* E12005. [13] Solomatov, V.S. and L.N. Moresi (2000) *JGR, 105,* 21795-21817.

TERRESTRIAL ANALOGS FOR RADAR SOUNDING OF EUROPA'S ICY SHELL: THE VIEW FROM ANTARCTICA.

D. D. Blankenship[1], M. E. Peters[1], and D. A. Young[1], [1]University of Texas Institute for Geophysics, JJ Pickle Research Campus, RM2200, 10100 Burnet Road, Austin TX 78758 (blank@ig.utexas.edu)

Introduction: The recent spectacular results of MARSIS [1] and SHARAD [2] at Mars have validated radar sounding as an effective tool for investigating cold planetary ice. To date, these experiments have not shown evidence for ice near its pressure melting point. However, magnetic studies of the icy moons of Jupiter [3] show evidence for extensive, salty subsurface oceans, and remote sensing data from the Cassini mission may indicate liquid water bodies associated with cryovolcanism at Enceledus and Titan. Terrestrial analogs for active subice water systems on Earth include Antarctic ice streams, ice shelves and icebergs. Here we review recent radar sounding results from Antarctica applicable to hypotheses for the distribution of water for Jupiter's moon Europa, a high priority target for future exploration.

Radar sounding models for Europa: A primary objective of future Europa studies will be to characterize the distribution of shallow subsurface water as well as to identify any ice-ocean interface. Another objective will be to understand the formation of surface and subsurface features associated with interchange processes between any ocean and the surface. Achieving these objectives will require either direct or inferred knowledge of the position of any ice/water interfaces as well as any brine or layer pockets.

Thermal factors: The thickness of ice that can be sounded on Europa is determined by the absorption of electromagnetic waves in the ice (which is dictated by its temperature and impurity content) and the scattering characteristics of the ice body (including the surface and basal interfaces as well as any volume scatterers). In previous work, three ice formational scenarios have been used to infer both impurity distributions and temperature/depth regimes in Europa's icy shell [4, 5]. The first scenario is a "marine-ice" europan crust formed by processes similar to those for ice that accretes beneath the large ice shelves of Antarctica. This regime is characterized by slow freezing or melting on the lower side of the icy crust. Impurities present in the ocean tend to be rejected from the ice lattice during the slow freezing process. A second scenario is characterized by very rapid freezing of ocean water injected into linear fracture zones caused by "tidal/tectonic" processes. Because large temperature gradients will be present, this process could lead to ice with properties similar to terrestrial sea ice. Both the "marine-ice" and the "tidal/tectonic" scenarios would be characterized by a temperature/depth profile for a simple thermally conducting ice layer modified by any tidally generated deformational heat flux [6]. A third ice formation scenario is based on the idea of convection in an isothermal layer under a thermally conducting rigid ice crust up to a few kilometers in thickness, possibly characterized by diapirism. This convecting ice scenario implies ice very similar to that for the tidal/tectonic scenario although subject to a dramatically different thermal regime.

Compositional factors: Radar sounding models of Europa associated with these ice formation scenarios generally assume a sulfate dominated Europa ocean noting that radar absorption due to impurities at temperatures below any eutectic for the constituent salts is expected to arise primarily from impurities such as "soluble" chlorine or sulfuric acid. In these models, a significant consideration is that insoluble impurities such as sulfate salts at temperatures below the eutectic would have similar impact on absorption as dust at similar concentrations. For temperatures above the eutectic for any salts, brine would form in the ice giving it electromagnetic properties similar to those for terrestrial sea ice.

Structure and water within and beneath the Antarctic Ice Sheet: Tension fractures dominate the surface of the Antarctic the ice sheet where ice streaming (i.e., basal sliding) begins, whereas tension fractures dominate both the surface and base of the ice where grounded ice sheets (or ice streams) transition to floating ice shelves. The process that controls the distribution of these fractures is the balance between the strain rate gradient (i.e., the acceleration of the ice) and the ability to accommodate this strain through annealing (which is a function of temperature). Similarly, pervasive and nearly chaotic shear fractures characterize the lateral boundaries of the ice streams over regions that are many times the ice thickness in width. The ice streaming process that controls the position and width of these zones is dominantly stress concentrations at the boundaries of gravity-driven slab flow.

Geothermal flux and frictional heating from ice streaming contribute to melting at the base of the ice sheet. This water collects in areas of sufficiently low hydraulic gradient and is known to migrate in response to changes in the surface slope of the ice.

Application to Europa: Tension-fracture and shear-zone evolution proposed for the hemisphere-scale ridges (with bands) on Europa are a result of tidal flexure and non-synchronous rotation that may have

analogs in the onset, shear-margin and grounding-line evolution of the sub-continental scale Antarctic ice streams. Similarly, the migration of brines resulting from thermal or compositional diapirism on Europa may have analogs in the hydraulic evolution of the water systems beneath these ice streams. In addition, tension fracturing of the ice shelves and icebergs that form over the ocean downstream of the ice streams should provide an excellent analog for characterizing the ice–ocean interface of a tidal/tectonic Europan ice shell.

Recent Antarctic Observations: Begining in 2000, we have flown an advanced nadir pointing radar sounder on a Twin Otter aircraft over many of the Antarctic analogs described above. This fully coherent radar [7] operates in chirped pulse mode at 60 MHz and 15 MHz bandwidth. High and low-gain channels allow for recording both weak bed echoes and strong surface echoes simultaneously and without range-dependent gain control. Coherent data acquisition includes integrations of 16 returned radar signals about every 15 cm along-track. Pulse compression and unfocussed SAR processing using additional along-track integration were significant components of our data analysis.

Ice Streams: Figure 1A [8] shows an unprocessed subsurface profile across Kamb Ice Stream in West Antarctica. The figure also shows low- [Figure 1B] and high-resolution [Figure 1C] imaging obtained from synthetic aperture radar techniques for both reflecting interfaces and scattering centers.

Full 2-d focused SAR processing
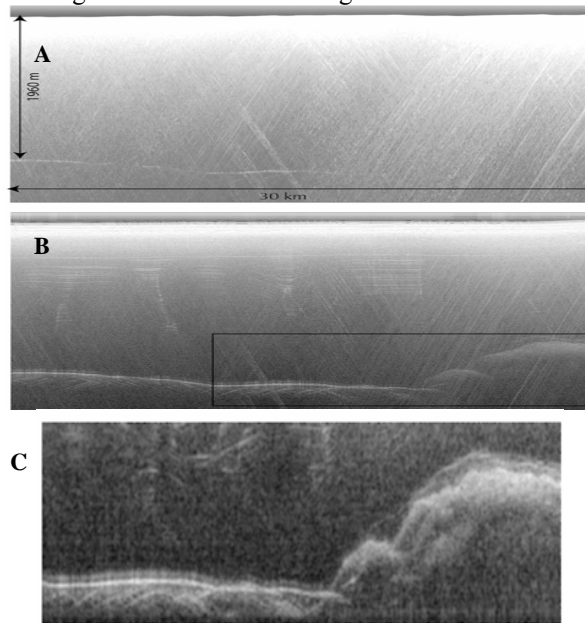
Figure 1: Radar sounding of Kamb Ice Stream, Antarctica.

Analysis methods applied to these data include using echo amplitudes to compute reflection coefficients for inferring the dielectric properties of subglacial materials. In addition, echo phase analysis provides the location of dominant scattering centers as well as interface roughness estimates. Combining the results from these independent analysis allows us to study in detail the evolution of both tensional and shear dominated ice stream margins, as well as the migration of sub-ice water associated with ice sheet evolution.

Icebergs: Figure 2 is profile across Antarctic iceberg B-15 which was surveyed in December 2004. The low gain data was analyzed to evaluate basal diffractors over a range of look angles and identify corner reflectors which were interpreted as the lower edges of basal cracks [9].
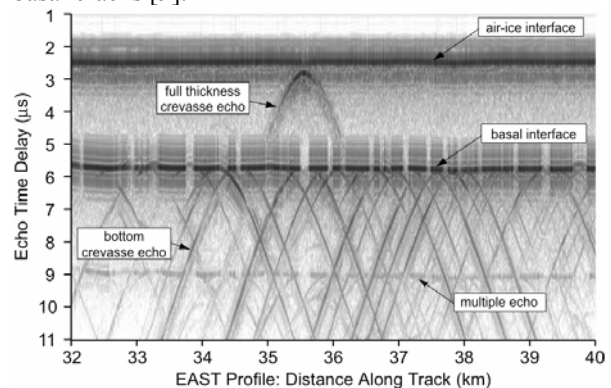
Figure 2. A radar sounding profile over iceberg B15A showing echoes from bottom crevasses at the ice-ocean interface. Also shown is the echo from a large water-filled crevasse extending through the 275~m thick iceberg. From [9]

The radar echo strengths are consistent with modeled predictions and the combined results were used to classify the crevasses. The classification includes major crevasses filled with sea water and incipient/freezing crevasses subject to marine ice accretion.

References: [1] Picardi G. et al. (2005) *Science* 310, 1925-1928. [2] Phillips et al., (2006) *AGU Fall Meet*. [3] Kivelson, M. (2000) *Science* 289, 1340-1343. [4] Blankenship D. D. et al. (1999) *University of Texas Institute of Geophysics, Report No. 184.* [5] Moore, J.C. (2000) *Icarus* 147, 292-300. [6] Chyba, C.F. et al. (1998) *Icarus* 134, 292-302. [7] Peters, M. E. et al. (2005) *J. Geophys. Res. 110,* B06303. [8] Peters. M. E. et al., in press, *IEEE Geosci. Remote Sensing Letters.* [9] Peters. M. E. et al., (2007), *IEEE Geosci. Remote Sensing Letters.*

OPPOSITION SURGES ON ICY AND ROCKY MOONS. B. J. Buratti, J. Bauer, and M. D. Hicks. Jet Propulsion Laboratory, California Institute of Technology (4800 Oak Grove Drive, Mailstop 183-501, Pasadena, CA 91109; bonnie.j.buratti@jpl.nasa.gov).

Introduction: Most planetary satellites exhibit a large increase in brightness as their faces become fully illuminated to an observer. This "opposition surge" occurs whether the body is rocky or icy, and it seems to occur on virtually all airless bodies. So far Umbriel [1] and asteroid 1173 Anchises [2] are the only such bodies that have been shown to lack a surge.

The classical explanation for the opposition surge is that it is due to shadow hiding: mutual shadows cast by surficial particles rapidly disappear as the surface becomes fully illuminated to the observer. With this physical explanation, the amplitude and functional form of the surge indicate important properties of the regolith, including the size and the size distribution of particles, and their compaction state [3]. These properties in turn yield important clues to the collisional history of the satellite and the existence of phenomena such as cold-trapping of volatiles, volcanic activity, and recent resurfacing.

More recently, a second type of opposition surge has been discovered that occurs at small solar phase angles (a fraction of a degree). These surges are very sharply peaked and they are not compatible with shadow–hiding mechanisms. First observed on Europa [4, 5], many more bodies have been shown to possess this sharp spike in brightness, including rocky bodies such as the Moon [6,7]. This surge has been attributed to coherent backscatter, a phenomenon in which photons following identical but reversed paths in a surface interfere constructively in the backscattering direction to increase the brightness by up to a factor of two.

Observations: An example of this second type of opposition surge is illustrated in Figure 1, which shows the solar phase curve of Triton observed from Table Mountain Observatory. Like many high albedo surfaces, Triton exhibits a very small phase coefficient (Triton's excursion in solar phase angle is limited to less than two degrees from the Earth). However, when the solar phase angle is smaller than 0.1 degree (which is not attained every year), the satellite exhibits a surge of about 15% in brightness. This phenomenon has important implications for the geometric and bolometric Bond albedos for the satellites that exhibit it.

A similar but smaller surge has been observed on the Moon [7], although the lunar solar phase is much larger for solar phase angles greater than one degree, and on Enceladus [6]. Unpublished observations of the Saturnian satellites also show a sharply peaked surge.

Modeling: Unlike shadow hiding in a loose regolith, which predominantly affects the singly scattered component of radiation, coherent backscatter is a multiple scattering phenomenon and it should be most important for high albedo surfaces such as those of icy satellites. In the visible, the theory suggests that it should be important only at very small solar phase angles [8]. Because the width of the coherent backscatter opposition surge is greater at longer wavelengths (since the path length of a photon is greater), measurements at different wavelengths are particularly valuable as diagnostic and modeling tools. It is important to separately account for and model coherent backscatter, so the component of the surge due to shadow hiding can be modeled in terms of the microtexture of the surface.
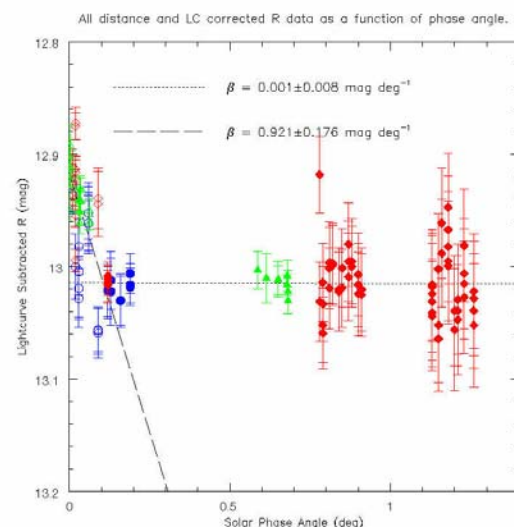
Figure 1. The solar phase curve of Triton.

References: [1] Buratti, B. J. et al. (1992) *A.J. 104,* 1618-1622. [2] French, L. et al. (1987) *Icarus 72,* 325-341. [3] Irvine, W. (1966) *JGR 71,* 2931-2937. [4] Buratti, B. J. et al. (1988) *Nature 333,* 148-151.[5] Domingue, D. et al. (1995). *Icarus 115,* 228-249. [6] Verbiscer, A. et al. (2004) *Icarus 173,* 66-83. [7] Buratti, B. J. et al. (1996) *Icarus 124,* 490-499. [8] Hapke, B. (1990). *Icarus 88,* 407-417.

The Enceladus Water Plume and Its Interactions with the Saturnian Plasma. M.H. Burger[1], C. Paty[2], E.C. Sittler[1], R.E. Johnson[3], [1]NASA/GSFC, Greenbelt, MD, 20771, Matthew.Burger@gsfc.nasa.gov; [2]Southwest Research Institute, San Antonio, TX; [3]University of Virginia, Charlottesville, VA

Introduction: The water plume at Enceladus' south pole ejects ~300 kg/s of neutral H_2O molecules into Saturn's inner magnetosphere [1][2]. The low plasma density and cool electron temperatures result in low loss rates which give this material time to spread out in their orbits around Saturn to form a full neutral water torus at Enceladus' orbital distance. Because the ejection speed from Enceladus is slow compared to the orbital velocity, this torus is closely confined to Enceladus' orbital distance [3] (Figure 1).
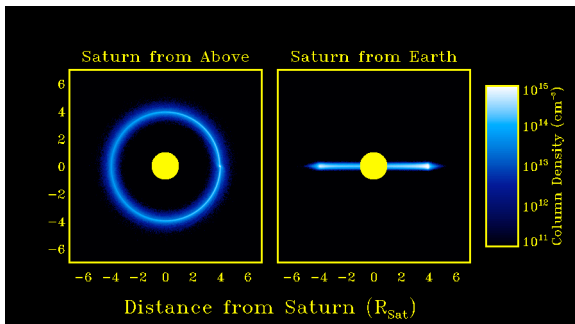
Figure 1: Enceladus water torus as seen from above Saturn's north pole (left) and from Earth (right). The brightness enhancement seen at the rightmost point in the torus is due to increased water density in the Enceladus plume.

Mass loading of material in the Enceladus plume was reported by both the Cassini Plasma Spectrometer (CAPS) [4] and Cassini Magnetometer (MAG) [5]. The dominant mass loading process is charge exchange between water molecules in the plume and the ambient plasma ions [2]. Acceleration of the fresh pickup ions slows the plasma as it flows through the plume region. Johnson et al. [3] point out that the large abundance of H_3O^+ in the plasma [4] implies charge exchange and ion-neutral reactions are occurring at relative velocities much lower than the co-rotation velocity (26 km/s). Neutrals created through charge exchange at velocities less than $2^{1/2}$ times the orbit speed are gravitationally bound to Saturn and are a possible source of secondary tori [3], such as the OH cloud observed by HST [6] and atomic oxygen cloud observed by UVIS [7].

Mass Loading Near Enceladus: We use a Monte-Carlo model of neutrals escaping from the south pole to populate the neutral torus. H_2O ejected from the surface are ionized through charge exchange reactions, electron impact ionization, and photoionization. Because the latter two processes are slow and charge exchange dominates, there is little net change in

the plasma ion content, although the region near the plume is a region of enhanced plasma mass loading due to production of fresh pickup ions through charge exchange and ion-neutral reactions. These reactions can alter the plasma composition through the addition of H_2O^+ created from the neutral H_2O and the removal of O^+ and OH^+ which are neutralized and continue on trajectories at their original velocity but unaffected by Saturn's magnetic field.

The acceleration of pickup ions from the neutral velocity (approximately Enceladus' orbital speed of 13 km/s) to full magnetic field co-rotational speed (39 km/s) produces a perturbation in the magnetic field as field lines drape around the ionized obstacle [5][8]. Our estimate of the mass loading rate in a water plume with a source rate of 300 kg/s, consistent with the stellar occultation observations by UVIS [1], is ~2-3 kg/s, in agreement with modeling of the mass loading required to produce the observed perturbations in the MAG data [8]. We are extending the modeling analysis of Burger et al. [2] to understand the effects on plasma flow velocity, density, temperature, and chemistry as it flows through the H2O plume.

Modeling Neutral Tori: As shown by Johnson et al. [3], the large H_3O^+ fraction in the Saturnian magnetosphere requires a low velocity collisions between ions and neutrals. There are two regions in which these reactions can occur: near Enceladus in the water plume or farther from Enceladus (although still at Enceladus' orbital distance) in the water torus. Although slowing might be expected in the plume due to the enhanced mass loading, Khurana et al. [8] have shown that no significant slowing occurs. In the torus, the large ion temperatures produce thermal velocities comparable to the bulk flow velocity such that a fraction of the ions will have a low velocity relative to the neutrals. We explore the charge exchange rate in the torus between water group ions and H_2O neutrals necessary to produce the OH and O clouds which have been observed between 3 and 10 R_S from Saturn.

References: [1] Hansen, C.J. et al. (2006), *Science, 311,* 1422-1425. [2] Burger, M.H. et al. (2007), *JGR*, in press. [3]Johnson, R.E. et al. (2006), *ApJ, 644*, L137. [4] Tokar, R. L. (2006), *Science, 311*, 1409. [5] Dougherty, M.K. et al. (2006), *Science, 311*, 1406-1409. [6] Shemansky, D.E. (1993), *Nature, 363,* 329-331. [7] Esposito, L.W. (2005), *Science, 307*, 1251. [8] Khurana, K.K(2007) *JGR,* in press.

FLUVIAL FLOW ON TITAN: CONTEXT FOR GEOMORPHIC INTERPRETATION. D. M. Burr[1], [1]Carl
Sagan Center, SETI Institute (515 N. Whisman Rd, Mountain View, CA, 94043, USA, dburr@seti.org).

Introduction: Previously hypothesized on the basis of Titan's volatile-rich atmosphere and surface conditions [e.g., 1], fluvial flow now appears confirmed by Cassini-Huygens imagery of Titan's surface at multiple wavelengths. Data from the Titan Radar Mapper, the Imaging Science Subsystem (ISS), the Visual and Infrared Mapping Spectrometer (VIMS) and the Hugyens Descent Imager/Spectral Radiometer (DISR) have all been interpreted as showing fluvial channels [e.g., 2,3,4,5]. In support of such interpretation, this abstract first reviews the theoretical basis for morphological similarity between terrestrial and Titan fluvial features, then discusses an approach for estimating discharge for fluvial channels on Titan.

Theoretical work: Fluvial channels and channel networks result from erosion of sediment or bedrock and subsequent transport of this eroded material. Eventual deposition of this sediment can also furnish evidence of fluvial processes. Comparing each of these three processes under terrestrial and Titan conditions lays out a theoretical basis for fluvial channel and network formation on Titan.

Erosion. Erosion occurs in terrestrial channels through multiple processes. Quarrying is the plucking of blocks of material from the channel floor, and requires preparation of the bedrock through hydraulic wedging of sediment into pre-existing discontinuities [6]. Abrasion is the gradual removal of material from the channel rock surface through forcible impact by sediment in the flow [6], and effected by material traveling as bedload on the channel floor; experiments show that fine-grained sediments traveling in suspension make poor abrasive tools [7]. Lastly, cavitation results when sufficiently high local flow velocities produce low pressure resulting in bubbles; the advection and subsequent collapse of these bubbles produce a micro-hammering effect [8, 9, 6].

Each of these processes depends on external circumstances, such as the pre-existence of discontinuities and the availability of appropriately sized sediment. For similar flow conditions of slope, discharge, and sediment supply, basic theoretical considerations and simple laboratory experiments show that these processes should operate at similar rates on Titan as they do on Earth [10]. An integrated model of precipitation, open-channel flow, and sediment transport [11] supports the interpretation of features at the Hugyens landing site [5] as being formed by rainfall and overland flow.

Transport. Sediment is transported by flowing liquid in three modes [e.g., 12]. Bedload moves by roll-ing, sliding, or saltating along the channel floor. Suspended load is material keep aloft in the water column by turbulence. And washload is the finest fraction of sediment, which is evenly distributed in the water column. These categories are distinguished by ratioing the settling velocity of the particle to the flow shear velocity (a proxy for the upward forces on a particle) [13, 14]. Threshold values of this ratio are derived experimentally for each category [see 15 and references therein]. Because the settling velocity of a given size particle changes with gravity, particle density, and fluid viscosity, threshold curves must be re-calculated for these parameters.

Following work by [15] on Martian fluvial sediment transport, such calculations have been presented for Titan fluvial sediment transport [16]. The results show that flow velocities and minimum flow depths on Earth and Titan (Fig. 1) are within an order of magnitude of each other for a given grain size.

Deposition. The Hjulström curve shows that sediment deposition occurs at lower flow velocities than does sediment erosion [e.g., 12]. To be recognizable from orbit as fluvial, sediment deposits must form distinct, coherent structures such as subaqueous dunes, streamlined bars, or deltas. Such bedforms are composed of bedload (and, to a much lesser degree, suspended load); washload is not deposited except as a thin layer in very quiescent lakes (e.g., as varves). The Huygens data are interpreted as showing large, water-ice rich sediment rounded during transported [5], of a size that would reasonably move as bedload on Titan. In comparison, organic sediments are orders of magnitude smaller [5], of a size that would reasonably move as washload. This difference in size and therefore transport category between water ice and organic sediment grains implies that on Titan bedforms within fluvial channels and deltaic deposits at channel mouths should be comprised primarily of water ice [17]. In contrast, organic sediment should be carried through the channel system and, where deposited in terminal seas or lakes due to infiltration or evaporation, should form a drape. This provides a criterion for identifying fluvial deposits.

Summary. For all other conditions being equal, erosion and sediment transport processes should operate at similar rates on Titan as on Earth. Fluvial deposits are expected to be composed primarily of water ice sediment, not organic material.

Discharge estimation: Given that fluvial processes are physically similar on Earth and on Titan, we can expect a similar morphology between terrestrial

and Titan fluvial channels for similar inputs (e.g., precipitation rate and amount). This similarity provides a handle for calculating discharge from Titan channels using terrestrial empirical relationships.

Instantaneous or volumetric discharge is a fundamental parameter in fluvial geomorphology, and of great interest for its usefulness in quantifying the hydrologic cycle on Titan. It refers to the volume of liquid and sediment moved per time and is estimated as the product of flow width, depth, and velocity. The same discharge on a lower gravity body requires a greater width and depth than on a higher gravity body, in order to account for the lower flow velocity due to the smaller driving force [18]. Given a similarity of process, empirical data of terrestrial river width and discharge [19] may be scaled for extraterrestrial gravity [20]. Following this approach, the proportionate increases in flow width for any given discharge value may be calculated for Titan [see 21 for results].

As discussed by [20], distinguishing the true flow dimensions is necessary for valid application of this approach. Flow channels commonly sit within alluvial valleys, as can be seen in terrestrial examples, and application of this technique to the valley instead of the inset flow channel would proportionately overestimate the discharge. The importance of this distinction is demonstrated by [11], who estimate a flow width of only 1-30 meters for the Huygens channels.

Thus, an accurate discharge calculation using this approach requires determination from imagery of an inner channel. Although such a discovery has not yet been widely published, inner channels, bedforms, or other features indicating true flow width may well be discernable in high-resolution Radar images. In addition, the combined use of multiple datasets has revealed information about the morphology of inferred fluvial features that was not distinguishable in either dataset alone [e.g., 4]. Such cross-data correlations will contribute to untangling the fluvial geomorphology of Titan, and making subsequent inferences into Titan fluvial processes.

References: [1] Ori G.G. et al (1998) *Planet. Space Sci.* 46 (9/10), 1417–1421. [2] Elachi C. et al (2006) *Nature* 441, 7094, 709-713, doi:10.1038/nature04786. [3] Porco C. C. et al. (2005) *Nature* 434, 159-168. [4] Barnes J. W. et al. (2007) *LPSC XXXVIII* Abstract #2028. [5] Tomasko M. et al. (2005) *Nature* 438, 763-778. [6] Hancock G. S. et al. (1998) AGU Monograph 107, p. 35-60. [7] Sklar L.S. and Dietrich W.E. (2001) *Geology* 29(12), p. 1087-1090. [8] Barnes H.L. (1956) *Am. J. Sci.* 254, 493-505. [9] Hammitt F.G. (1980) Cavitation and Multiphase Flow Phenomena, McGraw-Hill, 423 pp. [10] Collins G. C. (2005) *GRL* 32, L22202, doi:10.1029/2005GL024551. [11] Perron J. T. et al. (2006) *JGR* 111, E11001, doi:10.1029/2005JE002602. [12] Knighton D. (1998) Fluvial Forms and Processes, Arnold, 383 pp. [13] Rouse, H. (1937) *Trans. Am. Soc. Civ. Eng.* 102, 463–543. [14] Bagnold, R. A. (1966) U.S. Geol. Surv. Prof. Paper 422-I. [15] Komar, P. D. (1980) *Icarus* 42, 317–329. [16] Burr D. M. et al. (2006) *Icarus* 181, 235-242, doi: 10.1016/j.icarus.2005.11.012. [17] Burr, D. M. (2007) *Lunar Planet. Sci.* XXXVIII Abstract #2222. [18] Moore, J. M. et al. (2003) *GRL* 30, 2292, doi: 10.1029/2003GL019002. [19] Osterkamp W. R. and Hedman E. R. (1982) U.S. Geological Survey Professional Paper 1242, 37 p. [20] Irwin R. P. et al. (2005) *Geology* 33(6), 489-492, doi:10.1130/G21333.1. [21] Jaumann, R. and 15 co-authors (2007) *Lunar Planet Sci XXXVIII*, Abstract# 2100.
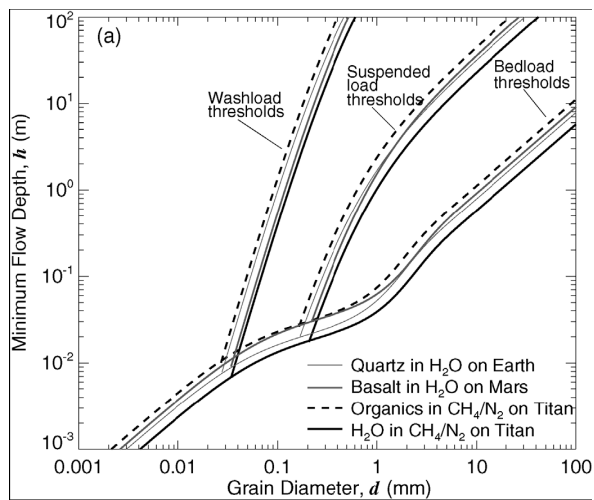
Figure 1: Plot showing similar minimum flow depths required to carry quartz on Earth, basalt on Mars, and organic material and ice on Titan over an arbitrary slope of 0.001 m/m. (from [16])

SEARCHING FOR CONSTRAINTS ON THE CHRONOLOGY OF THE OUTER SOLAR SYSTEM FROM SATELLITE GEOPHYSICS.

J. C. Castillo-Rogez[1], D. L. Matson[1], T. V. Johnson[1], J. I. Lunine[1,2], (1) Jet Propulsion Laboratory, California Institute of Technology, 4800 Oak Grove Drive, Pasadena, CA 91109. (2) Lunar and Planetary Lab, 1629 E. University Blvd. Tucson, AZ 85721-0092.

Introduction: Recent astronomical observations suggest that the lifetime of gas and dust sufficient for making giant planets around Sun-like stars may be typically only two to five million years [1, 2]. This time constraint can now be met by formation models for giant planets [3, 4]. Thus if short-lived radioactive isotopes (SLRI) with half-lives of ≤ 10 My were present in the circumstellar disk, they would be included in any planets formed. These isotopes would supply heat as they decayed. The challenge is to search for observations that test the validity of this scenario. In the Solar System, we believe that models of medium-sized satellites can be used for this purpose. Initial results suggest that they can also yield constraints on the time of formation and chronology of the outer Solar system. We address the reasons supporting this suggestion, status of our understanding of this problem, and the outstanding issues.

Context: The SLRI that are most significant for modeling the thermal evolution of Solar system objects are ^{26}Al and ^{60}Fe. Their origin (^{26}Al from Solar X-Wind, [5]; or both from supernova injection, [6]), their distribution in the early Solar system, and their initial concentrations are still matters of some debate. The recent discovery of calcium-aluminum inclusions in samples of the comet Wild 2 [7] (*Stardust* mission) is the latest major development. We use the CAI formation date as the reference time for our satellite models discussed below and the initial concentrations of ^{26}Al and ^{60}Fe have been defined for that time on the basis of meteorite studies.

Small satellites in the outer solar system (less than 1000 km in radius) provide the right conditions for the heat from SLRI to express itself in terms of observable geophysical properties. Temperatures of accreting materials are low (less than 100 K), and the small satellites gain a negligible amount of heat during accretion compared to the larger icy satellites. It is difficult to heat them with long lived radioactive isotopes (LLRI) since they lose heat too fast. That is, the time scale required for LLRI decay to heat the interior up to water ice creep temperature is much longer than the time scale for these objects to cool. Whether or not tidal dissipation is a significant heat source is a crucial issue.

The possible geophysical significance of SLRI was first mentioned by [8]. The modeling of icy satellites that included SLRI was suggested by several authors [e.g., 9]. However these studies used the amount of SLRI included in the models as a free parameter. Also, they did not develop the relationship between SLRI content and accretion date. The abundance of SLRI in the rock fraction is now better known, except for a large uncertainty in ^{60}Fe. The models must include this range. Otherwise, the main variable is the date of accretion. Within the uncertainties of the ^{60}Fe abundance, that date and the rock fraction fix the amount of radioactive isotopes in the model.

We have been searching for evidence that SLRI were available in the early, outer Solar system, using coupled thermophysical-dynamical modeling of the icy satellites. If SLRI are present, then the main parameters determining the satellites' evolution are the silicate mass fraction x_s and the time of formation. Significant SLRI heating lasts no longer than the first 10 My after accretion. Depending on x_s, SLRI decay heat will affect the evolution of porosity, thus lithospheric properties, or also result (for large x_s) in rapid, and complete, melting of the ice, drastically affecting the long-term evolution of the satellite.

First Results: We have suggested [10] that Iapetus formed between 2.5 and 5 My after CAIs production. Our objective was to explain Iapetus' non-hydrostatic shape and current spin rate. We showed that heat from SLRI decay results in early porosity decrease, necessary to maintain the 33-km non-hydrostatic difference between the equatorial and polar radii. The presence of ammonia could have played a similar role in decreasing porosity. However, ice thermal conductivity (even with ammonia present) is large and promotes rapid cooling before despinning could happen. We found that SLRI are needed to promote conditions suitable for tidal dissipation that triggered Iapetus' despinning and brought it to its present, synchronous, spin rate.

This study highlighted a series of uncertainties in the current understanding of icy satellites. First, the importance of convection in satellites, which are small, cold, and volumetrically heated for most of their history is currently work in development by Sotin *et al.* and Barr and McKinnon. Also, most large icy satellites undergo significant melting during accretion have already partially differentiated by the end of accretion. In small satellites, the internal temperatures progress slowly to the ammonia-water eutectic. The fate of this ammonia hydrate melt as a function of initial ammonia content has not been modeled. Neither has been its role in tidal dissipation. As mentioned above, the conditions in which tidal dissipation can become a significant heat source is a major modeling issue. No data are available for dissipation under the conditions of forcing frequency and temperature that apply to

these satellites.

An alternative approach to the latter issue consisted of constraining Mimas' dynamical evolution from its current, anomalously large free eccentricity [11]. We found that the dissipation factor of Mimas' ice between 80 and 220 K (the maximum temperature achieved in Mimas for times of formation longer than 6 My after CAIs), is greater than $3x10^3$

There is a need for experimental data on the dissipative properties of planetary materials at tidal forcing frequencies. This is the reason why this work has served as a rationale for developing a new laboratory at the Jet Propulsion Laboratory to measure, among other properties, the dissipation factor of various ices, for temperature as low as 80 K [12].

The Importance of Comparative Planetology: The concept that we can use the medium-sized Saturnian satellites to date the formation of the outer Solar system is viewed as "*an extraordinary claim that requires spectacular evidence*" (Steve Saunders, personal communication). We argue that the Mimas-Enceladus paradox is such evidence. It is the spectacular demonstration that tidal friction in a cold satellite is a marginal heat source. Both Mimas and Enceladus have the same, short, cooling time scale, and should follow a similar evolutionary path if they did not accrete SLRI. However, the warm temperatures reached in Enceladus' interior, necessary to explain the south pole geyser's content in molecular nitrogen and methane [13] cannot be explained by models that do not include SLRI. If we consider that Enceladus contains three times as much rock (in mass) as Mimas, then the solution to the paradox is obvious. SLRI heating results in early melting and differentiation of a rocky core in Enceladus [14].

More generally, comparative planetology and multidisciplinary studies are keys to progress in this research. Comparative planetology of satellites at the scale of the Saturnian system and between the Uranian and the Saturnian satellites is crucial because these objects cover a large range of densities and sizes (Figure 1). It is then possible to compare pairs of objects (e.g., Mimas and Enceladus, Rhea and Iapetus, Enceladus and Ariel, etc.) A multidisciplinary approach is also necessary to integrate available observational constraints in models. It might not be possible to find evidence of SLRI inclusion during accretion for all the satellites, considered individually, because in some cases there is little remaining evidence about their early history. Crater distribution, internal structure, current shape, hydrostatic equilibrium, geological activity can be symptomatic of early conditions. Extreme end-members, *e.g.*, rock-rich satellites, require special attention.

A rapid survey (Figure 1) indicates that several satellites share with Enceladus a relatively high x_s and dynamical properties favorable to significant tidal heat production over the long term. This is the case for example of Ariel. Could both Ariel and Enceladus have undergone a similar early history involving hydrothermal activity? Could Ariel currently exhibit

intense geological activity? Can the difference in formation times of the Uranian and Saturnian satellites be assessed by studying these satellites?

In the same vein, could the fact that Callisto might be partially differentiated (i.e., late times, [15]), provide a further clue regarding the chronology of the outer solar system?

Figure 1. *Distribution of outer planet medium-sized satellites as a function of their rock mass fractions and the theoretical amount of tidal heating per kilogram of ice.*
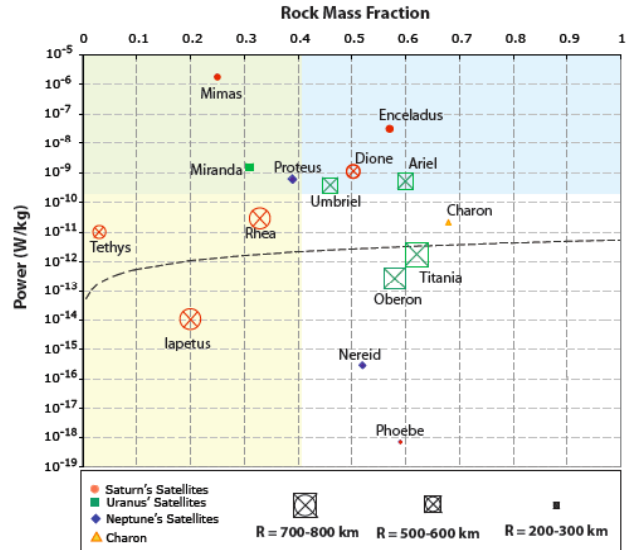
Summary: We propose a new research direction whose implications are many. First, evidence that [26]Al was present in the early history of the outer Solar system, would constrain the origin of this isotope, and as such the origin of the Solar system itself. This research would also open the door to coordinating the different chronological scales used by the different fields in planetary sciences: cosmochemical, dynamical, geochronology, crater counting, and now satellite geophysics. As such, it is crucial that efforts be undertaken to search for further evidence of the effects of SLRI on outer Solar system objects, or for alternative approaches to successfully model observations at these satellites.

References: [1] Najita and Williams (2005) *ApJ* 635, 625. [2] Calvet et al. (2005) *ApJ* 630, 185. [3] Mayer et al. (2002) *Science* 298, 1756. [4] Boss (2007) *ApJ* 661, L73. [5] Shu et al. (1993) *Science* 271, 1545. [6] Vanhala and Boss (2005) *ApJ* 575, 1144. [7] McKeegan (2006) *Science* 314, 1724. [8] Urey (1955) *PNAS* 41, 127. [9] Prialnik and Bar-Nun (1991) *ApJ* 355, 281. [10] Castillo et al. (2007a) *Icarus* in press. [11] Castillo *et al.* (2007b) in preparation. [12] Hays *et al.* (2007) this workshop. [13] Matson *et al.* (2007) *Icarus* 187, 569. [14] Matson *et al.* (2007), this workshop. [15] McKinnon (2006) *LPS* 37, 2444.

BRIGHT TERRAIN TECTONICS AND THE EVOLUTION OF GANYMEDE.   Geoffrey C.

Collins,   Physics   and   Astronomy   Dept.,   Wheaton   College,   Norton   MA   02766,
gcollins@wheatoncollege.edu.

Introduction: The bright grooved terrain that covers two thirds of the surface of Ganymede records a dramatic period in Ganymede's evolution. Many models have been proposed to explain what happened on Ganymede, including internal differentiation [1, 2], an episode of enhanced tidal heating and internal melting [3, 4], hemispheric-scale convection cells [5], nonsynchronous rotation [6], and/or tidal despinning followed by polar reorientation [7]. All of these mechanisms have also been proposed in one way or another to have affected other satellites in the outer solar system. Like its smaller cousins Enceladus, Dione, Tethys, Miranda, and Ariel, Ganymede's surface exhibits both old, heavily cratered terrain and younger terrain resurfaced by tectonic (and possibly also cryovolcanic) activity. As a large type locality for icy satellite tectonic processes, it is important to understand the origin of grooved terrain on Ganymede.

The record of bright grooved terrain: The first step in observationally addressing the evolution of Ganymede is to decipher the message recorded by the grooved terrain. The lineaments that make up grooved terrain are divided into thousands of "sets," where grooves share a similar orientation and morphology within each set. Their cross-cutting relationships show that the stress direction and strain magnitude has changed over time in various regions of Ganymede. Some groove sets are extensive, covering thousands of kilometers in length. In order to link grooved terrain observations with the theoretical predictions that come from various models of Ganymede evolution, we must compile a strain history of Ganymede. This compiled strain history, representing the best of our observational knowledge so far, answers the questions: What was the direction of least compressive stress in the lithosphere while grooves were forming? How much did the surface deform in response? How did the direction of stress change over time? Let us address these questions in turn.

The direction of least compressive stress is a fundamental prediction of many models to ex-plain the formation of grooved terrain. Measuring this paleo-stress direction involves linking the observed grooves to a stress orientation. At high resolution, the features that make up grooved terrain appear to be almost all extensional features, such as tilt block normal faults or horst and graben sets [8], and quantitative analysis of craters as strain markers has backed up this morphological interpretation [9]. Some transtension and strike-slip motion has been observed [8, 9, 10], but the motions appear to be relatively small. No unambiguous contractional features have been observed. Thus, if grooves predominantly represent extensional strain, the direction of least compressive stress should have been predominantly orthogonal to the grooves at the time of their formation. A database of the locations and orientations of all the grooves on Ganymede observable with current data has been assembled [11], and recently revised based on the updated control coordinate network [12]. This database serves as the foundation for further understanding of global groove tectonics.

The strain magnitude in grooved terrain has been measured in two different ways. Almost all large craters start very close to circular, and any crater that has been deformed by grooved terrain formation makes an ideal strain marker. We have developed a method of using craters as strain markers that disentangles the pure shear and simple shear components of the strain [9]. Using this method, we have found some narrow sets of high-relief grooves that have extended by over 50% (and one well over 100%). A more areally extensive set of moderate-relief grooves exhibits 15% extensional strain. Other areas of bright terrain with very subdued groove morphologies have insignificant strain (0% is in the error bars). These strain measurements using crater geometry have been backed up by independent measurements using the geometry of the normal faults themselves [13].

Cross-cutting relationships between groove sets can be a guide for unraveling the history portion of the strain history. First, we have taken the groove database and separated it all into groove

sets based on co-location, orientation, and morphology (a preliminary version of this is in [14]). Next, these groove sets need to be put into a time sequence. This can be done manually for small areas [15, 16], but with several thousand groove sets across the globe, a full manual sort is prohibitively confusing. Computers can assist the time sequence sorting process, by finding the best sort through a large, sometimes ambiguous data set [17]. The investigator keeps track of local cross-cutting relationships (and the confidence in those interpretations), and the computer takes that information and performs a sort that preserves the most confident interpretations. This has been tested in a couple of large and complex regions of Ganymede (e.g. [18]), and we are presently working our way up to a full global groove sequence sort.

Preliminary results: There are two pieces of observational information that we can use to discriminate among the proposed mechanisms for grooved terrain formation. One of them is the total amount of strain represented by grooved terrain, and the other is the stress orientations and their evolution with time.

The large amount of extension observed on Ganymede may be driven by internal melting during a past heating event, which could produce about a 1.5% increase in surface area [3], or by internal differentiation, which would produce an increas in surface area of up to 6% [2]. By taking the strain measurements made in high resolution Galileo observations and applying them to similar areas of bright terrain seen globally at lower resolution, we have been able to estimate the total amount of extension represented by grooved terrain. The exact answer depends on the details of assumptions about which kind of terrain observed at moderate resolution represents what amount of strain observed at high resolution, but the estimate of surface area increase is nominally 7%, and does not go lower than 4%. Thus, examining models of interior differentiation in more detail may be a promising avenue. However, just because we don't see evidence for contractional deformation doesn't mean it can't be hiding through compaction and creep of the lithosphere elsewhere [19], so the observed surface area expansion is not a completely hard constraint at this point.

Regions of Ganymede have been sorted into time sequences, but these are still in the process of being linked together into a global picture of the time sequence of grooves. However, we do have a global map of the youngest sets of grooves, and these have been run through a comparison with various sources of global stress fields to find the least-squares fit of a stress field to the observed grooves. So far, the best fit stresses to the youngest set of grooves on Ganymede is stresses due to differentiation and 60° of nonsynchronous rotation. As we go farther back in the time sequence, we will see if this relationship holds up, and if there is a logical progression of stresses with time (as one would expect with nonsynchronous rotation).

The limitation in much of this work is that, though we have moderate resolution (1-3.5 km/pixel) data for most of the surface of Ganymede, we must interpret the strain and time sequence details based on several small high resolution "postage stamps" collected by the Galileo mission. A future mission to the Jupiter system can collect much more uniform and high resolution data to help us decipher the history of Ganymede and its implications for the mechanisms that drive icy satellite tectonics.

References: [1] Squyres, *GRL* (1980); [2] Mueller and McKinnon, *Icarus* (1988); [3] Showman *et al.*, *Icarus* (1997); [4] Zuber and Parmentier, *JGR* (1984); [5] Bianchi *et al.*, *Icarus* (1986); [6] Zahnle *et al.*, *Icarus* (2001); [7] Murchie and Head, *GRL* (1986); [8] Pappalardo *et al.*, *Icarus* (1998); [9] Pappalardo and Collins, *J. Struct. Geol.* (2005); [10] DeRemer and Pappalardo *LPSC* (2003); [11] Collins *et al.*, *LPSC* (2000); [12] Becker *et al.*, *LPSC* (2001); [13] Michaud and Collins, *LPSC* (2007); [14] Patterson *et al.*, *LPSC* (2007); [15] Collins *et al.*, *Icarus* (1998); [16] McBee and Collins, *LPSC* (2002); [17] Crawford and Pappalardo, *Astrobiology* (2004); [18] Martin *et al.*, *LPSC* (2006); [19] Pappalardo and Davis, this meeting.

NEAR-INFRARED SPECTRA OF KUIPER BELT OBJECTS: MORE THAN JUST WATER ICE.

Jason C. Cook[1], **Steven J. Desch**[2], **Ted L. Roush**[3] [1]Southwest Research Institute, Boulder, CO, 80301 (jccook@boulder.swri.edu), [2]Arizona State University, Tempe, AZ, 85287, [3]NASA Ames, Moffett Field, CA 94035.

Introduction: Remote sensing via near-infrared (NIR) spectroscopy is the only method available to examine the surface composition of Kuiper Belt Objects (KBOs). Crystalline water ice, which requires $T > 100$ K for formation, has been observed on several KBOs including Charon. In addition to water ice, ammonia hydrates have also been seen on Charon [1], and possibly Quaoar [2]. Both ices have relatively short lifetimes (few Myrs, 1) when exposed on the surface [1] and requires a mechanism like cryovolcanism [1-3].

Observations: Understanding whether or not cryovolcanism occurs on Charon and KBOs requires obtaining NIR spectra of KBOs, preferably similar in size to Charon ($r \approx 606 \pm 8$ km; 4). [2] obtained spectra of (50000) Quaoar ($r \approx 630 \pm 90$ km; 5) from 0.9 to 2.5 μm using the CISCO spectrograph on Subaru. The spectrum shows a red slope of $27 \pm 1\%/1000$ Å, and features due to crystalline water ice at 1.5, 1.65 and 2.0 μm. [2] also suggested the presence of a feature at 2.21 μm, like that seen on Charon. Unpublished K-band observations found in the Subaru archive from 2005 show this feature is present and it shifts from night to night suggesting ammonia hydrate is found in several hydration states. Fig. 1 shows the average observations from 2004 and 2005. The data are rebinned to 60 Å/pix, and shown with 3σ error bars.

Spectra from 1 to 2.5 μm of (90482) Orcus ($r \approx 473 \pm 36$ km; 6) were originally obtained by [7] using the ISAAC instrument on the VLT. The spectrum has a neutral to blue slope similar to Charon. [7] reported the presence of the 1.5 and 2.0 μm features of water ice, but lacked the signal to positively identify the 1.65 and 2.21 μm feature. Additional Orcus data from 2005 were found in the Gemini North archives using the NIRI spectrograph. These observations showed large features near 1.23 and 2.23 μm, the later suggests pure NH_3. These data were observed on only one occasion and appear weak when averaged with the 2004 data. If these features are real, they suggest Orcus has a patchy surface. The data from both runs are combined in Fig. 2 at 60 Å/pix resolution with 3σ error bars.

Finally, spectra of (55636) 2002 TX_{300} were obtained using the Gemini North NIRI spectrograph in August 2003. While the signal-to-noise of this data is quite low, it is an improvement in signal over what was originally reported by [8]. Like Orcus, the NIR slope of 2002 TX_{300} is neutral-to-blue [9]. These spectra show deep water ice features, and strongly suggest crystalline ice is present. A depression in the spectrum around 2.25 μm suggests ammonia may also be present here too, but higher quality data are clearly needed to make a definitive detection. The observations of 2002 TX_{300} are shown in Fig. 3 at a resolution of 60 Å/pix resolution with 3σ error bars.

Hapke Models: Hapke models were developed for each KBO. The spectral components were broken into three groups of materials: ices, blue and red absorbers. The ices examined included amorphous and crystalline water ice [10,11,12], NH_3 [13] and its hydrate [14], CO_2 [15,16], and CH_3OH [17]. The blue materials included the Charon dark neutral absorber (*dna*, 18), the phyllosilicates: montmorillonite [19], kaolinite [20], and serpentine [21], and the salt, mirabilite [22,23]. The Charon *dna* was originally developed by [18] to improve fits to Charon's spectrum. *Dna* likely represents a composite of several materials which is slightly red at $\lambda < 1.9$ μm, and blue elsewhere. The phyllosilicates and salt all have different blue slopes, and all except mirabilite lack any identifiable features other than those at 1.4 and 1.9 μm due to the presence of water in these minerals. The red materials include amorphous carbon [24], the silicate olivine [25], and Triton, Titan and Ice I tholins [26-28].

Initial models of Quaoar mix water ice, one blue and one red material. These models minimize χ^2 for a mixture of water ice, Triton tholin and *dna*. This model is shown as the blue curve in Fig. 1. Additional models were then developed substituting *dna* for other red and blue components until a similar, if not smaller, χ^2 was found. A mixture of water ice, Triton and Titan tholins, kaolinite, and ammonia hydrate best matched the spectrum of Quaoar (red curve in Fig. 1). The various other ices had little, if any, effect. Similar procedures were followed for Orcus and 2002 TX_{300}. The Orcus model use mixture of water ice, Triton tholin, montmorillonite, and ammonia hydrate, and the 2002 TX_{300} model uses a mixture of amorphous and crystalline water ice, montmorillonite and mirabilite.
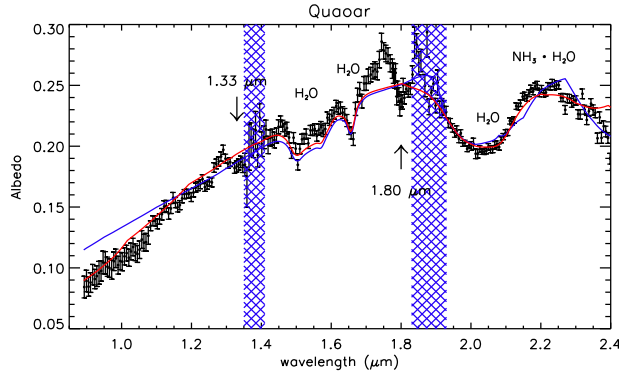
Fig. 1 NIR spectrum of Quaoar.
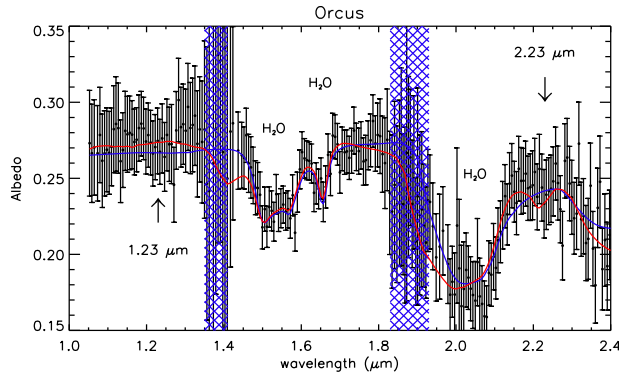
Fig. 2 NIR spectrum of Orcus.
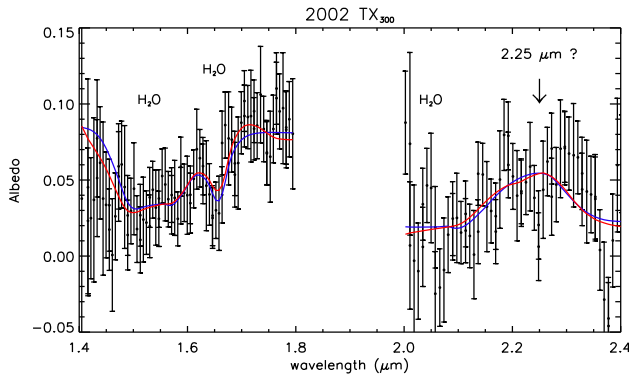
Fig. 3 NIR spectrum of 2002 TX$_{300}$.

Discussion: Absent from the fits are the features seen at 1.80 and 1.33 μm on Quaoar and 2.23 and 1.23 μm on Orcus. The 1.23 and 1.33 μm features are near H$_2$O features, but do not make a match. The feature at 1.80 μm on Quaoar appears close to the edge of an optical window, but maintains a signal representative of most of the data. The feature also does not appear to be an artifact of removing the telluric and solar spectra and it is present in two grating positions. [2] likely did not

report it because they lacked the additional 2005 data. The asymmetric shape of this feature resembles montmorillonite and mirabilite features, however shifted blueward 0.1 μm and redward 0.03 μm, respectively. [29] measured the effects of temperature on several salts and showed the 1.77 μm feature of mirabilite shifts to shorter wavelengths at colder temperatures, opposite from what is needed. However, a similar feature in MgSO$_4 \cdot$12H$_2$O shifts to 1.79 at 50 K but the observations do not match other features of this salt. If true, KBOs might not only have water ice and ammonia hydrate on the surface, but phyllosilicates and/or salts. Such materials can only be formed in the presence of liquid water, and strongly suggest cryovolcanism is a likely resurfacing mechanism.

References: [1] Cook, JC et al., 2007, ApJ, in press. [2] Jewitt, D & Luu, J, 2004, Nature, **432**, 731. [3] Desch, SJ et al., LPSC, #**38**, 1901. [4] Gulbis, AAS et al., 2006, Nature, **439**, 7072. [5] Brown, ME, Trujillo, CA., 2004, AJ, **127**, 2413. [6] Stansberry, J. et al., 2007, in *Kuiper Belt Objects*, in press. [7] de Bergh, C et al., 2005, A&A, **437**, 1115. [8] Licandro, J et al., 2006, A&A, **457**, 329. [9] Grundy, WM et al., 2005, Icarus, **176**, 184. [10] Schmitt, B, et al., 1998, Optical Properties of Ices from UV to Infrared, in *Solar System Ices*, p. 199. [11] Roush, TL, 1997, Lunar and Planetary Science Conference, **28**, 199. [12] Grundy, WM & Schmitt, B, 1998, J. Geophys. Res., **103**, 25809. [13] Martonchik, JV et al., 1984, Applied Optics, **23**, 541. [14] Brown, RH et al., 1988, Icarus, **74**, 262. [15] Hansen, G, 1997, Adv. in Space Research, **20**, 1613. [16] Hansen, G, 1997, JGR, **102**, 21569. [17] Cruikshank, DP et al., 2005, Icarus, **175**, 268. [18] Buie, MW & Grundy, WM, 2000, Icarus, **148**, 324. [19] Roush, TL, 2005, Icarus, **179**, 259. [20] Egan, WG & Hilgeman, TW, 1979, Optical Properties of Inhomogeneous Materials: Applications to Geology, Astronomy, Chemistry, and Engineering, p. 105. [21] Bauer, JM et al., 2002, Icarus **158**, 178. [22] Crowley, JK, 1991, Journal of Geophys. Res., **96**, Issue B10, 16231. [23] Clark, RN et al., 2003, USGS Digital Spectral Library splib05a, U.S. Geological Survey, Open File Report 03-395. [24] Rouleau, F, & Martin, PG, 1991, ApJ., **377**, 526. [25] Fabian, D et al., 2001, A&A, **378**, 228. [26] Khare, BN et al., 1984, Icarus, **60**, 127. [27] Khare, BN et al., 1993, Icarus, **103**, 290. [28] Khare, BN et al., 1994, Bull. Am. Astron. Soc., **26**, 1176. [29] Dalton, JB et al., 2005, Icarus, **177**, 472.

HEMISPHERIC AND TOPOGRAPHIC ASYMMETRY OF MAGNETOSPHERIC PARTICLE IRRADIATION FOR ICY MOON SURFACES. J. F. Cooper[1] and S. J. Sturner[2], [1]Heliospheric Physics Laboratory, Code 672, NASA Goddard Space Flight Center, 8800 Greenbelt Road, Greenbelt, MD 20771 (John.F.Cooper@nasa.gov), [2]CRESST/UMBC, Astroparticle Physics Laboratory, Code 661, NASA Goddard Space Flight Center, 8800 Greenbelt Road, Greenbelt, MD 20771 (sturner@milkyway.gsfc.nasa.gov).

Introduction: All surfaces of icy moons without significant atmospheres, i.e. all except Titan in the giant planet systems, are irradiated by hot plasma and more energetic charged particles from the local magnetospheric environments. This irradiation can significantly impact the chemical composition, albedo, and detectable presence of signs of life on the sensible surfaces, while also limiting lifetimes and science operations of orbital spacecraft for extreme radiation environments as at Europa. Planning of surface remote sensing and lander operations, and interpretation of remote sensing and in-situ measurements, should include consideration of natural shielding afforded by the body of the moon, by any intrinsic or induced magnetic fields as at Ganymede, and by topographic structures.

Moon Body Shielding: The physical presence of the moon produces perturbation of flows for hot plasma and more energetic charged particles corotating with the magnetic field of the central planet. The particles gyrate around local magnetospheric field lines, move up and down along these field lines between magnetic mirror points, are carried past the moon by corotation with the planetary magnetic field, and undergo gradient-curvature drift, either in the prograde orbital direction for protons and positive ions or retrograde for electrons and negative ions. Since these multiple kinds of motions are involved, the interaction and impact distributions at the moon surface are complex. In the case of Europa, electrons below 10 MeV preferentially impact the trailing hemisphere, higher energy electrons above 20 MeV impact the leading hemisphere, and large gyradius ions have more global impact distributions. The electron impact distribution is consistent with radiolytic sulfate distributions on Europa, concentrated on the trailing hemisphere, and may also account for CO_2 distributions on Callisto. Overall, irradiation fluxes and dosages are much lower on the leading hemisphere of Europa, an important consideration in the search for chemical composition of internal origin and for any organic signs of life. For a low-altitude orbiter, the leading hemispheric orbital segments offer lower radiation levels from electrons and facilitate the more radiation-sensitive observations while also extending the lifetime of spacecraft systems, a critical consideration for currently envisaged Europa orbit missions.

Magnetic Shielding: The intrinsic dipole magnetic field of Ganymede offers a refuge from surface and orbital spacecraft irradiation by Jovian magnetospheric electrons and lower energy (< 10 MeV) protons. This natural magnetic shielding is most effective within several hundred kilometers of the surface and within the region of closed dipolar field lines. Regions associated with open field lines in the polar hemispheres of Ganymede are relatively unshielded. Differences in color and CO_2 abundance between the open and closed field line regions of the moon surface are suggestive of magnetic shielding effects. Induced magnetic fields from subsurface conducting layers, e.g. salty oceans, would shift the position of the open/closed field line boundary on Ganymede and produce periodic perturbations of surface irradiation distributions on other moons without intrinsic dipole fields.

Topographic Shadowing: The diurnal shadowing of solar illumination by topographic structures, e.g. crater walls and cliffs, is familiar to planetary geologists, but more continuous shadowing effects arise for energetic particle irradiation from gyration motions. This effect becomes particularly strong when the particle gyroradiusis is comparable (high energy heavy ions) or much smaller (electrons and lower energy protons) than the curvature scale of the surface. At Europa the gyroradii of the dominant radiation dosage components, keV to MeV electrons, is comparable to the sub-km scale of topographic relief, so surface topography becomes an important factor in surface irradiation dosage distributions. Near the equator of Europa, the irradiation flux from the zenith direction, e.g. as would be relevant at the bottom of a deep crevice otherwise exposed dirurnally to solar illumination, would be zero. Since particles of one charge, positive or negative, move in only one respectively opposite direction of gyration around the local magnetic field line, there are east-west asymmetries in surface irradiation fluxes. Thus an east-facing cliff face could be shielded on one side by the cliff mass and on the other by gyration.

Conclusion: Remote sensing and landed observational strategies should exploit the natural physical and magnetic shielding afforded by the global hemispheric and surface topographic structures of icy moons imbedded in planetary magnetospheres, e.g. for separation of internal and external sources of composition.

Vapor Pressures and Heats of Vaporization of Some Organic Acid Ices. Paul. D. Cooper[1,2], Marla. H. Moore[2] and Reggie. L. Hudson[3], [1]Department of Chemistry and Biochemistry, MS 3E2, George Mason University, Fairfax, VA 22030-4444 (pcooper@gmu.edu), [2]NASA Goddard Space Flight Center, Astrochemistry Branch, Code 691, Greenbelt, MD 20771 (Marla.H.Moore@nasa.gov), [3]Department of Chemistry, Eckerd College, 4200 54th Avenue South, St Petersburg, FL 33711 (hudsonrl@eckerd.edu)

Introduction: Identifying frozen acids on solar system surfaces has been more difficult than identifying solid H_2O, H_2O_2, O_2, or O_3. It has been known for some time that there is a close match between sulfuric acid hydrates and the near-IR spectrum of Europa [1]

Carbonic acid (H_2CO_3) is another molecule of interest, being the dominant product when $H_2O + CO_2$ ice mixtures are either irradiated or photolyzed [2-4], The temperature range over which $H_2O + CO_2$ can be processed to form H_2CO_3 has not been investigated, and essentially nothing on the vapor pressure of this acid has been published. That such information is needed is demonstrated by a suggested match of weak 3.88-μm features on Ganymede and Callisto with H_2CO_3 [5]. The spectra, formation, and stability of H_2CO_3 at different temperatures also have implications for its likely presence and detection on surfaces from Mars to beyond Pluto.

Of similar interest is formic acid (HCOOH) and acetic acid (CH_3COOH). While both species have been detected in the ISM, formic acid has also been observed in cometary comae. Both species may also be formed on icy satellite surfaces – formic acid is known to be produced in irradiated $H_2O + CO$ ices and acetic acid is likely produced in $CH_4 + CO_2$ ices.

The formation and thermal evolution of these acids is important in understanding the surface chemistry of icy satellites.

Results: We will present data on a series of laboratory experiments designed to measure the vapor pressures of the three organic acids listed above, as well as heats of vaporization for each acid. These experiments utilize infrared spectroscopy of thin-film ice samples to measure these properties.

We have used the transmission of infrared light by a thin ice film deposited onto a cooled optical window to measure absorption spectra of formic and acetic acid at different temperatures. We observed the rate of loss of the ice, R, defined as the number of molecules leaving the unit area in unit time, and using the Knudsen equation (1), where m is the molecular mass of the species, T is the temperature, and k is the Boltzmann constant, the vapor pressure p, was calculated.

$$R = \frac{p}{\sqrt{2\pi mkT}} \qquad (1)$$

From the vapor pressures obtained at different temperatures, the Clausius-Clapeyron (2) equation was used to determine the heat of vaporization.

$$\ln\left(\frac{p_2}{p_1}\right) = -\frac{\Delta H}{R}\left(\frac{1}{T_2} - \frac{1}{T_1}\right) \qquad (2)$$

Carbonic acid was synthesized on a polished aluminum mirror from an irradiated mixture of $H_2O + CO_2$. The absorption spectrum was measured using the reflectance method. We will provide data to show whether or not carbonic acid is thermally stable and sublimes into the gas phase (and has a measurable vapor pressure), or whether it undergoes thermal decomposition to H_2O and CO_2.

References: [1] Carlson R.W. et al., (1999) *Science, 283,* 2062. [2] Moore, M.H. and Khanna, R. (1991) *Spectrochimica Acta, 47A*, 255. [3] Gerakines, P.A., Moore, M.H., and Hudson, R.L. (2000) *Astronomy & Astrophysics, 357,* 793. [4] Brucato J.R., Palumbo, M.E., Strazzulla, G., (1997), *Icarus 125*, 135. [5] Hage, W, Liedl, K.R., Hallbrucker, A., and Mayer, E., *Science 279*, 32.

CARBON DIOXIDE ON THE SATELLITES OF SATURN. Dale P. Cruikshank, NASA Ames Research Center, Mail Stop 245-6, Moffett Field, CA, 94035. Dale.P.Cruikshank@nasa.gov

The spectral signature of solid CO_2 (the C-O asymmetric stretching mode at 4.27 μm) is seen in the Cassini VIMS data for several satellites of Saturn [1,2,3,4]. It often appears strongest in geographic regions of low albedo, compared to the higher albedo regions dominated by H_2O ice; this may be an effect of band contrast rather than true spatial association. In all cases, although to varying degrees, the CO_2 band is shifted to shorter wavelengths than is seen in pure CO_2 at 80 K in the laboratory, suggesting that CO_2 is complexed in one or more ways with another molecule or material. Lab spectra and *ab initio* calculations of molecular complexes of CO_2 with 1, 2, and more H_2O molecules [5] show that the wavelength shift seen on some satellites can be explained in this way. The CO_2 band on Hyperion is different from that on the other satellites in that its band is further shifted and has a different profile. Both of these spectral parameters are matched by the type II clathrate of CO_2 in H_2O [6]. Although CO_2 clathrate has been postulated to occur on Mars and Enceladus, its spectroscopic signature has not been seen until this identification on Hyperion. The implications of CO_2 clathrate on Hyperion are far reaching in terms of its propensity to decompose explosively [7], Hyperion's low bulk density, the distribution of low-albedo (organic rich) material on its surface, and other features of this satellite.

References: [1] Clark, R. N., et al. (2005) *Nature 435*, 66, [2] Buratti, B. J., et al. (2005) *Ap. J. Lett. 622*, L149, [3] Brown, R. H., et al. (2006) *Science 311*, 1425, [4] Cruikshank, D. P., et al. submitted, [5] Chaban, G. M., Bernstein, M. P., and Cruikshank, D. P. (2007) *Icarus 187*, 592, [6] Prasad, P. S. R., Shiva Prasad, K., and Thakur, N. K. (2006) *Current Science 90*, 1544, [7] Kieffer, S. W., et al. (2006) *Science 314*, 1764.

SURFACE COMPOSITIONS OF THE ICY SATELLITES. J. B. Dalton, Carl Sagan Center, SETI Institute, 515 N. Whisman Road, Mountain View CA 94043, dalton at carlsagancenter.org.

The icy satellites of the Outer Solar System exhibit a range of chemical compositions. Over the past decade, a combination of ground- and spacecraft-based remote sensing observations, supported by laboratory work and theoretical calculations, has steadily shed additional light on the makeup of these enigmatic bodies. From the ubiquitous water ice to the bizarre products of photolysis and radiolysis, commonalities and differences among bodies emerge which testify to the similarities in formation histories and evolutionary processes. In so doing, they reveal the extraordinary breadth of possibilities inherent in the process of planetary formation.

MODELING EUROPA'S SURFACE COMPOSITION WITH CRYOGENIC SULFATE HYDRATES J. B. Dalton[1], [1]Carl Sagan Center, SETI Institute, 515 N. Whisman Road, Mountain View CA 94043. dalton at carlsagancenter.org

Introduction: The surface of Europa has been found to consist predominantly of water ice along with hydrogen peroxide, sulfur dioxide, and carbon dioxide ices [1]. Irradiation by charged particles and communication with the interior may also have led to the creation of additional surface compounds [2,3]. Disrupted terrains on Europa reveal spectral evidence for such an additional component. Near-infrared reflectance spectroscopy from Galileo NIMS (Near-Infrared Mapping Spectrometer) indicates that this material is highly hydrated, as evidenced by strongly asymmetric absorption features attributed to waters of hydration at 1.5 and 2.0 microns [4].

Cryogenic Spectroscopy: Alone, no single material yet studied can account for the observed spectral character of the reddish, disrupted Europan terrain. Earlier work based on available room temperature spectra of terrestrial hydrated salts [5] suggested that mixtures of bloedite, hexahydrite, epsomite and mirabilite could approximate the Europa spectrum. However, several absorption band strengths and positions could not be reproduced using room temperature spectra. It has since been demonstrated that, at the cryogenic temperatures relevant to the surface of Europa (~100K), spectra of hydrates can be markedly different [6] from room temperature observations.

Linear Mixture Analysis: A linear mixture model has now been applied to the Galileo NIMS spectra of dark terrain, using only cryogenic laboratory spectra as mixture endmembers. These included ordinary water ice Ih of varying grain sizes, Mg and Na sulfate brines, epsomite ($MgSO_4 \cdot 7H_2O$), hexahydrite ($MgSO_4 \cdot 6H_2O$), magnesium sulfate dodecahydrate ($MgSO_4 \cdot 12H_2O$), mirabilite ($Na_2SO_4 \cdot 10H_2O$), sulfuric acid hydrate ($H_2SO_4 \cdot 8H_2O$) and bloedite ($Na_2Mg(SO_4)_2 \cdot 4H_2O$). Taken individually, the cryogenic hydrated salts can still reproduce much of the observed spectral character; yet, they can not reproduce the Europa spectrum as well as their room temperature spectra could [6,7].

Modeled Abundances: When run using only hydrated salts and brines as spectral endmembers, the model selected bloedite, mirabilite, and hexahydrite as the most abundant species. This is in accord with predictions based on room temperature models [5]. Interestingly, the abundances of the other endmember materials, including brines and the dodecahydrate, were iteratively diminished to negligible levels. The inclusion of cryogenic sulfuric acid hydrate based upon earlier work [6,8,9] significantly improves the spectral match beyond what can be achieved using either sulfuric acid hydrate alone, or hydrated salts alone. The best fit achieved using the entire suite of cryogenic spectra (except for sulfuric acid) is shown in Figure 1. Many of the modeled band strengths, shapes and widths do not correspond to the Galileo observations. Several spectral absorption features arising from the salts (arrows) do not correspond to features observed in the Europa spectrum. Notably, the band center positions of
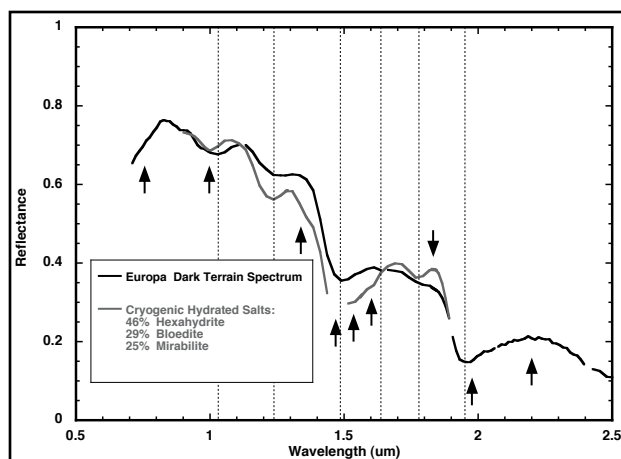
Figure 1. Europa spectrum modeled with linear mixture of cryogenic hydrated salts. Arrows indicate differences between modeled and observed spectral features.
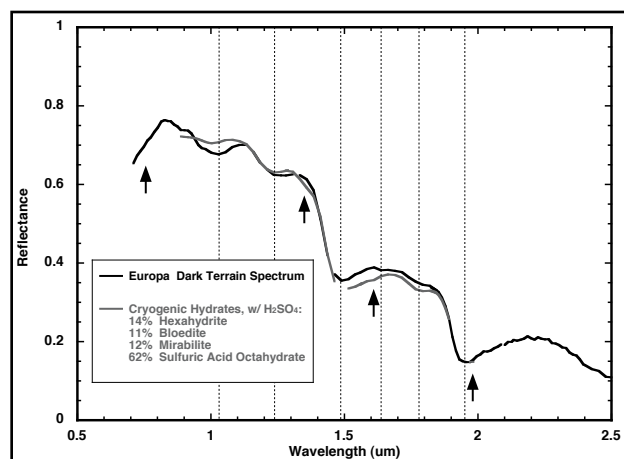
Figure 2. Europa spectrum modeled as linear mixture, including sulfuric acid hydrate. While improved, the spectral match still remains imperfect, suggesting an additional component or physical effect.

the Europa 1.5-micron and 2.0-micron asymmetric water absorptions (vertical lines) are not reproduced, while the band strengths vary from the observed band depths. A peak at 1.85 microns can be traced to the spectral character of bloedite at this wavelength. Three small absorption features within the 1.5-micron water absorption feature complex do not have counterparts in the Europa spectrum. The proportions of hydrated salts differ from those derived in previous work, with 45% hexahydrite, 29% bloedite and 25% mirabilite producing the best spectral match.

Figure 2 demonstrates the effect of adding sulfuric acid hydrate to the model. Although not perfect (arrows), the band positions and strengths more closely approximate the observed spectral character. The algorithm prefers a high (>50%) abundance of the sulfuric acid hydrate, but does not eliminate the hydrated salts entirely. Here the model selects 14% hexahydrite, 11% bloedite and 12% mirabilite along with 65% sulfuric acid hydrate to produce the best available match to the Europa observations.

While the spectral match is significantly improved over previous estimates, the modeled spectrum in Figure 2 still bears a number of discrepancies. The 2.0-micron feature still does not occur at exactly the correct frequency, and there is a subtle feature in the modeled spectrum just shortward of the 1.65-micron crystalline water ice feature which is not apparent in the Europa observations. A known cation-OH stretch at 1.35 microns, which is apparent in the hydrated salt spectra but not in the Galileo NIMS observations [6], persists in all model simulations. This could indicate structural effects on the crystal lattice, or the possibility that these materials are not appropriate analogues.

Dark Terrain Spectral Match: The dark terrains on Europa give rise to a spectrum resembling that of cryogenic mixtures of hydrates, suggesting that Europa contains these hydrates. However the spectral match remains imperfect, suggesting that the surface materials may exhibit radiation damage effects which have not yet been quantified experimentally. It is possible that the predicted mixtures, subjected to particle irradiation, could produce an even closer match. The spectral effects of such radiation damage are just now beginning to be understood. Alternatively, there may be additional components which have not yet been studied. Further, it must be remembered that there may be a physical reason to reject a material. The thermal and radiation stability of mirabilite, for example, are too low for it to have persisted over the geologic age of Europa's surface [10]. It is now clear that since the surface of Europa is not at room temperature, that room temperature materials cannot be present. Good spectral correlation between room temperature measurements and spacecraft observations is not sufficient to claim an identification. Still, modeling of the surface composition with cryogenic laboratory spectroscopy of sulfate hydrates indicates that their structural, chemical, and physical properties make them useful analogues for the Europa surface material.

Conclusions: Linear spectral modeling of the Europan dark terrain using cryogenic endmember spectra lends credence to the idea that the surface may be comprised of a mixture of materials. The spectral characteristics of hydrated sulfate compounds provide strong analogs to the behavior observed in the Galileo NIMS measurements. Remaining discrepancies may be explained by additional components or as yet unquantified radiation damage to the crystalline structure of the surface materials. Additional laboratory work on the spectra of candidate compounds is needed to confirm or reject their possible presence. Further laboratory efforts to reproduce the observed spectral effects through irradiation of ices and hydrates has the potential to explain the enigmatic spectral character of Europa's surface. This knowledge will improve understanding of the parent materials and processes which gave rise to the present surface, with applications to understanding the interior and its composition.

References: [1] Carlson R.W. et al. (1999a) *Science 283,* 2062-2064. [2] Cooper J.F. et al. (2001) *Icarus 149*, 133-159. [3] Nimmo F. et al. (2005) *Icarus 177*, 293-296. [4] Dalton, J.B. (2003) *Astrobiology 3*, 771-784. [5] McCord T.B. et al., (1999) *J. Geophys. Res. 104*, 11824-11852. [6] Dalton J.B. et al. (2005) *Icarus 177*, 472-490. [7] McCord T.B. et al. (2002) *J. Geophys. Res. 107*, 4-1. [8] Carlson, R.W. et al. (1999b) *Science 286*, 5437-5440. [9] Carlson R.W. et al. (2002) *Icarus 157*, 456-463. [10] McCord T.B. et al. (2001) *J. Geophys. Res. 106*, 331-3320. [11] Carlson R.W. et al. (2005) *Icarus 177*, 461-471.

DISTRIBUTION OF VOLATILE ICES ON HYPERION.

J. B. Dalton[1] and D. P. Cruikshank[2], [1]Carl Sagan Center, SETI Institute, 515 N. Whisman Road, Mountain View CA 94043. dalton at carlsagancenter.org, [2] NASA Ames Research Center, Mail Stop 245-6, Moffett Field, CA, 94035. Dale.P.Cruikshank at nasa.gov.

Introduction: Compositional mapping of the surface of Hyperion using Cassini VIMS observations indicate a heterogenous surface dominated by water ice but with substantial additional materials. Abundant carbon dioxide, as evidenced by a spectral absorption at ~4.25 microns, persists throughout the satellite. Localized deposits of low-albedo material exhibit spectral absorptions indicative of C-H and C-N bonds. The host materials for these features are not yet known but are suggested to occur on other Saturnian satellites [1,2]. Additional smaller absorption features suggest organic matter, possibly including polycyclic aromatic hydrocarbons (PAHs).

Band Depth Mapping of Cassini Observations: Two Cassini VIMS observations of moderate spatial resolution and four observations of high spatial resolution were selected for analysis based upon the presence of large contiguous regions of low-albedo material. Band depth maps were created for spectral absorption features of water (2.0 microns), CO_2 (4.25 microns) and C-N (2.42 microns). These were overlaid upon calibrated ISS images to determine correspondence with geologic units. The most prominent morphologic features on the surface of Hyperion are irregular to subcircular topographic lows containing the low-albedo material [3]. While absorption due to water ice was clearly strongest in the bright surface regions away from these features, some water ice was present in all VIMS spectra. Absorption due to CO_2 varied throughout the observations; while strong in the low-albedo material, the CO_2 absorption at 4.25 microns was also observed to vary in intensity throughout the bright icy regions. These variations are not linked to morphologic or topographic variations, though occasional enhancements are seen in the immediate vicinity of small impacts. This indicates a heterogeneous distribution of CO_2 within the water ice that makes up most of the surface [4]. This may be due either to exogenic influences (e.g. implantation, radiolysis) or a result of endogenic formation and/or emplacement. The C-N feature, by contrast, was found to be strongest in the low-albedo material and weak or absent elsewhere.

Weak Absorption Features: Additional absorption features observed in the 3- to 5-micron spectral range are suggestive of additional, possibly organic components. A feature occurring at 3.28 microns matches generic absorption characteristics of PAHs [4,5] but, though several channels wide, lies just above the 1-σ detection threshold. Other features which take up several VIMS channels occur longward of 4 microns but have not yet been positively identified. As with carbon dioxide, the strengths of these absorption features do not appear closely correlated with surface morphology or geologic units other than the topographic lows containing the low-albedo material.

Conclusion: Compositional analysis of Cassini VIMS observations indicate heterogeneous distributions of materials over the surface of Hyperion. Some materials, notably those exhibiting C-N and C-H absorption, are highly concentrated in the low-albedo materials which tend to be concentrated in topographic lows. However it appears that volatile ices, notable CO_2, are also distributed heterogeneously throughout the bright icy terrains as well. This has implications for the formation and subsequent evolution of Hyperion.

References: [1] Clark, R. N., et al. (2005) *Nature 435*, 66-67. [2] Brown, R.H. et al., (2006) *Science 311*, 1425-1428. [3] Thomas, P. et al., *Science, submitted*. [4] Cruikshank D.P. et al., *Science, submitted* [5] Bernstein M.P. et al. (2005) *Ap. J. 161*, 53-64.

THE SURFACE OF IAPETUS. Tilmann Denk (FU Berlin) and the Cassini ISS Team.

Iapetus, the Saturnian moon with the extreme global brightness dichotomy, has been studied intensively by the instruments of the Cassini spacecraft since Saturn arrival in 2004. Among the most important discoveries and observations by the Imaging experiment (ISS) were an equatorial ridge that spans around Iapetus' circumference over most parts of the leading side, several huge basins with diameters of several hundred kilometers, the true nature of the "moat" feature as a crater, a color dichotomy in contrast and in addition to the brightness dichotomy, the correlation between bright- and dark-rim craters on the leading side with planetographic latitude, the absence of bright spots (bright-floor craters) larger than ~1/2 km within the dark terrain, or the first images of the southern hemisphere and the leading side.

Furthermore, an unambiguous confirmation and good quantification of the Voyager discoveries of the ellipsoidal to irregular shape of Iapetus, of huge bright mountains on the anti-Saturn side, of the old surface age, of numerous craters within the dark terrain, or of the suspected similarity of the crater-size-frequency distribution on the dark terrain compared to the bright terrain was possible.

Best imaging coverage so far is at ~3/4 km/pxl resolution over the northern leading side from the "B/C flyby" at New-Year's Eve 2004/2005. On September 10, 2007, the first and only targeted Cassini flyby within 6 years into orbit is scheduled, bringing the spacecraft as close as 1615 km to the surface. Closest approach will occur over the highest parts of the ridge. On the outbound trajectory leg, the trailing side will be visible at low phase angle.

THE CASSINI TARGETED IAPETUS FLYBY WILL TAKE PLACE IN SEPTEMBER, 2007.

T. Denk[1], G. Neukum[1], Th. Roatsch[2], A.R. Hendrix[3], F.J. Pelletier[3], and N.J. Strange[3], [1]FU Berlin (Tilmann.Denk@fu-berlin.de), [2]DLR Berlin, [3]JPL.

The ISS camera onboard the Cassini Spacecraft orbiting Saturn has observed the enigmatic moon Iapetus for over three years now, but always from great distance. The so-far closest approach occurred at New-Year's Eve 2005 when a range of 124000 km was achieved. Numerous discoveries have been made so far [e.g., 1,2,3]: The equatorial ridge on the leading and anti-Saturn side, a latitude dependence of the characteristics of the dark terrain, an unusually high number of giant impact basins, the latitudinal dependence of bright and dark crater rims, a global color dichotomy that shows different boundaries than the more obvious brightness dichotomy, the true (crater) nature of the "moat" feature, and so on. Earlier discoveries from Voyager data [4,5] such as the irregular boundary between the bright and the dark hemispheres, the giant bright mountains on the anti- and sub-Saturn side ("Voyager" mountains), the ellipsoidal shape of the whole moon, impact craters within the dark terrain, the reddish color of the dark terrain, etc., have been confirmed. Promising attempts were made to explain the formations of the brightness and color dichotomies [6,7] and the ellipsoidal shape [8]. Besides many unanswered questions, a major missing piece is a very close-up view on the surface. This is planned for the targeted flyby on Sept. 10, 2007. Our Cassini group at FU and DLR in Berlin has the responsibility for the imaging observation planning.

The spacecraft will approach Iapetus over the mainly unlit, very-low albedo Saturn-facing hemisphere. Closest approach will occur at 1600 km altitude over the anti-Saturn side. This area is close to the (as far as we know) highest parts of the ridge. On the outbound trajectory, Cassini will look back on the as-yet only poorly imaged bright trailing side of Iapetus at low phase angle. A spacecraft trajectory tweak to significantly improve the observation conditions [9] was approved by the project in early 2007.

There will be many scientific highlights during the flyby. A few examples are: Spatial resolution down to 10 m/pxl with the ISS narrow angle camera; ridge imaging at high and low phase angles; a large mosaic of the equatorial transition zone; global mapping of the trailing side at ~400 m/pxl; the only SAR observation of an icy satellite (RADAR); a star occultation to look for a tenuous atmosphere (UVIS); very high-resolution thermal observations (CIRS); best-ever examination of outer-solar system dark material (VIMS); and much more.

A small subset of questions that might be addressed with these data are: What is the geologic nature and origin of the ridge and the bright "Voyager" mountains? How far does the ridge extend into the trailing side? What is the thickness of the dark terrain blanket? Does it harbor small bright "holes" due to recent small impacts? What is the chemical and mineralogical nature of the dark material? How is the distribution of the dark material on the trailing side? What is the overall cause for the existence of the tremendous brightness dichotomy, the color dichotomy, the complex brightness patterns on the transition zones?

References: [1] Porco, C.C., *et al.* (2005): Cassini Imaging Science: Initial Results on Phoebe and Iapetus. *Science 307*, 1237-1242. [2] Denk, T., *et al.* (2005): LPSC XXXVI, abstracts #2262 and #2268. [3] Giese *et al.* (2007): The Topography of Iapetus' Leading Side. *Icarus*, in press. [4] Morrison *et al.* (1986): The Satellites of Saturn. In: *Satellites*, UofA Press, 764-801. [5] Denk *et al.* (2000) LPSC XXXI, abstract #1596. [6] Spencer, J.R. *et al.* (2005), 37th *DPS*, abstract #39.08. [7] Denk *et al.* (2006) 38th DPS Conference, abstract #69.07. [8] Castillo-Rogez *et al.* (2007): Iapetus' Geophysics: Rotation Rate, Shape, and Equatorial Ridge. *Icarus*, doi:10.1016/j.icarus.2007.02.018. [9] Pelletier, F.J. (2006): Cassini Iapetus-1 Flyby Variations. JPL IOM-343J-06-049.

Fig.1: Anti-Saturn side of Iapetus, observed in October 2004 at ~7 km/pxl. In September, 2007, it is planned to image the bright "Voyager" mountains and the equatorial ridge at very high resolution (down to ~10 m/pxl).
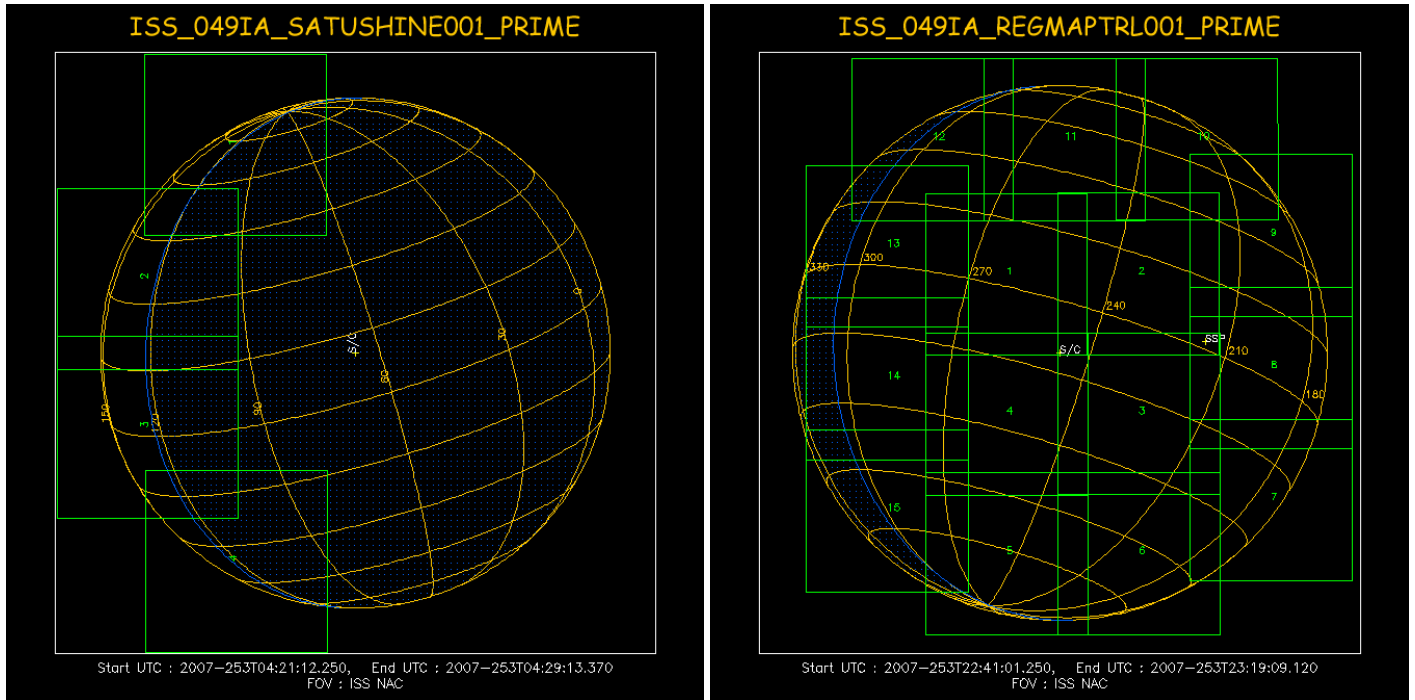
Fig. 2: Iapetus global mapping examples before (left) and after closest approach (right). Spatial resolution will be ~490 m/pxl and ~440 m/pxl, respectively. 270°W marks the center of the trailing side.
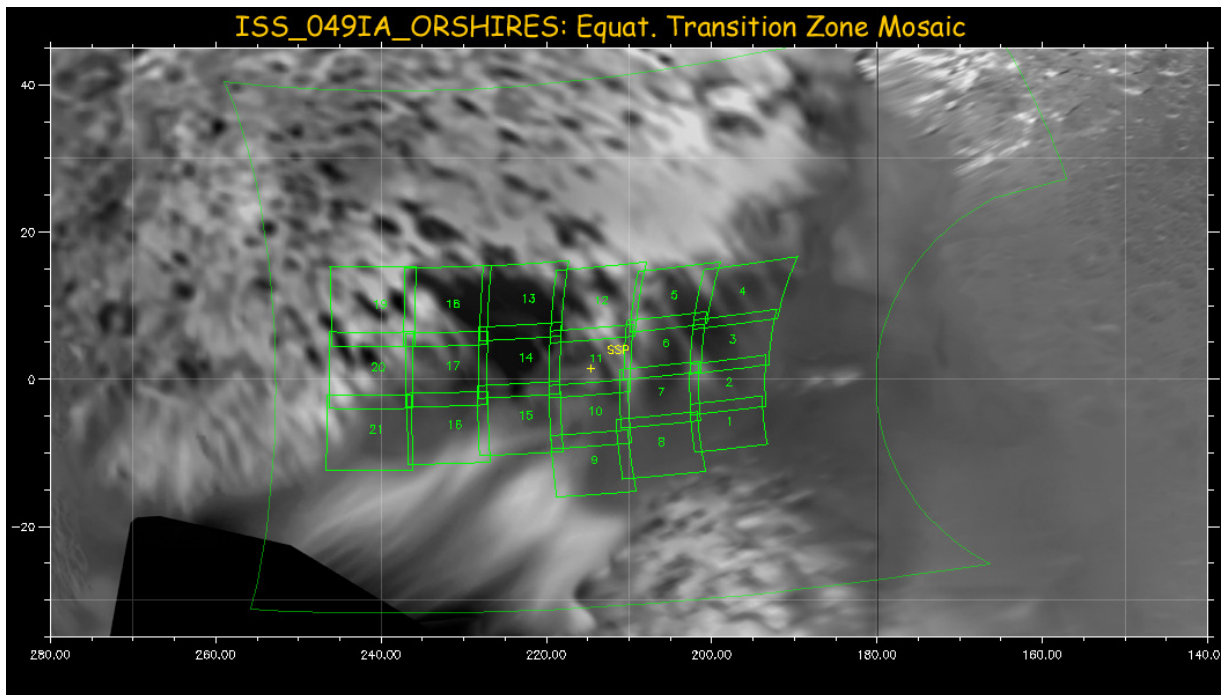
Fig. 3: Planned equatorial transition zone 4x3+3x3 mosaic. The ISS narrow-angle camera images will have a spatial resolution of 82-131 m/pxl. This is the largest of eleven mosaics planned for the time period -55 to +180 min around closest approach.

VOLUMETRIC AND OPTICAL STUDIES OF HIGH PRESSURE PHASES OF MgSO$_4$·H$_2$0 WITH APPLICATIONS TO EUROPA.
A. J. Dougherty[1], D. L. Hogenboom[1], and J. S. Kargel[2], [1]Dept. of Physics, Lafayette College, Easton, PA 18042, e-mail: doughera@lafayette.edu, hogenbod@lafayette.edu, [2]Department of Hydrology and Water Resources, The University of Arizona, Harshbarger Building, PO Box 210011, Tucson, AZ 85721-0011, e-mail: kargel@hwr.arizona.edu.

Introduction: We report optical and volumetric measurements of MgSO$_4$ in H$_2$O at high pressures using a volumetric cell with sapphire windows. Magnesium sulfate was chosen because it is a likely constituent of Europa's ocean and icy shell [1,2]. In addition, magnesium sulfate minerals are common terrestrial evaporite phases, and they also probably occur on Mars [3]. These salts may play several major roles: they could depress melting points, alter buoyancy relations of key phases, form thick layers of bedded seafloor sediments, and allow explosive aqueous eruptions. It is therefore useful to know their high pressure and low temperature phase behavior.

In previous work, we have focused on pressures less than 200 MPa, or the Ice I regime[4,5]. In this work, we will examine slightly higher pressures where the phases of ice are denser than liquid water, but less dense than the eutectic liquid. Some preliminary results from this work are presented below. This work also complements our work with the Na$_2$SO$_4$·H$_2$O system [6,7].

Experiments: We have studied samples with a concentration of 17 wt.%, which is close to the eutectic composition at one atmosphere. About one mL of sample is contained in a pressure cell consisting of a standard high-pressure fitting called a cross. This stainless steel block has four ports. Two opposing ports contain replaceable plugs that have sapphire windows sealed with epoxy. The third port contains a plug with a silicon diode thermometer, and the fourth port connects the cell to the pressure system. A transducer in the pressure system responds to changes in the volume of the system yielding a voltage that varies approximately linearly with volume. This system allows simultaneous measurements of pressure, temperature, and volume changes, along with optical images of the crystals. We are currently rebuilding the system for better operation at pressures above 200 MPa.

The main solid phases relevant for this work are epsomite (MgSO$_4$·7H$_2$O, indicated by MS7) and MgSO$_4$·11H$_2$O (MS11), previously identified as MS12.[6]. For the 17 wt.% concentration used in this work, MS11 is the stable state, but long-lived metastable states of MS7 can also be observed. Generally, the presence of metastable states and the overall sluggish dynamics of the hydrated salt systems make accurate measurements of the phase boundaries challenging.

Results at 350 MPa: The results for a run at a nominal pressure of 350 MPa are shown in Fig. 2. After pressurizing and warming the liquid to point (a), we supercooled the sample down to about 242K. Approaching point (b), a small increase in voltage signaled the formation of a less dense mixture just before the main freezing transition at point (c). We have not yet identified the phases involved. In this run, only a small portion of the crystal was visible in the corner of the window. However, in another run at a nominal
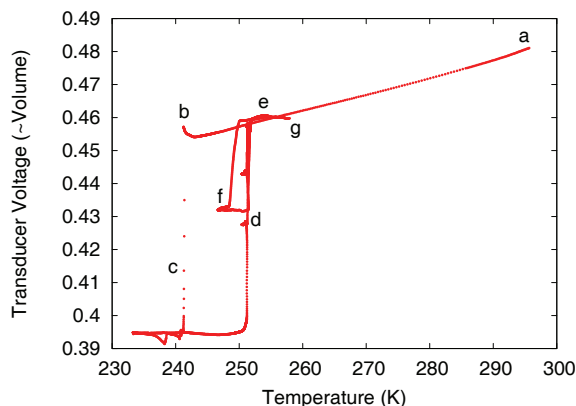
Figure 1. Transducer voltage (varies approximately linearly with volume) versus Temperature for a run at a nominal pressure of 350 MPa.

pressure of 250 MPa, we observed the crystals shown in Fig. 2 in similar circumstances. In both the runs at 250 and at 350 MPa, the growth of these crystals is accompanied by an overall *decrease* in the density of the solution.

Figure 2. Magnesium sulfate hydrate crystals at a pressure of 249 MPa and a temperature of 242.5 K.

Additional cooling produced a sharp drop in volume (c), presumably due to the formation of a dense hydrate along with additional ice, and perhaps a eutectic solid mixture of the two. Further cooling resulted in no significant changes. Upon warming to about 251K, eutectic melting commenced, and the volume began to quickly increase (point d). However, unlike the melting transitions we typically observed at lower pressure, this transition was not reversible. After slight cooling, crystals in the image began to resolidify, but the volume did not decrease. (Note the small horizontal line segment at point (d).) Subsequent warming again dissolved most of the material, but a few crystals remained at point (e). These crystals raised the sample volume above the value it had when it was a homogeneous liquid being cooled in the first hours of the run. These remaining crystals appear to be the same ones observed in the initial crystallization at point (b).

We observed such a low-density state in every run at high pressure. At this stage of the project, we are unable to conclude whether this low-density state is a metastable mixture of ice III or ice V together with MS7 or MS11 and a depleted solution, or whether it is a previously unreported sulfate hydrate of lower density than MS11. These findings are consistent with our earlier study of this system, where we also found possible evidence of a low-density sulfate[8].

After cooling again until about 250K, the system froze rapidly. Thin dendrites, presumably of ice, grew out ahead of the interface until the system froze solid at point (f).
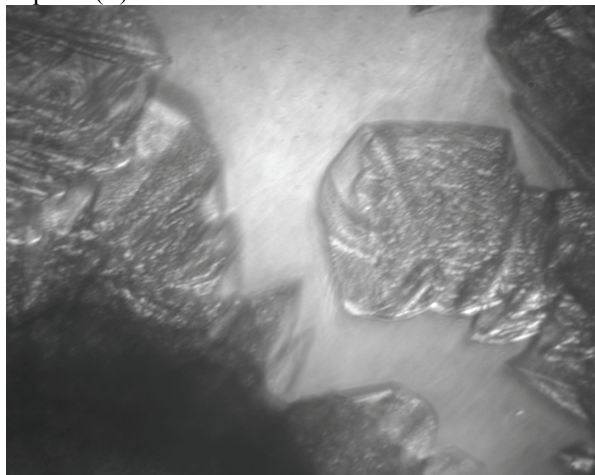
Figure 3. Dendritic ice crystals growing at a pressure of 350 MPa. The MgSO₄ hydrate crystals are at the lower left.

Further warming (back to (d) again) repeated the previous stages, including a second unsuccessful reversal attempt between (d) and (e).

Results: The variety of phases, the sluggish dynamics, and the lack of reversibility make it difficult to determine thermodynamic phase transitions accurately at this pressure. Our current best estimates for the transition temperatures at pressures up to 350 MPa are shown in Fig. 4.
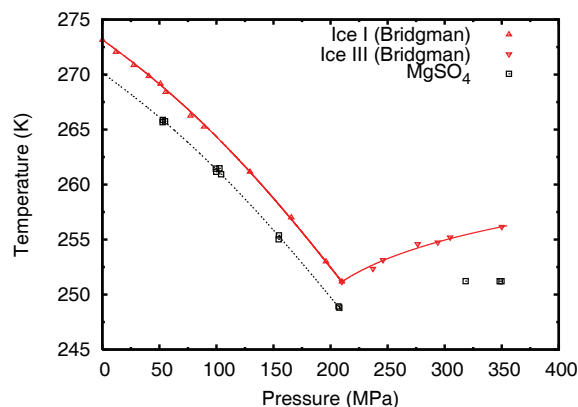
Figure 4: Transition temperatures for the MgSO₄·H₂O system as a function of pressure. Shown for comparison are the Ice I and Ice III melting temperatures from Bridgman[9].

Overall, the freezing point depression is relatively small for this material. For pressures less than 200 MPa, the difference between the ice and eutectic temperatures appears to decrease with increasing pressure. Above 200 MPa, the trend is unclear. Additional data are needed to clarify the phases involved in that pressure range.

We are currently building an improved version of the apparatus that should handle pressures above 200 MPa more reliably and enable us to obtain more complete data over that pressure range. In future work, we expect to consider ternary systems, such as $Na_2SO_4 \cdot MgSO_4 \cdot H_2O$. Other systems under consideration include ammonium sulfate, which may be important for Titan[10].

References: [1] Hogenboom, D.L. *et al. LPS XXX,* Abstract #1793. [2] Dougherty, A. J. *et al. LPS XXXVII*, Abstract #1732. [3] McCord, T.B. *et al.* (1998) *Science*, 280, 1242. [4] Kargel, J.S. *et al.* (2000) *Icarus* 148, 226-265. [5] Squyres, S.W. *et al.* (2004) *Science*, 306. [6] Peterson, R.C. and Wang, R. (2006) *Geology* 34, 957-960. [7] Hogenboom, D.L. *et al.* (1995) *Icarus* 115: 258-277. [8] Hogenboom, D.L. *et al. LPS XXXVI*, Abstract #1825. [9] Bridgman, P.W. (1911) *Proc. Amer. Acad. Arts Sci.* 47, 441. [10] Fortes, A.D., Grindrod, P.M., Trickett, S.K., Vocadlo, L., Icarus (2007) 188: 139-153.

NEAR-INFRARED SPECTRA OF UV-PHOTOLYZED LABORATORY ANALOGS OF PLANETARY ICES.
P. A. Gerakines[1] and C. R. Richey[1], [1]Department of Physics, University of Alabama at Birmingham, CH 310, 1530 3rd Ave S, Birmingham, AL 35294-1170, gerak@uab.edu.

In this abstract we describe the development of laboratory techniques required to create thick (10-100μm) UV-photolyzed ices. Three techniques are under study in our laboratory, including a closed-cell technique that allows UV photolysis within the cell. Preliminary results from these techniques will be discussed.

Significant chemical and physical information about icy planets and satellites can be realized from their observation at near-infrared wavelengths [1]. Work in the literature, often utilizing comparisons between the observed data and near-IR laboratory reflectance spectra of single-component unprocessed ices, has deduced the general composition of some icy surfaces [2]. These surfaces are exposed to ultraviolet and particle irradiation from various sources, and these forms of energy are thought to drive non-thermal chemistries there [3]. Therefore, the spectra of single-component, unprocessed laboratory analogs do not provide the best representations of icy surfaces in these energetic environments.

Laboratory studies using spectra of ice analogs in the mid-infrared range (λ = 2.5-25 μm) clearly indicate a complex series of chemical reactions can take place in these environments [4-6], but there is a dearth of spectroscopic analyses that have included laboratory spectra of photolyzed ices in the near-infrared range (λ = 1.0-2.5 μm). At the University of Alabama at Birmingham, we are equipped to create samples of UV photolyzed ices and obtain both their near- and mid-IR spectra. In this way, we are able to combine both techniques for maximal information.

Due to the small penetration depth of UV photons into an ice—on the order of 1 μm—thin ices have commonly been the focus of photochemical experiments. The low absorption strengths of near-IR features of molecular ices dictate that a much thicker ice is required for the identification of product features at these shorter wavelengths [7]. Therefore, the combination of UV photolysis for processing and near-IR spectrscopy for analysis is not straightforward.

To achieve significant levels of processing throughout such an ice layer, photolyzed ices must be (1) built up in stages or (2) deposited simultaneously with the photolysis. Some preliminary work on this topic has been presented earlier [8,9], and we will discuss more recent results using these two techinques.

Figures 1 and 2 display the near-IR (9000-4500 cm^{-1}, 1.1-2.2 μm) and mid-IR (4000-400 cm^{-1}, 2.5-25 μm) spectra for a pure CO_2 sample at 7 K that has been built up in stages. For this experiment, 10 layers with a thickness of 1 μm have been consecutively deposited and photolyzed. Despite the strong product absorption features in the mid-IR (Fig. 2), the near-IR features of products (Fig. 1) are absent. We have therefore shifted our focus to other techniques.

Most recently we have implemented a new technique that utilizes a closed gas cell of similar design to those used in previous ice studies [2], but modified to allow for the inclusion of UV photolysis. A schematic

Figure 1.

pure CO_2 layered experiment: near-IR

10 layers, 256m of photolysis /layer

7K pure CO_2 deposit

Figure 2.

pure CO_2 layered experiment: mid-IR

10 layers, 256m of photolysis /layer

7K pure CO_2 deposit
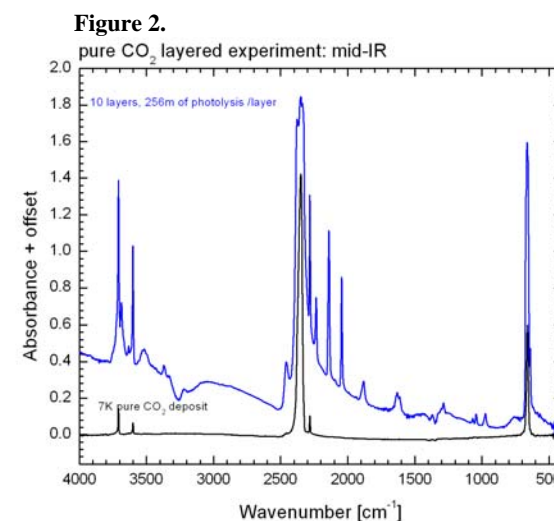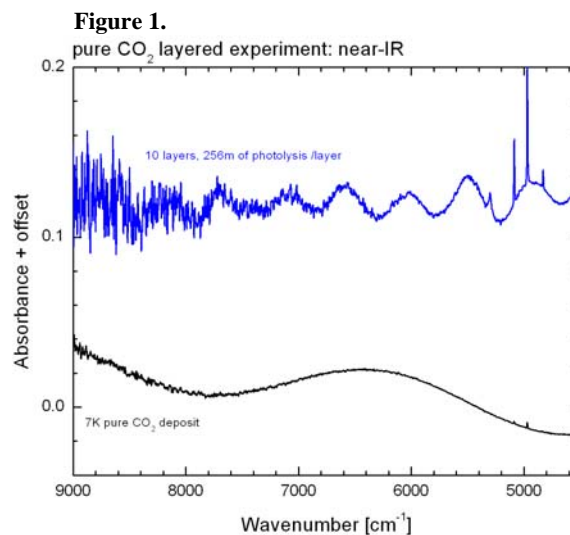
of the gas cell is given in Figure 3. In summary, the cell has a triangular cross section in which two windows allow the transmission of the spectrometer's IR beam and the third allows the transmission of UV photons into the cell. Gases are allowed to condense on the IR-transparent windows but not the UV-transparent window. We will discuss the preliminary results we have obtained thus far.

The ultimate goal of our work is to provide funda-

Figure 3. New gas cell design.

mental laboratory data with which near-IR observations (e.g., from spacecraft instruments such as Galileo NIMS, Cassini VIMS, HST NICMOS, or JWST, or ground-based telescope instruments such as NIRSPEC on Keck or SpeX on the IRTF) may be compared.

References: [1] see e.g., Roush T. L. (2001) *JGR, 106,* 33315-33323. [2] see e.g., Quirico E. et al. (1999) *Icarus, 39*, 159-178 or McCord T. B. et al. (2002), *JGR, 107*, 10.1029/2000JE001453. [3] see Johnson R. E. and Quickenden T. I (1997), *JGR, 102,* 10985-10996. (1997) or Delitsky M. L. and Lane, A. L. (1998), *JGR, 103*, 31391-31403. [4] Gerakines P. A. et al. (2000), *Astron. Astrophys, 357*, 793-800. [5] Gerakines P. A. et al. (1996), *Astron. Astrophys., 312,* 289-305. [6] Gerakines, P. A. et al. (2001), *JGR, 106,* 33381-33386. [7] e.g., Gerakines, P. A. et al. (2005), *ApJ, 620,* 1140–1150. [8] Cook A. M. et al. (2002), *BAAS 34*, 908. [9] Richey, C. R. et al. (2004), *LPSC XXXV,* Abstract#1450.

BIOGEOCHEMICAL AND SPECTRAL CHARACTERIZATION OF A SULFUR-RICH GLACIAL ECOSYSTEM AND POTENTIAL ANALOG TO EUROPA D. G. Gleeson[1,2,3], R. T. Pappalardo[2], S. E. Grasby[4], A. S. Templeton[1,3] & J. R. Spear[5]. [1] Department of Geological Sciences, University of Colorado at Boulder; [2] Jet Propulsion Laboratory, California Institute of Technology; [3] NASA Astrobiology Institute, [4] Geological Survey of Canada, Natural Resources Canada, Calgary; [5] Division of Environmental Science and Engineering, Colorado School of Mines.

Introduction and relevance: Borup Fiord Pass, in the Canadian High Arctic, is home to sulfur-rich springs abundant in microbes, which discharge onto the surface of glacial ice, releasing H_2S and forming deposits of native sulfur, gypsum and calcite [1]. The presence of sulfur in three oxidation states indicates a complex series of redox reactions, and preliminary investigations support the hypothesis of biological mediation of the sulfur chemistry.

Figure 1 - Sulfur-rich deposits on the ice, observed during the 2006 field season. Foreground scale is ~10m across the image.

The Borup Fiord Pass site is of particular astrobiological and planetary interest for several reasons. The chemistry of Europa's non-ice surface material [2, 3], possibly representative of the composition of its subsurface ocean, may be paralleled by the sulfur-rich chemistry of the supraglacial deposits. At a minimum the juxtaposition of ice and sulfur chemistry provides a valuable opportunity to evaluate and enhance our ability to identify and map the distribution of sulfur minerals on ice by reference to ground truth, allowing us to test remote sensing and in-situ techniques for application to Europa. From another perspective, if the connection between microbial communities present in the system and the local geochemistry is established, the extensive deposits can effectively be viewed as biosignature on a large enough scale to allow detection from orbital measurements. In addition, understanding the complex biogeochemical system operating in this extreme environment could lend insights to possible microbiologic niches at icy moons such as Europa.

Here we present our initial efforts to understand the biogeochemical processes which have led to the deposition of these sulfur-rich materials on the ice, and

investigate how well these materials can be characterized by use of remote sensing techniques.

Field and Remote Sensing measurements: A field expedition to Borup Fiord Pass was undertaken June-July 2006 to investigate the complex biogeochemistry of the site, and to provide ground truth for spectroscopic analyses of hyperspectral satellite imagery of the area.

Geochemical measurements obtained at spring sample sites included temperature, flow rates, pH, Eh, dissolved oxygen, and sulfide and sulfate contained within the spring waters. Sampling was also carried out on solid deposits for later laboratory analysis of major and trace ions and isotopic compositions. Biological samples for the same sample sites were obtained and preserved for culturing, microscopy and microbiological analysis.

Spectral reflectance measurements were collected by an ASD FieldSpecPro field spectrometer. Higher resolution field spectra of the sulfur-rich materials were obtained using illumination from a probe attached to the field spectrometer, increasing signal-to-noise ratios for these spectra, while many hundred more spectra were collected using natural illumination on a clear day.

Hyperspectral imagery of the site from the Hyperion instrument on EO-1 were obtained in a similar timeframe to the fieldwork.
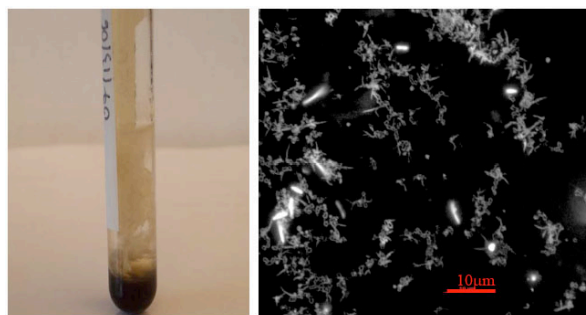
Figure 2 - FeS gradient tube (left) made with an artificial seawater medium shows rapid and abundant formation of S^0 when inoculated with sulfur-rich sample BF06-05A. Fluorescence microscopy (right) confirms the presence of microbial cells (bright rods) growing in the new S^0 deposits. No S^0 was formed in abiotic controls.

Analyses: Preliminary geochemical analyses of the spring waters have shown them to be high in salts, containing large amounts of sulfate (1786 mg/L). The results of these analyses were utilized to design targeted culturing experiments to determine which microorganisms mediate the biogeochemical

transformation of sulfur, and their varied modes of metabolism in this extreme environment. These culturing experiments were set up under environmental conditions similar to those in the field and were inoculated with returned samples. The experiments were designed to select for psychrophilic sulfide-oxidizing bacteria that could produce S^0, as observed on the ice. Rapid growth and elemental sulfur deposition was observed in the gradient tubes (Figure 2) at temperatures of 4˚C as sulfide in FeS was oxidized while abiotic controls showed no S^0 production. The only carbon source provided was CO_2, suggesting potentially autotrophic growth.

Parallel experiments targeting heterotrophic sulfate-reducing bacteria, which may be the source of H_2S produced from gypsum-derived sulfate, were also attempted, but the samples had not been appropriately preserved under anoxic conditions to successfully initiate the robust growth of sulfate-reducing bacteria in the laboratory. Preliminary sequencing of DNA extracted from returned samples has indicated the presence of known groups of sulfate-reducing microorganisms (e.g. classes of delta-Proteobacteria), while a small fraction of the total sequences do not correspond with any in the public databases (Figure 3).
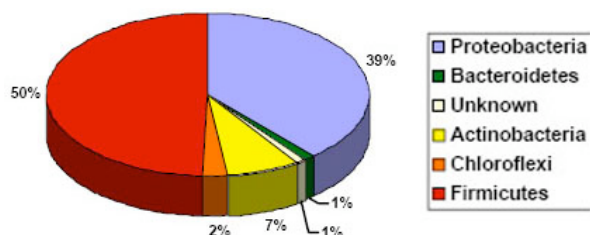
Figure 3 - Pie chart showing broadly-defined microbial community composition for a sulfur-rich sample (BF06-04a) collected in the summer 2006 field sampling. A small fraction of the total sequences do not correspond with any in the public databases.

The main spectral signatures emerging from the hyperspectral imagery of the area of interest are those of ice and sulfur. There may also be evidence for the bound water contained within gypsum in certain of the field spectra (Figure 4). Interpretation of the field spectra is aided by high resolution laboratory spectra of samples returned from the field.

Comparisons between satellite and in-situ spectral measurements taken across a grid are ongoing. Subpixel mapping of the distributions of the deposits has been achieved using both sulfur-rich spectrally pure Hyperion pixels, and certain of the field spectra collected in-situ as endmember spectra, and similar results are found for both.
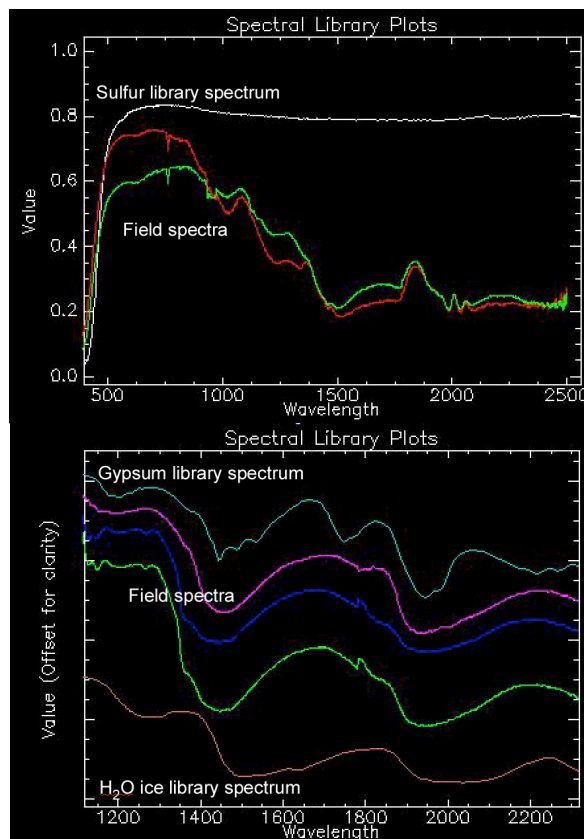
Figure 4 - Top: Field spectra match the sulfur curve in the 400-500 nm range. Bottom: Offsets in the shape and location of water absorption bands in the field spectra relative to those of the H_2O ice may be evidence for the bound water within gypsum.

Preliminary conclusions: Spectral analyses of the site have detected elemental sulfur on the ice from hyperspectral satellite imagery obtained from orbit, consistant with field spectra and geochemical analyses. While efforts are continuing to refine our spectral identifications and mapping of the spring deposits, the successful remote detection of these S^0-rich deposits, out of equilibrium with their environment, is of interest.

Preliminary evidence for microbial mediation of the sulfur transformations in this environment has been provided by our culturing experiments. Further exploration of the varied modes of metabolism which may exist in this extreme environment is necessary, via both further culturing experiments and DNA analyses. Much work remains to be done before we can fully understand the significance of this unique site, both as an analog to Europa, and as an extreme ecosystem, with a remotely detectable surface geochemical expression.

References: [1] Grasby, S.E. et al., (2003) *Astrobiology,* 3, 583-596. [2] McCord T.B. et al, (1998) Science, Vol. 280, 1242-1245. [3] Carlson R.W. et al., (1999) Science, Vol. 286. no.5437, 97-99.

VOLCANIC DEPRESSIONS AND LAVA LAKES ON EARTH, MARS, VENUS, IO AND TITAN. Tracy K.P. Gregg[1] and Rosaly M. Lopes[2], [1]Department of Geology, 876 Natural Sciences Complex, University at Buffalo, Buffalo, NY 14260-3050 (tgregg@geology.buffalo.edu), [2]Jet Propulsion Laboratory, MS-183-601, Pasadena, CA 91109 (Rosaly.M.Lopes@jpl.nasa.gov).

Introduction: Volcanic depressions are common on the terrestrial planets [e.g., 1]. On Earth, calderas typically form from collapse following: 1) an explosive evacuation of a substantial amount of magma (on the order of cubic kilometers or more) from a storage chamber [e.g., 2]; or 2) repeated injection into and effusive evacuation from a magma chamber of a smaller amount ($10^6 - 10^8$ km^3) of magma [e.g., 3]. It is not yet certain if either of these mechanisms are responsible for the large volcanic depressions observed on Io and Titan [4]. Furthermore, terrestrial calderas formed by repeated magma injection and eruption may become the home for lava lakes [3], as has been proposed for some volcanic depressions on Io [4]. In this paper, we will compare the morphologies of calderas on Io and Titan with those on Earth and other bodies, discuss possible origin, eruption processes, and global distribution.

Titan, like Io, also appears to have a young surface, as very few impact craters have been found so far [4, also this volume]. In contrast to Io, few calderas have been seen on Titan, and resurfacing seems to be accomplished by a more complex interplay of geological processes [6].

Ionian Paterae: Volcanic depressions are the most common form of volcanic feature on Io [4], and are called "paterae" because they show little (if any) topographic relief, but are characterized by flat-floored, steep-walled depressions that, in some cases, are filled with lava flows [7]. Lopes et al. [4] proposed that patera volcanism, most likely in the form of lava lakes, is the most widespread type of volcanic activity on Io. This has important implications for Io's resurfacing because, if the activity remains confined within calderas for long periods of time, resurfacing is likely being accomplished by processes other than spillage of lava on the surface. Geissler et al. [10] analyzed plume deposits and proposed that they could account for most of Io's resurfacing.

To date, 428 paterae have been identified on Io's surface [7]. Of these, 36 contain bright "islands" of material on their otherwise dark floors. An analyses of this subset of Ionian paterae [8] reveals that most paterae are <2000 km^2, and all but 4 are <6000 km^2. This distribution suggests that either: 1) paterae form through a process that favors small paterae, and these paterae then remain the same size throughout their lifetime; or 2) paterae form small and grow to be large over time. If the latter is true, then paterae size may be directly related to paterae age. By comparing the paterae dimensions to estimated resurfacing rates on Io, we can obtain estimates for paterae life-spans and growth rates. Resurfacing rates [9] indicate that an inactive paterae should be filled in with ash or lava within ~3 million years or less, depending on the initial paterae depth [7]. If all paterae appeared 30 Ma [10] at the size of the smallest paterae yet identified (5 km^2), growth rates of 70 ± 100 m^2/year are obtained. These are reasonable rates for terrestrial effusive calderas; in contrast, terrestrial explosive calderas form in a geologic instant.

Loki Patera is the largest volcanic depression on Io, and is ~200 km^2 across. Its behavior and morphology are unique [8,11], and represents an exceptional style of volcanism that does not have a straightforward terrestrial analog.

Titan: Cassini instruments, the RADAR in particular, have provided evidence of cryovolcanic features on Titan [12]. The Synthetic Aperture (SAR) mode of the RADAR provided images of about 15% of Titan's surface to date. Cryovolcanic features are not ubiquitous on Titan, but SAR images have revealed several caldera-like features, as well as radar-bright flows, a circular volcanic feature named Ganesa Macula, and several flows and craters identified as of possible cryovolcanic origin. The two Titan features that have most confidently been identified as calderas are part of the Ara Fluctus and Rohe Fluctus. Ara Fluctus is a scalloped feature similar in morphology to a feature on the grooved terrain on Ganymede [12] interpreted as a caldera and flow [13]. The Rohe Fluctus feature is a caldera-like feature and associated flow. Rheological modeling on the flow [12] indicate it to be a high-viscosity material, most likely a mixture of ammonia-water or ammonia-water-methanol [12]. The formation of calderas on Titan is not yet understood, but it is unlikely that explosive volcanism played a significant role [12, 14].

Mars and Venus: Both Mars and Venus contain an abundance of volcanic features, and to date, all evidence suggests that the volcanoes on these planets produce mostly basaltic lavas [e.g., 15, 16]. One might infer, therefore, that martian and venusian calderas formed primarily via repeated intrusion into and effusion of fluid magma out of a shallow chamber. Calderas on venusian and martian shield volcanoes are

display strikingly similar morphologies to those found on terrestrial basaltic shield volcanoes [1], but the extraterrestrial calderas are 1 – 2 orders of magnitude larger than their terrestrial counterparts. Like Earth, Mars displays calderas that experienced explosive behavior [e.g., 17], but these martian calderas are more morphologically similar to terrestrial effusive calderas.

The available resolution of radar imagery for the venusian surface (~250 m/pixel) is not sufficient to identify whether the venusian calderas contained lava lakes. Recently, Hansen [18] proposed that venusian crustal plateaus are the solidified remains of enormous lava "ponds" that formed from large impact events, and were not related to the formation of a volcanic caldera.

Given the morphologic similarities between martian and terrestrial calderas, it seems likely that at least some of the martian calderas hosted lava lakes at some time. The available images for Mars have ever-increasing resolution and topographic data. A solidified lava lake can be identified with high-resolution topographic data (<20 m/pixel vertical resolution) by seeking a lava flow surface within a caldera that has reached an equipotential surface. Comprehensive high-resolution (<10 m/pixel) imagery could help to constrain the difference between lava flows and a lava lake on a caldera floor, by revealing individual flow margins, or the pseudo-polygonal cracking that forms on the surface of solidifying basaltic lava lakes on Earth.

Comparisons: Large volcanic depressions on Earth appear to be formed from either explosive or repeated effusive volcanic eruptions. The morphologies of calderas on Mars and Venus are consistent with formation via repeated effusive eruptions. The Ionian paterae, however, appear unique in comparison (Figure 1) suggesting that their formation and evolution cannot be directly analogous to what is observed for caldera formation on Earth. The calderas on Titan are more morphologically similar to those on Earth, Mars and Venus than to those on Io, suggesting potential similarities in formation.

References: [1] Mouginis-Mark, P. and S.K. Rowland, 2001, *Geomorphology 37(3-4):*201-223. [2] Lipman, P,W., 2000, Calderas in *Encyclopedia of Volcanoes,* Academic Press, pp. 643-662. [3] Walker, G.P.L., 2000, Basaltic volcanoes and volcanic systems, in *Enclyclopedia of Volcanoes*, Academic Press, pp. 283-290. [4] Lopes, R.M. et al., 2004, *Icarus 169(1):*140-174. [6] Lopes, R.M. et al., 2007, *Icarus 186*:395-412. [7] Radebaugh, J. et al., 2001, *J. Geophys. Res. 106(12):*33,005. [8] Black, S.M., 2006, M.S. Thesis, University at Buffalo, 79 pp. [9] Geissler, P. et al., 2004, *Icarus 169(1):*29-64. [10] Matson, D.L., and others, 2001, *LPSC XXXII,* #1938. [11] Lougen, J.L., 2006, M.S. Thesis, University at Buffalo, 118 pp. [12] Lopes, R.M. et al., 2007, I*carus 186*:395-412. [13] Prockter, L., 2004, in *Volcanic Worlds,* Praxis Press, pp. 145-178. [14] Lorenz R., 1996, Planet. Space Sci. 44(9):1021-1028. [15] Bandfield, J., 2002, *J. Geophys. Res. 107(6)*, doi:10.1029/2001JE001510. [16] Crumpler et al., 1997, in *Venus II*, University of Arizona Press, pp. 697-756. [17] Greeley, R. and D.A. Crown, 1990, *J. Geophys. Res. 95(5):*7133-7149. [18] Hansen, V.L., 2006, *J. Geophys. Res. 111(E11010)* doi:10.1029/2006JE002714.
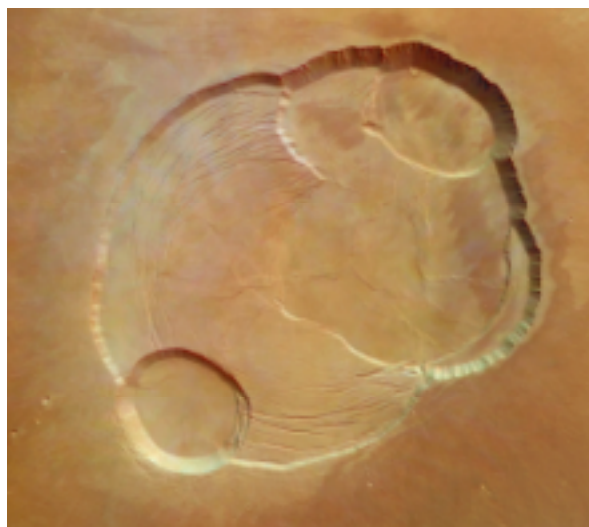
Figure 1A. Caldera of Olympus Mons, Mars. Image width is ~100 km. (Image courtesy of ESA/DLR/FU.)
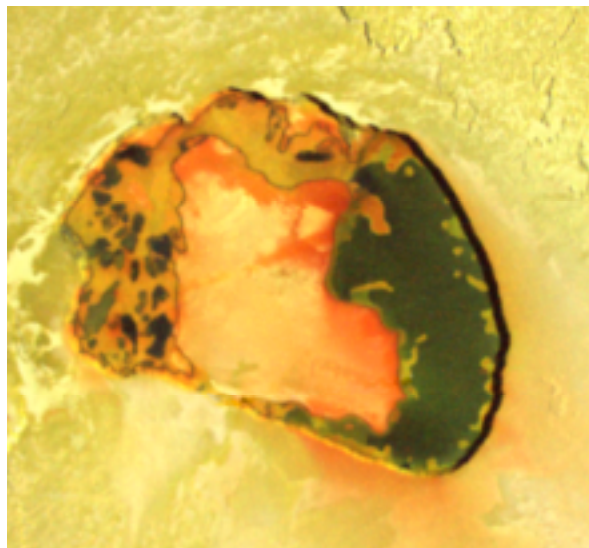
Figure 1B. Tupan caldera, Io. Caldera is ~75 km across. (Image courtesy of NASA/PIRL/LPL/UA.)

Magnetometer constraints on the ocean salinity and ice shell thickness of Europa. K. P. Hand[1,2] and C. F. Chyba[2], [1]Stanford University, Dept. Geological & Env. Sciences, 450 Serra Mall, Stanford, CA 94305, khand@stanford.edu, [2]Princeton University Dept. of Astrophys. Sciences, Peyton Hall, Princeton, NJ, 08544.

Introduction: We have recently provided new constraints on the salinity of the europan ocean and the overlying ice shell thickness [1]. Using the Galileo magnetometer results [2,3] and physical limits on the conductivity of aqueous solutions we find that for an amplitude ratio of A = 0.97±0.02 the ocean must be near saturation and the ice shell is 4 km thick. Accounting for the ±0.02 on A we find a maximum thickness of ~15 km and a minimum thickness of near zero thickness.

These results are for both a three-layer sphereical model (mantle, ocean, ice) and a five layer half-space model (core, mantle, ocean, ice, ionosphere). An ionosphere cannot account for the high amplitude, however additional modeling should help us better constrain the influence of the plasma [4].

Here we present results for extended ranges of A values, focusing on 0.9 < A < 1.0. At low values for A, near saturation salt levels permit an ice shell of ~25 km. Interestingly, solution with low A and thin ice shells permit near freshwater oceans (< 5 g salt per kg H_2O).

Finally, we consider sulfuric acid as a possible means for enhancing conductivity. H_2SO_4 has been proposed as an important surface compound [5] and comparisons with NIMS data indicate that solutions with [1:1:1] $MgSO_4$:Na_2SO_4:H_2SO_4 provide the best fit to the hydrate features in the spectra. Results show that H_2SO_4 can increase conductivity on small scales for oceanic engineering purposes [8] and on its own H_2SO_4 in solution is slightly more conductive than ocean salts [9]. Sulfuric acid cannot, however, significantly modify our results for the high-amplitude magnetometer results, *i.e.* an ice shell on the order of a few kilometers thickness is still requied to explain the observations.

References: [1] Hand K. P. and Chyba C. F. (2007) *Icarus,* doi:10.1016/j.icarus.2007.02.002 [2] Zimmer C. et al. (2000) *Icarus., 147,* 329-347. [3] Schilling N. (2004) *J. Geophys. Res,* 109. [4] Schilling N., pers. comm. [5] Carlson, R.W. (1999) *Science*, 286, 97-99. [6] Dalton J. B. et al. (2005) *Icarus., 177,* 472-490. [7] Orlando T. et al. (2005) *Icarus., 177,* 528-533. [8] Lin T. F. et al. (1991) *IEEE*:0-7803-0202-8, 1629-1631. [9] Handbook of Physics & Chemistry, (1978) CRC Press, Inc.

FAR ULTRAVIOLET OBSERVATIONS OF ICY SATELLITE ATMOSPHERES AND PLUMES.

C. J. Hansen[1] and A. R. Hendrix[1], [1]Jet Propulsion Laboratory, Mail stop 169-237, 4800 Oak Grove Dr., Pasadena, CA 91109; candice.j.hansen@jpl.nasa.gov.

Introduction: The potential for investigating the atmospheres and eruptive activity of icy satellites at far ultraviolet wavelengths has been demonstrated by the Cassini Ultraviolet Imaging Spectrograph (UVIS). UVIS has observed the oxygen atmosphere of Europa, determined upper limits for the potential oxygen atmosphere of Rhea, and constrained volatile activity of Phoebe. The biggest scientific payoff was the UVIS investigation of Enceladus' water vapor plume. The spatial dimension of the Cassini UVIS FUV channel adds the capability to map emissions, which often enhances the data interpretation.

Techniques: We have used two primary methods to study gases associated with icy satellites: long integration observations of gas emissions, and stellar occultations. In the FUV there are useful emission lines for common important gases such as oxygen (130.4 and 135.6 nm) and nitrogen (114.3 and 149.3 nm). Stellar occultation observations offer the opportunity to detect the broader absorptions of molecules such as water vapor, CO, CO_2, and O_2.

The Cassini UVIS has 4 channels: an extreme ultraviolet spectrograph (EUV), a far ultraviolet spectrograph (FUV), a Hydrogen-Deuterium Absorption Cell, and a High Speed Photometer (HSP). The UVIS FUV channel uses a 2 dimensional microchannel plate detector to cover 1024 spectral channels, spanning 111.5 to 190.0 nm, by 64 ~1 mrad spatial pixels. The EUV channel also uses a microchannel plate for similar simultaneous collection of spatial and spectral data. The wavelength range of the EUV channel is 55 to 110 nm. The HSP is sensitive to the same wavelength range as the FUV. The HSP is read out every 2 or 8 msec [1].

Specific Investigations: Cassini has observed all of Saturn's major icy satellites. Additionally, Io and Europa data were acquired as Cassini flew past Jupiter.

Sputtered Atmospheres - Europa. Europa has a thin O_2 atmosphere sputtered from its water ice surface. Discovered by HST [2] the predominance of 135.6 over 130.4 emission was indicative of O_2 as the primary constituent. The 130.4 emission feature is a multiplet, and is excited by resonant solar scattering and electrons. The 135.6 feature is also a multiplet, but is a forbidden transition, excited only by electron impact dissociation. The ratio of the two is indicative of whether the oxygen is atomic or molecular.

UVIS found that in addition to the bound molecular oxygen atmosphere there is atomic oxygen extending further out. The spatial dimension of the data allowed us to separate the contribution of atomic oxygen of Io's torus from atomic oxygen associated with Europa [3].

Sputtered Atmospheres - Rhea. Rhea is the largest of Saturn's icy moons, and the only one massive enough to potentially have a gravitationally bound atmosphere [4]. We selected 10 data sets to investigate whether spectral features indicative of the presence of an oxygen atmosphere could be detected. These were all observations with a typical duration of 90 min and stationary pointing. The data was calibrated and flat-fielded after summing over time. We then summed eight spectral pixels containing the 130.4 nm multiplet and eight spectral pixels containing the 135.6 nm multiplet. Eight spectral pixels between the two features were summed to use for background determination and subtracted from each of the oxygen feature sums. Signal above background was then plotted for the 130.4 spectral band and the 135.6 spectral band vs. UVIS spatial pixel to look for a morphologic association of oxygen with Rhea.

Although there are oxygen emission features in the data we believe these are associated only with the oxygen permeating Saturn's system [5], not with Rhea. The signal levels are consistent with the system oxygen, and there is no morphological indication that the oxygen is bound to Rhea.

We have calculated an upper limit to the oxygen from the UVIS detection threshold [6]. UVIS sensitivity at 130.4 nm is 3.4 counts/sec-kRayleigh. For a 90 min duration observation the detection threshold at 130.4 nm is 2.72 Rayleighs or $(1/4pi)*2.72 \times 10^6$ photons/cm^2-sec-ster. Solar scattering constrains the amount of atomic oxygen that is detectable (the probability for electron excitation is far lower). The probability for solar photon scattering (g-val) at Saturn is 1.8×10^{-7} / sec. Column density can be calculated from I = [O] * l *g-val where l is the path length. The upper limit atomic oxygen column density is then [O]= $2.72 \times 10^6 /(1.8 \times 10^{-7}) = 1.5 \times 10^{13}$ cm^{-2}. Similarly the upper limit for molecular oxygen column density is determined by the signal due to electron impact dissociation probability. UVIS sensitivity at 1356 is similarly 3.4 counts/sec-kRayleigh, thus required signal is again 2.72 Rayleighs for a positive detection. For emission due to electron impact dissociation, I= $[O_2]*[e-]*k*l$. For an electron density of 5/cm^3 and k = 3.5×10^{-9} cm^3/sec at 20 eV, $[O_2] = 2.72 \times 10^6$ / (5 x $3.5 \times 10^{-9}) = 1.6 \times 10^{14}$ cm^{-2} [6].

Phoebe Volatile Activity. The possibility that Phoebe could have formed originally in the outer solar

system motivated us to look for evidence of volatile activity analogous to Chiron. Total integration time on Phoebe was 10.3 hours. The spectrum shows no evidence of oxygen, nitrogen or carbon monoxide emissions that would be anticipted if volatile activity were present. Upper limits to oxygen and C abundance were calculated as above [7].

Enceladus' Plume. Two stellar occultations were observed during two close Cassini passes by Enceladus. The first showed no indication of the presence of an atmosphere. The second showed the clear absorption signature of a gas on ingress but not egress. This was the initial evidence that Enceladus has a regionally confined plume rather than a globally distributed atmosphere. The absorbing gas was identified to be water vapor and the column density was determined at different altitudes corresponding to the track of the star. Simple assumptions with regard to the velocity (we assumed thermal velocity at a temperature of 145 K) and spatial distribution allowed the flux of water from Enceladus to be computed [8]. As Cassini approached Saturn we observed atomic oxygen filling the system [5]. The source was a mystery until the discovery of the plume of water vapor spewing from Enceladus. The calculation of the flux of water from Enceladus showed that this is an adequate amount to maintain the oxygen in the system against losses. Conversely, observations of the oxygen in the system can be used as a proxy for monitoring Enceladus' levels of eruptive activity. Data analysis shows that the number density of system oxygen has changed, occasionally dramatically [5].

More sophisticated modeling of the plume, validated by comparison to the vertical distribution of water vapor determined from the stellar occultation data, verified the flux numbers. The velocity that best matched the data was 300 to 500 m/sec which implies that the source is venting from some depth beneath the surface, inconsistent with simple sublimation of a surface source [9].

A new stellar occultation observation will be acquired in October 2007, shown in Figure 1. The geometry of the occultation will carry the star approximately parallel to Enceladus' limb, through the jets of gas coming from the tiger stripes that blend to become Enceladus' plume. The UVIS HSP will be used to detect fluctuations in density, which will help to determine the ability of the gas to loft solid particulates of ice.

Escaping gases. Stellar occultations and emission feature profiles can be used to derive the profile of a gas escaping from Saturn's icy moons, such as hydrogen. Hydrogen emission feature profiles were reported on in 2005, however results were tentative [10]. The

profiles are being updated with the new UVIS flat field calibration. We will also report on the acquisition and analysis of new stellar occultation data from Tethys, Dione and Rhea.

References:
[1] Esposito, L. et al (2004) *SSR, 115:299-361*. [2] Hall, D. T. et al (1995) *Nature* 373:677-679. [3] Hansen, C. J., D. Shemansky and A. Hendrix (2005) *Icarus* 176:305-315. [4] Saur, J. and D. Strobel (2005) *Astrophys. J.*, 620:L115-L118. [5] Esposito, L., *et al* (2005) *Science* 307:1251-1255. [6] Jones, G. et al (2007) submitted to *Nature*. [7] Hendrix, A. R. and C. J. Hansen (2007) submitted to *Icarus*. [8] Hansen, C. J. *et al* (2006) *Science* 311:1422-1424. [9] Tian, F. *et al* (2007) *Icarus*, in press. [10] Hendrix, A. R. and C. J. Hansen (2005) *BAAS* 37:706.
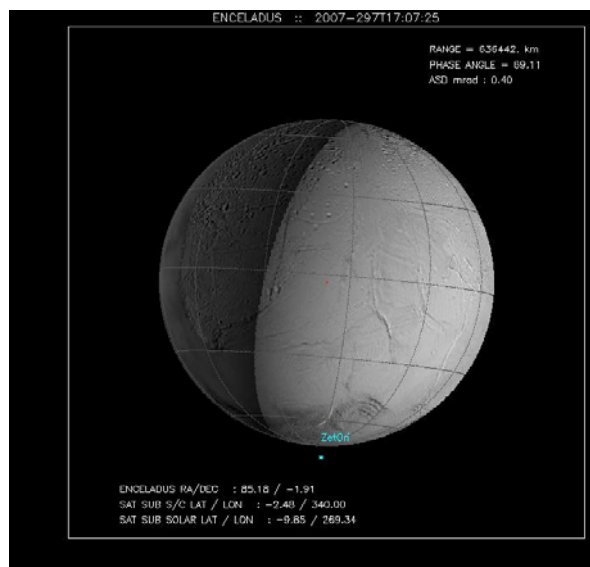
Figure 1. The geometry of this occultation will carry the UVIS field of view horizontally through Enceladus' plume, which may allow us to detect individual gas jets coming from the tiger stripes.

PROGRESS ON RECTIFYING AND RECALIBRATING GALILEO/NIMS OBSERVATIONS OF THE ICY GALILEAN SATELLITES. G. B. Hansen, Space Science Institute, Department of Earth and Space Science, University of Washington, Seattle, WA 98195 (ghansen@rad.ess.washington.edu).

Introduction: Our goal is to complete a radiometric recalibration and rectification of the Galileo Near Infrared Mapping Spectrometer (NIMS) dataset for the three icy Galilean satellites of Jupiter. As this is completed, we will perform water ice modeling of the recalibrated cubes, including amorphous/crystalline ice mapping that we have done before [1] as well as modeling the full spectrum with ice and non-ice models to determine grain size and abundance of water ice on Ganymede [2], and later possibly Callisto and Europa.

The rectification of about half of the NIMS observations of Ganymede had previously been completed. The recalibration involves starting with the raw instrument data records, removing dark levels and patterns, and applying a new radiometric calibration that principally improves the results at wavelengths below 1 µm. At high phase angles (>95–100°), the instrument viewed through parts of a rotating section of the spacecraft, generically called "booms", which cause the periodic obscuration of the target with added reflected and thermal energy. The effects of the booms were originally poorly compensated for, and we intend to introduce a procedure that properly identifies the affected data, and that also recovers data that has been only partially obscured. This boom correction is first needed for several high-phase Ganymede observations. Other rectification procedures to be developed include an accurate radiometric calibration for the highest gain state in orbits before E6 (used primarily for Callisto observations), and improved radiation spike removal in observations where the spike density is more than about 50% (used primarily for Europa observations).

The NIMS Instrument and its Data: The NIMS is an imaging spectrometer that records a 0.7–5.3 µm spectrum for each element of an image [3]. There are up to 408 wavelengths that could be measured, recorded in 17 discrete regions corresponding to individual detectors, but often only 200 or fewer were archived. The spectra are built up by making up to 24 exposures on each detector while stepping the spectrometer grating. The spectral image is constructed from instantaneous fields-of-view (IFOV) that are spatially Nyquist sampled, such that adjacent IFOVs from the same grating position overlap by one half. The IFOVs of the other grating positions lie in between these positions, assuming constant scan platform motion, The spatial oversampling allows one to image each observation in a camera projection with pixels about half the size of the IFOV (0.5 mrad square). Ide-

ally, this could be done utilizing detailed telemetry on spacecraft and scan platform position, but in practice, only less accurate modeled motions were available in most cases.

Results: We are studying the observations of the three icy Galilean satellites, Europa, Ganymede, and Callisto. NIMS returned about 30 cubes each for Callisto and Ganymede, and about 60 for Europa (about half of them from the extended mission). About 10-15% of the Ganymede observations are affected by booms, while as many as 30% of the Callisto observations are. Only a few percent of the Europa observations, all in the extended mission, are affected by booms.

Aside from using the correct dark levels and radiometric calibration, we also correct (1) offsets at wavelengths between adjacent detector regions from incorrect dark values or incorrect radiometric calibration, (2) odd-even and other wavelength patterns from incorrect odd-even dark values and/or incorrect spectral reconstruction in regions of high spatial contrast, and (3) improperly corrected booms. Radiation spikes that occur in the data must be removed before projection; we use our own routine that performs well and is well tested (e.g., [1], [5]).

Ganymede: We have completed the recalibration of three new Ganymede observations to date. The camera projection footprint algorithm for projecting the NIMS cubes (NIMSGEOMF) had disappeared from the
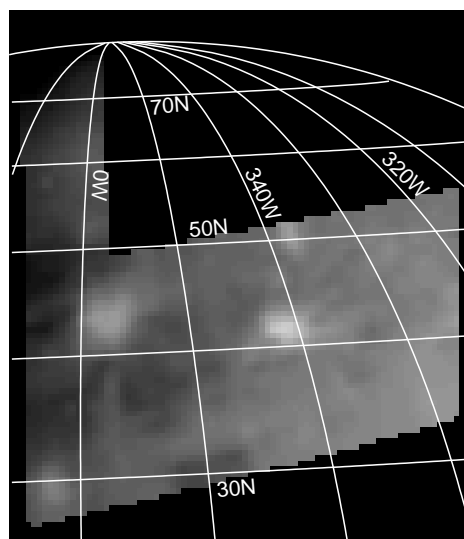
Figure 1. 0.7-µm image of the G7 HILAT observation with location grid.
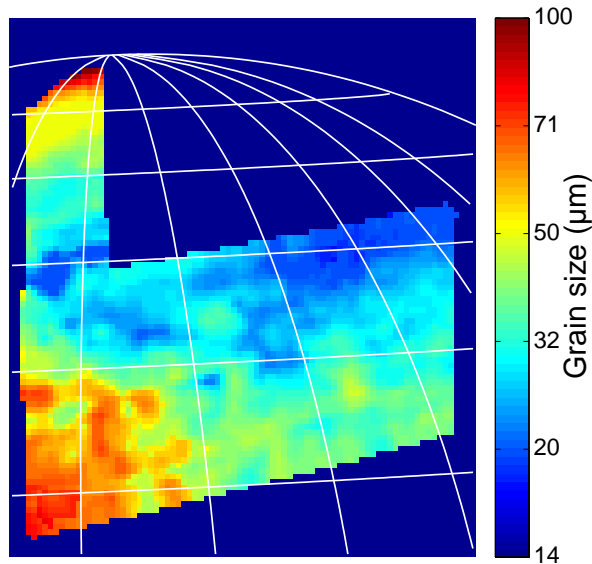
Figure 2. Grain size map for G7 NHILAT.
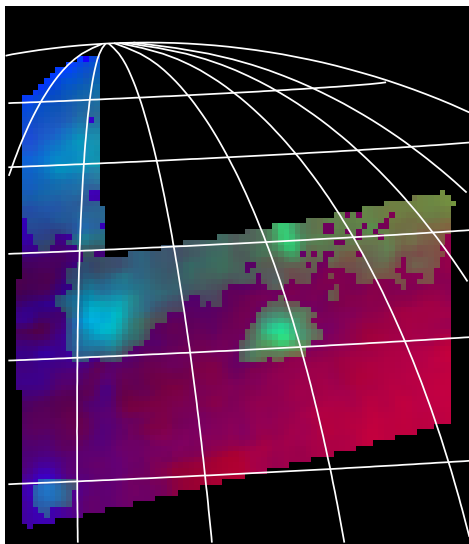
Figure 3. Color map showing Ganymede non-ice as red, Europa non-ice as green and water ice/snow as blue.

latest ISIS releases. So we had to resurrect the program, which now works well. We continued the crystalline/ amorphous analysis of these cubes [1], which we have already finished for the 13 Ganymede cubes processed previously (e.g., Figs. 1–2).

We have started on a new method to map the water ice grain size and abundance, starting with these new cubes. The current model uses linear mixing, with only one grain size, and a mixture of two scaled non-ice spectra for Ganymede [4] and Europa [6] (Fig. 3). This model assumes segregated ice and non ice, which we have found to be generally applicable for Ganymede and Callisto [1]. Unlike [1], we are now using a plane-parallel bi-directional reflectance model for the ice

spectrum, using the appropriate lighting geometry for each pixel. The fits are good, even though multiple grain sizes and a non-uniform scaling of the non ice spectrum (see [1]) would improve some of the fits.

Gain State 4 Calibration: The latest calibration (mainly detectors 1-2) was derived from a global Europa observation at gain state 2. The gain states 3 and 4 calibration followed by using existing fixed ratios between the gain states. The gain state 4 calibration did not appear to work well with Callisto observations. The calibration after orbit E6 was shown to be good using (1) a low-phase leading hemisphere global observation of Callisto on orbit G7 that was compared to telescopic measurements, and (2) a double observation of Europa in orbit E11 using both gain states 3 and 4. The early gain state 4 calibration is still to be finished.

Europa Despiking: We have successfully completed despiking an observation of Europa (E6 TER-INC) that had 70-80% spikes in the region beyond 3 µm. This has revealed surprising results that are being reported elsewhere. We expect that this procedure should be generally applicable to Europa observations.

Boom Detection and Correction: We have completed our first study of boom correction using a distant Callisto observation at 123° phase. Some of the smaller booms seem to block less at longer wavelengths and a thermal model for the partially blocked pixels can be removed. This process can be automated to some extent as we investigate it further.

Future Work: We will continue Ganymede calibration and modeling (dependent somewhat for the full correction of boom-affected cubes). This is straightforward, and the amorphous/crystalline mapping is also fully developed. We may need to also add the Callisto-type non-ice spectrum, non-constant scaling of the non-ice, and mixed grain sizes to the ice modelling routine to improve fits.

The completion of the Ganymede dataset is dependent on a quick adaptation and familiarization of the boom correction routines that we have developed.

We also plan to continue looking at Europa data sets with the goal of repeating the success of our first encounter with the Europa data.

References:
[1] Hansen G.B. and T.B. McCord (2004) *JGR, 109*, E01012. [2] Hansen G.B. *et al.* (2006) *Eos, 87(36)*, Abs. P41B-05; Hansen G.B. *et al.* (2006) *BAAS, 38*, 540. [3]Carlson R.W. *et al.* (1992) *Space Sci. Rev., 60*, 457–502. [4] McCord T.B. *et al.* (2001)**,** *Science, 292*, 1523–1525. [5] Hibbitts C.A. *et al.* (2000) *JGR, 105*, 22541–22557; Hibbitts C.A. *et al.* (2003) *JGR, 108(E5)*, 5036. [6] McCord T.B. *et al.* (1998) *Science, 280*, 1242–1246; McCord T.B. *et al.* (1999) *JGR, 104*, 11827–11852.

WIDESPREAD CO$_2$ AND OTHER NON-ICE COMPOUNDS ON THE ANTI-JOVIAN AND TRAILING SIDES OF EUROPA FROM GALILEO/NIMS OBSERVATIONS. G. B. Hansen, Space Science Institute, Dept. of Earth and Space Science, University of Washington, Seattle, WA 98195 (ghansen@rad.ess.washington.edu).

Introduction: The Near Infrared Mapping Spectrometer (NIMS) on the Galileo Jupiter orbiter observed the Jovian system in the infrared spectral range from 0.7-5.3 µm. Absorption bands found in the 4-µm region of the reflectance spectrum of the icy Galilean satellites have been attributed to bond vibrations of simple radicals and compounds such as CO$_2$, SO, SH, CN and CH {1, 2, 3]. These discoveries were made first on Ganymede and Callisto only, because of the large density of radiation spikes in the early data from Europa prevented any useful analysis of this spectral region. Towards the end of the prime mission, some distant, low spatial resolution (200-300 km per NIMS pixel) observations of the trailing hemisphere of Europa were made with spike densities comparable to typical Callisto and Ganymede observations. Analysis of these data revealed CO$_2$, SO$_2$, [4] and H$_2$O$_2$ [5] compounds. The best analysis of the abundant hydrated compounds (salts) found on the trailing side of Europa [6] yielded a noisy, low reflectance spectrum from 3.3 to 5.3 µm.

Observation Details and Calibration: The NIMS builds up spectral images by building a spectrum over 20 mirror positions (Nyquist sampled) and up to 408 wavelengths (Nyquist sampled for all 408). These wavelengths are sensed by 17 discrete detectors, each of which covers a small region of the spectrum. The third dimension of the spectral image is filled out by scanning the instrument field-of-view slowly perpendicular to the mirror motion [7]. Each such scan is called a swath, and many NIMS observations are built up of two or more swaths, generally acquired in a raster mode.

The NIMS observations of the icy satellites are now being reexamined and recalibrated using new techniques [8]. This involves determining the best dark values and radiometric calibrations for each observation. The Europa observations awaited an improved technical processes: to determine the best values for the spectra longer than 3 µm, where the good data is outnumbered by radiation spikes by a ratio of 2:1 or more. The first Europa observation to be processed was on the E6 orbit that was known to have fewer spikes overall than many other orbits. The first observation in this orbit was named TERINC (Terra Incognito), and consisted of two NIMS swaths (downloaded) covering the central latitudes of Europa between about 140 and 260 degrees western longitude with a phase angle of 36 degrees (see Fig. 1). The southern swath was taken in a
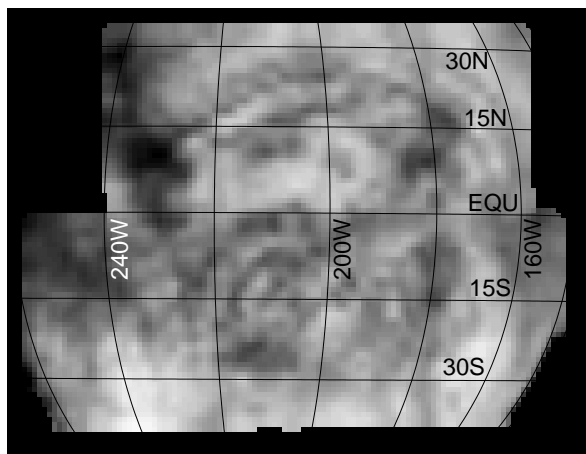
Figure 1. Approximate albedo image of the first wavelength of the E6 TERINC observation. The albedo ranges from 56% (hydrate) to beyond 80% (ice).

higher gain state and exhibits some saturation from 1.1–1.45 µm near the sub-solar point. This observation used half the available wavelengths and one detector (2.40–2.67 µm) was not working by this time (giving a total of 192 wavelengths).

The observation was dark-corrected and radiometrically calibrated using the best dark and calibration values and wavelength list. The wavelengths up to 2.4 µm were despiked using our usual procedure (see [2] for information on wavelengths and despiking). The standard despiking uses a 3x3x3 NIMS pixel analysis that throws out outliers until a good fit to a 3-D hyper surface can be made; this hyper surface is used to predict the actual value at the center if it is a spike. The parameters to the procedure are a percentage of large outliers to eliminate on the first pass, then three passes to identify outliers with varying criteria. The short wavelength process yielded about 20% spikes.

For the wavelengths longer than about 2.75 µm the same despiking was used with much tighter first-pass parameters. This despiking was repeated three times to remove most of the visible spikes. Then a few hundred remaining small spikes were manually removed up to 4.4 µm. Beyond this wavelength the instrument only has a few digital numbers (DN) of signal, and contains no information other than general level. These wavelengths were further processed by averaging and smoothing the spectrum over 4x4 NIMS pixels, and constraining all the spectra in that block to match this average within 1.5 DN. The final frequency of spikes in
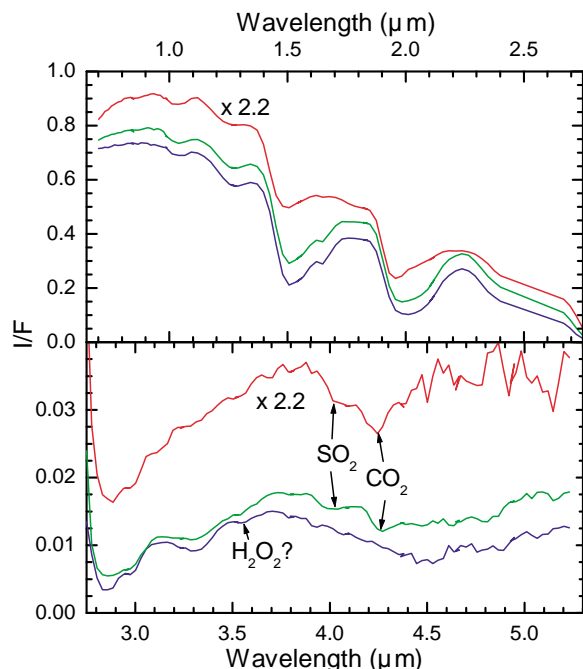
Figure 2. Example spectra from E6 TERINC.

Figure 3. (top) Map of 4.25 µm band depths from 0 (blue) to 30% (dark red).

Figure 4. (bottom) The frequency of different band-depths as a function of albedo

this region was 70-80%. Because of this aggressive approach, there is undoubtedly some averaging over adjacent pixels or wavelengths that occurs that must be taken into account when comparing to observations of the other satellites.

Results: Average spectra from three locations are shown in Fig. 2. One is from an almost pure hydrate region (red) while the other two are from more ice-rich areas (blue and green). The longwave portion (bottom graph) shows a smooth rise to a possible inflection near 4.0 µm (SO_2) and a band at 4.25 µm (CO_2) for the hydrate. The icy spectra have a Fresnel peak near 3.1 µm and a smooth peak at 3.6 and dip at 4.5 µm characteristic of fine-grained snow. On some ice-rich spectra there are additional bands centered near 4.0 and 4.25 µm, and a band near 3.5 µm attributed to H_2O_2 [5].

Since the 4.25-µm band (CO_2) is contained within one NIMS detector and is not affected by detector overlap offsets (like e.g. the 4.0-µm band), it was simple to map its distribution using methods described by Hibbitts *et al.* [2]. This map is shown in Fig. 3 and shows band depths exceeding 30%. Compared to the image in Fig. 1, it appears that the strong bands are concentrated in the hydrate-rich areas, and this is shown most clearly in a plot showing the fraction of all pixels of a given albedo that have band depths greater than a given level. Here it can be seen that nearly all the darkest pixels have band-depths greater than 15%, and a quarter of them have band-depths greater then 25%.

A preliminary map of the 4.0-µm band shows weaker absorption and a different distribution. This analysis requires data from two detectors to define the continuum and will take more work to do correctly.

Conclusions: Absorption bands attributed to CO_2 and SO_2 have been found on the anti-Jovian and trailing sides of Europa for the first time. A first analysis shows that the CO_2 appears to be associated with the darker hydrate (salt) materials, as it has also been shown to occur mainly in the non-ice materials on Callisto and Ganymede [2, 3]. Since the hydrate seems to be associated with the interior of Europa [6], the source of the CO_2 may be internal, rather than produced by some radiolytic processes on the surface.

References:
[1] McCord T.B. *et al.* (1997) *Science, 278*, 271–275; McCord T.B. *et al.* (1998) *JGR, 103*, 8603–8626. [2] Hibbitts C.A. *et al.* (2000) *JGR, 105*, 22541–22557. [3] Hibbitts C.A. *et al.* (2003) *JGR, 108(E5)*, 5036. [4] Smythe W.D. *et al.* (1998) *BAAS, 30*, Abs. 55P.07, 1448. [5] Carlson R.W. *et al.* (1999) *Science, 283*, 2062–2064. [6] McCord T.B. *et al.* (1998) *Science, 280*, 1242–1246; McCord T.B. *et al.* (1999) *JGR, 104*, 11827–11852. [7] Carlson R.W. *et al.* (1992) *Space Sci. Rev., 60*, 457–502. [8] Hansen G.B. and T.B. McCord (2004) *JGR, 109*, E01012; Hansen G.B. *et al.* (2006) *Eos, 87(36)*, Abs. P41B-05; Hansen G.B. *et al.* (2006) *BAAS, 38*, 540.

CRYOGENIC PROPERTY MEASUREMENTS ON ICY COMPOSITIONS WITH APPLICATION TO SOLAR SYSTEM ICES.

C. C. Hays[1], J. C. Castillo-Rogez[1], K. L. Mitchell[1], M. Barmatz[1], F. Zhong[1], H. Englehardt[2], W. Smythe[1], D. L. Matson[1], R. T. Pappalardo[1], R. M. C. Lopes[1], S. M. Gudipati[1], L. E. Robshaw[3,1] C. Neish[4], J. I. Lunine[4], and J. S. Kargel[5], [1]Jet Propulsion Laboratory, California Institute of Technology, 4800 Oak Grove Drive, Pasadena, CA 91109. E-mail: Charles.C.Hays@jpl.nasa.gov, [2]Department of Geophysics, California Institute of Technology, [3]Lancaster University, Environmental Sci. Dept., Lancaster, UK, [4]Dept. of Planetary Sci., University of Arizona, [5]Department of Hydrology and Water Resources, Univ. Arizona.

Introduction: To fully appreciate the discoveries made by the *Cassini-Huygens* and *Galileo* missions, to prepare for the *Dawn* and *New Horizon* missions, and to look forward to potential missions to Europa, Enceladus, and Titan, we present the motivations, objectives, and preliminary experimental results for a new experimental cryo-ices initiative launched at JPL. This work is a joint effort among experimentalists and theorists at JPL, in collaboration with specialists in icy material properties the world over.

Science Motivation: In response to observations and theoretical modeling need for realistic input we are developing an experimental initiative aimed at understanding the link between ice composition (including structure) and icy satellite observations.

Icy satellite internal evolution. Internal evolution models depend upon accurate characterization of the elastic moduli, deformation pathways and mechanisms, and solid-state rheology of the component materials. Ice rigidity and viscosity play a role in the modeling of convection, differentiation, , ice behavior at premelting conditions, cryovolcanism, and other geological activity. Spacecraft observations of planetary surfaces, which can provide use with more information on the history of the satellites, regard geological features such as lithospheric response to loading, crater relaxation, folding/faulting as a function of strain rate. The role of ice properties in many of these processes is addressed by [1]. Also these properties play a major role in the tidal response of the bodies, and associated tidal dissipation. For the icy moons of the outer satellites, cosmochemical arguments suggest that these materials will be dominated by water, with variable amounts of materials plausibly including ammonia [2], methane clathrate hydrates [3], salts [4], and other materials.

Enceladus' resurfacing processes. A major discovery of the Cassini-Huygens mission is the observation of a hot region surrounding Enceladus' South pole, associated with a surface likely less than 1 My old, faults (the "tiger stripes"), and intense plume-generating activity [5, 6]. Plausibly cryovolcanic landforms have been identified on Titan [7-9], which may be ammonia hydrate slurries and which are associated with methane, and possibly containing organics. Cryovolcanic activity has been suggested to be responsible for resurfacing and/or landform construction on the

surfaces of Ganymede, Miranda, Ariel, Triton, and others, driven by radiogenic heating and/or tidal heating [10]. However, our understanding of mechanisms behind these processes is limited; in particular, how ice responds mechanically to tidal stresses, and the behaviour of eruptive materials during flow, are poorly constrained.

Titan's complex environment. Titan's atmospheric and crustal volatile chemistry produce a complex assemblage of materials, in some cases beyond those of other icy bodies, that may be mobilized surficially and in the upper crust [11], and could exhibit a wide range of behaviours. These may play an important role in limnologic (lake) [12], fluvial, sedimentary, aeolian [13], glacial and periglacial processes [11, 14]. Despite some successful characterization of Titan's surface and atmospheric materials by Cassini VIMS spectral analysis [15], it is unclear whether Cassini will be able to determine much of the range of important surface materials through Titan's obfuscating atmosphere Therefore, in order to understand the materials involved in the various processes on the surface of Titan, we need to use a less-direct approach.

We use combinations of observation, theory and experiment to relate primarily morphological observations of surface features to the processes and materials that could have formed them. On Titan, such materials most likely include liquid methane and/or ethane, cryovolcanic ammonia hydrate slurries (possibly containing organics), and a variety of carbonaceous compounds, organics, tholins, salts and hydrates.

In the above cases, our ability to relate landforms and other observations to the processes that formed them is sorely limited by physical models that contain incomplete databases of the physical properties of the candidate materials. These properties include the rheological behaviour of candidate cryovolcanic slurries, the loss tangent of liquid methane/ethane, rates of dissolution and wetting angles of liquid methane and ethane on candidate surface materials, and the mechanical properties and mobility of surface solids (water-ice, ammonia hydrates, acetylene, etc.).

Experimental Approach: A range of experiments are being devised which will improve our ability to model ice-rock body internal evolution and geological processes using modern synthesis and characterization

techniques under cryogenic conditions. Initial experiments will involve pure water (H_2O), methanol-water (CH_3OH-H_2O), ammonia-water (NH_3-H_2O) and ammonia-water-methanol mixtures, relevant to a range of icy satellites and processes. Ammonia is considered to be play and important role in Titan cryovolcanism, whereas methanol is chosen primarily due to its suitability as an experimental analog as well as its each-of-use in the laboratory, although it has been considered previously as a potential cryovolcanic material in the outer solar system (e.g. [16]). Where beneficial, we will determine basic thermophysical properties and phase diagrams using a Differential Scanning Calorimeter.

Solids. First, we plan to analyze samples from terrestrial glaciers, which are relevant to both the terrestrial and planetary geology and geophysical communities. Terrestrial glaciers appear as realistic analogs for modeling processes taking place in icy satellite outer icy shells [17-19]. These results will better enable us to predict the long-term evolution of terrestrial glaciers and ice shelves.

Also, we will develop specimen with controlled properties. The synthesis methods for icy specimens will exploit equilibrium and non-equilibrium methods. Equilibrium methods, e.g., conventional (slow) freezing in a mold, will provide microstructural length scales, *d*, in the range ~200 μm to 10 mm (with and without preferred orientation, e.g., columnar grains). Non-equilibrium methods, e.g., rapid-quenching, will vitrify the specimens, and we will control the specimen microstructure (e.g., grain size) via low temperature annealing.

Post-synthesis microstructural characterization will be performed using Cryogenic Optical Microscopy integrating a cross-polarizer to analyse thin sections, and a Cryogenic Scanning Electron Microscope.

Mechanical property measurements on solid specimens will be performed between 80 and 270 K with a cryogenically cooled Instron measurement system. Compression measurements will be conducted as a function of temperature, strain-rate, microstructural length scale and orientation. The time dependent viscous response will also be measured by performing creep (applied load versus time) measurements over the same range of temperatures. Using low-frequency cyclic loading, we will measure the dissipation factor at frequencies approaching satellite orbital frequencies. We will report preliminary mechanical property measurements of Antarctic glacial specimens at cryogenic temperatures. These measurements will be of great importance to support the preparation of flagship missions to Enceladus, Titan, Europa, and the Jupiter System currently under study.

Fluids. In order to improve our understanding of effusive cryovolcanism, we will measure rheological properties of liquid and mixed (slurry) materials between 80 and 300 K using a cryogenically cooled *Brookfield* rotational rheometer, based on the experimental procedures of Kargel *et al.* [16], but over a much wider range of parameters and with a greater degree of automation. Control and data acquisition will be carried out using a *LabView* custom interface. The results will be integrated into parallel modeling efforts that include the slurry rheology modeling discussed above.

We will report preliminary measurements of the temperature dependence of the viscous response for several compositions in the Methanol-Water System $(CH_3OH)_x(H_2O)_{1-x}$. Also, we will describe an experiment designed to measure methane wetting and dissolution on water ice. These experiments will be carried out in order to explore the effects of the presence of methane lakes on Titan's surface.

We are developing the capability to investigate more complex materials relevant to surface processes on Titan, including methane-ethane phase studies, hydrocarbons such as acetylene and benzene, as well as tholins and clathrates, which should exhibit a range of rheological and mechanical properties from fast-moving fluids to glacial creep.

References: [1] Durham and Stern (2001) *Ann. Rev. Earth Planet. Sci., 29*, 295-330. [2] Tobie G. *et al.* (2005) *Icarus*, *175*, 496-502. [3] Prieto-Ballesteros *et al.* (2005) *Icarus*, *177*, 491-505. [4] Kargel J. S. (1991) *Icarus*, *94*, 368-390. [5] Spencer *et al.* (2006) *Science, 311*, 1401-1405. [6] Porco *et al.* (2006) *Science, 311*, 1393-1401. [7] Elachi C. *et al.* (2005) *Science, 308*, 970-974. [8] Sotin C. *et al.* (2005) *Nature, 435*, 786-789. [9] Lopes R. M. C. *et al.* (2007) *Icarus* 186, 395-412. [10] Schenk, P. M. and Moore, J. M. (1998). *Solar System Ices*, 551-578. [11] Kargel J. S. *et al.* (2007) *LPS 38,* 1992. [12] Stofan E. R. *et al.* (2007) *Nature, 445*, 61-64. . [13] Lorenz R. D. *et al.* (2006) *Science, 312*, 724-727. [14] Mitchell K. L. *et al.* (2007) *LPS 38*, 2064. [15] Clark R. N. *et al.* (2006) *Eos. Trans. AGU 87(52)*, Fall Meet. Suppl., Abstract P11A-03. [16] Kargel *et al.* (1991) *Icarus, 89*, 93-112. [17] Sandwell S. *et al.* (2004) *JGR, 109*, E11003. [18] Duval P. and Montagnat M. (2004) *Workshop on Europa's Icy Shell*, Abstract #7001. [19] Barr A. and McKinnon W. B. (2007) *JGR* 112, L02012.

ULTRAVIOLET MEASUREMENTS OF THE SURFACES OF THE ICY SATURNIAN SATELLITES.

Amanda. R. Hendrix[1] and Candice. J. Hansen[1], [1]Jet Propulsion Laboratory/California Institute of Technology, Mail Stop 230-250, Pasadena, CA 91109; arh@jpl.nasa.gov.

Introduction: The Cassini mission has provided a unique opportunity to make high-resolution, multi-spectral measurements of Saturn's icy moons, to investigate their surface compositions, processes and evolution. Here we present results from the Ultraviolet Imaing Spectrograph (UVIS). This instrument allows for the first measurements of the icy satellites in the extreme ultraviolet (EUV) to far-ultraviolet (FUV) wavelength range.

The icy satellites of the Saturn system exhibit a remarkable amount of variability: Dark, battered Phoebe orbiting at a distant 200 R_S, black-and-white Iapetus, the wispy streaks of Dione, cratered Rhea and Mimas, bright Tethys and geologically active Enceladus. Phoebe, Iapetus and Hyperion all orbit laregely outside Saturn's magnetosphere, while Mimas, Enceladus, Dione Tethys and Rhea all orbit within the magnetosphere. Furthermore, Mimas, Enceladus, Tethys, Dione and Rhea all orbit within the E-ring – so the extent of exogenic effects on these icy satellites is wide-ranging.

Goals of Investigation. After 3 years in orbit around Saturn, we present a comprehensive overview of UVIS results from Phoebe, Tethys, Dione, Iapetus, Mimas, Enceladus and Rhea, focusing on surface investigations. We expect that the UV signatures of these icy satellites are strongly influenced not only by their composition, but by external effects and magnetospheric environments. We study the EUV-FUV reflectance spectra to learn about the surface composition, map out water ice grain size variations, investigate effects of possible coating by E-ring grains, examine disk-resolved and hemispheric compositional and brightness variations, and investigate the presence of radiation products such as O_3 and H_2O_2.

Instrument and Datasets: We present results from Cassini's December 31, 2004 flyby of Iapetus and the June 11, 2004 flyby of Phoebe. The range to Phoebe (radius=107 km) at closest-approach was 2068 km, while the Iapetus closest-approach distance was 124,000 km. Data from the inner icy satellites have been acquired on many close flybys, including Mimas on August 2, 2005 (47,000 km), Enceladus on July 14, 2005 (175 km), Tethys on September 15, 2005 (3200 km), Dione on October 11, 2005 (1000 km), Rhea on November 26 2005 (500 km) and Hyperion on September 26, 2005 (514 km).

The Cassini UVIS [1] uses two-dimensional CODACON detectors to provide simultaneous spectral and one-dimensional spatial images. Two spectro-graphic channels provide images and spectra in the EUV (563-1182 Å) and FUV (1115-1912 Å) ranges. The detector format is 1024 spectral pixels by 64 spatial pixels. Each spectral pixel is 0.25 mrad and each spatial pixel is 1 mrad projected on the sky. The UVIS has three selectable slits. The high-resolution slit is 0.75 mrad wide for the FUV channel (1.0 mrad for the EUV channel), the low-resolution slit is 1.5 mrad wide for the FUV channel (2.0 mrad wide for the EUV channel) and the occultation slit is 8.0 mrad wide for both the FUV and EUV channels. The high- and low-resolution slits have spectral widths of 2.75 Å and 4.8 Å, respectively, in both the FUV and EUV channels, while the occultation slit has spectral widths of 24.9 Å and 19.4 Å in the FUV and EUV slits, respectively. The FUV low-resolution slit illuminates 6 spectral pixels, and the EUV low resolution slit has 5. Two-dimensional spatial maps are built up by using motion of the spacecraft to scan the UVIS slit across the body (Fig. 1).
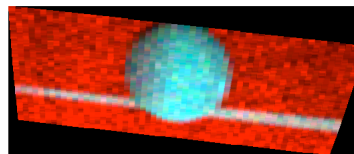
Fig. 1. FUV image of Rhea, shown with the rings in the background. Brightness variations due to surface features are visible. Red = Ly-α (1216 Å), blue=1600-1800 Å, green=1800-1900 Å.

Results:

Reflectance Spectra. The reflectance spectrum is obtained by ratioing the raw spectrum, with background subtracted, to a solar spectrum. We define reflectance as

$$r = I/F = P/(S/\pi)$$

where P is the calibrated signal from the satellite with background subtracted, in kR/Å. The solar flux is denoted by S, where $S = \pi F$. We use the solar data as measured by SOLSTICE on the SORCE spacecraft [2] at the appropriate solar longitude for the day of each observations scaled to the heliocentric distance of the moon on the day of the observation.

The FUV reflectance spectra of all of the icy Saturnian exhibit the strong water ice absorption feature at 165 nm. Sample spectra of Enceladus and Tethys are shown in Fig. 2. Overplotted are spectral models including water ice only. The model simulates the large

absorption feature, but does not accurately fit the data at wavelengths <1600 Å or at wavelengths >1800 Å. We investigate the possible sources of these discrepancies.

Spectral Models. To model the reflectance spectra of the icy satellites, we intimate mixture models (after e.g.,[3]) We use of optical constants of water ice [4] and of candidate non-ice species. The spectral model of water ice for various grains sizes is shown in Fig. 1. Sample spectral models are shown overplotted on the satellite reflectance data in Fig. 2. The non-ice species largely are featureless in this wavelength region and do not constrain compositional models.
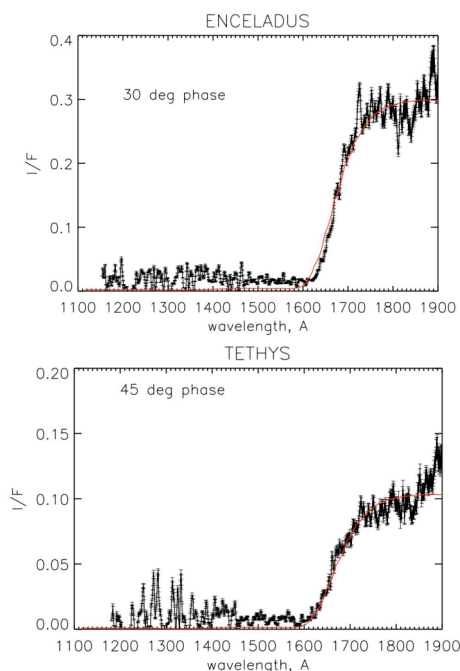
Fig. 2. Sample FUV reflectance spectra of the icy Saturnian satellites. Overplotted are spectral models of pure H_2O ice.
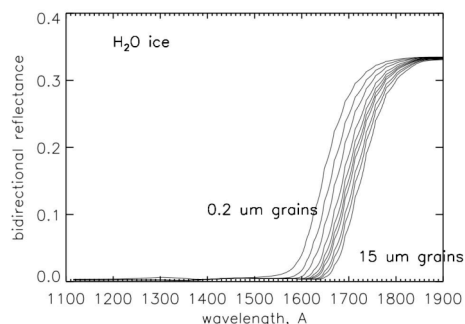
Fig. 3. Models of water ice reflectance spectra for several grain sizes, using optical constants [4].

The H_2O ice absorption feature is present even in the low latitudes of the apex region of the dark leading hemisphere of Iapetus (Fig. 4); the H_2O ice band depth increases with latitude away from the apex. Comparisons with Phoebe and Hyperion show that both of those bodies are richer in water ice that the Iapetus dark terrain. If either of those bodies is the source of the Iapetus dark material, water ice has been lost in the impact process; or, perhaps a more likely scenario is that the water ice has been lost subsequent to impact on Iapetus. We consider the idea that the dark material is warm enough at low latitudes, partly due to the slow rotation of Iapetus [5] that water ice has largely segregated from the lowest latitudes; the fact that water ice is present in the lowest, warmest latitudes suggests that the coating process is recent or ongoing.
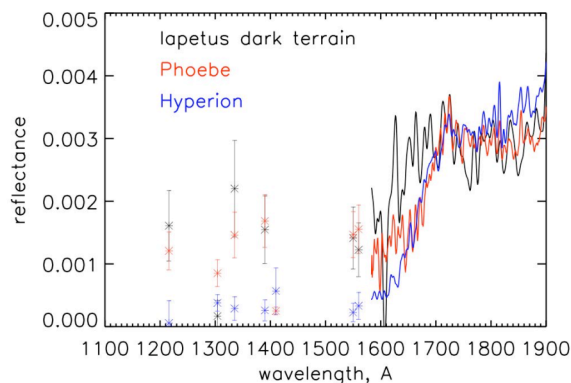
Fig. 4. Scaled reflectance spectrum of Iapetus's dark terrain (lowest latitudes) compared with disk-averaged spectra of Hyperion and Phoebe. The H_2O ice absorption feature is present even in the lowest latitudes of the dark Iapetus terrain, though it is not as strong as on Phoebe or Hyperion.

References: [1] Esposito et al. (2004) *Space Sci. Rev, 115,* 299-361. [2] McClintock et al. (2000) *Proc. SPIE, E.O.S. V, 4135,* 225-234. [3] Roush, T. L. (1994) *Icarus, 108,* 243-254. [4] Warren, S. J. (1984) *Appl.Optics, 23,* 1206-1225. [5] Spencer et al. (2005) *LPSC XXXVI.*

THE ICY GALILEAN SATELLITES AS MEASURED BY THE GALILEO UVS. Amanda. R. Hendrix[1] and Robert E. Johnson[2], , [1]Jet Propulsion Laboratory/California Institute of Technology, 4800 Oak Grove Dr., MS 230-250, Pasadena, CA, 91109, arh@jpl.nasa.gov, [2]University of Virginia, Thornton Hall B103, PO Box 400238, Charlottesville, VA 22904, rej@virginia.edu.

Introduction: We investigate the effects of exogenic processes on the icy Galilean satellites (Europa, Ganymede and Callisto), by analyzing Galileo UVS data to determine the spatial distribution of the UV absorption features. Ultraviolet wavelengths sense the topmost layers of the surface, and are therefore very sensitive to exogenic effects. A thorough analysis of Galileo UVS data can lead to a determination of the abundances and distribution of radiation products such as H_2O_2, O_3 and SO_2. Important connections with the external environment have been obtained for bands associated with H_2O_2 on all three icy Galilean satellites [1], for bands associated with SO_2 on Europa [2], and for bands associated with O_3 on Ganymede [3]. These studies were all performed before the Galileo mission was complete and therefore with incomplete data sets. Therefore, use the full UVS data set to determine the distribution and band depths of various features and then associate these when possible with abundances of radiation products, for all three icy moons.

Preliminary Results: We have investigated all spectra of Callisto and classified them by overall spectral shape in the NUV: some regions were found to be relatively spectrally red or blue over portions of the NUV wavelength range. We have found distinct trends in spectral shape across the surface. At high southern latitudes, the spectra tend to "roll over" at wavelengths >280 nm – suggesting the shoulder of an absorption feature with a band center ~350 nm (Fig. 1). At lower latitudes, in both the Asgard and Valhalla regions, such a spectral shape is not seen. We find that the Asgard region is spectrally red at wavelengths >280 nm while the spectra of the Valhalla region are spectrally flat at wavelengths >280 nm. The lower latitudes are generally darker and largely spectrally redder than the high southern latitude region. This suggests that an absorber is present at high latitudes, which is weathered away by charged particle or UV bombardment at low latitudes. We investigate possible sources for this absorption, and whether it could be due to an organic species.
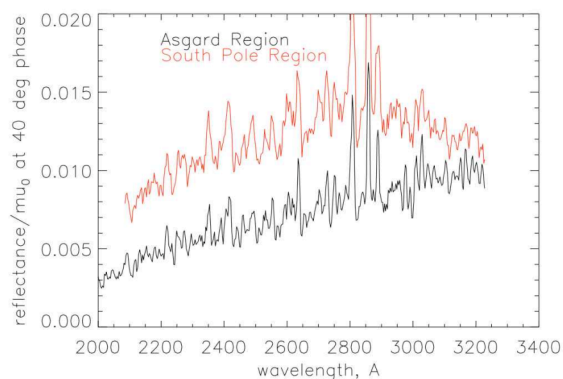
Fig. 1. Galileo UVS reflectance spectra of two regions on Callisto – the low latitude Asgard region and the high south pole region. The south pole region is somewhat brighter and the spectrum appears to show the shoulder of an absorption band. Scattered data points in the spectra are due to mismatches with the solar spectrum.

References: [1] Hendrix et al. (1999) *Lunar Planet. Sci., XXX* #2043 [2] Hendrix et al. (1998) *Icarus, 135*, 79-94 [3] Hendrix et al. (1999) *J. Geophys. Res.*, *104*, 14169-14178.

PHYSISORPTION: TRAPPING VOLATILES IN THE SURFACES OF ICY SATELLITES. C. A. Hibbitts[1] and J. Szanyi[2], [1]Johns Hopkins Univ. Applied Physics Laboratory, 11100 Johns Hopkins Rd., Laurel, Md. 20723, email: karl.hibbitts@jhuapl.edu, [2]Pacific Northwest National Laboratory, EMSL, Richland, Wa., 99352, email: janos.szanyi@pnl.gov.

Introduction: Frozen water and non-ice materials dominate the surfaces of the icy satellites orbiting Jupiter and Saturn [1,2,3,4]. Observations by spacecraft and earth-based telescopes have also discovered a few additional materials at lower abundances. Of these, carbon dioxide is one of the most prevalent, having been detected over much of Callisto, Ganymede, Iapetus, Phoebe, and to a lesser extent on Europa, Enceladus, Dione, Hyperion, and Saturn's F-ring [5,6,7,8,9,10,11,12,13]. On Ganymede and Callisto the molar CO_2 abundance is estimated to be ~ 0.1 % [14,15,16]. However, its physical state and origin remain only partly understood.

In an attempt to address the question of how it is held in these satellites' surfaces, we have measured the infrared (IR) ν_3 feature of CO_2 adsorbed onto a selection of minerals that are potential compositional and spectral analogs to the nonice materials on these satellites. This is particularly relevant to the Galilean satellites Callisto and Ganymede where the CO_2 detected by infrared spectroscopy is most likely contained within the nonice material [8,15]. Results from these laboratory experiments support the hypothesis that some of this CO_2 may be physisorbed. This mechanism of binding the CO_2 to the surface places few constraints on the origin or host material of the CO_2.

CO_2 in the satellites' surfaces: The shape and position of the infrared reflectance minimum for the CO_2 ν_3 band at ~ 4.26 µm is distinctly different from that of pure CO_2 ice or gas, and is consistent with CO_2 trapped in one or more host materials [e.g. 8]. Spectral mixing models demonstrate that most of the CO_2 on Callisto and Ganymede responsible for the distorted ν_3 band cannot be in the ice, which is large-grained, but is contained within the non-ice material [15,16]. Additionally, the surfaces of the Galilean and at least some of the Saturnian satellites are sufficiently warm that the CO_2 must be stabilized in a host material to prevent its escape into space. The spectral characteristics of the CO_2 absorption band are also similar on several of the Galilean and Saturnian satellites [16,9,10]. This similarity implies similar physical states for the trapped CO_2 and possibly a single trapping mechanism

Physisorption: We propose that this trapping mechanism may be physisorption. Physisorption is caused by weak inter-molecular van der Waals forces between the adsorbate molecules and areas of asymmetric charge distribution within the adsorbing host

material. The van der Waals force can exist between CO_2 and an adsorbant when a charge asymmetry in the adsorbent induces a weak dipole within the otherwise symmetric CO_2 molecule. This partial electronic polarization of the CO_2 is thus a function of the structure of the host molecule and the charge distribution within the host molecule. Complex silicates offer excellent structures for the adsorption of CO_2 because of their significant asymmetric distribution of charges within a unit cell and their large microporosity offering many sites for CO_2 to adhere [17]. This results in considerable absorption. However, at room temperature, the strength of the van der Waals bond is insufficient to keep the CO_2 adsorbed when the host material is exposed to vacuum.

Results and Conclusions: We have found that CO_2 can remain physisorb onto some clays when the CO_2 partial pressure is effectively zero under ultrahigh vacuum (UHV) if the adsorbant is cooled to the surface temperatures of the icy satellites of Jupiter and Saturn (Figure 1). CO_2 remains adsorbed onto the clay mineral montmorillonite for > 10s of minutes when exposed to a vacuum of ~1 $\times 10^{-8}$ Torr at ~ 125K. However, CO_2 does not adsorb onto serpentine, goethite, or palagonite under these conditions. A small
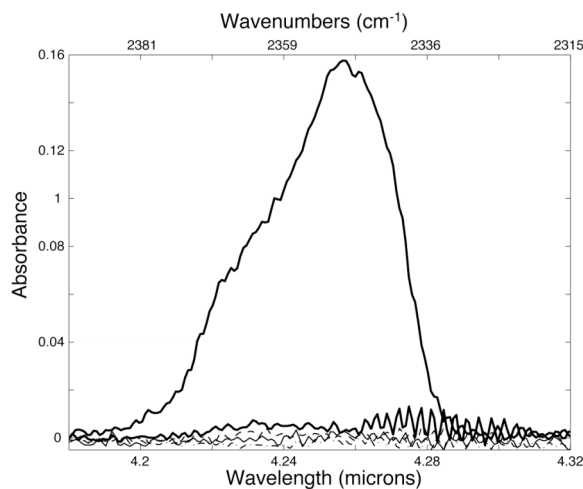
Figure 1. CO_2 adsorption onto nonice materials at ~ 125-142K under ~1x10^{-8} Torr. Ca-montmorillonite strongly adsorbs CO_2 (thick black line). Kaolinite may adsorb a small amount (thick black line). Serpentine, goethite, and palagonite (thin lines) do not adsorb detectable quantities.

amount may adsorb onto kaolinite. These are materials materials that may have similar microporosities, but whose unit cells possess much less charge asymmetry than smectites. When heated above 150K under vacuum, the CO_2 desorbs from the montmorillonite within a few minutes. We infer that the presence of a strong charge asymmetry which can induce a strong dipole in the CO_2 molecule is the most important requirement for physisorption at cryogenic temperatures.
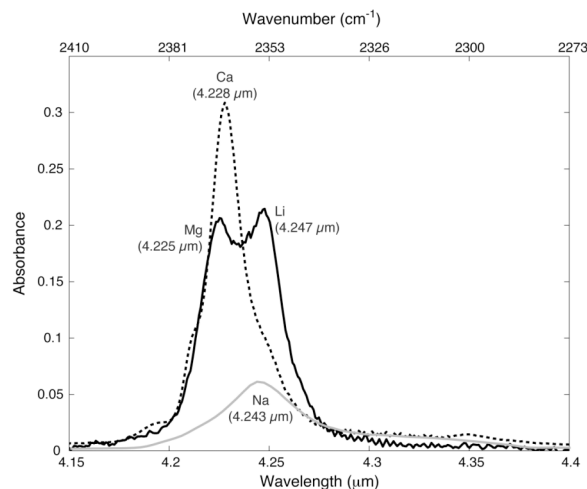
Figure 2. . Room-temperature spectra of CO_2 physisorbed onto various montmorillonite minerals. The cation composition of the montmorillonite affects the shape of the absorbance spectrum. Black: Mg,Li. Gray: Na (scaled x8), Dotted: Ca.

The strength of adsorption and the spectral characteristics of the adsorbed CO_2 infrared ν_3 absorption band near 4.25 μm also can depend on the composition of the adsorbent (Figure 2). The ν_3 absorption band of CO_2 adsorbed onto montmorillonite at 125K is similar to that of the CO_2 detected on the Saturnian and Galilean satellites (Figure 3) and is markedly different from CO_2 adsorbed onto the same montmorillonite at room temperature. The temperature-dependency may signify that different sites are accessd by CO2 at cryogenic and room temperatures. The temperature dependency in the stability of the CO2 and on its spectral characteristics, and the compositional dependency on the spectral characteristics of the CO2 are consistent with the adsorption process being physisorption. We postulate that this mechanism may explain the presence and spectral characteristics of the CO_2 detected in the surfaces of the Jovian and Saturnian icy satellites.

References: [1] Johnson, T.V., McCord, T. B. 1971., Astrophys. J., 169, 589-594, [2] Pilcher, C. B., Ridgeway, S. T., McCord, T. B. 1972., 178, 1087-1089; [3] Clark, R. N. 1980., Icarus, 44, 388-409 [4] Clark, R. N., Steele, A., Brown, R. H., Owensby, P. D. 1984., Icarus, 58, 265-281, [5] Carlson, R., 39 col-

leagues 1996, Science, 274, 385 - 388, [6] Carlson, R. W. 2001., Bull. Amer. Astron. Soc., 33, 1125, [7] Smythe, W. D., Carlson, R. W., Ocampo, A., Matson, D. L., McCord, T. B., and the NIMS team. 1998., Bull. Amer. Astron. Soc., 30, 1448, [8] McCord, T. B., 12 colleagues. 1998., J. Geophys. Res., 103, 8603–8626, [9] Buratti, B. J., 28 colleagues 2005., The Astrophysical Journal, 622, 2, L149-L152, [10] Clark, R.N., 25 colleagues 2005a., Nature, 435, 66-69 [11] Clark, R.N., 24 colleagues 2005b., Bull. Amer. Astron. Soc., 37, 705, [12] Brown, R.H., 24 colleagues 2006., Icarus, (in press), [13] Filacchione, G., 27 colleagues 2006., Icarus, (in press), [14] Hibbitts, C. A., McCord, T. B., Hansen, G. B. 2000., J. Geophys. Res., 105, 22541-22557., [15] Hibbitts, C. A., Hansen, G. B., McCord, T. B. 2002., J. Geophys. Res., 107, E10,5084, [16] Hibbitts, C. A., Hansen, G. B.., Pappalardo, R., McCord, T. B. 2003., J. Geophys. Res., 108, DOI 10.1029/2002JE001956, [17] Chiou, C. T. 2002., J. Wiley & Sons, pp 86-105.
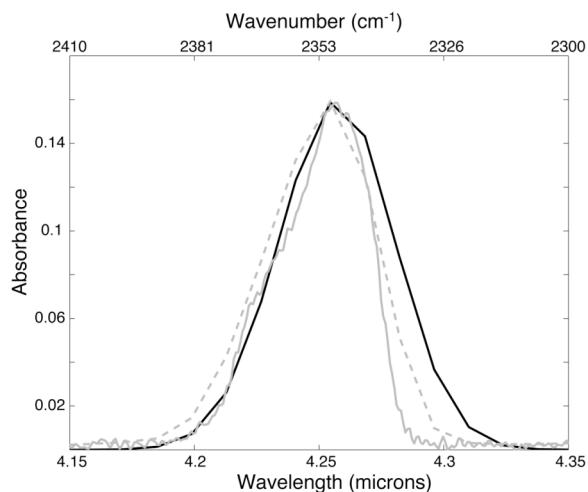
Figure 3. The laboratory spectrum of CO_2 physisorbed onto Ca-montmorillonite at 125K is similar to the Galileo NIMS spectrum of CO_2 in the surfaces of the Galilean satellites. Black line: NIMS spectrum CO_2 in the surface of Callisto (scaled x 0.17. Gray line: Laboratory data at full resolution of ~ 2nm (solid); and resampled to NIMS channels and spectral resolution (dashed).

LABORATORY STUDIES OF THE FORMATION AND STABILITY OF HYDRATES RELEVANT TO ICY SURFACES.

R. L. Hudson[1,2] and M. H. Moore[2,3], [1]Deparment of Chemistry, Eckerd College, St. Petersburg, FL 33733, USA (hudsonrl@eckerd.edu), [2]Goddard Center for Astrobiology, NASA Goddard Space Flight Center, Greenbelt, MD 20771, USA, [3]Code 691, Astrochemistry Branch, NASA Goddard Space Flight Center, Greenbelt, MD 20771, USA (Marla.H.Moore@nasa.gov).

Introduction: Ices on planetary satellites of the outer Solar System are characterized by a variety of compositions, temperatures, and radiation environments. However, the dominance of H_2O in many ices suggests that this molecule strongly influences the chemistry and the spectroscopy of all other observed materials. It further suggests that the formation of hydrates and hydrated ions may be common.

Two molecules to which these ideas might apply are SO_2 and NH_3, both of which are observed in the outer Solar System. For SO_2, the application is to Europa, where the intense jovian magnetospheric radiation can convert SO_2, in the presence of H_2O-ice, into a variety of sulfur-containing ions. The overall amorphous structure for such a mixture will slowly convert, on warming, into that of a crystalline hydrate, with a yield that is balanced by the radiolytic destruction of the hydrates themselves as part of a sulfur cycle. Beyond Jupiter, NH_3 is thought to exist on Miranda, Charon, and Quaoar, a possible source being cryomagma brought up to cold surfaces where it is quenched. For these latter three objects, the radiation environments are less intense and the temperatures lower than near Jupiter, but hydrates might still form and undergo radiation-induced chemical changes. In all cases, thermal processing might still promote dehydration of SO_2- and NH_3-hydrates on surfaces. Unfortunately, significant gaps exist in our knowledge of hydrate formation, stability, and chemistry for the relevant physical conditions.

Results: To study all of these processes, we have prepared H_2O-rich mixtures of both SO_2 and NH_3 in order to investigate their thermal and chemical stability and evolution in high-radiation environments, such as icy moons of the outer Solar System [1], [2]. For Europa applications, we have recorded the mid-infrared spectra of 0.8 MeV proton-irradiated SO_2 and H_2O + SO_2 ices in order to measure the radiolytic half-life of SO_2 itself, as well as to identify radiation products. Formation of several sulfur-containing ions has been documented and, on warming the irradiated ices, hydrated sulfuric acid was observed. The thermal evolution of the hydrate in a vacuum is one of slow H_2O loss to yield pure sulfuric acid. As an example, Figure 1(a) is the IR spectrum of H_2O + SO_2 (3:1) after irradiation to a dose of 15 eV $molec^{-1}$ at 86 K. Spectrum (a) evolves with warming, as shown. Reference spectrum (d) is for crystalline H_2SO_4 monohydrate, $H_2SO_4 \cdot H_2O$, at 210 K [3]. These spectra have different scaling factors, as indicated, and are stacked for clarity. By 260 K, the monohydrate has evolved into sulfuric acid, with the spectrum of trace (f).

We also have completed low-temperature IR spectroscopic studies (1 to 20 μm) of H_2O + NH_3 mixtures, with an emphasis on features in the near-IR region, which is accessible to ground-based observers. Conditions for the formation and thermal stability of the
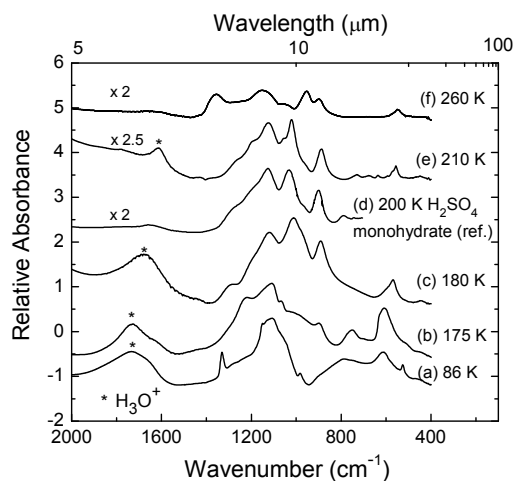
Figure 1
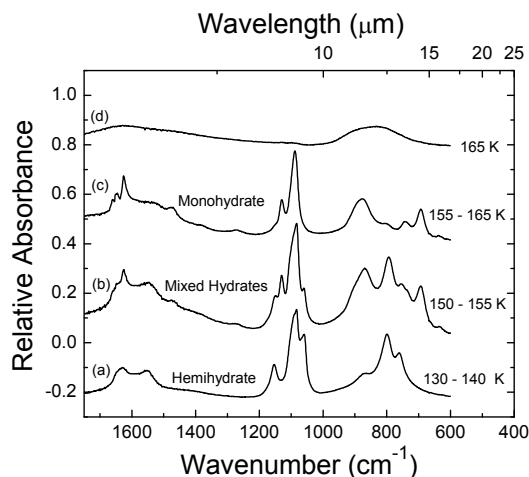
Figure 2

ammonia hemihydrate ($2NH_3 \cdot H_2O$) and the ammonia monohydrate ($NH_3 \cdot H_2O$) have been examined. The former undergoes a slow loss of NH_3 in a vacuum environment, to give the monohydrate. Figure 2 shows this thermal evolution of $2NH_3 \cdot H_2O$ from trace (a) to a mixture of $2NH_3 \cdot H_2O$ and $NH_3 \cdot H_2O$ hydrates in (b), and then to (c) after a complete the conversion to $NH_3 \cdot H_2O$. Additional warming removes the remaining NH_3 to give spectrum (d), which is characteristic of H_2O-ice. Again, spectra are stacked for clarity.

IR band positions of both SO_2 and NH_3 in different H_2O-ices have been tabulated at 86 K and higher, and compared to the positions for SO_2 and NH_3 hydrates. We report spectral shifts that depend on both concentration and temperature. The radiation-induced amorphization of hydrates was observed and the radiolytic destruction of SO_2 and NH_3 in H_2O-ices was measured. We also have tabulated IR spectral positions of sulfur- and nitrogen-containing ions. Implications of these results for the formation, stability, and detection of SO_2 and NH_3 on outer satellite surfaces will be discussed.

References: [1] Moore, M. H., Hudson R. L., Carlson, R. W., 2007. The radiolysis of SO_2 and H_2S in water ice: Implications for the icy jovian satellites. Icarus (in press). [2] Moore, M. H., Ferrante, R. F., Hudson R. L., Stone, J. N., 2007. Ammonia-water ice laboratory studies relevant to outer Solar System surfaces. Icarus (in press). [3] Couling, S. B., Nash, K. L., Fletcher, J., Henderson, A., Vickerman, J. C., Horn, A. B., 2003. Identification of surface molecular hydrates on solid sulfuric acid films. J. Amer. Chem. Soc. 125, 13038-13039.

THE ROLE OF TIDES IN TECTONIC FORMATION AND ERUPTION ACTIVITY ON SATELLITES IN THE OUTER SOLAR SYSTEM. Terry Hurford, NASA Goddard Space Flight Center, Code 698, Greenbelt, MD 20771 (hurfordt@core2.gsfc.nasa.gov).

Tides play a major role in the evolution of satellites in the outer solar system. These small bodies should be cold dormant worlds yet many of these bodies exhibit relatively young surfaces. Tidal friction provides a source of internal heat that allows resurfacing. Where tidal heating is dominant active resurfacing can be currently observed. Tides also generate global stresses on these moons, which can crack and displace the surface crust, contributing to the resurfacing of these bodies. Evidence for tidally driven tectonic formation is visible in the tectonic record.

Tidal Control of Eruptions on Enceladus. T. A. Hurford[1], P. Helfenstein[2], G.V. Hoppa[3], R. Greenberg[4] and B. G. Bills[1,5], [1]Planetary Geodynamics Laboratory, NASA Goddard Space Flight Center, Greenbelt, MD 20771, USA. [2]CRSR, Cornell University, Ithaca, NY 14853, USA. [3]Raytheon, Woburn, MA 01801, USA. [4]Department of Planetary Science, University of Arizona, Tucson, AZ 85721, USA. [5]Institute for Geophysics and Planetary Physics, Scripps Institution of Oceanography, La Jolla, CA 92093, USA.

Introduction: Enceladus is a small moon that Saturn every 1.37 days at an average distance of about 238,000 km, between Mimas and Tethys. Due to its proximity to Saturn, tidal dissipation should have quickly circularized the orbit. However, a 2:1 mean motion resonance with Dione, which orbits just beyond Tethys, and is ~15 times more massive than Enceladus, excites the orbital eccentricity, maintaining its value at the currently observed 0.0047.

In 2005, Cassini's Imaging Science Subsystem (ISS) detected plumes near Enceladus' South Pole in three high-phase (rear illumination) images [1]. Triangulation of the plumes places their sources near the South Pole where the terrain is dominated by a series of youthful-looking parallel rifts called, "tiger stripes" (Fig. 1) [1]. The Composite Infrared Spectrometer (CIRS) showed that the "tiger stripe" features are significantly warmer than the surrounding terrain [2] and are thus considered likely sources of the plumes [1,2].

Tides and Plumes on Enceladus: Saturn creates a substantial tide-raising potential throughout Enceladus, distorting the body. The exact size of the tide raised at the surface is dependent on the physical properties of Enceladus' interior structure. However, even if Enceladus' bulk properties tend to resist deformation, its low surface gravity would still result in a sizable tide. A conservative estimate of the height of the primary tide is 500 m.

Enceladus' finite eccentricity causes daily oscillations in the magnitude and location of the tidal bulge, producing patterns of stresses on its surface similar to those studied on Europa [3,4,5]. The state of stress at each point on the surface cyclically changes as the tidal shape of the body changes. Over Enceladus' orbital period, horizontal stresses resolved across the tiger stripes alternate from compressive to tensile, perhaps allowing the faults to open at some point in the orbit, and expose a subsurface volatile reservoir of liquid water or clathrate [6], creating an eruption. Then, within a few hours, once again the stress becomes compressive, forcing cracks to close, ending any possibility of an eruption until the next cycle. To test the hypothesis that observed eruption plumes come from these cracks, we have analyzed the stresses along each tiger stripe rift to check whether any of the features were under tension during the observations.

The three observing sequences (January, February, and November) showed plume activity at different locations in Enceladus' orbit. During the January observation, Enceladus was about an eighth of an orbit past apocenter. 46% of the total tiger stripe length was in tension during the hour-long imaging sequence (Fig. 2a). An additional ~1% (between 225° and 45° longitude) began under tension and switched to compression over the hour. During this part of the orbit, the rifts were in the process of closing as the stresses in the region become compressive.

At the start of the February (Fig. 2b) observations, taken at about at an eighth of an orbit before pericenter, only 16% of the tiger stripes remained in tension and again ~1% switched to tension over the next hour. One would expect that the plumes in the February detection might be similar to the plumes in January.

Finally, during the November observation sequence, taken near apocenter (Fig. 2c), 82% of the tiger stripes experienced tension during the intire imaging sequence and 7% switched from compression to tension. The viewing geometry makes it difficult to determine exactly which tiger stripes are active in the image. However, large portions of the system are in tension allowing multiple discrete sources to erupt as seen in the observations.

A Cassini imaging sequence planned for a 1.5 hour period on 24 April 2007 took place, while Enceladus is about one fifth of an orbit past pericenter. We find that during this time 57% of the tiger stripes will be in tension. Similar to the November 2005 observations, a significant portion (6%) of the features will be in the process of opening up during the upcoming observing sequence, as the tension across them changes from compression to tension (Fig. 2d). Thus, this observational sequence could reveal an especially active phase.

References: [1] C. C. Porco, *et al*., *Science* **311**, 1393 (2006). [2] Spencer, J.R. et al. Cassini encounters Enceladus: Background and the discovery of a south polar hot spot. *Science* **311**, 1401-1405 (2006). [3] Melosh, H. J. Global tectonics of a despun planet. *Icarus* **31**, 221 (1977). [4] Hoppa, G., Tufts, B. R., Greenberg, R. & Geissler, P. Strike-Slip Faults on Europa: Global Shear Patterns Driven by Tidal

Stress. *Icarus* **141**, 287 (1999). [5] Hurford, T. A. Tides and Tidal Stress: Applications to Europa. Ph.D. Thesis, The University of Arizona (2005). [6] Kieffer, S. *et al.*, *Science* **314**, 1764-1766, (2006). [7] Roatsch, T., et al. High Resolution Enceladus Atlas derived from Cassini-ISS images. submitted to *Planetary and Space Sciences* (2006).
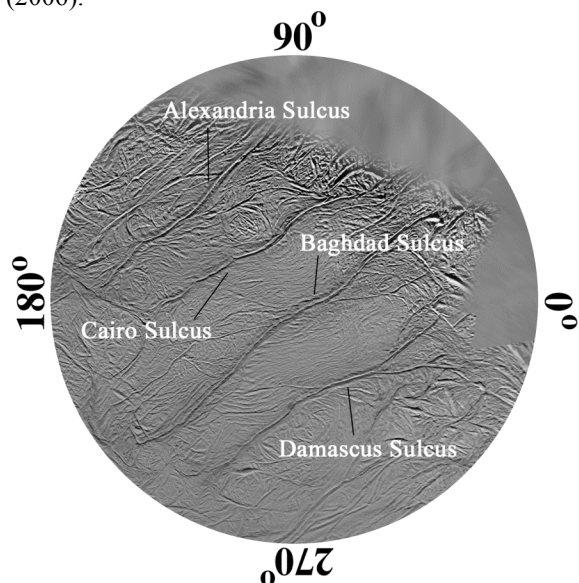
Fig. 1. The south polar region, from a high resolution atlas of Enceladus by Roatsch *et al.* [7], is shown
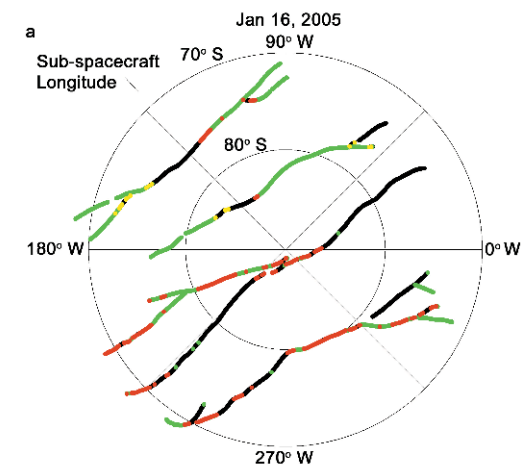
from 65°S poleward.

Fig. 2. The stress state across the faults is shown during each observation sequence (a-c), along with the predicted state during the planned April 2007 observation (d). Along each tiger stripe, the color indicates its stress state. Black means that portion of the feature was in compression during the entire imaging sequence while green means that it was in tension. Yellow indicates that the stress normal to the feature switched from compression to tension, opening the rift during the imaging sequence and red indicates that the stress normal to the feature switched from tension to compression.
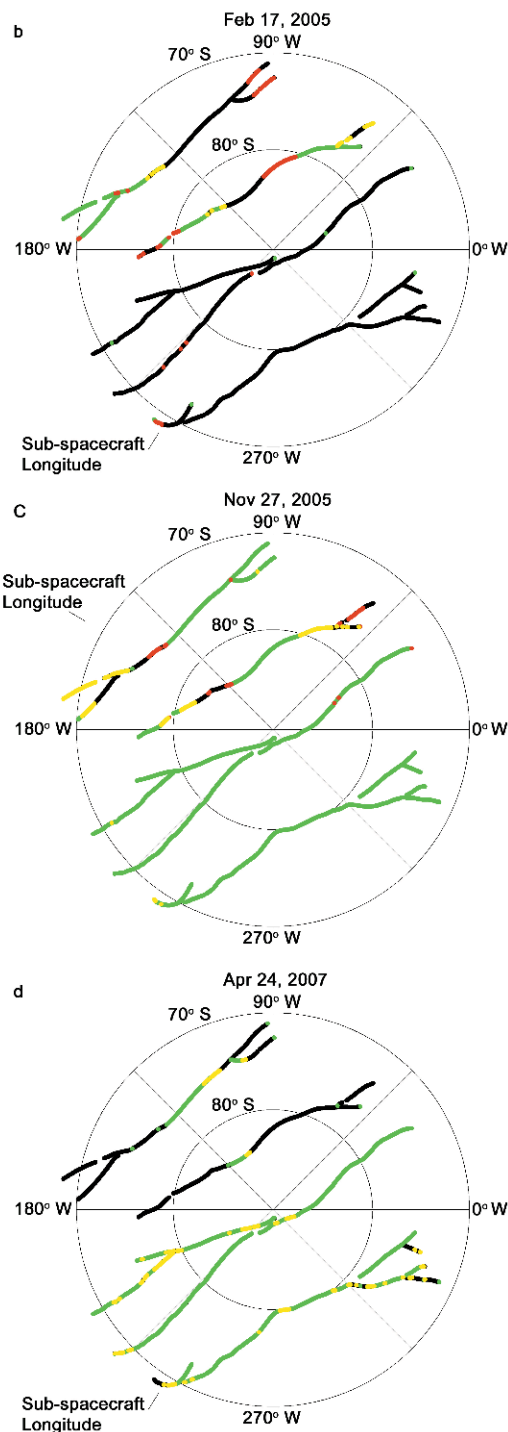
ENCELADUS: INTERNAL DYNAMICS AND HEAT PRODUCTION BY TIDAL FRICTION. Hauke Hussmann, Matthias Grott and Frank Sohl, DLR Institute of Planetary Research, Rutherfordstr. 2, 12489 Berlin, Germany (e-mail: hhussman@uni-muenster.de)

Introduction: Tidal friction can be a major heat source of outer planet satellites. Io and Europa are prominent examples for which tidal heating plays a major role (Io) [1] or contributes significantly to the overall energy budget (Europa) [2]. The Cassini spacecraft has detected ongoing geologic activity near the south pole of Saturn's moon Enceladus [3,4]. In contrast, its north-polar region is heavily cratered and appears to have been geologically inactive for a long time. Such a strong focus of internal heating and activity towards the south pole of Enceladus is a major difference compared to Io and Europa. We propose that this hemispheric dichotomy is caused by the satellite's interior dynamics and that a degree-one convection pattern is driving the south-polar activity [5]. The required internal heating rate is in the range of the estimated heat production of several GW [4] in Enceladus. We investigate under which conditions such heating rates can be provided by tidal friction.

The Model: Thermal convection in Enceladus is studied by modeling the satellite as an icompressible viscous fluid undergoing creeping flow. The equations of mass, momentum, and energy conservation are solved numerically using appropriate mechanical and thermal boundary conditions at the surface and core mantle boundary. The core size and the internal heating rate are varied to search for solutions in which a one-degree pattern develops. The core sizes represent different degrees of differentiation.

As a first approach we calculate the amount of heating due to inelastic tidal deformation for similar structure models independently from the convection model. Inelastic deformation is determined by the imaginary parts of the tidal Love numbers h_2, k_2, and l_2. The heating rate for a synchronously rotating satellite is proportional to the imaginary part of k_2 [1]. For the present orbital state we calculate the heating rates for models with and without internal liquid layers. Tidal amplitudes are deduced from h_2 for the various models.

Results and Conclusions: We investigated a number of core sizes and internal heating rates for which degree-one convection occurs. Best conditions for degree-one convection to develop are small cores, large heating rates and a decoupling between core and mantle, i.e. a free-slip boundary condition. The numerical simulations imply that a core radius of less than 120 km and an energy input at a rate of 3.0 to 5.5 GW would be required for degree-one convection to prevail. This is within the range of the observed ther-mal power near Enceladus' south pole [4]. Provided that Enceladus is not fully differentiated, degree-one convection is found to be a viable mechanism to explain Enceladus' hemispheric dichotomy. The models presented do require an incomplete differentiation of Enceladus, which may be inferred from dedicated flybys during Cassini's extended mission. In case of full differentiation, a core size of about 160 km is expected based on the mean density of the satellite. Such a large core would imply a thin convecting layer on top which would not allow for large scale structures to prevail.

Heating rates due to tidal friction would in principle be sufficient to power the observed activity on Enceladus. However, this will require a decoupling of the outer ice shell from the deep interior. Without a decoupling layer the heating rates would be about an order of magnitude too small to be consistent with Enceladus' output of energy. It is difficult to explain the focusing of activity towards the south-pole within the framework of tidal deformation, which would be symmetric, provided that the internal structure is symmetric. One-degree convection, which can develop even if the heat sources are distributed homogeneously may be one possibility to concentrate tidal heating in one hemisphere. The tidal Love numbers, h, k and l describe a satellite's response to the external periodic forcing and do strongly depend on the satellite's internal structure, chemical composition, thermal state, and frequency of the forcing. These global parameters (or linear combinations of the latter) can be deduced from line-of-sight gravity field measurements acquired during close flybys, from orbiting spacecraft, and from measurements at the satellites' surfaces. To confirm (or rule out) the presence of a global liquid layer at Enceladus, different flyby geometries would be extremely useful. Deducing the degree of internal differentiation of Enceladus would be important to further constrain the models presented.

References: [1] Segatz et al. (1988) *Icarus, 75,* 187 – 206. [2] Hussmann et al. (2002) *Icarus, 156,* 143 – 151. [3] Porco, C.C. et al. (2006) *Science, 311,* 1393–1401. [4] Spencer, J.R. et al. (2006) *Science., 311,* 1401 - 1405. [5] Grott, M. et al. (2007) *Icarus, in press.*

Cassini RADAR Altimeter Observations of Titan. William T. K. Johnson[1], Philip S. Callahan[1], Yonggyu Gim[1], G. Alberti[2], E. Flamini[3] S. Hensley[1], R. D. Lorenz[4], R. Orosei[5], H. A. Zebker[6], and the Cassini RADAR Operations Team, [1]Jet Propulsion Laboratory, California Institute of Technology, 4800 Oak Grove Drive, Pasadena, CA 91109, wtkjohnson@jpl.nasa.gov, [2]Consorzio di Ricerca su Sistemi di Telesensori Avanzati, 80125 Naples, Italy, [3]Agenzia Spaziale Italiana, 00131 Rome, Italy, [4]Space Department, Johns Hopkins University Applied Physics Lab, Laurel, MD 20723, [5]Istituto di Astrofisica Spaziale e Fisica Cosmica, Istituto Nazionale di Astrofisica, 00133 Rome, Italy [6]Stanford University, Stanford, CA 94305

Introduction: During the design of the Cassini RADAR it was recognized that different types of radar data have different value for the purpose of interpreting the properties of the main RADAR target, the haze-enshrouded moon Titan[1-2]. The closest approach time was reserved for Synthetic Aperture Radar (SAR) which provides information about geological features, then altimetry which provides topography of the surface, then scatterometry, and finally radiometry-only modes were allocated successively further out portions of a Titan pass. Altimetry data have now been collected on the inbound and outbound portions of thirteen passes of Titan. While the collection and processing of terrain height data from a spacecraft in a hyperbolic trajectory is a technical challenge the Cassini RADAR altimetry data in particular have shown unusual processing and interpretation obstacles well beyond any previously collected altimetry data. Here we discuss the data collected to date and examine some possibilities of terrain models that might fit the data.

Data Acquired: The altimetry data are generally collected while the spacecraft is between 4000 and 10,000 km (up to 16,000 km on some passes) on the inbound and outbound legs of a Titan pass which usually has a closest approach distance of about 1000 km. The ground tracks of each portion are approximately 600 km in length on the surface of Titan. The distribution on Titan appears somewhat random as the flyby trajectory is governed mainly by the Cassini orbiter tour that reflects the desires of all the instrument teams and navigational constraints such as gravity. Data were collected during Titan passes "A", 3, 8, 13, 16, 19, 21, 23, 25, 27, 28, 29, and 30. Except for Titan pass 30 (T30), all data were acquired as described above. The acquisition sequence for T30 was specifically designed so that data would be collected over a swath that has previously been imaged by the SAR, providing a much-needed geologic context for the observations. The areas for which both altimetry and SAR are available had been very sparse pre-T30. In this latest pass (12 May 2007) the inbound altimetry portion coincides with nearly 2500 km of the T28 SAR swath so that a much wider range of geometries is available. At the time of this abstract we have completed only a very preliminary survey of the data and a

more comprehensive analysis will be presented at this workshop.

Processing: The altimeter return comes from a footprint on the surface that varies with range from about 60 km in diameter at long range (16,000 km) to about 25 km at near range (4000 km) down to about 6 km in T30 which was enabled by operating in the altimeter mode at Cassini's minimum distance from Titan. The 4.25 MHz bandwidth altimeter signal gives approximately 30 m range resolution when the frequency-encoded pulse is compressed. These reduced radar echoes are combined with spacecraft ephemeris to give an accurate surface height. Navigation solutions for Cassini relative to Titan are throught to be accurate to better than 100 m.

Following pulse compression several different types of altimetry processing have been applied to the data including leading edge detection, tracking the radar echo centroid, and maximum likelihood estimation (MLE). The results from early passes have shown very little terrain relief and some disagreement between the methods. Experience with radar sounder data, such as from the MARSIS instrument on the ESA Mars Express mission [3], suggests that "radargrams" might be useful as a visual aid in determining how best to do the height estimate and what the elevation surface profile might resemble. We present several examples of Cassini radargrams ranging from a smooth flat surface to very complex returns. Features within the radargrams show that removing radar effects such as changing antenna footprint, signal level, Doppler spread, and range rate will be a challenge because some of the effects are dependent on the surface characteristics.

Surface Models: The SAR data [4-6] have revealed several types of surfaces including lakes, dune-like formations, channels, and cryovolcanic features but no obvious Earth-like mountain systems. "Mountains" appear to be low in elevation and limited in spatial extent.

Overall, the altimeter data show the mean radius of Titan to be very close to the nominal value of 2575 km. Typical slopes found over the length of many altimeter tracks are $<\sim 0.2$ m/km. In edge detected data, only a few features higher than 150 m on approximately 100 km scales have been seen with

occasional relief of >500 m. Perhaps, as shown in Figs. 1 and 2, the most intriguing feature of the altimeter echoes is the wide range of "depths" seen.
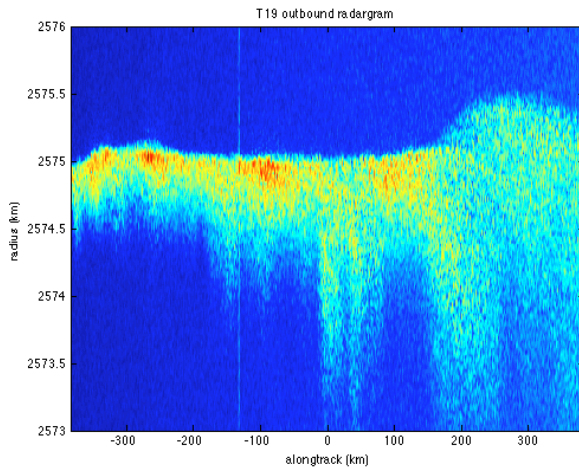
Figure 1: Radargram of T19 altimetry : Red represents strongest signal while the width is related to the surface properties such as material and slope. The spacecraft altitude varies from about 4000 km on the left to 10,000 on the right.
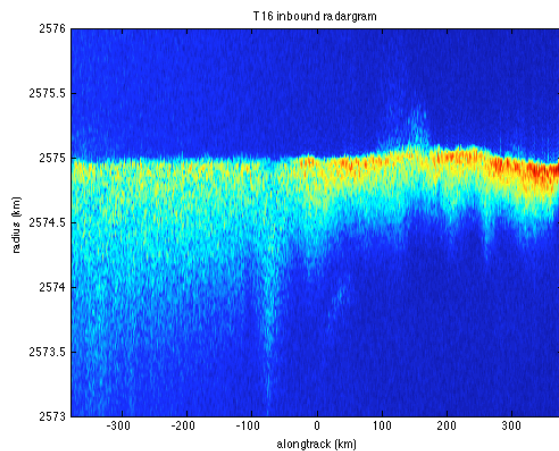
Figure 2: Radargram of T16 altimetry: The altitude variation is opposite that in Fig. 1.

Some data show fairly sharp, hard flat surface returns while other echoes must be from areas which have several hundreds of meters of relief with very few flat areas as the echoes are spread out much more than we expect from beam spreading or other effects. The deep echoes seem to be generally correlated with terrain that is bright either optically or in SAR, but much more overlap between data types will be necessary to validate the models.

References: [1] Elachi, C. et al., 2005, Space Science Rev 117. [2] Elachi, C. et al., 2006, Nature, 441. [3] Picardi, G. et al., 2005, Science 310, [4] Stofan, E. et al., 2006, Icarus 185. [5] Lopes, R. et al., 2007, Icarus 186. [6] Lorenz R. et al., 2006, Science 312

THEORY OF GEOCHEMICAL/GEOLOGICAL HOMOLOGY APPLIED TO HYDROCARBON AND ORGANIC SUBSTANCES ON ICY SATELLITES AND OTHER SOLID PLANETARY OBJECTS. Jeffrey S. Kargel (kargel@hwr.arizona.edu), Dep't. of Hydrology & Water Resources, University of Arizona.

Abstract: Under the appropriate conditions of temperature, pressure, differential stress, and so on, and placed in the right configurations, planetary materials undergo folding and faulting, diapirism, glacial-style flow, melting, sublimation and condensation, physical breakdown of lithologic structure into mineral grains, eolian transport, and other physical changes that constitute geologic activity. Homologous series of hydrocarbon and organic materials provide well-populated series of physical properties and numerous substances from which natural planetary, satellite, and minor bodies select as geologically active materials. Almost any processes that do geologic work on silicates and ices also should do geologic work on hydrocarbon and organic materials where those substances are sufficiently abundant.

Introduction: There are particular types of physical transformations of materials that are quite general to almost all geologic substances and which exhibit comparable phenomenology even when the substances being compared are very different. Under the appropriate conditions, geologic materials melt, sublimate, evaporate or condense, precipitate from solution or saturated atmospheres, dehydrate or hydrate, dissociate or react, they soften and flow in a ductile manner or become brittle and fracture, break into constituent mineral grains and are prone to eolian and fluvial transport, and so on.

This theoretical framework of geological and chemical homology has not been considered at any length for carbonaceous and organic materials. Such extension may imply that these substances also can form volcanoes, sand dunes, river valleys, marine coastal features, glaciers, thermokarst, and many of the landforms once known only on Earth. The Cassini and Huygens missions to Titan have highlighted numerous familiar features produced, it seems, by exotic substances.

Geologic/geochemical homology: This schema, general to all geologically active bodies but applied here to organic/hydrocarbon materials, derives from several theorems and axioms:

1. The solid planets and minor bodies are assemblages of many naturally occurring substances.
2. Electronic classes of materials (e.g., polar molecules, and apolar molecules, acids and bases, silicates, oxides, free metals, large ion lithophile elements, chalcophile elements, etc.) have particular affinities (by dissolution or bonding) for other substances in their class or affinities to react with or repel members of other classes.
3. Each planetary object contains numerous individual substances and reactive or interactive/soluble mixtures.
4. Each substance and each reactive or soluble combination has unique physical properties.
5. Together, the substances comprising each object span a wide range of physical properties.
6. Each planetary object retains materials that exist as condensed phases or gravitationally bound gases and lose (or never accrete) others that are too volatile for the prevailing conditions or too reactive to exist in pure and unreacted form.
7. For any set of planetary surface and interior conditions, there are substances that will be close to or cross over key melting transitions, vapor saturation curves, Gibbs' free energy transitions, or other transformations, or are prone to crystalline deformation or other marked changes of state or physical configuation.
7. Some materials will be so closely situated to key phase transitions or physical instabilities under the range of oscillating surface conditions on a planet that they will unidirectionally or repeatedly undergo these chemical transitions or physical changes on time scales shorter than the age of the planetary object.
8. The materials which undergo the aforementioned changes on time scales shorter than the changes of other materials are those which are dynamic in geological, geochemical, geomorphological, or climatic senses.
9. Each planetary object, being composed of many substances, selects materials that are dynamic in this geologic context.
10. Regardless of surface environments and available energy, some selection of materials are able to undergo notable physical changes and thus produce geologic activity, and they do so on timescales shorter than the changes effected by other substances and processes. These fast-responding materials are responsible for creating the observable surface landforms and landscapes; more slowly responding substances have their visible surface effects erased by the fast-acting materials. The geologic record is the sum of effects of all overprinting processes.
11. These physical changes are of just a few generic types: melting/solidification, evaporation or sublimation, dissociation, solid-state creep, dissolution, and so on.

12. Landforms shaped by similar physical changes share some similar qualities.

13. We can expect to see repetitions of familiar processes and familiar landforms on worlds throughout the Solar System and beyond.

Of course, like human and animal faces composed of several generic features, there are myriad combinations of more subtle differences that make for unique planetary surfaces. However, from the general schema above flows the concept that certain types of geologic activity and associated landforms are widespread, even if completely different materials are involved and details differ. This concept is by now fairly well established in the planetary science community for silicate worlds and increasingly is recognized as applying also to worlds made of volatile molecular ices, thus giving a physical-chemical basis to planetary data interpretation based on analog reasoning.

This theory may have perhaps its finest expression waiting to be discovered among organic and hydrocarbon materials from Earth outward to the Kuiper Belt.
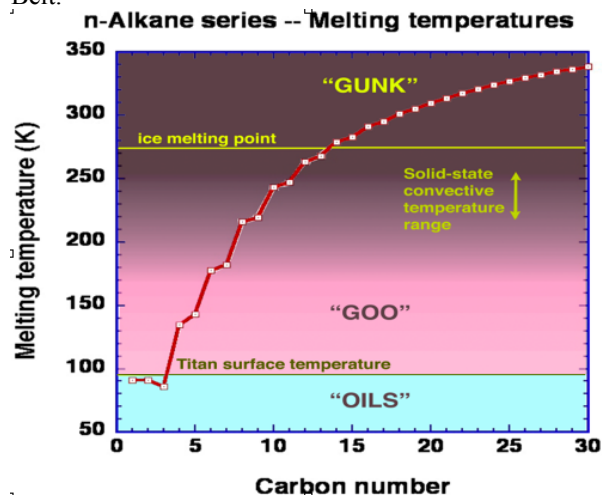
Figure 1. Melting points of the alkane series. The prevailing surface temperature of Titan also is indicated, showing that methane, ethane, and propane exist as liquids (or as a multicomponent solution also including nitrogen and argon), but butane and heavier alkanes would be solids. On Triton (surface temperature = 38 K) even methane would be solid, though within its icy crust geothermal heating would cause it to become a soft, deformable solid, perhaps giving rise to tectonic deformation. On Ceres, on the other hand, where mean global surface temperature is about 147 K, even butane and pentane would be liquids near the surface. Near Earth's surface (T = 270-310 K), hydrocarbons lighter than C14 are liquids or gases, C14 through C18 may oscillate between liquid and solid states, and those heavier than C18 are solids. For reference, ordinary candle paraffin includes a dominant fraction of C18-C28 alkanes, along with some hydrocarbons of other homologous series.

Not only is there a wide range of properties represented by these materials, but that range is heavily populated by physically incrementally distinct substances. This is illustrated in Figure 1 by the small variations in the series of melting temperatures, and in Figure 2 with the densities, of the alkanes. In the carbonaceous matter of many chondritic meteorites alkanes occur mainly in the C20's; and in Titan's atmosphere they are C1 and C2. Terrestrial petroleum includes a wide range of alkanes from C1 through about C30. Alkanes also are abundant in comets and other objects of the outer Solar System.
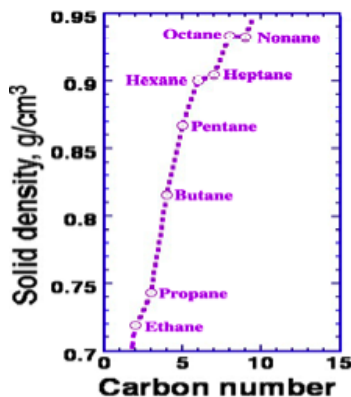
Figure 2. Densities of C2-C9 alkanes. Heptane and lighter alkanes are less dense than ice Ih; octane and nonane have about the same density as ice; heavier alkanes are more dense.

There are many cosmically abundant hydrocarbon and organic materials from which carbonaceous planets can select for just the right behavior in each given geologic role, such as in polar condensation, glaciation, fluvial activity, geyser eruptions, solid-state crustal diapirism, crustal folding and faulting, or cryovolcanism. Extending the logic of point 9 to point 13, above, there ought to be a series of superb landform analogs even among objects differing markedly in surface temperature and other environmental characteristics. Each set of active substances will adjust their geological roles as latitude and obliquity vary; as heliocentric distance varies; as solar flux increases over time; as radiogenic heat declines; or as satellites move into or out of resonances favorable to tidal dissipative heat generation. Shifting geologic roles also occur due to the global loss of volatiles to space, and to photolytic, metamorphic, hydrothermal, or metabolic conversions of volatiles to other molecular forms.

SHEARING-INDUCED TECTONIC DEFORMATION ON ICY SATELLITES: EUROPA AS A CASE STUDY.

S. A. Kattenhorn, J. M. Groenleer, S. T. Marshall, and J. C. Vetter. University of Idaho, Dept. of Geological Sciences, PO Box 443022, Moscow, ID 83844-3022, U.S.A. (simkat@uidaho.edu).

Introduction: Brittle deformation on the icy satellites can be the result of numerous processes. On Earth, many of these processes are related in some way to plate tectonics; however, plate-like motions are rare on Europa [1]. A dominant driving force may be tidal deformation, which caused the majority of the fracturing on Europa [2-7] and possibly in the south polar region of Enceladus [8-9]. Such deformation is prevalent where the ice shell responds to the oscillations of tidal bulges above a liquid layer on any icy satellite having an orbital eccentricity [4]. Surface fracturing can also be driven by endogenic processes such as diapiric uplift [10], spreading due to gravitational collapse, folding and warping of the ice shell [11], flexure alongside a surface load [12], and impact events [13].

Regardless of the source of stress in a deforming ice shell, another type of tectonic deformation that may plate a significant contributor to the strain history and surface morphology is that due to shearing effects. Shearing of a pre-existing structure (whether it be a discrete crack or a weak zone of finite width) loaded by any source of differential stress, may induce locally perturbed, high magnitude stress fields that cause localized deformation [14]. We outline the mechanics of secondary tectonic deformation due to shearing and provide examples of its significance in the tectonic history of Europa. Similar deformation could potentially be found on other icy satellites, particularly if there is a significant source of stress to drive shearing, such as from tidal forcing.

Secondary Tectonic Deformation: When a pre-existing discontinuity is reactivated by horizontal shear stresses, resultant lateral motions turn the discontinuity into a strike-slip fault. For the case of a constant maximum compressive principal stress direction acting at some oblique angle to a fault, motion occurs when the Coulomb failure criterion is met: $\tau \geq \mu\sigma_n$, where τ is shear stress, σ_n is normal stress, and μ is the coefficient of static friction. Tidal stresses on a satellite with orbital eccentricity rotate during the course of the orbit, so the mechanics of motion along the fault may vary during the day [15]. Tensile stresses may cause a discontinuity to open during the orbit, in which case there is no frictional resistance to shear motion. Evidence for both dilational shear motion and frictional shear motion has been described on Europa [14].

Because sheared lineaments on icy satellites must have a finite length, linear elastic fracture mechanics predicts that concentrations of stress occur at the tips

of the shearing discontinuities. In fact, the entire region adjacent to a strike-slip fault experiences a perturbation to the regional stress field, resulting in localized zones of extension and compression arranged antisymmetrically about each fault tip (Fig. 1a). Localized deformation in these zones of increased stress is referred to as secondary tectonic deformation and may include fracturing and crustal thinning in extensional quadrants, and folding, pressure solution, or crustal thickening in compressional quadrants.
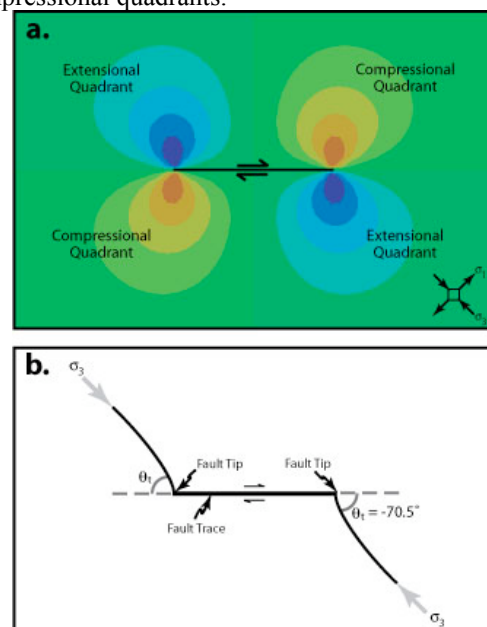
Fig. 1. (a) Quadrants of locally increased extension (blue colors) and compression (orange colors) adjacent to a right-lateral fault. (b) Tailcracks form at fault tips and propagate into the extensional quadrants. The maximum compressive stress is σ_3. Tailcrack angles are shown as θ_t. Both (a) and (b) are for a right-lateral fault. The left-lateral case is the mirror image.

Application to Europa: Shearing of lineaments and secondary tectonic deformation have played an important role in Europan tectonics.

Tailcracks. Stress concentrations at fault tips may induce secondary cracks called tailcracks that propagate into the extensional quadrants (Fig. 1b). The angle of the tailcrack (θ_t) is commonly around 70° but may be less if there is a component of opening along the fault during shearing [14]. Tailcracks have been identified on Europa [14, 16-17] and should be relatively easy to identify on any icy satellite (Fig. 2).
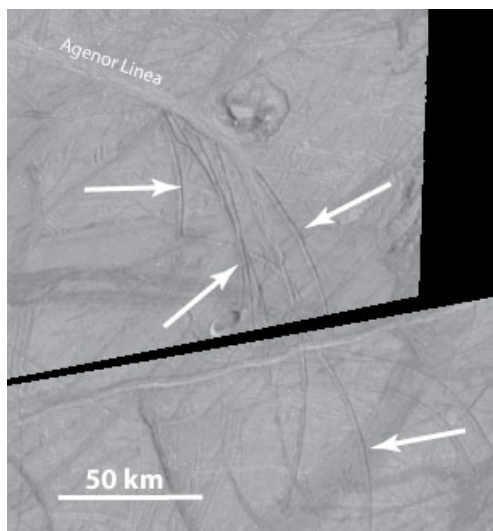
Fig. 2. Tailcracks at the SE tip of Agenor Linea, which experienced concomitant dilation and shear [14].

Anti-cracks. These are very subtle contractional features that form in the compressional quadrants at the tips of a shearing lineament. They have been described at Argadnel Regio [18] but are uncommon.

Cycloidal cracks. Although cycloids on Europa have been shown to trace out the changing direction of the maximum tensile diurnal tidal stress during the orbit [5], there is a period of time during which crack growth ceases while stresses continue to rotate. During this time, shear stresses are resolved onto the tip region of the arrested cycloid segment. Cycloid cusp angles and geometries are compatible with having formed by a tailcrack process, thus initiating a new cycloid segment that then propagates into the extensional quadrant driven onwards by the tidal stresses [19].

Cusp angles are thus analogous to tailcrack angles and must similarly be dictated by the exact ratio of shear-to-normal stress (τ/σ_n) resolved onto the cycloid tip at the instant of cusp growth. Our analysis of Europan cycloids in the northern trailing hemisphere reveals that it is always possible to find a point in the orbit at which the required τ/σ_n ratio occurs needed to account for measured cusp angles (Fig. 3) [20]. This point in the orbit occurs later than when the maximum tension is achieved, implying that new cycloid segments are only able to form due to the effects of shearing and tailcrack development at the tip of a previously formed segment. Hence, initial cycloid growth is likely triggered by shearing along, and cracking away from, an older lineament.

Crustal contraction. Shearing of a pre-existing lineament produces shear heating that may be responsible for thermal upwelling and the construction of ridge ramparts to either side of a central crack [21].

Our analysis of ridges showing strike-slip offsets reveals that they could not have formed purely due to lateral motions. Instead, apparent offsets were also produced than can only be reconciled with crustal convergence at ridges during shearing and heating [22].
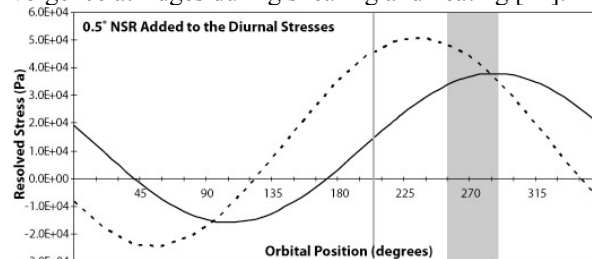
Fig. 3. Shear stress (dashed curve) and normal stress (solid curve) resolved onto a cycloid tip where a cusp developed. The gray area represents the point in the orbit where the ratio of the stresses was exactly right for the cusp to form. The vertical gray line is the point at which the the tensile principal stress is maximized.

Conclusions: Shearing of lineaments on Europa has contributed to the tectonic deformation through the creation of strike-slip faults and associated development of secondary tailcracks and anti-cracks, the initiation of cycloid segments, and the accommodation of crustal contraction along ridges. Similar deformation could conceivably occur on other icy satellites.

References: [1] Patterson, G. W. et al. (2006) *JSG, 28,* 2237–2258. [2] Helfenstein, P., Parmentier, E. M. (1985) *Icarus, 61,* 175-184. [3] McEwen, A. S. (1986) *Nature, 321,* 49-51. [4] Greenberg, R. et al. (1998) *Icarus, 135,* 64-78. [5] Hoppa, G. V. et al. (1999) *Science, 285,* 1899-1902. [6] Figueredo, P. H., Greeley, R. (2000) *JGR, 105,* 22,629-22,646. [7] Kattenhorn, S. A. (2002) *Icarus, 157,* 490-506. [8] Porco, C. C. et al. (2006) *Science, 311,* 1393-1401. [9] Hurford, T. A. et al. (2007) *Nature,* in press. [10] Collins, G. C. et al. (2000) *JGR, 105,* 1709–1716. [11] Prockter, L. M., Pappalardo, R. T. (2000) *Science, 289,* 941-943. [12] Billings, S. E., Kattenhorn, S. A. (2005) *Icarus, 177,* 397-412. [13] Melosh. H. J. (1989) Impact Cratering: A Geologic Process. [14] Kattenhorn, S. A. (2004) *Icarus, 172,* 582-602. [15] Hoppa, G. V. et al. (1999) *Icarus, 141,* 287-298. [16] Prockter, L. M. et al. (2000) *JGR*, *105*, 9483-9488. [17] Schulson, E. M. (2002) *JGR*, *107*, doi:10.1029/2001JE001586. [18] Kattenhorn, S. A., Marshall, S. T. (2006) *JSG*, *28*, 2204-2221. [19] Marshall, S. T., Kattenhorn, S. A. (2005) *Icarus*, *177*, 341-366. [20] Groenleer, J. M., Kattenhorn, S. A. (2006) *Eos, Trans. AGU*, *87*, P31D-08. [21] Nimmo, F., Gaidos, E. (2002) *JGR*, *107*, 1-8. [22] Vetter, J. C., Kattenhorn, S.A. (2005), *LPSC, XXXVI*, abstract #1053.

THE INTERACTION OF ENCELADUS' WATER PLUME WITH SATURN'S MAGNETOSPHERE.

Krishan K. Khurana[1], Matt H. Burger[2], Jared S. Leisner[1], Michele K. Dougherty[3], and Christopher T. Russell[1], [1]Institute of Geophysics and Planetary Physics, UCLA, Los Angeles, CA, 90095, kkhurana@igpp.ucla.edu, [2]NASA-GSFC, Greenbelt, Maryland., [3]Imperial College, Department of Physics, London SW7 2AZ, U.K..

Introduction: In this presentation, we analyze the magnetic field data from the three close flybys and several distant flybys of Enceladus by the Cassini spacecraft. We show that Enceladus acts as an obstacle to the magnetized flow resulting in field line draping around it. Detailed modeling using an Alfvénic interaction model reveals that the center of the draping region is offset below Enceladus by several Enceladus radii consistent with a plume generated tenuous atmosphere located below Enceladus. We show that the effective diameter of the plume generated obstacle is at least 6 moon radii (R_E) and the obstacle is displaced by several R_E south and downstream of Enceladus. The strength of the interaction current that links Enceladus with Saturn's ionosphere is $< 10^5$ Amps (40-60% of the Neubauer limit [1]). From the strength of the current produced by the interaction, we estimate that the mass picked up by the magnetospheric plasma within 5 R_E of Enceladus is < 3 kg/s. In addition, we show that Enceladus does not possess a measurable internal magnetic field or an induction interaction field because there is little inducing field in Saturn's magnetosphere.
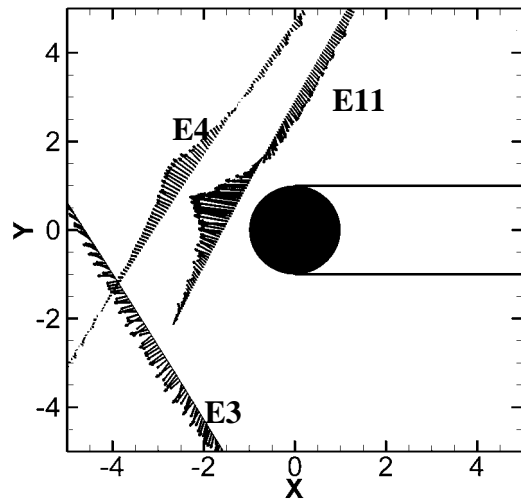
Figure 1. The trajectories of Cassini and perturbation field vectors in the XY plane of Enceladus interaction (ENIS) coordinates. In this coordinate system, X points along the orbital motion of Enceladus, Y points towards Saturn and Z completes the triad. Only those portions of the trajectories are shown which satisfied the criterion -5 R_E < X, Y < 5 R_E.

Trajectory and Data: Figure 1 shows the flyby trajectories in the XY projection of the ENIS coordinate system described in the caption of the figure. During all three close flybys, Cassini was upstream of Enceladus near the closest approach. Also superposed on the trajectories are the magnetic perturbation vectors (observation - background) projected into this plane. The perturbations are observed over a large region of space suggesting that the interaction region is several times larger than Enceladus. In addition, the field strength is seen to strengthen (not plotted) consistent with the diversion of a flow around an obstacle. The observed magnetic field perturbations rule out an internal magnetic field in Enceladus because a scalar field should fall off as r^{-3} or faster from Enceladus [2]. The perturbations are also inconsistent with a dipolar electromagnetic induction field originating from an interior conductor. This is expected because in the frame of Enceladus, there is no appreciable changing field imposed by the axisymmetric field of Saturn. The perturbations however are consistent with an origin in an Alfvén-wing current system as discussed in the next section.

Modeling: We use a model of the current system first used to model Io's interaction with Jupiter's magnetosphere [3,4]. The model was originally devised for studying the Alfvénic interaction of a conducting object with a flowing magnetized plasma. Neubauer [5] showed how it can be modified for the mass-loading situation by replacing the ion/neutral and electron/neutral collision frequencies with effective collision frequencies. Figure 1 shows a cartoon representation of the model used in this work. The mass-loading region is assumed to be spherical and displaced below and downstream of Enceladus. The plasma pick-up currents flow across the plasma pick-up region in the direction of the background electric field which is directed outwards from Saturn. The currents enter and exit the interaction region through the Alfvén wings. The computational Alfvén wings are composed of 180 "infinite" length line-segments (90 in northern and 90 in southern hemisphere) each of which originates from the pick-up region and extends infinitely to the Saturnian ionosphere along the two characteristics given by

$$\mathbf{V_A}^{\pm} = \mathbf{V_0} \pm \mathbf{B_0}\big/\sqrt{\mu_0 \rho} \qquad (1)$$

where $\mathbf{V_0}$ is the flow velocity, $\mathbf{B_0}$ is the background vector field and ρ is the plasma mass density. The magnetic field from the currents is calculated from Biot-Savaart equations.
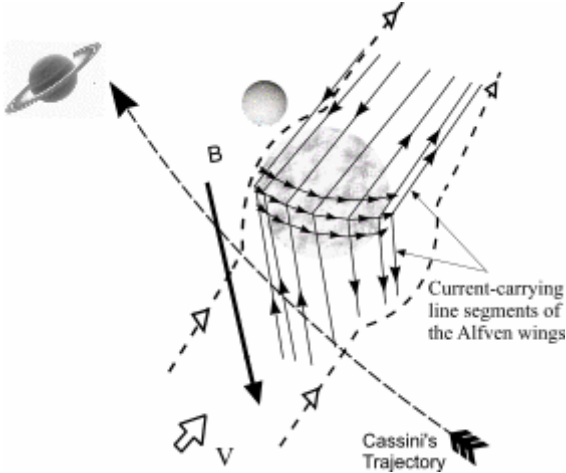
Figure 2. A cartoon of the current systems through the modified source region located below Enceladus. The currents are drawn into the source region along the Alfvén characteristics and then move along the surface of the source region. The currents exit the source region on the side away from Saturn.
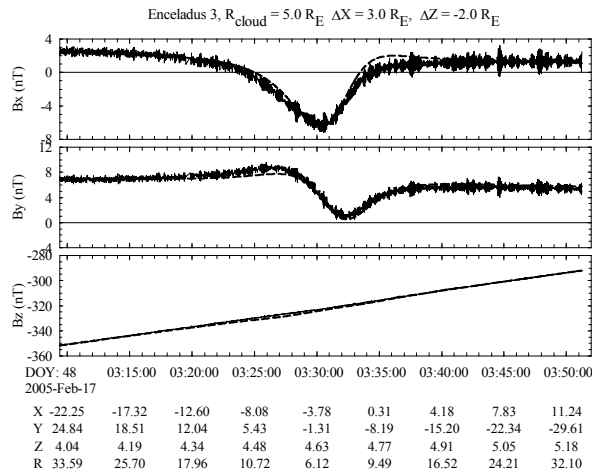
Figure 3. Magnetic field data obtained during the E3 flybys of Enceladus (solid) and the best fit model field (dashed) using the model shown in Figure 2. The model fit parameters are indicated in the title of the figure.

We treat the effective size and the location of the source as fit parameters. The resulting best fit for the first Enceladus flyby (E3) is shown in Figure 3. The

required size of the source and the shift required for the source location are displayed in the title of the figure. For the E4 and E11 flybys, we were able to get solutions with a source size of $\sim 3\ R_E$. However, for the E3 flyby, both the source size and its location had to be changed significantly from the E4 and E11 values. These differences point to temporal changes in the interaction presumably from changes in the extent and strength of the plume.

We have also examined several distant flybys of Enceladus by Cassini (not shown here). They show that an extended pick-up region exists around the orbit of Enceladus. The pick-up appears to be enhanced in the downstream region of Enceladus.

Summary and Discussion: The modeling results confirm that the water plume located near Enceladus' south pole is the source of neutrals and plasma in Saturn's magnetosphere. The plume strength appears to be variable and only a fraction (< 3 kg/s) of the 300 kg/s of neutral material gets ionized in the immediate vicinity of Enceladus. Additional pickup must be occurring in the neutral torus extending outward from the orbital location of Enceladus. Thus Enceladus' plume is a source for both the magnetospheric plasma and the neutral cloud (6).

Recently Burger *et al.* [7] simulated Enceladus' plume by a three-dimensional Monte-Carlo neutral cloud model. They show that the observations require two sources of water to fit the observations from the INMS instrument. One of the sources is a distributed global neutral component with a source rate of 8×10^{25} H_2O/s (2.4 kg/s). However the dominant source is a plume from the southern regions with a neutral source rate of 10^{28} H_2O/s (300 kg/s). They further show that out of this ~ 300 kg/s neutral source rate, the amount that gets picked up by the plasma (that is ionized, mainly through charge exchange) in the vicinity of Enceladus is between 1.5 and 3 kg/s, an estimate that is very close to our estimate of 0.6–2.8 kg/s. Complete results of the modeling from all three flybys will appear in a JGR manuscript which is in press [8].

References: [1] Neubauer, F. M. (1980), *JGR*, 85, 1171. [2] Dougherty, M.K. et al. (2006), *Science, 311,* 1406-1409. [3] Herbert, F., *JGR,* (1985), *90,* 8241. [4] Khurana, K. K. et al.(1997), *Geophys. Res. Lett., 24,* 2391. [5] Neubauer, F. M., (1998) *JGR*, 104, 3863. [6] Johnson R.E. et al. *APJ,* 644:L137–L139. [7] Burger et al. (2007), *JGR* in press. [8] Khurana et al. (2007), *JGR,* in press.

MUCH LIKE EARTH: DISTRIBUTION AND INTERPLAY OF GEOLOGIC PROCESSES ON TITAN FROM CASSINI RADAR DATA.

R.M.C. Lopes[1], E.R. Stofan[2], G. Mitri[1], L. E. Robshaw[3], K.L. Mitchell[1], C. A. Wood[4], J. Radebaugh[5], R.L. Kirk[6], S.D. Wall[1], R. Lorenz[7], J. I. Lunine[8], J. Craig[1], F. Paganelli[1], L. Soderblom[6], and the Cassini RADAR Team, [1]Jet Propulsion Laboratory, California Institute of Technology, 4800 Oak Grove Drive, Pasadena, CA 91109, Rosaly.M.Lopes@jpl.nasa.gov, [2]Proxemy Research, Bowie, MD 20715, [3]Environmental Sciences Department, Lancaster University, Lancaster LA1 4YQ, UK, [4]Wheeling Jesuit University, Wheeling, WV 26003, [5]Geological Sciences Department, Brigham Young University, Provo, UT84602, [6]U.S. Geological Survey, Branch of Astrogeology, Flagstaff, AZ 86001, [7]Johns Hopkins Applied Physics Laboratory, Laurel, MD 20723, [8]Lunar and Planetary Laboratory, University of Arizona, Tucson, AZ85721.

1. Introduction: The variety of geological processses on Titan is rivaled in our Solar System only on Earth. Results from the Cassini-Huygens mission obtained so far have revealed a wide range of geologic and climatological processes, and a complex interaction between the surface and atmosphere [e.g. 1-13]. We use data obtained by Cassini's Titan Radar Mapper to analyze the distribution of different types of geologic processes occurring on Titan's surface, both endogenic and exogenic, and to derive temporal relationships between these processes, at least at local scales. The distribution and interplay of geologic processes is important to provide constraints on models of the interior and of surface-atmosphere interactions.

2. Data: Cassini carries a multimode Ku-band (13.78 GHz, λ=2.17 cm) radar instrument [1] that is used in a Synthetic Aperture Radar (SAR) mode at altitudes under ~4,000 km, resulting in spatial resolution ranging from ~350 m to >1 km. SAR coverage is dependent on spacecraft range and orbital geometry. Radar backscatter variations in SAR images can be interpreted in terms of variations of surface slope, near- surface roughness, or near-surface dielectric properties. On Titan, the likely surface materials (water ice, water-ammonia ice and other ice mixtures, hydrocarbons, tholins) are different from those of bodies previously imaged with planetary radars, and volume scattering may be significant [1,2,3]. The SAR images of Titan now comprise a rich dataset that covers ~15% of Titan's surface, well distributed in both latitude and longitude, although with more coverage on the leading hemisphere (0-180°). Although the coverage is still far from comprehensive, it is sufficient for revealing the geologic processes that shaped Titan's young surface. We mapped the SAR images in terms of characteristic morphology of geological features and their radar backscatter in order to determine possible emplacement sequences and the overall distribution of geologic processes with latitude and longitude. As with any geological mapping, the ultimate aim is to be able to interpret how geologic processes have affected a planetary surface in space and time and to provide constraints on the planet's interior structure and on exogenic processes that modify the surface.

3. Distribution of Geological Processes: All the major planetary geologic processes – volcanism, tectonism, impact cratering and erosion – appear to have played a role in shaping Titan's complex surface.

*Impact cratering***:** To date, only three impact structures have been conclusively identified on Titan: Menrva, Sinlap, and Ksa; and a few others have been tentatively identified [7]. All three craters definitely identified are on the leading hemisphere, which, as Lorenz et al. [7] discussed, is consistent with the impactor model of Korycansky and Zahnle [14]. However, the SAR coverage at present is insufficient to draw definite conclusions about global crater populations.

*Tectonism***:** Among the features interpreted to be of tectonic origin are ridge-like features and elevated blocks [8]. Individual mountains heights, estimated from radarclinometry, are mostly between 500m-1500 m [8]. Radebaugh et al. [8] discusses four possible origins for the mountains and blocks, including crustal compressional tectonism and upthrusting of blocks. The other possible origins are creation of high blocks and low grabens through extension, dissection and erosion of a pre-existing layer, and deposition of blocks as impact ejecta. Although all processes may be at work, we argue that mountain ridges, which are mostly in the equatorial regions, are compressional in origin. High-pressure ice polymorphs could exist on Titan between the ocean and the rocky interior [15]. Mitri and Showman [15] have shown that during the cooling of Titan, the radial expansion of the ice-I layer is, in general, counterbalanced by the radial contraction of the ice high pressure layer. Therefore, a global contraction of Titan could occur during its cooling and cause compressional tectonism [15].

Cryovolcanism: The SAR swaths revealed several features that likely resulted from cryovolcanism, including radar-bright flows, caldera-like features, and a circular volcanic feature named Ganesa Macula, plus several flows and craters identified as of possible cryovolcanic origin. VIMS data has identified other features [16, 17] and, in one case, provided further evidence for a RADAR identification [18]. Cryovolcanic features are not ubiquitous on Titan. There is an apparent concentration in the Ganesa Macula region, which

has led to the suggestion that this may be a possible hot spot or even Tharsis analogue [4].

Erosional processes: Erosion appears to be widespread on Titan. Fluvial processes are extremely important on Titan and are a major factor in modifying the morphology of other geologic features. SAR data has revealed evidence of vast fields of aeolian deposits, which are well correlated with VIMS data [19].

Fluvial processes and possible surface liquids: Channels and radar-dark terrains are candidates for liquids, either past or present. There is plentiful morphological evidence that liquids have flowed on Titan [1, 6, 12, 13], but it is not straightforward to differentiate between cryovolcanism and fluvial processes for the origin of some flows and channels, particularly when they are located on or near a cryovolcanic feature such as Ganesa [3]. Lakes at high northern latitudes provide evidence for surface liquids [5]. Numerous channels are seen associated with these lakes and, in some cases, connecting them.

Aeolian processes: Dune-like features were identified by SAR, covering regions 100s of kilometers in extent [6], suggesting a significant supply of sand-sized material, which is likely produced by fluvial erosion [13]. Dunes are concentrated in the equatorial regions, below latitudes of ~60°, consistent with lower latitudes being relatively dry [20].

4. Interplay of processes: Although stratigraphic relationships are hard to establish from the available data, they are sufficiently clear in places that a picture of Titan's geologic evolution is emerging. Erosion processes, both from fluvial and aeolian activity, play a major and ongoing role modifying Titan's surface.

Erosion of impact craters: Removal of impact craters by burial and erosion is likely, given the evidence for fluvial, aeolian, and cryovolcanic processes. The terrain surrounding the impact basin Menrva indicates that erosional processes have degraded the SW outer rim in particular. Several other tentatively identified impact craters have radar-bright rims and radar-dark interiors. Two examples, in particular, are seen to be partially covered by dune material. It is likely that numerous craters have been buried or partially buried by aeolian deposits; in some cases, only the rims are left exposed. Fluvial erosion also seems to have played a major role, particularly in areas such as Xanadu. Lorenz [7] pointed out that the size-density distribution of craters on Titan is similar to Earth's, indicating rapid obliteration by erosion and burial. It is not yet clear what the role of cryovolcanism has been on crater obliteration, as so far cryovolcanic processes are not seen to be as widespread as erosional processes.

Erosion of mountains: Peak morphologies and surrounding, diffuse blankets are suggestive of erosion [8]. Most of the possible tectonic features appear to be at least partially degraded and embayed by surrounding plains units. Radebaugh et al. [8] argue that fluvial runoff has played a significant role. Cassini VIMS data have identified that, at least for one mountainous area east of Xanadu, there are spectral differences between the mountainous area and the surrounding terrain [17], perhaps implying that material that coats the surrounding plains is not present on the mountains. The same analysis showed this to be the case for channels as well; perhaps the thin coating has been removed by erosion on channels and mountainous areas.

Cryovolcanism: a young process? The cryovolcanic features so far identified [4] are located mostly at high northern latitudes. It is unclear whether Ganesa Macula has suffered fluvial erosion, as the origin of channel-like features on its flanks could be volcanic or fluvial [4]. The large flow fields so far identified [1, 4] do not show any evidence of fluvial erosion, perhaps implying that they are quite young. Tobie et al. [21] suggested that extrusive activity and outgassing recommenced on Titan relatively recently (~500 Ma).

Wind and Liquids: the methanological cycle. Mapping of the currently available SAR data indicates that fluvial features are widespread in both latitude and longitude and appear at many different scales. At high latitudes, fluvial erosion appears to be the dominant modification process, at least at the high northern latitudes. Erosion by aeolian activity may dominate the lower latitudes and dunes are seen in places to overlay fluvial deposits.

Each of the SAR swaths has provided insights into the geologic processes that shape the complex and youthful surface of Titan. These snapshots await integration into the larger set of swaths to be obtained during the Cassini mission before a comprehensive model of the geologic evolution of Titan can be developed.

References: [1] Elachi, C. et al., 2005, Science, 308. [2] Elachi, C. et al., 2006, Nature, 441. [3] Stofan, E. et al., 2006, Icarus 185. [4] Lopes, R. et al., 2007, Icarus 186. [5] Stofan et al., 2007, Nature, 445 [6] Lorenz, R. et al., Science, 312. [7] Lorenz, R., et al. 2007, GRL, 34. [8] Radebaugh, J., et al., 2007, Icarus, Submitted. [9] Lorenz, R., et al., Planet. Sp. Sci., Submitted. [10] Radebaugh et al., 2007, Icarus, Submitted. [11] Mitri, G., et al., 2007, Icarus, 185. [12] Tomasko, M. et al., 2005, Nature 438. [13] Atreya, S. et al., 2006, Planet. Sp. Sci., 54 [14] Korycansky and Zahnle, 2005, Planet. Sp. Sci., 52. [15] Mitri and Showman, 2007, Icarus, Submitted. [16] Sotin et al. 2005, Nature 435. [17] Barnes, et al., GRL [18] Le Corre, L., et al., LPSC 38, # 1828. [19] Soderblom et al. 2007, Planet. Sp. Sci., in press. [20] Rannou et al., 2006, Science 311. [21] Tobie, G., et al., 2006, Nature 440.

IMPACT CRATERING ON TITAN – CASSINI RADAR RESULTS R. D. Lorenz[1], C. A. Wood[2], J. I. Lunine[3], S. D. Wall[4] , R. M. Lopes[4], K. L. Mitchell[4], F. Paganelli[4], Y. Z. Anderson[4], L. Wye[5], H. Zebker[5], E. R. Stofan[6] and the Cassini RADAR Team [1]Space Department, Johns Hopkins University Applied Physics Laboratory, Laurel, MD 20723. [2]Wheeling Jesuit College, Wheeling, WV 26003 [3]Lunar and Planetary Laboratory, University of Arizona, Tucson, AZ 85721, U.S.A. [4]Jet Propulsion Laboratory, California Institute of Technology, Pasadena, CA 91109, U.S.A. [5] Stanford University , Stanford CA 94305, USA. [6]Proxemy Research, Bowie, MD 20715 rlorenz@lpl.arizona.edu. .

Summary: As Cassini SAR imaging coverage of Titan approaches ~20%, a general picture of Titan's cratering style is emerging. Significant differences in style from craters in other satellites are noted in this progress report.

Introduction – Crater Density: If Titan were cratered to the same extent as some other Saturnian satellites (or Ganymede and Callisto), it would have >10,000 impact craters [1] with diameter 20km or more (above the atmospheric shielding threshold below which the differential density would decline). However, even the earliest Cassini data showed a lack of observable craters overall [2,3]. A survey [4] of the first ~10% of Titan's surface imaged by Cassini RADAR finds that the large-crater (>300km) population may be consistent with other Saturnian satellites (figure 1), but there is a striking dearth of medium-sized impacts (e.g. 30-100km dia). Indeed, the slope of the size-frequency distribution is very shallow (~0.5), much like the Earth, suggesting that similar processes may be responsible for the obliteration of the craters. A crater retention age of several hundred Myr (roughly the same as Earth or Venus) is indicated [3,4]. Most impacts and candidate impacts have been observed on the leading face (consistent with synchronous rotation and a leading/trailing asymmetry of impact rate in accordance with models) but sampling bias is present and obvious terrain type differences may yield a longitudinal variation in crater preservation.
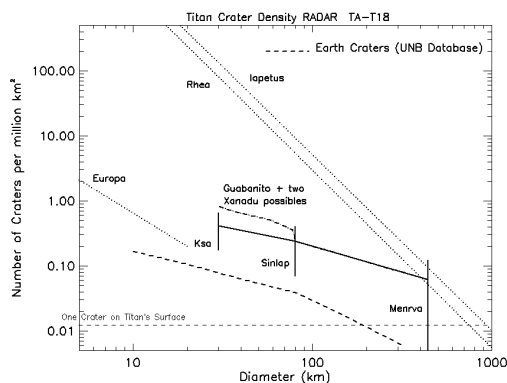
Fig.1 *Titan cumulative size-frequency plot (thick solid line with bars) for TA-T18, compared with Earth, Rhea/Iapetus, and Europa [7]. Some uncertainty (factor ~2) pertains to a number of structures which may or may not be of impact origin, but even taking these into accout, medium-sized craters are a factor of ~100-1000 depleted from what one would expect in the Saturn system.*

So far only 3 impact structures are securely-enough identified to have IAU-approved names (see figure 2) – we discuss these in turn.
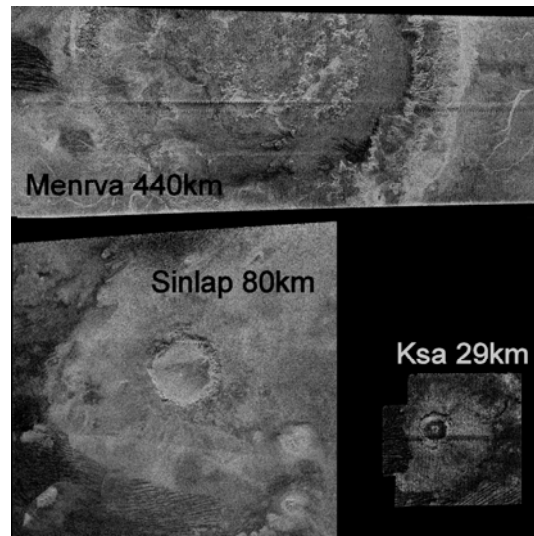
Fig.2 *Montage at same scale of Titan craters . North is up – note the tendency of fluvial channels and Aeolian features to trend eastwards and the better-preserved Eastern rim of Menrva. Near-horizontal stripes across the whole images are radar imaging artifacts. Radar illumination is from above with approximate incidence angles of 21°, 14° and 34° respectively.*

Menrva: This impact basin is centered near 87° W, 19° N and had been noted as a dark annular feature in near-IR imaging [2]. RADAR shows the crater morphology clearly. The outermost edge is 440km in diameter, The steep inner wall is bright, exhibiting numerous radial grooves and chutes, but does not obviously suggest a 'multi-ring impact basin' of the type seen on Ganymede and Callisto for craters of this size. The southern and western regions of the floor are relatively bland, suggesting it may have been flooded. The center of the basin appears elevated and is rough-textured, with bright hummocky hills defining an inner ring about 100 km in diameter. The western rim shows more signs of erosion than the eastern rim. Fluvial features appear to be associated with the basin, but small-scale features in the crater rim and in the central hills are preserved, suggesting that erosion has been rather limited since crater formation. The Cassini RADAR team is presently exploring ways of measuring the topography of Menrva to constrain post-impact modification such as viscous relaxation.

Sinlap : This 80-km crater, at 16° W, 11° N shows no evidence of a raised rim. It appears to be flat-floored, yet craters on Ganymede of this size [5] have domed floors due to viscous relaxation, and central pits, perhaps indicating that their transient cavity came close to a subsurface layer of lower viscosity. There is no indication of such features, nor of a central peak or peak ring. The floor seems flat, similar to some lunar lava-flooded craters or to craters with lacustrine deposits on Mars. Radar geometry gives [6] a crater depth of 1300 ± 200 m for a depth/diameter ratio of ~0.016. This shallowness may be due to the crater being significantly modified by infilling. The crater is asymmetrically surrounded by a blanket of SAR-bright material biased toward the eastern side : the inner part of this blanket has some radial striation. In places it extends more than two crater radii beyond the rim.

Ksa : The T17 flyby in August 2006 showed a 29km diameter crater named Ksa not far from Menrva. Again, this structure shows the recurring pattern of 'intrusion' of aeolian material from the West. A large and sharp-edged ejecta blanket is reminiscent of the fluidized ejecta around many Martian craters, suggesting a significant influence of the atmosphere in constraining the ejecta plume expansion, and the possibility of surface volatiles. In terms of its floor, Ksa is interesting in having a central structure suggestive of a peak ring : evidently 29km is above the transition diameter

Suspiciously-Circular Features and other potential impact structures : A number of circular or near-circular features form bright rings in both radar and optical data – many of these may have an impact origin (e.g. figure 3). The dark floors suggest infilling, perhaps by aeolian sediment – in the case of Guabonito, duneforms are evident.
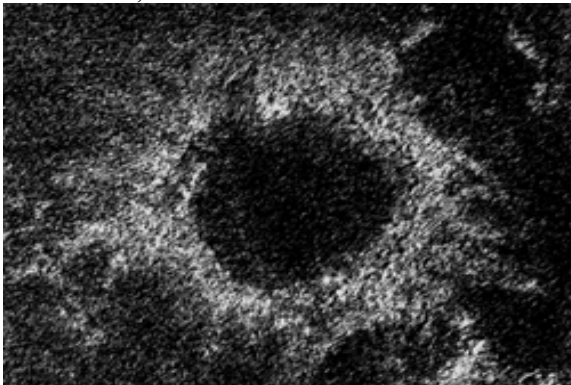
Fig 3. *Unnamed feature, possibly an oblique impact structure observed on T16 – inner part is 65km across, a typical size for 'suspiciously circular features' on Titan.*

The large leading-face bright region Xanadu appears geologically distinct and has a number of likely (but highly degraded) impact structures.

Further study of these, and their implications for the age of Xanadu, are under way.

As coverage builds up, a few more 'conventional-looking' impact structures have turned up (e.g. figure 4). The modest resolution of Cassini SAR (300-1000m) makes detailed characterization of small structures difficult, however.
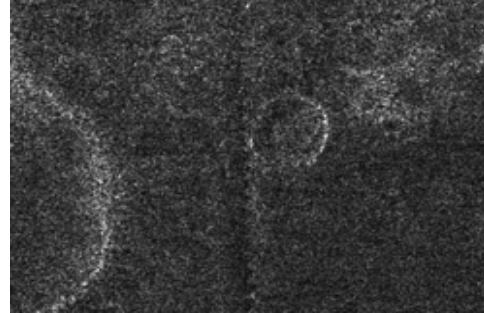
Fig.4 *Unnamed 14km diameter feature, evidently a depression (radar illumination from left) observed on T29.*

Conclusions and Comparisons : As on other bodies, impact craters provide a window into the crustal properties of Titan. Titan's craters are quite distinctive, sometimes having a 'soft' appearance and in many ways, notably in their ejecta and post-impact modification, are more comparable with craters on the terrestrial planets than on other icy satellites.

The lack of observed multi-ring impact structures places some constraint on crustal thickness (i.e. when Menrva formed, the lithosphere was evidently ~50km or more thick). Ongoing Cassini data may shed light on the geographical distribution of craters, and any large-scale variations in crater density or style (e.g. the older but unburied structures seen in Xanadu). Investigations on a future mission might include higher-resolution optical and radar imaging data to permit identification and analysis of smaller craters, together with altimetry to constrain relaxation and subsurface radar sounding to probe structures presently hidden by burial (e.g. does Sinlap have a buried central peak or peak ring?). Such subsurface sounding, as on Mars, may reveal entirely new impact structures beneath the surface of Titan's hydrocarbon lakes and sand seas.

References: [1] Lorenz, R., Planetary and Space Science 45, 1009-1019, 1997 [2] Elachi, C. et al,, Science, 308, 970-974, 2005. [3] Porco, C.C., et al, Nature 434, 159–168, 2005. [4].Lorenz R. D. et al., Geophys. Res. Lett., 34, L07204, doi:10.1029/2006GL028971, 2007. [5] Schenk, P., Journal of Geophysical Research 98, 7475-7498, 1993 [6] Elachi, C., et al., Nature, 441, 709– 713, 2006 [7] Schenk, P. et al., 427-453 in F. Bagenal et al. (eds) Jupiter, CUP, 2004.

NEAR INFRARED SPECTRA OF PURE ICES AND MIXTURES RELEVANT TO ICY SATELLITES. R. M. E. Mastrapa[1], M. P. Bernstein[2], and S. A. Sandford[2], [1]SETI Institute 515 N. Whisman Road Mountain View, CA 94043, [2]NASA Ames Research Center MS 245-6, Moffett Field, CA 94035, rmastrapa@arc.nasa.gov.

Introduction: For decades, ices have been detected on the satellites and small bodies of the Solar System by spacecraft and ground-based telescopes. Meanwhile, laboratory measurements have lagged behind these discoveries. The few measurements made are often in the wrong wavelength range, temperature regime, or phase. The advantages of laboratory measurements include high signal to noise and spectral resolution. Bridging the gap between lab and Solar System spectra involves calculating the complex index of refraction of an ice, then using these values to create model spectra.

Infrared Spectroscopy: The primary application of infrared spectroscopy is remote detection of surface composition. To accomplish this we need to know the locations and relative strengths of an ice's absorptions in the infrared. For ices relevant to the Solar System, the absorptions in the 1-5 μm range are the result of molecular vibrations. An example of the vibrations seen in H_2O-ice is given in Figure 1.
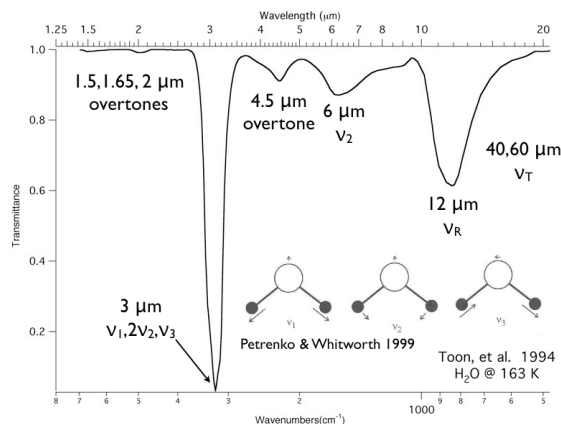
Figure 1. A model transmittance spectrum of a 1 μm thick slab of hexagonal H_2O-ice calculated from optical constants from Toon (1994) and Grundy and Schmitt (1998). Inset: the molecular vibrations of the H_2O molecule (Petrenko and Whitworth, 1999).

Beyond identifying composition, infrared spectra can be used to interpret the physical state of the surface materials. For example, the infrared features of H_2O-ice are temperature and phase dependent e.g. (Schmitt et al., 1998), Figure 2. Clark (1980) showed that the infrared spectrum of H_2O-ice is also dependent on grain size and amount of contamination by other materials. Band depth analysis can be used

to show these variations.
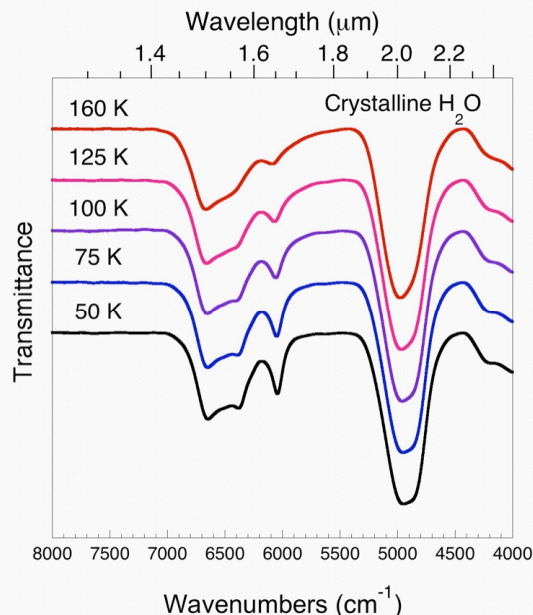
Figure 2. Transmittance spectra of crystalline H2O-ice at 50, 75, 100, 125, and 160 K. The spectra are offset for clarity.

Lab Measurements: The vast majority of infrared measurements of ices were made for comparing to ISM observations. Therefore, they were made at low temperatures < 30 K and at > 2.5 μm. For the purposes of ground based observing, the visible and near infrared 0.5-2.5 microns are the most effective at seeing through the Earth's atmosphere. Spacecraft can make measurements at wavelengths longer than 3 μm, but H_2O-ice is usually saturated in this region, making the spectrum difficult to interpret. The wavelength range from 3-5 μm is still relevant since this is where the fundamental or strongest vibrations are for many ices.

Infrared lab measurements are made in transmission or reflection. Reflection is useful in identifying features, but is not easily converted to optical constants. Transmission needs to be done with thin samples either vapor deposited or in a closed cell. Closed cell measurements are limited by the fact that the sample is not under vacuum, and therefore cannot make metastable phases such as amorphous H_2O-ice. For spectra of H_2O-ice in the mid infrared (3-5 μm), ice samples only need to be a few microns thick for strong absorptions to appear. To see the relatively weak combination features in the 1-3 μm range, one needs to prepare a sample that

is on the order of tens of microns thick, saturating the fundamental at 3 μm. To see features shortward of 1.5 μm, a sample hundreds of microns thick is necessary, but cannot be made by thin film deposition since the sample begins to deviate from a flat surface into a mound. Thus, each individual ice composition presents a unique problem depending on the target wavelength range, phase, etc.

Scattering of icy surfaces is poorly understood. Scattering models are for particulate matter, but ices that can sublimate and sinter together should not be treated as particles. Few scattering studies have been performed on thin films of ices, and it is unknown how this scattering can affect the infrared spectrum.

Mixtures: The presence of CO_2 and CH_4 in H_2O-ice create a spectrum that is not the same as a model mixture of the pure end members (Bernstein et al., 2005; Bernstein et al., 2006). The features are temperature and H_2O-ice phase dependent and could be used to interpret the state of mixing on an icy surface. Few studies have looked at the effect on features shortward of 3 μm.

Irradiation: Irradiation causes phase and chemistry changes, sputtering loss e.g. (Bernstein et al., 1995; Mastrapa and Brown, 2006). However, long term effects on the bulk structure, i.e porosity, density, scattering properties, are unknown. Laboratories are limited to specific particle types and energy ranges based on available equipment. Also, it is difficult to measure optical constants of irradiated samples because the ice thickness changes due to sputtering.

What is needed? Some pure substances have still not been measured. Some have been measured, but at the wrong temperature or spectral range. For what measurements there are, only few have been used to derive proper optical constants, and many of them are not appropriate for conversion. Very few mixtures have been investigated at temperatures or with compositions relevant to satellites. Scattering properties of ices are also poorly understood. In addition, the long-term effects of radiation and gardening are not well understood, nor are how they impact porosity, etc. Future laboratory work in these areas is critical to our ability to interpret current data sets.

Bernstein, G. M., et al., 1995. Organic compounds produced by photolysis of realistic interstellar and cometary ice analogs containing methanol. Astrophysical Journal. 454**,** 327-344.

Bernstein, M. P., et al., 2005. Near-infrared laboratory spectra of solid H2O/CO2 and CH3OH/CO2 ice mixtures. Icarus. 179**,** 527-534.

Bernstein, M. P., et al., 2006. Near-infrared spectra of laboratory H2O–CH4 ice mixtures. Icarus. 181**,** 302-308.

Clark, R. N., 1980. Ganymede, Europa, Callisto, and Saturn's Rings: Compositional Analysis from Reflectance Spectroscopy. Icarus. 44**,** 388-409.

Grundy, W. M., Schmitt, B., 1998. The temperature-dependent near-infrared absorption spectrum of hexagonal H_2O ice. Journal of Geophysical Research. 103**,** 25809-25822.

Mastrapa, R. M. E., Brown, R. H., 2006. Ion irradiation of crystalline H_2O--ice: Effect on the 1.65-mum band. Icarus. 183**,** 207-214.

Petrenko, V. F., Whitworth, R. W., 1999. Physics of Ice. Oxford University Press, Oxford, England.

Schmitt, B., et al., Optical properties of ices from UV to infrared. In: B. Schmitt, et al., Eds.), Solar System Ices. Kluwer Academic Publishers, Norwell, MA, 1998, pp. 199-240.

Toon, O. B., et al., 1994. Infrared optical constants of H2O ice, amorphous nitric acid solutions, and nitric acid hydrates. Journal of Geophysical Research. 99**,** 25631-25654.

THE EARLY HISTORY OF ENCELADUS: SETTING THE SCENE FOR TODAY'S ACTIVITY. D. L.

Matson[1], J. C. Castillo-Rogez[1], S. D. Vance[2], A. G. Davies[1], Torrence V. Johnson[1], [1]Jet Propulsion Laboratory, California Institute of Technology, M/S 230-260 4800 Oak Grove Drive, Pasadena, CA, 91109, E-mail: Julie.C.Castillo@jpl.nasa.gov, [2]Department of Earth and Space Sciences, Box 351310, Seattle, WA 98195.

Introduction: Several scenarios have been proposed to explain the thermal state of Enceladus as inferred from Cassini observations. These models focus on how the South Pole thermal anomaly developed and how it can sustain a heat output of 3 to 7 GW. Some models propose that this thermal anomaly was triggered by - and still involves - the presence of a thermal anomaly in the rocky core [1, 2]. In those models, significant heat flow from the core drives a hotspot in the outer icy shell of the satellite.

Another constraint on the thermal state reached by Enceladus's core during its evolution comes from the South Pole geyser's composition. Matson *et al.* [3] have suggested that the observed molecular nitrogen comes from the decomposition of ammonia at temperatures of about 850 K (between 575 K and 850 K if catalysts are involved). These temperatures can be realized during hydrothermal activity at the interface between a hot core and liquid water.

What conditions in Enceladus's early history could have led to the formation of a core that became sufficiently hot in the long run to power a hotspot located within the ice, driving hydrothermal circulation? The implication is that the satellite differentiated, and that the core became consolidated enough to prevent cooling from deep hydrothermal circulation. The latter situation is not obvious, as the maximum pressure inside Enceladus is less than 40 MPa. This pressure is similar to that on Earth's ocean floors. At these pressures, terrestrial rocks, compacted by gravity, retain significant porosity (between 20 and 40% depending on their nature).

We consider different possible scenarios, as functions of the initial conditions (composition, heat budget, etc.), leading to the formation and the long-term evolution of a rocky core inside Enceladus.

Initial conditions and differentiation: Two key parameters play a determining role in the long-term evolution of Enceladus: the extent of freezing point suppression for water by aqueous species such as ammonia, and the time of formation with respect to calcium-aluminum inclusions (CAIs). The latter parameter determines the amount of short-lived radiogenic isotopes (SLRIs), especially ^{26}Al and ^{60}Fe, that accreted in the satellite [4].

If ammonia and SLRIs are not accreted, the interior temperature barely reaches the water ice melting point and differentiation is only partial.

Spectroscopic observations [5] indicate the presence of a few percent ammonia and suggest that ammonia may have accreted in Enceladus. Further evidence comes from the observation of N_2 in Enceladus's geyser, which can be explained by the decomposition of ammonia (discussed above). The mechanisms for differentiation at the ammonia-water eutectic temperature are not well constrained. However, if we assume that conditions allow the separation of the silicate from the ice, then dry silicate sinks to the center. At temperatures below 300 K, the kinetics of serpentinization reactions are extremely slow, and may not react all of the silicate phase over the lifetime of Enceladus. As a result, Enceladus's core is a probably mixture of rock with up to 40% of ice. In the long term, temperatures reach the water ice melting point due to long-lived radiogenic isotope decay (at about 1 By after formation). This affects only the inner 150 km (Figure 1).

If Enceladus formed less than 4 My after CAIs (Figure 2), differentiation and silicate hydration occur rapidly, taking place during the SLRI decay heat pulse. Serpentinization of the whole silicate phase is likely achieved within a few My following formation. The increased rock volume upon serpentinization may eliminate permability in the core. Alternatively, anisotropic expansion may maintain a network of cross-fractures that allow continued fluid circulation [6, 7]. This situation takes place regardless of whether ammonia is present The combined heat produced from silicate hydration (increasing the temperature by 120 K) and ^{60}Fe decay (an increase of up to 400 K) brings the core temperature up to 600 K in less than 10 My.

Long-term evolution of the core. The composition of the core determines its thermal conductivity, with consequences for its long-term thermal evolution. This parameter ranges between 0.5 and 3 W/K/m depending on the nature of the silicate phase [8].

Penetration depth of the hydrothermal flow is a function of permeability, which in turn is influenced by tectonic and micro-mechanical processes [7, 9]. In the long term, the formation of sulfur compounds fills pores and this further inhibits hydrothermal circulation [10]. If the above factors are manifest on Enceladus, this satellite's core can have easily reached temperatures necessary for melting hydrated silicates (*i.e.*, between 1000 and 1150 K).

Laboratory measurements of basalts dissipative properties at frequencies only a couple orders of mag-

nitude greater than Enceladus' tidal forcing frequency yield dissipation factors less than 100 for temperatures greater than 800 K.

For a few melt-percent, the viscosity drops, and the dissipation factor tends toward unity [11, 12]. Significant tidal heating takes place and can maintain a warm core over the long term. Lateral heterogeneities of composition and viscoelastic properties, cooling from hydrothermal circulation, difference in tidal heating between the poles and the equator [13] are likely to give rise to lateral thermal anomalies. Terrestrial analogs (subglacial or suboceanic volcanic activity) indicate that water should remain in the magma due to pressure [14]. However, these terrestrial analogs contain only a few percent water and it is likely that most of the water exsolved during magma production and upwelling. If so, this could give rise to explosive magmatic events [15].

Conclusion: We have shown two types of evolutionary scenarios for Enceladus' core, depending on the initial inventory of SLRI, and, thus, the time of formation of the satellite with respect to the production of CAIs. Because of Enceladus' very low internal pressure, a compact silicate core *per se* can exist only if water is trapped in the structures of the silicate phases so that these minerals reach the close packing limit. In order to form a hot core, models must accrete active SLRIs. Specific properties of hydrated silicate associated with the initial heat "pulse" due to SLRI decay can lead to silicate melting, resulting in volcanism. Tidal heating can maintain partially molten regions over the long term.

References: [1] Tobie G. et al. (2006) *Eos Trans. AGU*, 87(52), Fall Meet. Suppl., Abstract P13B-0172. [2] Collins G. and Goodman J.C. (2007) *Icarus* in press. [3] Matson D. L. et al. (2007) *Icarus*, *Icarus* 187, 569. [4] Castillo J. C. et al. (2007) *Icarus* in press. [5] Brown R. H. et al. (2006) *Science*, 311, 1425-1428. [6] O'Hanley, D.S. (1992) *Geology*, *20*, 705-708. [7] Vance S. *et al.* (2007) Submitted to *Astrobiology*. [8] Clauser C. and Huenges E. (1995) *Rock Physics and Phase Relations, A Handbook of Physical Constants, AGU Reference Shelf 3*. [9] Vance, S. *et al.* (2007) Submitted to *Icarus*. [8] McKinnon W. B. and Zolensky M. E. (2003) *Astrobiology*, 3, 879-897. [11] James M. R. et al. (2004) *J. Volcan. Geoth. Res.*, 3001, 1-15. [12] Matson D. L. et al. (2006) *Bull. Am. Astron. Soc.*, 38, 30.01. [13] Tobie G. et al. (2005) *Icarus*, 177, 534-549. [14] Wilson L. and Head J. W. (2001) *LPS* XXXII, Abstract #1013. [15] Wilson L. et al. (1999) *MPS*, 34, 541-557.
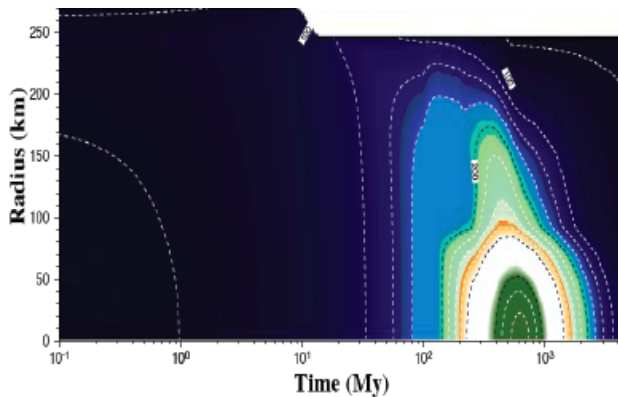
Figure 1. Thermal evolution for a model of Enceladus including a few percent ammonia, formed more than 7 My after CAIs.
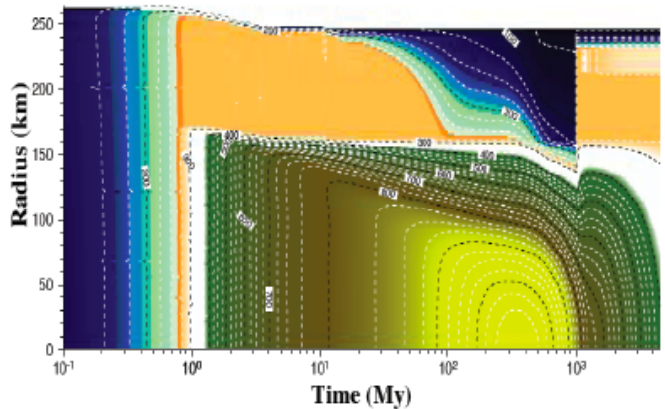
Figure 2. A thermal evolution model of Enceladus accreted 4 My after CAIs.
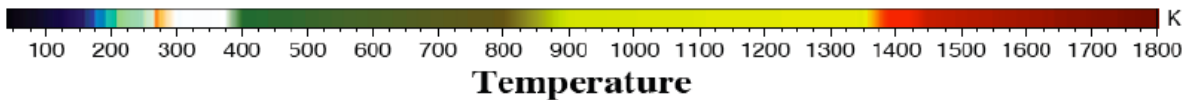
REORIENTATION OF ICY SATELLITES DUE TO IMPACT BASINS. I. Matsuyama, *Dept. Terrestrial Magnetism, Carnegie Institute of Washington, (matsuyama@dtm.ciw.edu)*, F. Nimmo, *Dept. Earth & Planetary Sciences, U.C. Santa Cruz, Santa Cruz CA 95064 (fnimmo@es.ucsc.edu)*.

Limited attention has been paid to reorientation of the icy satellites of the outer solar system. [1] investigated how redistribution of volatiles might affect the rotational stability of Triton and Pluto. [2] and [3] modelled reorientation due to convective processes on Miranda and Enceladus, respectively, and [4] pointed out that Europa's variable ice shell thickness might lead to rotational instability. Here we will focus on the fact, first pointed out by [5] for the Moon, that the negative long-term load caused by a large impact basin can potentially reorient a planetary body.

We will consider the specific case of a tidally-deformed satellite which has no initial rigidity, and is thus purely hydrostatic. As the satellite cools, it will develop a rigid lithosphere; at some point in the cooling process, the impact basin forms and reorientation, opposed by the fossil tidal and rotational bulges, will take place. Because of these bulges, the angular reorientation θ_R depends on the initial colatitude θ_L^f and longitude ϕ_L^f of the applied load. By diagonalizing the resulting moment of inertia tensor, the following set of equations may be derived [6]:

$$Q \sin^2 \theta_L^f \sin(2\phi_L^f) = \sin^2 \theta_R \sin(2\phi_R) - 3 \sin^2 \theta_T \sin(2\phi_T)$$
(1)

$$Q \sin(2\theta_L^f) \cos(\phi_L^f) = \sin(2\theta_R) \cos(\phi_R) - 3 \sin(2\theta_T) \cos(\phi_T)$$
(2)

$$Q \sin(2\theta_L^f) \sin(\phi_L^f) = \sin(2\theta_R) \sin(\phi_R) - 3 \sin(2\theta_T) \sin(\phi_T)$$
(3)

Here (θ_R, ϕ_R) and (θ_T, ϕ_T) are the coordinates of the initial rotational and tidal axes, respectively, and Q defines the size of the load. The initial tidal and rotational axes must be perpendicular, and the reorientation angle is given by θ_R.

For reorientation along the meridian passing through the tidal axis, these equations simplify to give $Q \sin(2\theta_L^f) = 4 \sin(2\theta_R)$ while for reorientation along the meridian perpendicular to the tidal axis we obtain $Q \sin(2\theta_L^f) = \sin(2\theta_R)$. Thus, reorientation is larger if it occurs around the tidal axis, as expected [3].

The quantity Q describes the size of the load, and is given by [6]

$$Q = \frac{GM}{R^2} \frac{3\sqrt{5} G_{20}'^L}{R\Omega^2 (k_f^{T*} - k_f^T)}$$
(4)

Here R, M and Ω are the satellite radius, mass and angular rotation frequency, G is the gravitational constant, $G_{20}'^L$ is the dimensionless degree-two gravitational potential of the load and k_f^{T*} and k_f^T are the tidal Love numbers of the body without and with an elastic lithosphere, respectively. Note that here we have assumed that the rotation rate is unaffected by the reorientation.

We will calculate the gravitational potential imposed by an impact basin as follows. For a basin having an angular radius ψ and a constant depth h, the normalized degree-2 potential when $h \ll R$ is given by [3]

$$G_{20}'^L = \frac{\pi h \rho R^2}{M} \cos \psi \sin^2 \psi$$
(5)

where ρ is the surface density, and we are assuming that there are no other gravity anomalies present (e.g. a compensating mantle plug). The gravitational perturbation thus depends on the depth and angular size of the impact basin, as expected.

For simplicity, we have neglected the effect of the ejecta blanket and any central peak. The latter is unlikely to have a significant effect, as its mass is small compared with the total mass removed. The ejecta blanket, however, can reduce the effective potential anomaly, by a factor of ≈ 5 [5] if the blanket extends uniformly out to two basin radii and no material escapes the satellite. Scaling arguments [9] suggest that most ejecta is retained; however, the distribution of ejecta is hard to infer from Voyager-era data [7] and the quantity of material vapourized and thus permanently lost is unknown. Imaging by the *Cassini* spacecraft is likely to make the role of the ejecta clearer.

Equations (1)-(5) may be used to infer the reorientation caused by a given basin. To do so, we need to calculate the Love numbers k_f^{T*} and k_f^T. These will depend on the density and (for k_f^T) rigidity structures of the satellites, which are not in general well known. We will therefore make the conservative assumption that $k_f^{T*} = 1.5$, the value for a homogeneous fluid body, and that $k_f^T = 0$ (perfectly rigid). In this way, our estimate of the reorientation angle θ_R will be conservative.

Table 1 summarizes the location, diameter D and present-day maximum depth d_{max} of the impact basins we consider [7]. To be conservative, depth is defined as below the background elevation, rather than relative to the crater rim. Topographic profiles across these impact basins [7] suggest that they are generally flat-floored, and thus that our assumption of a constant-depth basin is reasonable. We therefore assume that $h = d_{max}$.

Figure 1 shows the polewards reorientation angle θ_R as a function of basin angular radius ψ and the centripetal acceleration of the satellite. The basin depth (2 km) and initial latitude ($\theta_L^f = 45°$) are kept constant and reorientation is assumed to occur around the tidal axis. As expected, larger basins lead to greater reorientation. Similarly, other things being equal, a satellite which is spinning faster experiences less reorientation, because the equatorial and tidal bulges are larger.

Table 1 tabulates the polewards reorientation θ_R expected for the real basin locations and depths. Herschel, because it is equatorial, produces almost no reorientation, despite its relatively large perturbation to the gravity field. Aeneas, being both shallow and relatively small, likewise produces little reorientation. Odysseus and Tirawa result in larger ($10.3°$ and $19.4°$, respectively) reorientations - the former because Odysseus is large, and the latter because Rhea is a slow rotator. For Titania, the nominal basin parameters resulted in no

Table 1: Impact basins

Body	R	P	Basin	Colat.	W. Lon.	D	d_{max}	ψ	Q	Δg	θ_R
	km	days		θ_L^f	ϕ_L^f	km	km			mGal	
Mimas	196	0.942	Herschel	$87°$	$-111°$	135	11	$19.7°$	-0.85	-12.8	$2.5°$
Tethys	530	1.888	Odysseus	$60°$	$-130°$	450	3	$24.3°$	-0.50	-13.1	$10.3°$
Dione	560	2.737	Aeneas	$64°$	$-46°$	175	3	$9.0°$	-0.15	-2.1	$2.6°$
Rhea	764	4.518	Tirawa	$54°$	$-150°$	350	5	$13.1°$	-1.07	-8.6	$19.4°$
Titania	790	8.706	Gertrude	$107°$	$-68°$	400	2	$14.5°$	-1.85	no solution found	
Titania	790	8.706	Gertrude	$107°$	$-68°$	400	1.3	$14.5°$	-1.2	-3.0	$18.1°$
Pluto	1152	6.38	unknown	$(45°)$	$(-90°)$	(602)	(2)	$(15°)$	(-0.73)	(-5.2)	$(23.4°)$

Here R and P are the satellite radius and period, D and d_{max} are the basin diameter and maximum depth (from [7]), Q is the dimensionless load (equation 4), θ_R is the amount of poleward reorientation, Δg is the degree-2 gravity anomaly at 100 km spacecraft altitude, calculated from G_{20}^L using the method given in [3], and ψ is the basin angular radius. Satellite data obtained from [8] and we assumed $\rho = 900\ kg\ m^{-3}$. For Titania, a solution could not be obtained with the nominal basin parameters. It is not known whether Pluto has any impact basins; the calculations presented here represent an example assuming the basin dimensions are comparable to those of the other icy satellites.
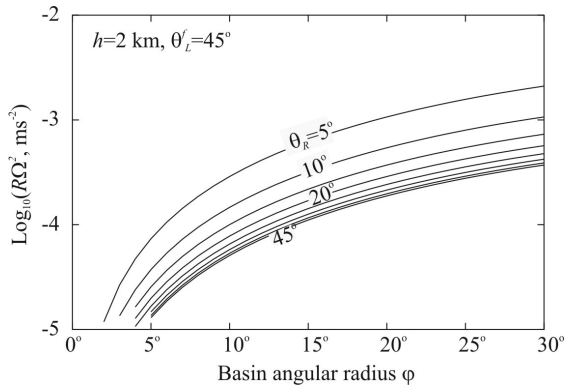
Figure 1: Polewards reorientation angle θ_R (plotted at $5°$ intervals) as a function of basin angular width ψ and satellite centripetal acceleration $R\Omega^2$, calculated using equations (1)-(5). Basin depth h=2 km, initial colatitude $\theta_L^f = 45°$; reorientation is assumed to take place around tidal axis (see text).

solution being found to equations (1)-(3). Reducing the basin depth gave a large reorientation ($18.1°$), primarily because of Titania's slow rotation.

Apart from the effect of an ejecta blanket, which is hard to quantify, the results presented in Table 1 will tend to underestimate the actual amount of reorientation. In particular, the relevant basin depth is that applicable as reorientation proceeded. Since reorientation and isostatic basin rebound occur on comparable timescales, the present-day basin depth is almost certainly an underestimate.

Our main conclusion is that, particularly for slow-rotating satellites, the presence of impact basins can lead to significant (tens of degrees) reorientation of these bodies. As with Enceladus [3], such reorientation is likely to have observable consequences. Perhaps most importantly, reorientation by tens of degrees will lead to stresses sufficient to cause fractures, and probably a global pattern of tectonic features [10]. Such pat-

terns are likely to be present on both Rhea and Tethys, and may be revealed by existing or future *Cassini* observations. Secondly, the expected apex-antapex asymmetry in impact crater distribution [11] will be smeared out if reorientation occurs [e.g. 12]. Finally, the impact basins are associated with negative degree-two gravity anomalies, tabulated in Table 1, of order 10 mGal, which may be detectable with sufficiently close spacecraft flybys. These gravity anomalies are comparable to those expected from the rotational and tidal deformation of a fluid body [13]. Thus, determination of satellite structure using the gravity coefficients J_2 and/or C_{22} [14] is likely to be significantly complicated by the presence of these large (and presumably uncompensated) impact basins.

Pluto and Charon are both slow rotators and thus prone to reorientation. Although no impact features are currently known, it is likely that both bodies possess basins of comparable sizes to those listed in Table 1. Taking $\psi = 15°$ and using the same basin parameters as for Fig. 1, the reorientation angle for Pluto is $23.4°$. Thus, if Pluto or Charon possess impact basins comparable to those examined here, reorientation is very likely to have occurred.

References

[1] Rubincam, D.P., *Icarus* 163, 469-478, 2003. [2] Janes, D.M. and H.J. Melosh, *JGR* 93, 3127-3143, 1988. [3] Nimmo, F. and R.T. Pappalardo, *Nature* 441, 614-616, 2006. [4] Ojakangas, G.W. and D.J. Stevenson, *Icarus* 81, 242-270, 1989. [5] Melosh, H.J., *EPSL* 26, 353-360, 1975. [6] Matsuyama, I. and F. Nimmo, *JGR*, submitted. [7] Moore, J.M. et al., *Icarus* 171, 421-443, 2004. [8] Lodders, K. and B. Fegley, *The Planetary Scientist's Companion*, 1998. [9] Veverka, J. et al. in *Satellites*, Univ. Ariz. Press [10] Melosh, H.J., *Icarus* 44, 745-751, 1980. [11] Zahnle, K. et al., *Icarus* 153, 111-129, 2001. [12] Plescia, J.B., *Icarus* 73, 442-461, 1988. [13] Murray, C.D. and S.F. Dermott, *Solar System Dynamics*, 1999. [14] Anderson, J.D. et al., *Icarus* 153, 157-161, 2001.

STEADY-STATE CREEP RESPONSE OF ICE-I/MAGNESIUM SULFATE HYDRATE. C. McCarthy[1], D.
L. Goldsby[1], R. F. Cooper[1], S. H. Kirby[2], and W. B. Durham[3], [1]Brown University, Dept. of Geological Sciences
Providence, RI 02912 (contact: christine_mccarthy@brown.edu), [2]U.S. Geological Survey, 345 Middlefield Rd.
Menlo Park, CA, 94025, [3]M.I.T., 77 Massachusetts Ave., Cambridge, MA 01239.

Introduction: As our knowledge about the icy moons of the outer solar system improves, ever more questions arise with regards to the nature of active tectonics in the icy shells, and the diversity of their surface expressions. One of the factors that may help explain the morphological diversity is the influence on rheology of the abundant cryominerals that are present in addition to water ice on many of these icy bodies. To date, very little is known about how the presence of secondary minerals affects the physical properties of ice. This work is part of an ongoing experimental investigation into the phase morphology and deformation behavior of several multiphase, ice-rich systems of interest to outer-planet study. In particular, we are examining ice/salt-hydrate binary systems with emphasis on some of the highly hydrated sulfates suggested by Galileo's Near-Infrared Mapping Spectrometer[1] and by laboratory[2] and theoretical studies[3]. Here we present a preliminary flow law for two-phase aggregates of Ice-I and $MgSO_4 \cdot 11H_2O$ ("MS11") deforming in steady-state that shows the relationship between differential stress σ, strain rate $\dot{\varepsilon}$, and temperature T.

Methods: Specimens in this study were prepared via crystallization from a homogeneous binary liquid solution; the protocol is described in detail in Ref. [4]. The approach produces two-phase solids intended to mimic material likely found at the base of the crust, in a crack system if rupture additionally involves upwelling of brine, or in any region experiencing catastrophic melting and subsequent solidification. The eutectic microstructure that results from the solidification reaction of system H_2O-$MgSO_4$ consists of regular and complex lamellae of MS11 (undecahydrate)[5] and Ice-I (Fig. 1) and can be predicted from the volume fraction of the phase having the highest partial molar entropy of solution and from the magnitude of that entropy[4].

Compressional creep tests were performed at three temperatures (230, 240, and 250K) using both a high-pressure apparatus (N$_2$ confining medium, P = 50 MPa) and a 1 atm, dead-weight apparatus [6]. In both settings, fully dense cylinders were deformed at constant load in uniaxial compression. The two data sets can be compared by incorporating an activation volume, V*, into the Dorn, or "power-law," model of creep, i.e.:

$$\dot{\varepsilon} = A\sigma^n \exp\left[\frac{-(E^* + PV^*)}{RT}\right],$$

where R is the gas constant, n the stress exponent, E* the activation enthalpy and A a factor associated with aspects of microstructure, chemical potentials and geometry. (For example, where grain size, d, also effects the relationship, the term can be expressed as A = $A'd^{-p}$). In this case, lacking knowledge of the effect of pressure on the effective viscosity of the MS11 phase, we simply used the published activation volume for water ice (V* = –13 cm^3 mol^{-1}) [7].

Results: The data at various temperatures are plotted as strain-rate vs. stress in Fig. 2. The steady-state creep results show that the eutectic aggregates have an effective viscosity that is at least an order of magnitude greater than that of polycrystalline ice-I at the same conditions.[8] We attribute this increase in strength to the unique microstructure of the eutectic material. The heterophase boundaries are found to be effective barriers to dislocation motion and thus influence the mechanism by which deformation occurs. Three separate creep regimes can be identified in Fig. 2. At the highest stress, and so far only obtainable in the high-pressure apparatus, is flow characterized by a stress exponent of n = 6±0.3. At intermediate stresses, a creep regime is observed that is characterized by n = 3–4. The activation enthalpy calculated for this regime is 91.6 kJ mol^{-1}. These two regimes are consistent with the steady-state response of materials exhibiting a lamellar eutectic morphology.[9] In such materials, two parallel mechanisms are believed to be acting in the regions, both dominated by dislocation motion. The high stress regime is associated with dislocation viscous glide and the intermediate stress regime with dislocation climb.[10] Finally, a low stress (< 2 MPa) regime is identified, with n = 1–2 and an activation enthalpy of 52.6 kJ mol^{-1}. Diffusion creep likely dominates such a regime. The ratio of activation enthalpies for the intermediate and low stress regimes is consistent with that predicted for water ice, with one difference: whereas no diffusion creep mechanism has been observed experimentally for water ice, one has been detected here with the eutectic aggregates. Again, the heterophase boundaries likely play a large role in the process. A study of eutectic Sn-Pb by [11] reports a low stress mechanism in which Coble creep is rate

limited not by diffusion of vacancies but by the emission and absorption of dislocations in the heterophase boundaries. Further experimental data is needed for the system H_2O-$MgSO_4$, as well as a detailed microstructural analysis before we can definitively say which mechanisms are acting. Not discussed here are the effects of grain size, or more accurately colony size and lamellar spacing, which effects we plan to explore shortly using a misting and high-temperature annealing process.

Conclusions: The mechanical behavior of the ice-I/MS11 aggregate shows a rheology distinctly different from single-phase ice. The flow laws here offer additional parameters to be considered in the tectonic modeling of Europa and other icy moons.

References: [1] McCord, T. B. et al. (1998) *Science*, 280, 1242-1244. [2] Dalton, J. B. et al. (2005) *Icarus, 177,* 472-490. [3] Kargel, J. S. (1991) *Icarus*, 94, 368-390. [4] McCarthy, C. et al. (2007) *American Mineralogist*, in press. [5] Peterson R. C. and Wang, R. (2006) *Geology*, 34:11, 957-960. [6] Goldsby D. L. and Kohlstedt, D. L. (2001) *JGR*, 106:B6, 11,017-11,030. [7] Durham, W. B. et al. (1997) *JGR*, 102:E7, 16,293-16,302. [8] McCarthy, C. et al. (2007) *LPSC XXXVIII*, #2429. [9] Bang, W. H. et al. (2005) *J. Elec. Mat.*, 34:10, 1287-1300. [10] Darveaux, R. (1992) *IEEE Trans*. 15:6, 1013-1024. [11] Schneibel, J. H. and Hazzledine, P. M. (1983*) J. Mat. Sci*. 18, 562-570.

Figure 2: Log-log plot of strain-rate versus stress for eutectic ice-I/MS11 aggregates at various temperatures. The triangles and one high stress point for 250 K are high pressure data that have been normalized from a confining pressure of 50 MPa to atmospheric pressure using an activation volume of -13 cm^3/mol. Stress exponent values have been obtained from the 240 K data and transcribed to the 230 K and 250 K data.

Figure 1: CSEM secondary electron image of fresh fracture surface of system H_2O-$MgSO_4$. Although the composition here slightly off eutectic (19.5wt% vs. C_E = 17.3wt%), the observed microstructure shows the lamellar and complex morphology that is representative of this system. In the image, the hydrate phase stands in relief while the ice phase is recessed due to sublimation.

AURORA ON GANYMEDE
Melissa McGrath

A set of Hubble Space Telescope Space Telescope Imaging Spectrograph observations of Ganymede made in November 2003 in a guaranteed time program (9296, PI H. Ford) for the Advanced Camera for Surveys will be presented for the first time. The monochromatic UV images in oxygen emission at 135.6 nm were obtained at ~335 deg orbital longitude shortly before Ganymede entered Jupiter eclipse. They compliment existing STIS observations of Ganymede obtained near western and eastern elongations that have been presented (Feldman et al. 2000; Eviatar et al. 2001; McGrath et al. 2004). They provide similar geometry to ground based observations obtained at Keck by Brown (2001) showing visible light oxygen emission with morphology that is unexplained to date. The UV and visible oxygen emission morphologies will be compared with each other, and also with visible surface features on Ganymede.

THE MIMAS PARADOX REVISITED *plus* CRUSTAL SPREAING ON ENCELADUS? William B. McKinnon[1] and Amy C. Barr[2], [1]Department of Earth and Planetary Sciences and McDonnell Center for the Space Sciences, Washington University, Saint Louis, MO 63130 (mckinnon@wustl.edu); [2]Department of Space Studies, Southwest Research Institute, 1050 Walnut St., Suite 400, Boulder, CO 80302.

Introduction: Enceladus presents a number of paradoxes or at least mysteries. One is the so-called Mimas paradox, which asks why Mimas is not as active as Enceladus despite its larger orbital eccentricity and closer orbit to Saturn [1]. We argue below that Mimas is simply misunderstood, and that there is no paradox. This does not mean that Enceladus is understood, however. Both the magnitude of the tidal heat flow observed, and its localization at the south pole are puzzles [2,3]. We present a simple model for crustal spreading at the south polar terrain that accounts for the heat flow and its localization.

The Mimas-Enceladus Paradox: In [3] it was pointed out that Mimas should be much more tidally heated than Enceladus, for the same tidal dissipation factor Q, which has become known as the "Mimas paradox." The tidal heating on Enceladus is maintained by its 2:1 mean motion resonance with Dione. It is an eccentricity-type resonance [4]:

$$n_E - 2n_D = -\dot{\varphi} \qquad (1)$$

where n_E and n_D are the mean motions of Enceladus and Dione, respectively, and $\dot{\varphi}$ is the rate of advance of their conjunctions. In this resonance, $\dot{\varphi} \equiv \dot{\omega}_E$ (= 0.0044° day[-1]), where ω_E is Enceladus' longitude of periapse, which results in the forcing of Enceladus' eccentricity (0.0047 at present). The dissipation associated with mechanical distortion of the body of Enceladus as it orbits Saturn *must* be the ultimate source of Enceladus' heat flow anomaly (and associated tectonics). The 2:1 resonance allows Enceladus to tap an effectively infinite reservoir of energy to drive its geological activity — the rotation of Saturn.

Mimas is also in a 2:1 mean motion resonance, with Tethys, but it is an inclination-type resonance [5]. In it

$$n_M - 2n_T = -\dot{\varphi} \qquad (2)$$

where n_M and n_T are the mean motions of Mimas and Tethys, respectively, but in this case $\dot{\varphi} = (\dot{\Omega}_M + \dot{\Omega}_T)/2$, where Ω_M and Ω_T are the longitudes of the *ascending nodes* of Mimas and Tethys, respectively. The periapse of Mimas' orbit precesses through its ascending node (i.e., is *not* locked to it, or to the mean value for the two satellites) and so the eccentricity of Mimas' orbit is not forced by the resonance. Mimas' eccentricity (0.02) must be a primordial remnant, possibly enhanced by previous, now disrupted, eccentricity resonances or resonances [6], or

due to some other dynamic event, such as a large impact (e.g., Herschel) or the formation of Saturn's rings (and the opening of the Cassini division).

If Mimas were as dissipative as Enceladus, its e would rapidly decay toward zero, releasing a total specific energy

$$\Delta E = \frac{GM_S e_M^2}{2a_M} \qquad (3)$$

where e_M and a_M are Mimas' eccentricity and semi-major axis, respectively, M_S is the mass of Saturn, and G is the gravitational constant. For $e_M = 0.02$, $\Delta E = 41$ kJ kg^{-1}, which for a composition dominated by cold ice (80% ice by mass, and 100 K) implies $\Delta T \approx 60$ K. A one-time temperature pulse of this magnitude would be of little lasting consequence to Mimas, and the energy reservoir available to Mimas would not be refilled. Its free eccentricity would stay damped.

The persistence of Mimas' present, finite free eccentricity is logically due to the cold and geologically inert nature of this small, icy moon (as is obvious to casual inspection). The tidal Q of Mimas must be large (>>100) for this eccentricity to survive for billions of years [5], but this does not seem implausible. There is no Mimas paradox.

Puzzles: The amount of tidal heating in Enceladus is ultimately limited by the torque Saturn can apply to Enceladus' orbit [e.g., 7]. Based on the present understanding of Saturn's Q, Enceladus' measured heat flow of 5.8 ± 1.9 GW cannot be supplied *in steady state*. This is one puzzle. The other is the concentration of heat flow and tectonics at the south pole, although given Enceladus' small size, perhaps a single, volcanically active province (compared with, say, Io) is not so unreasonable. Below we present a new mechanism – active crustal spreading – that may explain the heat flow and tectonics of the south polar terrain.

Active Spreading: Several sites have been proposed for tidal energy deposition at Enceladus' southern polar region. One possibility is a "hot zone" in a rock core [e.g., 8]; another is along major near-surface fractures (the "tiger stripes") [9]. We argue here for an intermediate depth: the bulk ice shell itself [10], which combines the virtues of maximal tidal flexing (if an ocean exists) and maximal volume. It is not certain if a core and ocean exist, but both are plausible from a thermal history standpoint [10,11] and are required if sufficient tidal heating is to occur in the overlying ice [e.g., 9].

A purely conductive ice shell, with an ocean maintained by tidal heating at the base of the shell, can supply a surface heat flow

$$q = \frac{621}{D}\ln\left(\frac{T_b}{T_s}\right)\left(1 - \frac{D}{R_E}\right) \quad (4)$$

where T_b and T_s are the ocean and surface temperatures, respectively, R_E the radius of Enceladus, and D the ice shell thickness [10]. For $T_b = 270$ K and $T_s = 70$ K, q varies from 5 to 30 mW m^{-2} as D decreases from 100 to 25 km, respectively. These heat flows can be compared to ≈ 80 mW m^{-2} obtained by averaging the observed thermal emission [2] over the entire South Polar Terrain (SPT) (poleward of 55° S [3]). Thus, to account for the magnitude of the thermal anomaly by viscous tidal dissipation alone, a large vertical fraction of Enceladus' ice shell (at the SPT) must be "hot" and dissipative. This large fraction is consistent with *solid state convection* in the shell, in that if convection can initiate, it will advect heat into the shell so that the shell reaches a temperature where it can deform tidally, become dissipative, and heat further [10].

If convecting, the magnitude of the southern polar thermal anomaly implies rather high Nusselt numbers, $Nu \sim 5$–15 for shell thicknesses between 100 and 50 km (convection in much thinner shells is less plausible [10]). The stagnant lid ("lithosphere") thickness should be ~ 10 km for $q \approx 80$ mW m^{-2}. Such a relatively thin lid (with respect to the full convective depth) and low brittle strength (due to Enceladus' low surface gravity of 0.11 m s^{-2}) calls the concept of stagnant lid convection into question. Rather, it is more likely that the cold surface boundary layer deforms and participates in the convective cycle (as the Earth's oceanic lithosphere does [12]). The entire SPT is in fact intensely deformed, with good evidence for compression along its structural boundary [2] and we propose that the central tiger stripes may actually be analogous to terrestrial spreading centers. We *are not* proposing a direct analogue to terrestrial midocean ridge spreading and plate tectonics, whose major mechanical driver is the negative buoyancy of downgoing slabs; rather, we envision a form of active spreading whereby upwelling viscous ice is directly coupled to the actively deforming surface.

If this concept has merit, CIRS measurements of the heat flux from Enceladus' surface as a function of distance from the tiger stripes [2] provide us with a unique opportunity to constrain the spreading rate, convective strain rate, and interior geodynamics of Enceladus. The classic solution to the heat flow from terrestrial spreading centers [e.g., 13] can be integrated over distance from the spreading center, x, to yield the average heat flow between $x = 0$ and $x = l$:

$$\langle q \rangle = \frac{1}{2l}\int_0^l q(x)dx = 2k\Delta T\sqrt{\frac{u}{\pi\kappa l}} \quad (5)$$

where u is the half-spreading velocity, ΔT is the temperature difference from the deep interior to the surface, and k and κ are the thermal conductivity and diffusivity, respectively, of subsurface ice. While the boundary conditions are different in the Enceladus case (radiation vs. constant T_s), at long times (large l) T_s asymptotes to the background radiative equilibrium temperature (T_{eq}) and the temperature profile at depth is the same as in the terrestrial solution. Hence the total heat extracted (and $<q>$) must also be the same in the limit of large l. Using the integral relation (Eq. 5) also frees us from the details of near-surface conductivity and the precise value of T_{eq}. The SPT is equivalent in area to a 270 km x 270 km square; if all four tiger stripes contribute equally to the spreading, then $l \sim 35$ km, and $u \sim 3.5$ cm yr^{-1} for $\Delta T = 200$ K. This further implies an average time (age) to recycle the SPT of ~ 1 Myr, and a strain rate $\tau^{-1} \sim 3$ x 10^{-14} s^{-1}, values that appear quite plausible.

Conclusion: The tiger stripes on Enceladus may represent the surface manifestation of deep mantle processes – in this case, locations where thermal buoyancy stresses due to tidal-heat-driven solid-state convection in Enceladus' ice shell have been able to rip its rheologically weak lithosphere and allow hot ice to rise to the surface. This hypothesis is consistent with the CIRS observation that the majority of the thermal emission from the SPT comes from near the tiger stripes themselves. The observed emission and a simple active spreading model are used to derive an age for the SPT of ~ 1 Myr. This estimate should be refined with a more detailed model of surface temperature evolution near the stripes.

References: [1] Squyres S.W. et al. (1983) *Icarus 53*, 319-331; [2] Spencer J.R. et al. (2006) *Science 311*, 1401-1405; [3] Porco C.C. et al. (2006) *Science 311*, 1393-1401; [4] Peale, S.J. (1986) in *Satellites* (J.A. Burns and M.S. Matthews, eds.) Univ. Ariz. Press, 159-223; [5] Peale, S.J. (1999) *Annu. Rev. Astron. Astrophys. 37*, 533-602; [6] Champenois, S., and A. Vienne (1999) *Icarus 140*, 106-121; [7] Meyer, J. and J. Wisdom (2007) *Icarus*, in press; [8] Matson D.L. et al. (2007) *Icarus 187*, 569-573; [9] Nimmo F. et al. (2007) *Nature 447*, 289-291; [10] Barr A.C. and W.B. McKinnon (2007) *Geophys. Res. Lett. 34*, L09202; [11] Schubert G. et al. (2007) *Icarus 188*, 245-235; [12] Solomatov V.S. (2004) *J. Geophys. Res. 109*, B01412; [13] Turcotte D.L. and G. Schubert (2002) *Geodynamics, 2nd Ed.*, CUP, ch. 4.

MEASURING TECTONIC STRAIN: FROM GANYMEDE TO ENCELADUS AND DIONE. R. L.
Michaud[1], R. T. Pappalardo[2], and G. C. Collins[1], [1]Physics and Astronomy Dept., Wheaton College, Norton MA
02766, [2]Jet Propulsion Laboratory, Pasadena CA.

Introduction: Many satellites of the outer solar
system exhibit prominent tectonic features. These
cracks, ridges, and other terrain features are indicative
of a dynamic past that we wish to further understand.
Strain measurement quantifies the magnitude of tec-
tonic movement, and may be used for models of inter-
nal evolution. It is also a way to compare tectonic
behavior among the icy satellites and terrestrial plan-
ets.

In previous work, we have used three different
methods of strain measurement to understand the tec-
tonics of Ganymede grooved terrain [1, 2]. For our
current project, we are using the same tools we have
developed on Ganymede to better understand the tec-
tonics of two of the Saturnian satellites: Enceladus and
Dione.

Methods: Accurate strain analysis depends on
knowledge of the image geometry. The first step in
any of our strain measurement methods is to process
the images. For the Saturnian satellites, we have been
processing available Cassini data through ISIS. We
are searching for images at high resolution that exhibit
impact craters cut by faults. By reprojecting the im-
ages into Lambert azimuthal projection, centered on
the centers of cut craters, we can minimize the geomet-
ric distortion on the images that would compromise
our measurements. There are three strain measurement
methods that we will be using in parallel to estimate
strain on Enceladus and Dione.

Method 1: Split Craters: If faults transect a pris-
tine crater, they will distort the shape of the crater rim
so that it is no longer a perfect circle. By comparing
the shape of a deformed crater with that of a circle, one
can calculate strain and therefore estimate the amount
of stress caused by the faults. In the split crater
method, the zone of faults that cuts the crater is nar-
rower than the diameter of the crater, and as a result
the crater will split apart so that there are two partial-
circle segments remaining (Fig. 1). To calculate strain,
we will measure approximately 10-20 points on the
rims of each of these segments. We then feed this data
into a circle fitting program that will approximate (by
minimizing the error) the original rim shape for each
half of the crater. Strain can then be derived by find-
ing the difference in circle centers.

Method 2: Distributed Deformation: If faults are
distributed across the diameter of the crater, the rim
will be stretched and take on the appearance of an el-
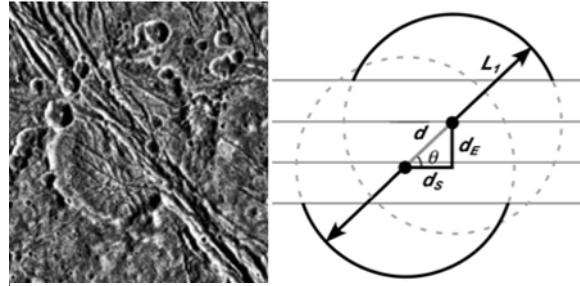
*Figure 1: An unnamed crater in Marius Regio on Gany-
mede demonstrates the split crater geometry that can be
used for strain measurement [1]. This crater is 23 km in
diameter and has undergone both extension and left-
lateral shear. Methods 1 and 3 both estimate over 50%
extensional strain in the fault zone that cuts this crater.*

lipse (see Fig. 2). As in to the split crater method, 10-
20 points along the crater rims will be recorded, but
the data is then put into an ellipse-fitting program,
which has more free parameters than the circle fitting
program. Strain can be calculated from the ratio be-
tween the major and minor axes of each ellipse, as well
as the orientation of the major axis.

Both methods 1 and 2 assume an initially circular
geometry for the crater rim, which is a valid assump-
tion for impactors striking the surface at more than a
10 degree angle [3]. However, for craters smaller than
about 10 km in diameter on Ganymede, irregularities
in the rim (probably from post-impact modification)
become significant and cause too much error in the
circle fitting routine [1].

Method 3: Fault Geometry: A method of strain es-
timation which is independent of any assumptions
about crater geometry, instead looks at the fault ge-
ometry. If we assume that the faults cutting the craters
are normal faults that cause grabens or tilt-blocking,
we can measure the widths of the fault scarps. After
correcting for the spacecraft look direction and making
assumptions for the fault dip angle, we can calculate
the extensional strain. It is important to note that this
method can be applied to areas without faulted craters
on Enceladus and Dione. The fault geometry method
will be used as a check for our other two techniques in
areas where craters are cut by faults. Checking strain
measurements this way on Ganymede produced similar
results, giving us confidence in all three of the meth-
ods outlined here. Inconsistencies between the fault
geometry method and the two strained crater methods

may arise due to secondary faulting or the difference in geometry between planar and listric faulting.

Discussion: With our strain measurements we will be able to place quantitative constraints on the tectonic histories of Enceladus and Dione. Our previous strain measurements on Ganymede have helped to determine a global strain value, which would be important in distinguishing between interior evolution models for the Saturnian satellites as well. It is important to be able to provide observational constraints for interior models such as those by Castillo *et al.* [4]. More broadly, the data may be used to compare tectonic features on other satellites in the outer solar system as a means of further understanding tectonic activity on these icy bodies.

At the meeting, we will be presenting the results of work performed during a summer internship to compare tectonic strain on Enceladus and Dione to the strain we have already measured on Ganymede.

References: [1] Pappalardo and Collins, *J. Struct. Geol.* (2005); [2] Michaud and Collins, *LPSC 38* (2007); [3] Gault and Wedekind, *Proc. 9 LPSC* (1978); [4] Castillo *et al.*, *LPSC 37* (2006).
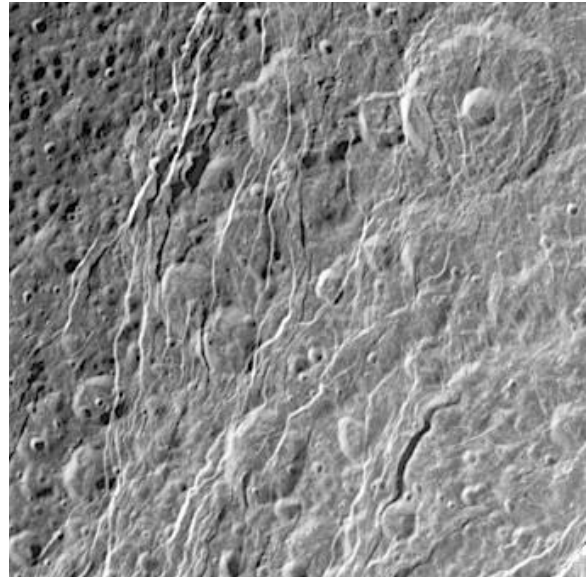
Figure 2: Craters cut by extensional faults on Dione. The geometry of these craters and fault scarps are the subject of this summer's research.

INTERACTIONS BETWEEN IMPACT CRATERS AND TECTONIC FRACTURES ON ENCELADUS AND DIONE.

D. J. Miller[1], A. N. Barnash[1], V. J. Bray[2], E. P. Turtle[3], P. Helfenstein[4], S. W. Squyres[4], and J. A. Rathbun[1], [1]University of Redlands (1200 East Colton Ave., Redlands CA 92373, USA), [2]Imperial College London (Exhibition Road, London, SW7 2AZ, United Kingdom), [3]Johns Hopkins University Applied Physics Laboratory (11100 Johns Hopkins Rd., Laurel, MD 20723-6099), [4]Cornell University (Ithaca, NY 14853-6801); *julie_rathbun@redlands.edu*.

Introduction: The majority of features observed on the icy satellites of Saturn are due to impact cratering and tectonics, so how those processes interact is important in the outer solar system. However, the morphology of the interaction is different on different Saturnian satellites. On Enceladus, the impact features appear to control the orientation of nearby linear tectonic features. On Dione, however, the impact features are substantially altered and extended by the action of linear tectonic features.

Enceladus: The surface of Enceladus can be divided into cratered and tectonic terrains (Rathbun et al., 2005). In the cratered terrains, tectonic features (that appear to be fractures) still occur. However, the orientation of the fractures appears to be controlled by the preexisting impact features (figure1), suggesting that the existence of the impact feature is affecting the fracturing process. One possibility is that the stress due to the impact crater's topography is interacting with the stress causing the tectonics. If that is the case, the stresses should be of similar magnitude and the fracture stress can be approximated by the topographic stress (Turtle and Melosh, 1997).

We have identified more than a dozed relevant impact craters and mapped the fractures and crater rims. Using the Interactive Data Language (IDL), we measured the trend of fractures in the region and calculated the angle of reorientation expected if each fracture's direction were to be radial near the crater (figure 2). We then measured the directions of fractures overlapping the crater and compared the actual direction to the expected direction. We found that approximately half of the fractures were reoriented in the expected way indicating that the impact features are influencing the orientation of fractures that overlap them.

The craters identified are all located at low latitudes on the anti-Saturn hemisphere of Enceladus. We will compare the size distribution and morphology of the identified craters to the general population (Bray et al., 2007) to see if any crater factors affect the observed reorientation.

Dione: Most of Dione's surface is heavily cratered. However, Cassini images have revealed that the ambiguous "wispy terrain" is actually composed of tectonic fractures (Wagner et al., 2006). We have made a preliminary map of these fractures (figure 3)

Figure 1: Three impact craters on the anti-Saturn hemisphere imaged during the 04EN close approach. All three have been disrupted by tectonics and the tectonic features deflect across the crater. Panel b shows graben occurring in perpendicular sets while panel c shows nearly radial defection of the fractures. In all cases, the craters remain circular throughout the deformation.

Figure 2: An example crater showing the mapping of fractures and the crater rim. Points along the crater rim are marked and a circle is fit to the points. Points along each fracture are marked and a line is fit to each. The angle of each fracture to both the radial direction and the regional fractures is calculated.

and have noticed that most of Dione's tectonics lie along two great circles. When the tectonic fractures in the wispy terrain interact with impact features, the crater's morphology is altered by the fracture. In several cases, the crater is split and extended in a way similar to interactions observed on Venus (Solomon et al., 1992; Rathbun et al., 1999) and Ganymede (Pappalardo and Collins, 2005). In these cases, the extension across the fracture can be derived by measuring the elongation of the impact crater's rim. We will present results of these measurements and estimates of the regional strain based on the measured extension. We will further test if the different tectonic sets affect the amount of extension or strain observed.

References:

Bray, V.J., D.E. Smith, E.P. Turtle, J.E. Perry, J.A. Rathbun, A.N. Barnash, P. Helfenstein, C.C. Porco (2007) Impact crater morphology variations on Enceladus, LPSC, 38, abs. 1873.

Pappalardo, R.T., and G.C. Collins (2005) Strained craters on Ganymede, J. Structural Geology, 27, 827-838.

Rathbun, J.A., D.M. Janes, S.W. Squyres (1999) Formation of Beta Region, Venus: Results from measuring strain, J. Geophys. Res., 104, 1917-1927.

Rathbun, J.A., E.P. Turtle, P. Helfenstein, S.W. Squyres, P. Thomas, J. Veverka, T. Denk, G. Neukum, T. Roatsch, R. Wagner, J. Perry, D. Smith, T.V. Johnson, C.C. Porco (2005) Enceladus' global geology as seen by Cassini ISS. Eos Trans. AGU, Fall Meet. Suppl., Abstract P32A-03.

Solomon, S.C., S.E. Smrekar, D.L. Bindschadler, R.E. Grimm, W.M. Kaula, G.E. McGill, R.J. Phillips, R.S. Saunders, G. Schubert, S.W. Squyres, E.R. Stofan (1992) Venus tectonics: An overview of Magellan observations, J. Geophys. Res., 97, 13,199-13,255.

Turtle, E. P. and H. J. Melosh. (1997) Stress and flexural modeling of the Martian lithospheric response to Alba Patera, Icarus, 126, 197-211.

Wagner, R., G. Neukum, B. Giese, T. Roatsch, U. Wolf, T. Denk, and the Cassini ISS team (2006) Geology, ages, and topography of Saturn's satellite Dione observed by the Cassini ISS camera. LPSC, 37, abs. 1805.
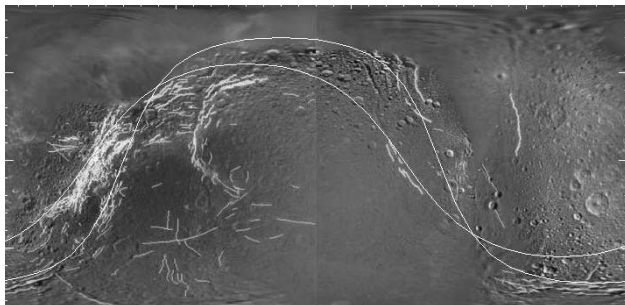
Figure 3: Cylindrical projection of a Dione global mosaic showing mapped tectonic fractures. Two great circles are superimposed which trace out the general directions of most of the tectonic features.

TITAN'S NORTH POLAR LAKES AS OBSERVED BY CASSINI RADAR: AN UPDATE. K. L. Mitchell[1], S. D. Wall[1], E. R. Stofan[2], R. M. C. Lopes[1], M. Janssen[1], B. Stiles[1], P. Paillou[3], G. Mitri[1], J. Lunine[4], S. J. Ostro[1], R. D. Lorenz[5], T. G. Farr[1], R. L. Kirk[6], J. Radebaugh[7] and the Cassini Radar Science Team. [1]Jet Propulsion Laboratory, Mail Stop 183-601, 4800 Oak Grove Dr., Pasadena, CA 91109-8099, USA <Karl.L.Mitchell@jpl.nasa.gov>. [2]Proxemy Research Inc., Laytonsville, MD. [3]OASU, UMR 5804, 33270 Floirac, France. [4]Lunar and Planetary Lab, Univ. Arizona, Tucson, AZ. [5]Space Dept., Johns Hopkins Univ. Applied Physics Lab, Laurel, MD. [6]USGS Flagstaff, Flagstaff, AZ. [7]Brigham Young University, Dept. of Geological Sci., Provo, UT.

Introduction: The north-polar lakes of Titan [1] are among the most spectacular discoveries by Cassini to date. Their anomalously radar-dark appearance is consistent with expectations for radar backscatter properties of lossy liquid hydrocarbons (methane and/or ethane, possibly with nitrogen), the presence of which was predicted by previous workers [2]. Furthermore, their areal coverage and location are consistent suggestions [3] that 0.2 – 2% high-latitude lake coverage would be sufficient to buffer atmospheric methane against photolysis, negating the need for continuous resupply by e.g. volcanism. Here we describe SAR observations over 7 north polar fly-bys, and discuss our attempts to understand the current state of the lakes, especially the meaning of coherent radar backscatter variations both within and between lakes.

Morphology and distribution: About 70% of the region polewards of 65 N has been imaged with a total of 7 SAR and 2 Hi-SAR scenes (Fig. 1). Of this, we map ~15% as lakes. On the assumption that the distribution is homogeneous, and similar in the southern hemisphere, we expect the final lake coverage of Titan to be within the 0.2 – 2% range. The first three fly-bys (T16, T18 & T19) revealed lakes exhibiting a range of morphologies, some in steep-sided depressions similar in appearance to volcanic crater lakes, glacial lakes or massive dolines (sinkholes), and others consistent with dammed lakes (e.g. Lake Powell) or submergent coastlines (rias), and the interpretation of these different morphologies has been a matter of some debate (e.g. [4,5]). The most recent data (T25, T28, T29 and T30) revealed even more variety, most strikingly the massive "great lakes", with surface areas of 10,000s of km^2 comparable with those of North America, and greater in terms of fractional coverage of the planet. The largest of these are greater in extent than any terrestrial lakes, leading to our informal use of the word "sea".

On-going mapping efforts have revealed that lakes of a given morphological class often appear in clusters, with steep-sided small lakes more often appearing at the lower latitudes. Many lakes are seen to be fed by channels, some short and stubby, indicating intersection with subsurface liquid methane reservoirs (equivalent to aquifer or water table), others long and sinuous, probably indicating that they are fed pluvially or via

artesian springs. This plethora of landforms suggests a dynamic system of liquid hydrocarbons, equivalent to terrestrial hydrologic system (informally we use the expression "methanologic"), underlain by variable surface materials [1,6,7].

Fig. 1: Polar stereographic projection (65 – 90 N) of Cassini SAR imagery, consisting of imagery obtained during T16, 18, 19, 25, 28, 29 and 30 fly-bys. Longitude given in non-standard degrees E.

Present-day state: While the interpretation of the extremely radar-dark patches as currently active (liquid) lakes remains the favored hypothesis, it has not been possible to completely rule out that we are merely seeing residues or some sort: muds, evaporites, or similar. We have argued previously [6] against the non-liquid interpretation for some, if not most, of the observed lakes. Besides the consistency with predictions based on present-day methane humidity [3], there is a broad range of observations and measurements consistent with models of lossy liquid hydrocarbons over a solid substrate, and although solids could not be completely ruled out, the characteristic properties would be extremely constrained, although not necessarily impossible. Furthermore, observations of some features, appearing morphologically similar to the small, steep-sided lakes, but in terms of backscatter properties similar to their surrounds, are best explained

as drained lakes containing little-to-no radar dark residues, which seems at odds with a radar-dark-residue hypothesis.
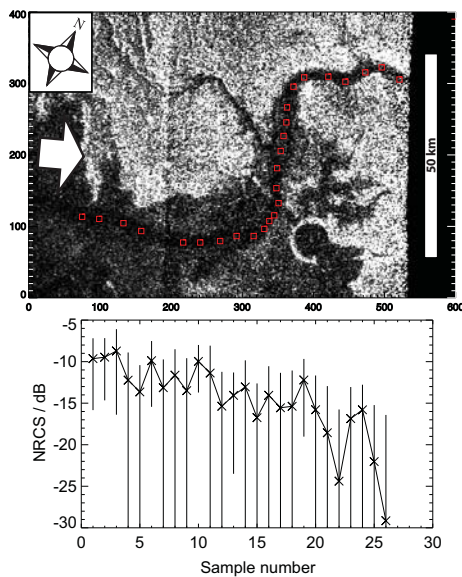
Fig. 2: Channel extending into the body of a lake (T29 fly-by). (top) Noise-subtracted SAR image, centred on 82.9N, 242W, with sampling sites (box sizes not representative of sampling areas). (bottom) Results of sampling 5x5 pixels, given in dB, numbers are from 1 (upstream, right of image) to 26 (downstream, left of image). Error is limited by the noise floor in some cases.
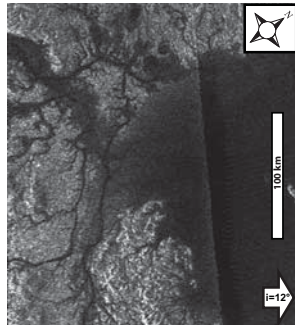
Fig. 3: Methanologically-complex region on the southern shore of "the Black Sea", centred on 75.7N, 260W, including east-to-west narrow rivers, and an approximately perpendicular north-south broad channel.

However, this light-dark dichotomy is not clear-cut for all the lakes. In many cases, there are variations in brightness both within and between lakes that are clearly not the result of noise or incidence-angle effects. This was expected; If methane is has a small loss tangent, the radar backscatter should decrease with increasing depth of liquid. Unfortunately, the loss tangent of the candidate liquids is poorly constrained. We might expect to be able to see through a few to many tens of metres before reaching the RADAR noise floor, but we cannot say more precisely than this at present, even if we assume no wind effects or "floaters". What

we perhaps did not expect to observe was that some of the lakes contained features consistent with "methanologic" structures; what appears to be intra-lake channels, usually continuations of other channel systems (e.g. fig. 2 top). The appearance is somewhat reminiscent of tidal flats, leading to renewed suggestions that we might be looking at some sort of dry or wet radar-dark solid residues; perhaps hydrocarbons or nitriles. More intriguing still are intra-lake channels that appear to cross each other (fig. 3).

Intra-lake channel analysis: In order to test the idea that some of the lakes might contain, or even be, something akin to tidal or mud-flats, we predicted that, if a channel extending into a lake body became progressively more radar-dark, this is consistent with a subaqueous system in which we were seeing an old channel through progressively greater depths of liquid. If instead the backscatter remained more-or-less constant, then this is more consistent with a channel incised into a present-day solid surface. The results of our test on only one channel (most are too small or noisy to present reliable statistics) are presented (fig. 2 bottom). Note that the incidence angle decreases slightly from right-to-left, meaning that we would expect, all things being equal, for channel materials to become systematically brighter downstream. Instead, the opposite is observed, clearly supporting the present-day-liquid hypothesis.

Discussion: So, what are we to make of the case in which the channels seem to cross one another? One explanation could be that, when the lake level reaches a critical threshold, it overflows into another, outside of the imaged area. The narrower channels are deeply incised rivers that are only active when local liquid levels are low. As liquid levels increase, these channels become submerged. As they increase further, the lake overflows into an adjacent regions, resulting in the broader of the channels which would therefore be more consistent with catastrophic flood plains, such as in the Channeled Scablands, USA. Clearly this is an untested model, but it is at least a coherent explanation as to how perpendicular channels might be established.

Although no single observation is completely unambiguous, the body of evidence supporting the present-day-liquid hypothesis is now overwhelming. In future work, we will refine our understanding of the dielectric properties of candidate lake materials in the laboratory, and use these to attempt to quantify lake depths based on multi-incidence angle SAR images.

References: [1] Stofan E. R. et al. (2007) *Nature, 445,* 61. [2] Lunine J. I. et al. (1983) *Science, 222,* 1229. [3] Mitri G. et al. (2007) *Icarus, 186,* 385. [4] Wood C. et al. (2007) *LPS XXXVIII,* Abstract #1454. [5] Mitchell K. L. et al. (2007a) *LPS XXXVIII,* Abstract #2064. [6] Mitchell K. L. et al. (2007b) *LPS XXXVIII,* Abstract #2081. [7] Mitchell K. L. et al. (in prep.).

THERMAL CONVECTION IN THE ICE-I SHELLS OF TITAN AND ENCELADUS. G. Mitri[1] and A. P. Showman[2], [1] Jet Propulsion Laboratory, California Institute of Technology (Giuseppe.Mitri@jpl.nasa.gov), [2] Department of Planetary Sciences and Lunar and Planetary Laboratory, University of Arizona.

Introduction: Cassini-Huygens observations have shown that Titan and Enceladus are geologically active icy satellites [1,2,3]. Titan should be partially differentiated into a rocky interior and an outer water layer [e.g., 4,5]. Accretion and differentiation probably caused widespread melting (at least in the outer layers), which would release ammonia and other trapped volatiles into the liquid layer [6,7].

Enceladus exhibits a complex tectonic history, with both extensional and compressional geologic features and a variety of surface ages that suggest a multi-billion-year tectonic history [8,9]. Enceladus appears to be hydrostatically relaxed and could be a differentiated body [10,11], although debate exists [e.g., 2]. The Cassini Ion and Neutral Mass Spectrometer (INMS) did not detect ammonia in the plume and obtained an upper limit ammonia abundance of 0.5% [12]. However, the plume reservoir may reside relatively close to the surface, and the ammonia abundance in the deep interior could well be greater.

At the critical Rayleigh number Ra_{cr}, convection jumps into a finite-amplitude state for a fluid with strongly temperature-dependent viscosity [13,14]. In our previous work [13], we have shown that for the ice shell of Europa, the conductive-convective transition produces radial expansion of a cooling ice shell. The rapidity of these switches implies that the stress build up, hence extensive fractures, could occur.

We explore the hypothesis for Titan and Enceladus that in the presence of an internal ocean, a conductive-convective transition of the ice-I shell can produce geological activity. To reach this objective, we perform numerical simulations of thermal convection with ConMan code for the ice-I shells, with Newtonian rheology and temperature-dependent viscosity. We assume that each satellite is differentiated into an outer ice/water layer overlying a silicate core. We further assume that each body contains an internal liquid-water ocean. This assumption is reasonably plausible for Titan [4,5], but less certain for Enceladus.

Results and Discussion: The results of our numerical simulations show that thermal convection in stagnant lid regime can occur in the ice-I shells of Titan and Enceladus under a range of conditions. Because of Rayleigh number Ra dependence on δ^3 / η_b where δ is the thickness of the ice shell and η_b is the viscosity at the base of the ice shell, and because the ammonia in the liquid layer strongly depresses the melting temperature of the ice, Ra equals its critical

value (~$3 \cdot 10^6$) at two critical thicknesses: for a relatively thin ice shell ($\delta_{cr,I}$) with a warm, low-viscosity base (Onset I) and for a thick ice shell ($\delta_{cr,II}$) with a cold, high-viscosity base (Onset II). Figs. 1 and 2 summarize the results of our numerical simulations on the thermal state of the ice-I shells on Titan and Enceladus, respectively. The models in Figs. 1 and 2 assumes a reference viscosity $\eta_0 = 10^{13}$ Pa s at 273 K. The basal temperature of the ice shell equals the sub-surface ocean temperature (left vertical axes). The right vertical axes give the basal viscosity of the ice shell. The solid lines show the heat flux (tidal and radiogenic) from the interior of the satellite in 10^{-3} W m^{-2}. We plot in dashed-dotted lines the critical Rayleigh number: the heat flux is transported by thermal conduction in the overhanging part of the plot (grey area) and by thermal convection in the underlying (white area). The dotted lines show the Rayleigh number $Ra_{tr} = 1 \cdot 10^8$ corresponding to a transition in the convective regime; see [13,14] for discussion.
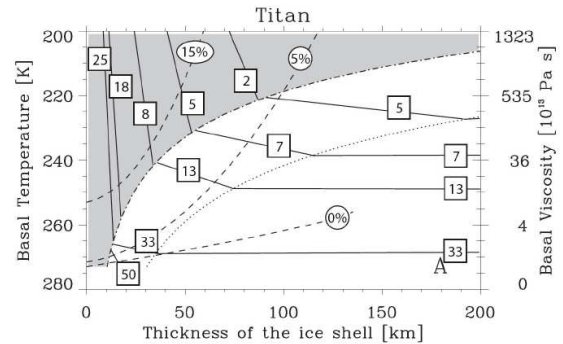
Figure 1. *Thermal state of the Titan ice-I shell. See the text.*

The dashed curves in Figs. 1-2 show the locus of basal temperatures/viscosities, heat fluxes, and ice-shell thicknesses for a specified initial ammonia-water concentration (0%, 5% and 15% for Titan in Fig. 1 and 0%, 1%, 2%, 3%, 4% and 5% for Enceladus in Fig. 2). Therefore, each point along a dashed line represents a possible state of the ice shell for that initial ammonia-water concentration. For a given mass of total ammonia, the system must remain along the relevant dashed curve as the heat flux changes. The dashed curves therefore correspond to evolutionary trajectories. There are several key points. First, small variations of ammonia concentration change drastically the thermal state of the ice shell. Second, the Onset-I transition implies that two solutions exist for a range of heat fluxes. As described in [13], this can

induce large and rapid changes in the ice-shell thickness, with consequences for surface tectonics. Third, because the addition of ammonia causes a decrease in Rayleigh number at large thicknesses, a qualitatively new convective-conductive transition occurs. This transition therefore differs qualitatively from Onset I because, at Onset II, *no steady-state solutions exist* for a range of fluxes (e.g. 0.0025 - 0.005 W m^{-2} for Titan with 5% initial ammonia concentration and $\eta_0 = 10^{13}$ Pa s). At heat fluxes within this range, the system would be forced to episodically oscillate between convective and conductive regimes on either side of Onset II over a timescale comparable to the thermal diffusion time, which is ~300 Myr for a 100-km-thick ice shell. During the oscillations, the ice-I shell would change in thickness. The oscillations between conduction and convection at Onset II could therefore have implications for surface tectonics.
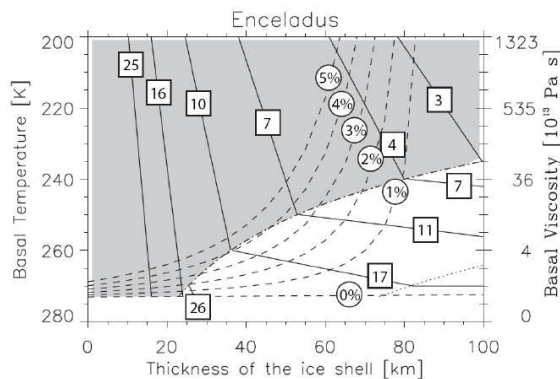
Figure 2. *Thermal state of the Enceladus ice shell. See text.*

For Enceladus, at Onset II, these arguments imply modest satellite expansion as the system oscillates from convective to conductive and satellite contraction as the system returns from conductive to convective. (The situation is more complex at Titan, because modest ice-I shell thickness changes caused by Onset-II oscillations may induce modest oscillations in the thickness of high-pressure ice phases, which cause a volume change counteracting that of thickness changes in the ice-I shell.) These effects would lead to surface strains, perhaps reaching ~10^{-3}, with associated elastic stresses of ~100 bars (which would alternate in sign from one part of the oscillation to another). Repeated oscillations around Onset II could therefore generate surface fractures and deformation, which could be either extensional or compressional depending on whether they formed during the conductive-to-convective or convective-to-conductive phase of the oscillation.

We emphasize that, for plausible ammonia abundances, the range of heat fluxes necessary for the sys-

tem to encounter Onset I and/or Onset II are within the plausible range of heat fluxes that could have occurred on Titan and Enceladus. For Titan, the expected radiogenic heating (assuming chondritic radionuclide abundances in the rocky portion) ranged from ~0.04 W m^{-2} early in solar system history to ~0.003 W m^{-2} today; tidal heating could have increased these fluxes by a modest amount. For Enceladus, the radiogenic heating flux is over an order of magnitude lower than on Titan, but tidal heating probably makes up the difference, at least episodically [15]. The episodic nature of the resurfacing on Enceladus [8] suggests that Enceladus' heat flux may have varied in time, perhaps by a large factor. Thus, given the probable variation of heat flux over time on Titan and Enceladus, it is quite plausible that these satellites encountered Onset I and/or Onset II during their histories.

High-pressure ice polymorphs (with a mean density of ~1300 kg m^{-3}) could exist on Titan between the ocean and the rocky interior. During the cooling of the planet, the radial expansion of the ice-I layer is, in general, counterbalanced by the radial contraction of the ice high pressure layer. Therefore, a global contraction of Titan could occur during its cooling. The radial contraction of Titan could build compressive surface structures. Enceladus lacks a high-pressure ice polymorph layer. We computed the stress during the radial expansion due to the Onset I as function of the ice shell temperature using the flow law of a Maxwellian viscoelastic body. The Onset I of Enceladus ice shell floating on an ocean produces tectonic stress of ~500 bars and fractures of few tens of km depth. The expected increase in surface area is 2·10^4 km^2; extensional fractures, graben formation, and perhaps necking instabilities could occur, helping to explain Enceladus' rifted terrain [8].

References: [1] Elachi et al. (2006) *Nature 441*, 709-713. [2] Porco et al. (2006) *Science 311*, 1393-1401. [3] Spencer et al. (2006) *Science 311*, 1401-1405. [4] Grasset et al. (2000) *Planet. Space Sci. 48*, 617-636. [5] Tobie et al. (2006) *Nature 440*, 61-64. [6] Lunine et al. (1983) *Science 222*, 1229. [7] Mousis et al. (2002) *Icarus 156*, 162-175. [8] Kargel and Pozio (1996) *Icarus 119*, 385-404. [9] Squyres et al. (1983) *Icarus 53*, 319. [10] Dermott and Thomas (1994) *Icarus 109*, 241-257. [11] Schubert (2007) *Icarus*, in press. [12] Waite et al. (2006) *Science 311*, 1419-1422. [13] Mitri and Showman (2005) *Icarus 177*, 447-460. [14] McKinnon, (2006) *Icarus 183*, 435-450. [15] Wisdom (2004) *Astron.l J. 128*, 484-491.

EROSION AND REGOLITH ON OUTER SOLAR SYSTEM SATELLITES.

Jeffrey M. Moore (NASA ARC, MS 245-3, Moffett Field, CA 94035, jeff.moore@nasa.gov).

Mass movement and landform degradation reduces topographic relief by moving surface materials to a lower gravitational potential. In addition to the obvious role of gravity, abrasive mechanical erosion plays a role, often in combination with the lowering of cohesion, which allows disaggregation of the relief-forming material. The identification of specific landform types associated with mass movement and landform degradation provides information about local sediment particle size and abundance and transportation processes. Generally, mass movements can be classified in terms of the particle sizes of the transported material and the speed the material moved during transport. Most degradation on outer planet satellites appears consistent with sliding or slumping, impact erosion, and regolith evolution. Some satellites, such as Callisto and perhaps Hyperion and Iapetus, have an appearance that implies that some additional process is at work, most likely sublimation-driven landform modification and mass wasting. A variant on this process is thermally driven frost segregation as seen on all three icy Galilean satellites and perhaps elsewhere. Titan is unique among outer planet satellites in that Aeolian and fluvial processes also operate to erode, transport, and deposit material.

IO'S SURFACE AND SO$_2$ ATMOSPHERE: FIRST DISK-RESOLVED MILLIMETRIC OBSERVATIONS

A. Moullet[1], E. Lellouch[1], R.Moreno[1], M.Gurwell[2], C.Moore[3]   [1]LESIA-Observatoire de Paris, 5 place J.Janssen 92195 Meudon, France   [2]CFA-Smithsonian institute, 60 Garden Street, Cambrige MA 02138, USA [3]The University of Texas at Austin, Austin, TX 78712, USA

Introduction: Io has a very tenuous atmosphere mainly composed of SO$_2$, which exhibits high spatial variability [1]. First interpretation of SO$_2$ disk-averaged lines at millimeter wavelengths suggested a very hot (250-700 K) and localized atmosphere (5-20 % of the surface) [2]. We report on the first disk-resolved millimeter-wave observations of Io's SO$_2$ atmosphere and continuum emission at 1.3mm, obtained with IRAM-Plateau de Bure interferometer (PdBI) [1].

Mapping of the SO$_2$ emission is needed to disentangle between temperature, distribution and dynamical effects. The ultimate goal is to distinguish between volcanic outgassing and SO$_2$ frost sublimation equilibrium as possible gas replenishment mechanisms .

Observations : Leading and trailing hemispheres were observed on January 28 and February, 2005. PdBI (6 antennas of 15m diameter) was employed in its then most extended configuration, producing a 0.5x1.5 arcsec HPHW synthetized beam: Io (1 arcsec) was resolved in its longitudinal direction. The target line was the SO$_2$ rotational line at 216.643 GHz and the spectral resolution was 40 kHz, adequate to resolve the 0.6 MHz line width. Continuum emission at 1.3 mm was observed in a broad 320 MHz band.

Continuum analysis: Total flux measurements of continuum emission indicate brightness temperatures of 93 K on the leading side and 99 K on the trailing side, which is significantly lower than surface temperatures [3]. The temperature difference between the two sides reflects the albedo changes.

On the trailing side, zero-point position of UV-plane visibilities is measured (Fig 1.). Best fit is obtained for a uniform brightness temperature. According to the thermal model proposed in [4], it implies very low variations of physical temperature and emissivity with solar zenith and emission angles, that constrain surface dielectric constant to low values (e<1.2). All

these results strongly suggest that we are actually measuring subsurface thermal emission.
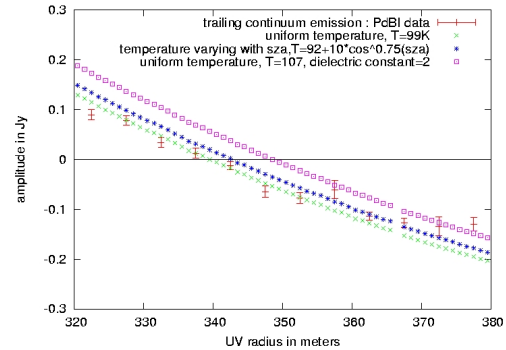
Fig. 1 : Trailing side continuum visibilities real-part around zero-point, plotted against temperature/emissivity models .
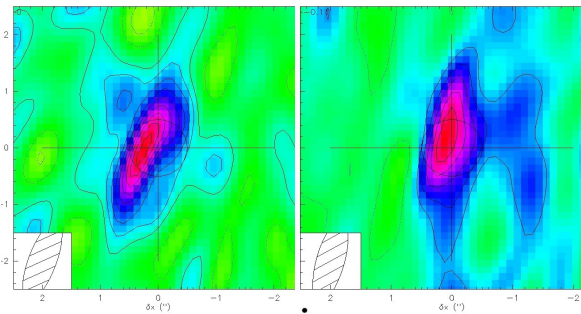
Fig. 2 : Interferometric maps of SO$_2$ emission at 216 GHz integrated over 600 kHz. Left: leading side, Right : trailing

Line data analysis : UV-plane analysis of the SO$_2$ emission maps integrated over the line width (Fig. 2) shows that:

- the emission region is marginally narrower than continuum: resolved size is 0.85($\pm$0.2) arcsec on the leading, and 0.55($\pm$0.2) arcsec on the trailing (40% and 70% of the disk, broader than previous estimates)
- the emission maximum is displaced (at 2 σ) to the (sky)-East with respect to continuum.

On the leading side, resolved spectra could be retrieved with enough S/N. This provides the first observational constraint on gas dynamics, showing:
- a Doppler shift gradient (Fig. 3) in the prograde direction with a 0.4$\pm$0.1 km/s limb-to-limb shift differ-

ence, and ~0.1 km/s redshift at central longitude
- high variations of the line width from 300 to 700 m/s
over the disk.
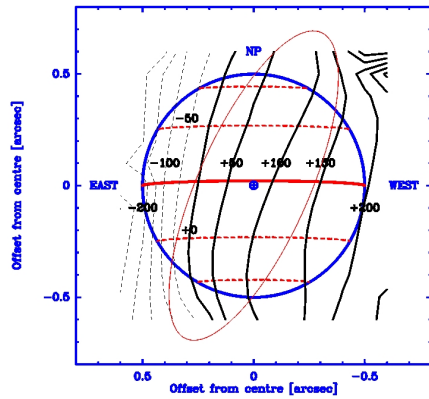
Fig. 3 : Doppler-shifts of the 216 GHz SO$_2$ line measured
over Io's disk. Unit is m/s.

Hydrostatic interpretation: Data was interpreted
through a radiative transfer model, assuming an hy-
drostatic atmosphere in LTE conditions, which is real-
istic for a sublimation-driven atmosphere.
Two SO$_2$ distribution models were tested :
- one based on HST spatially resolved data [5]
- one based on IR-disk-averaged spectra [3], more lo-
calized and with higher column densities than [5]
Column densities being fixed, free parameters are gas
temperature and dynamics. We find that SO$_2$ distribu-
tion model from [5] reproduces quite well data emis-
sion maps shapes, though the column densities pro-
posed appear ~ 30% too low to explain total flux.
The SO$_2$ line obtained on the leading side at PdBI is
fitted together with disk-integrated lines obtained in
1999 with IRAM-30m antenna (Fig. 4). Best fits of
SO$_2$ lines are obtained with atmospheric temperature
between 150-230 K, much colder than previous esti-
mations. A dynamic effect is also needed to explain
the line-width, such as a zonal wind. Low Doppler-
shifts of the disk-integrated data exclude a day-to-
night flow (typical for a sublimation-driven atmo-
sphere), then a prograde wind about 230±50 m/s wind
is preferred. This wind also reproduces the measured
Doppler-shift limb-to-limb difference (Fig. 3), but
with no red-shift at central longitude, and no variation
of the line-width across the disk.
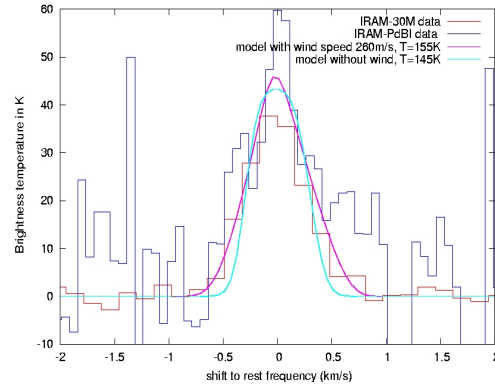
Fig. 4: IRAM PdBI and IRAM-30M SO$_2$ lines at 216 Ghz
with hydrostatic models from distribution model [3]

Volcanic interpretation: We used the DSMC mod-
els from [6] to describe volcanic plumes in terms of
column density, temperature and dynamics, and the
resulting SO$_2$ line emission. First calculations show
that the particles falling from the plume produce high
Doppler-shifts, whose sign depends on the plume posi-
tion. The presence of a sublimation layer over which
particles bounce lowers this effect. Based on known
plume positions, emission maps show that more gas is
needed to reproduce total flux and emission shape, as
well as the high redshift measured at western limb.

Conclusions: Interpretation of data through hydro-
static models is only partially satisfying : the distribu-
tions models can explain observed line flux, line
width, and emission shape, but the superrotating wind
hypothesis is not consistent with the red-shift observed
at central longitudes, and variations of the line-width
are not reproduced. Volcanic models can help this. A
sublimation layer should be still present to explain the
total emission flux, the emission shape and the recess-
ing wind at western limb. Further calculations will
help better constraining the contribution of each gas
source.

References: [1] Mc Grath M.A. et al. (2004) *in
Jupiter. The Planet, Satellites and Magnetosphere*,
457-483. [2] Lellouch E. (1996) *Icarus* 124, 1-21. [3]
Spencer J.R. et al. (2005) *Icarus* 176, 283-304. [4]
Wong M.C. And Smyth W.H. (2000) *Icarus* 146, 60-
74. [5] Feaga L. (2006) private communication. [6]
Zhang J. et al. (2003) *Icarus* 163, 182-197.

SHEAR HEATING IN THE OUTER SOLAR SYSTEM. F. Nimmo, J.H. Roberts, *Dept. Earth & Planetary Sciences, U.C. Santa Cruz, Santa Cruz CA 95064 (fnimmo@es.ucsc.edu)*, J.R. Spencer, *Dept. Space Studies, SWRI, Boulder CO 80302*, R.T. Pappalardo, *Jet Propulsion Laboratory, M/S 183-301, Pasadena CA 91109*, L.M. Prockter, *Applied Physics Laboratory, Laurel, MD 20723*, M.E. Mullen, *Dept. Astrophysics & Space Phys., U. Colorado, Boulder CO 80309.*

Strike-slip motion is predicted to be a consequence of diurnal tidal stresses [1], and strike-slip offsets are ubiquitous on Europa [2]. For satellites with low rigidities, non-zero eccentricities and short orbital timescales, strike-slip motion is expected to be relatively rapid and can thus lead to heating through friction or viscous dissipation [3]. Here I will review three consequences of shear heating: 1) double ridge formation; 2) vapour production on Enceladus and Europa; 3) its effect on convection.

Double Ridge Formation

Double ridges are a ubiquitous tectonic feature on Europa [4], and similar features, though at a larger horizontal scale, are also observed on Triton [5] (Fig 1). Shear heating leads to locally elevated temperatures in the subsurface, which could cause elevated topography along the shear zones. However, this topography would decay due to thermal diffusion unless shear heating was continuous. Thus, to maintain long-term topography requires either a permanent density contrast (e.g. due to melting and removal of dense salts [3,6]), or viscous upwelling which then gets frozen in as heating ceases [7]. The central trough of double ridges might be caused by melt drainage downwards and subsequent compaction of the overlying ice [3].

Vapour production

If heated ice is exposed directly to a vacuum, then sublimation and vapour production, rather than melting, will result. Thus, whether melting or vapour production occurs depends on the porosity and permeability of the subsurface ice, which in turn depends on pressure and temperature. In the case of Enceladus, it has been suggested [8] that shear heating is responsible for the vapour plumes [9] and high heat fluxes [10] observed at the south pole. An important consequence is that the majority of the heat observed is being advected by vapour which then recondenses in the near-subsurface [11]. Thus, in this case the permeability and porosity structure of the near-surface ice play a major role in the surface observables.

Since shear heating is inferred to have been important at both Europa and Enceladus, an important question is whether Europa might also be generating vapour plumes. The main differences between Europa and Enceladus are that the former has a higher surface temperature, higher gravity and likely a lower shear velocity. Figure 2 shows the output from a model identical to that in [8] except for these three parameters. It results in a brittle layer thickness of 2.4 km, a maximum subsurface temperature anomaly of 32 K and a total vapour production rate of 1 kg/s per km. The weighted vapour temperature is 137 K, resulting in a thermal velocity (0.44 km/s) much less than the escape velocity (2 km/s). Vapour which escapes the subsurface would thus rise ~70 km above the surface before falling back, potentially generating detectable surface albedo

features [12]. Vapour which instead recondenses in the near subsurface in a region 5 km wide would result in a surface temperature increase of 1.7 K, probably too small to be detectable with *Galileo* instruments.

The largest unknown affecting these results is the permeability structure of the subsurface ice on Europa, because it controls the degree to which vapour produced in the subsurface is mobile.

Effect on convection

Just as the insulating terrestrial continents have an effect on mantle convection [13], one might anticipate that a zone of near-surface shear heating affects convection in the underlying ice shell [7]. Figures 3 and 4 show the results from two Citcom [14] models of a tidally-heated convecting ice shell appropriate to Enceladus. Figure 3 shows the local tidal heating and Figure 4 the accompanying temperature structure. In each case the right hand panels include a shallow, near-surface zone of heat production similar to that inferred to be operating at Enceladus.

Even though the extra south polar heating is confined to shallow levels, it is clear that the deeper temperature structure is profoundly affected. The figures show that the stagnant lid is significantly thinned, there is an enlarged hot spot beneath the South pole, and the temperatures achieved suggest that local melting may be taking place [cf. 15].

Near-surface heating can thus affect deeper convection. Furthermore, the scenario shown here may help to explain the polar location of the hotspot on Enceladus [16]: a low-density diapir of the kind shown can cause reorientation. Alternatively, drainage of melt-water could result in subsidence and a subsurface sea [17]. Thus, near-surface shear heating can affect the global dynamics of icy satellites.

References

[1] Hoppa, G., et al. *Icarus* 141, 287-298, 1999.   [2] Hoppa, G. et al. *JGR* 105, 22617-22627, 2000.   [3] Nimmo, F. and E. Gaidos, *JGR* 107, 5021, 2002.   [4] Head, J.W. et al. *JGR* 104, 24223-24236, 1999.   [5] Prockter, L.M. et al., *GRL* 32, L14202, 2005.   [6] Pappalardo, R.T. and A.C. Barr, *GRL* 31, L01701, 2004.   [7] Han, L. and A.P. Showman, *LPSC* XXXVIII, 2277, 2007.   [8] Nimmo, F. et al., *Nature* in press. [9] Porco, C.C. et al., *Science* 311, 1393-1401, 2006.   [10] Spencer, J.R. et al., *Science* 311, 1401-1405, 2006.   [11] Kieffer, S.W. et al., *Science* 314, 1764-1766, 2006.   [12] Fagents, S.A. et al., *Icarus* 144, 54-88, 2000.   [13] Cooper, C.M. et al. *GRL* 33, L13313, 2006.   [14] Roberts, J.H. and S. Zhong, *JGR* 109, E03009, 2004.   [15] Sotin, C. et al. *GRL* 29, 1233, 2002.   [16] Nimmo, F. and R.T. Pappalardo, *Nature* 441, 614-616, 2006.   [17] Collins, G. and J.C. Goodman, *Icarus*, in press.   [18] Tobie, G. et al., *Icarus* 177, 534-549, 2005.
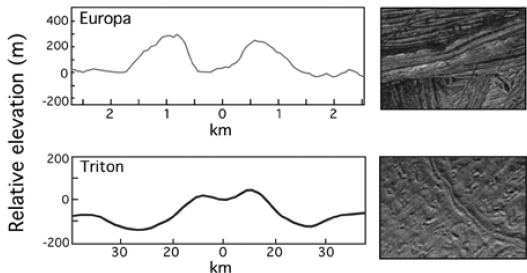
Figure 1: Topographic ridge profiles and images for Europa and Triton. From [5], Figure 2.

Local heat generation rate
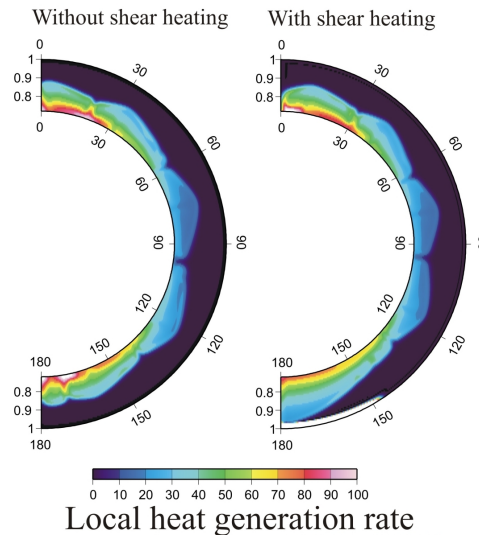
Figure 3: Laterally-averaged tidal heat generation rate in a convecting ice shell appropriate to Enceladus. Interior structure is from [16]. Tidal dissipation is calculated using approach of [18] assuming a constant ice shell viscosity of 3×10^{13} Pa s, and then modified based on the local temperature [15]. Note that no significant dissipation occurs in the stagnant lid (black). Units of heat generation are dimensionless; multiply by 1.2×10^{-8} to get $W\ m^{-3}$. Left-hand panel shows base case; right-hand panel includes a zone of shallow South polar heating. Heating is concentrated in the top 5 km and varies as $\sin^2 \theta$ south of $55°$S, where θ is latitude. Total shallow heat production is 7 GW. Note that the stagnant lid is thinned near the South pole.
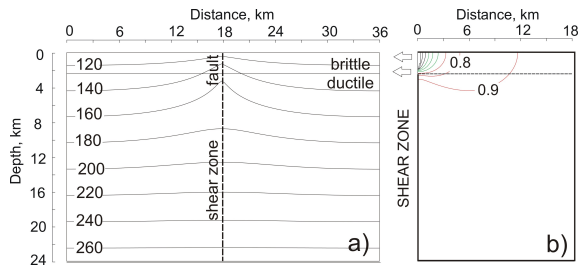
Figure 2: a) Temperature distribution due to shear heating for Europa. Model parameters are identical to Fig. 1 in [8] except $g = 1.3\ m\ s^{-2}$, shear velocity $u = 8 \times 10^{-6}\ m\ s^{-1}$ [3] and $T_s = 110$ K. Resulting vapour production rate is 1 kg/s per km of fault (α=0.1). b) Vapour density (normalized to maximum value of 2.6 $kg\ m^{-3}$ for the case in which vapour escape (arrows) only occurs laterally into shear zone.
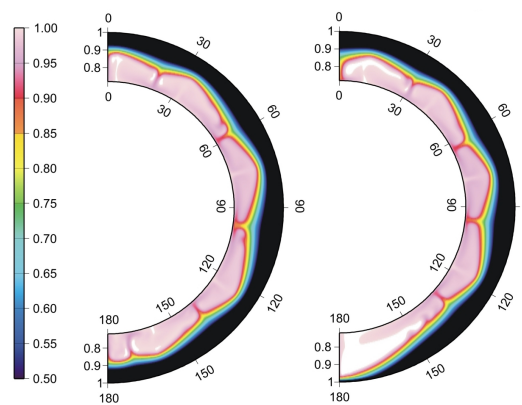
Temperature

Figure 4: As for Fig 3, except plotting dimensionless temperature. Convective calculations carried out using Citcom in 2D. Note the large temperature increase beneath the South pole in the right-hand panel.

LOKI, IO: MODEL AND OBSERVATIONS. N. A. Papapietro[1], J. A. Rathbun[1], and J. R. Spencer[2], [1]University of Redlands (1200 East Colton Ave., Redlands CA 92373, USA *jullie_rathbun@redlands.edu*), [2]Southwest Research Institute (1050 Walnut St., Suite 400, Boulder, CO 80302, USA).

Introduction: Loki is the largest and most powerful volcano on Io, the most volcanically active body in the Solar System. It is powerful enough that its eruptions can be observed in the infrared from earth-based telescopes. Measurements of Loki's activity level have been made for nearly two decades and have shown that Loki often erupts in a periodic and predictable fashion (Rathbun et al., 2002). These measurements are based on occultation light curves obtained while Io is in eclipse. Since no sunlight is reaching Io, all of the measured radiation is emitted from volcanoes. As Io passes behind Jupiter, the volcanoes disappear one at a time so their output can be measured from the resulting light curve. The light curves are measured at 3.5 microns in a methane absorption band so that Jupiter's reflected sunlight interferes as little as possible (Spencer et al., 1990). We have been making these observations at the Infrared Telescope Facility (IRTF) in Hawaii since 1992 (figure 1) with more frequency during the Galileo era (1996-2001) and the New Horizons era (2006-2007).

Loki Model: Based on the long history of Loki eruptions and the high spatial resolution data taken by the Galileo and Voyager spacecrafts, Rathbun et al. (2002) developed a model of Loki as a periodically overturning lava lake. Rathbun and Spencer (2006) constructed a quantitative version of this model and were able to match it to ground based observations taken by a variety of observers at a variety of wavelengths. This includes the 3.5 micron occultation data shown in figure 1, speckle data collected by MacIntosh et al. (2003), and adaptive optics measurements from Marchis et al. (2005). By altering the velocity at which the overturn propagates across the lava lake, the model matches the data from times when Loki was erupting periodically and those from more recent times when Loki was no longer erupting on a regular schedule. This change in velocity could easily be due to small changes in magma density or initial porosity of the solidifying crust.

Observations: While observing at the IRTF, we obtained eclipse images of Io in addition to the occultation light curves. While these 2.2 micron images have a low spatial resolution (figure 2), we can still derive Loki fluxes from them (Spencer et al., 1994). We have developed a systematic method for determining Io's flux and will present the results of these measurements and a comparison to the model described above. Io's flux is easily determined as long as the observations took place under photometric conditions. We hypothesize that Io's 2.2 micron brightness will be dominated by Loki. Since the spatial resolution is generally low (figure 2) isolating Loki's flux will be difficult. We will search the data for the best resolution images to compare Loki's brightness to the total brightness of Io to ensure this hypothesis is correct. We will also compare the temporal evolution of Loki's 2.2 micron brightness to the 3.5 micron brightness to
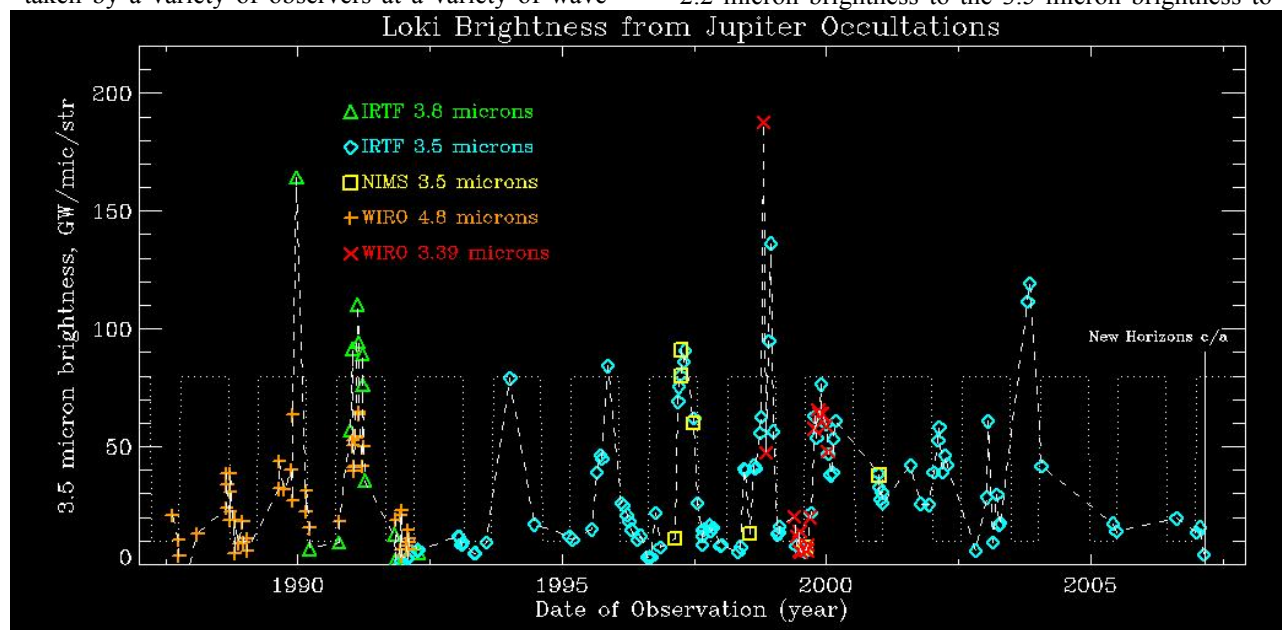
Figure 1: 3.5 micron brightness of Loki measured primarily from Jupiter occultations observations.

determine if Loki eruptions are as easy to pick out in the lower wavelength data. Finally, we will compare the measured 2.2 micron brightnesses to the model fits.
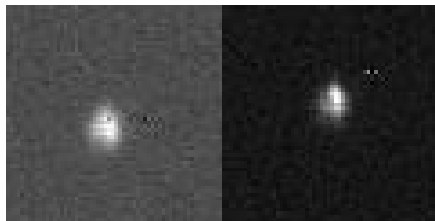
Figure 2: IRTF images of Io in eclipse on October 15, 2001. The left image was taken at 2.2 microns and the right at 3.5 microns. In both cases, Loki is the bright spot in the upper right.

Since the model was completed, more observations have taken place in support of the New Horizons mission (Rathbun et al., 2007). We were able to photometrically observe Jupiter occulting Io on four nights in 2006-2007. The data show that Loki is not currently erupting with its 3.5 micron brightness was measured to be less than 20 GW/micron/str. We will present the results of all our 2006-2007 observations and also compare them to the model. Four nights of successful observations still need to be analyzed and we also have two observing runs remaining.

References:

Howell, R. R., et al., Ground-based observations of volcanism on Io in 1999 and early 2000, *J. Geophys. Res.*, **106**, 33,129-22,139, 2001.

Macintosh, B. A., D. Gavel, S. G. Gibbard, C. E. Max, M. Eckart, I. dePater, A. M. Ghez, and J. Spencer, Speckle imaging of volcanic hotspots on Io with the Keck telescope, *Icarus*, **165**, 137– 143, 2003.

Marchis, F., et al., Keck AO survey of Io global volcanic activity between 2 and 5 mm, *Icarus*, **176**, 96– 122, 2005.

Rathbun, J. A., J. R. Spencer, A. G. Davies, R. R. Howell, and L. Wilson, Loki, Io: A periodic volcano, *Geophys. Res. Lett.*, **29**, 10.1029/2002GL014747, 2002.

Rathbun, J. A., and J. R. Spencer, Loki, Io: New ground-based observations and a model describing the change from periodic overturn, *Geophys. Res. Lett.*, **33**, 10.1029/2006GL026844, 2006.

Rathbun, J. A. and J. R. Spencer, Groundbased observations of Io in support of the New Horizons flyby, *this meeting*, 2007.

Spencer, J.R., M.A. Shure, M.E. Ressler, J.D. Goguen, W.M. Sinton, D.W. Toomey, A. Denault, and J. Westfall, Discovery of hotspots on Io using disk-resolved infrared imaging, *Nature*, **348**, 618-621, 1990.

Spencer, J.R., B.E. Clark, D. Toomey, L.M. Woodney, and W.M. Sinton, Io hot spots in 1991 - Results from Europa occultation photometry and infrared imaging, *Icarus*, **107**, 195-208, 1994.

WHERE'S THE COMPRESSION? EXPLAINING THE LACK OF CONTRACTIONAL STRUCTURES ON ICY SATELLITES. Robert T. Pappalardo[1] and Daniel M. Davis[2], [1]Jet Propulsion Laboratory, California Institute of Technology, Mail Stop 183-301, Pasadena, CA 91109, [2]Stony Brook University, Department of Geosciences, Stony Brook, NY 11794-3357.

Introduction: A longstanding question in outer planet satellite geology is: Where's the compression? Icy satellites are rich in structures interpreted as extensional-tectonic, most commonly from normal faulting [1-7]. Lanes of normal fault blocks on icy satellites can represent 10s of percent local extensional strain [4,7], but complementary contractional structures are rare. On Earth and the other terrestrial planets, contractional structures are dominated by reverse faults, most commonly as sets of thrust blocks [8]. To date, thrust blocks have been inferred only on the relatively small icy satellites, notably Dione [9] and Enceladus [10].

Here we consider issues of contractional structures on icy satellites, concluding that it is not surprising for such structures to be relatively rare, especially on larger satellites. Relevant issues include: 1) for a given vertical (overburden) stress, the differential stress required for contractional (reverse) brittle-frictional faulting is considerably greater than for extensional (normal) faulting, 2) extension leads to increased thermal gradients, so compressed regions tend to be stronger (cooler) than warmer (weaker) extended zones, 3) a very weak warm ice substrate allows contracting regions to be very broad, allowing them to accommodate large amounts of strain through creep at depth; and 4) significantly greater stress is required for brittle failure on higher gravity satellites.

Strength Envelopes: Fig. 1 illustrates the comparative lithospheric strength (absolute differential stress necessary for failure) as a function of depth, for several icy satellites with a range of surface gravities g (Ganymede, Europa, Dione, and Enceladus). Straight lines illustrate the failure strength of the pre-fractured (frictionally controlled) brittle lithosphere, assuming a friction coefficient $\mu_f = 0.69$ for pre-fractured ice with negligible cohesion [11]. Solid lines represent horizontal compression (least principal stress oriented vertically, $\sigma_3 = \rho g z$), and dashed lines are for horizontal extension (greatest principal stress oriented vertically, $\sigma_1 = \rho g z$), for lithospheric density $\rho = 1000$ kg m^{-3}. Satellite gravity significantly affects the slope of the frictional failure line. Curves of Fig. 1 illustrate the failure strength of the ductile lower lithosphere for thermal gradients of 20 and 40 K km^{-1}, and strain rates of 10^{-16}, 10^{-15}, and 10^{-14} s^{-1}. The ductile B rheology of [12] is adopted, assuming a surface temperature of 70 K (appropriate for higher latitudes on the jovian satellites, and lower latitudes on the saturnian satellites).

Lithospheric Failure Strength: It is well known that lithospheric strength is several times greater in compression than in extension. On Fig. 1, maximum lithospheric strength is approximated by the intersection of the brittle and ductile failure curves. Ganymede's lithosphere is ~3 times stronger in compression than in extension, for the same thermal gradient and strain rate. Ganymede's extensional-tectonic grooved

terrain [13] occurs in lanes typically 10s km wide representing extensional strains of 10s of percent [7], and lanes presumably formed sequentially in time. Extension is expected to create locally increased thermal gradients [14], with ~40 K km^{-1} appropriate to the formation of Ganymede's grooved terrain [13]. This thermal gradient implies a maximum lithospheric strength of ~2 MPa in extension. The extensional strain of any individual lane suggests compensation by compression elsewhere across Ganymede (unless the satellite expanded significantly during grooved terrain formation [15]). Thermal gradients in Ganymede's relatively broad, undeformed dark terrain were likely < 20 K km^{-1} [13], suggesting lithospheric strength ~11 MPa. The tendency for greater strength in compression, combined with an expected lesser thermal gradient in contracted terrains, implies that >5 times as much compressional stress is required to produce reverse faults on Ganymede compared to the extensional stress necessary to form grooved terrain normal faults. Analogous results are implied for Europa, which has a similar gravity (albeit different thermal gradients).

For small Enceladus, ~0.2 MPa differential stress permits frictional failure in extension, for a thermal gradient of 40 K km^{-1}. Analogous to Ganymede, ~6 times greater stress is necessary for reverse faulting in compression compared to the stress extension if the thermal gradient in contracted terrains is reduced by half. Nevertheless, the ~1.2 MPa stress required for reverse faultng of cool Enceladean lithosphere is relatively modest. For Dione, about twice the stress is required for failure as compared to Enceladus.

Discussion: It is difficult for an icy satellite lithosphere to fail brittlely in compression, so contractional strain must be absorbed in other ways. As suggested for the lunar megaregolith, some contractional strain can be accommodated by compaction of fracture porosity within the shallow brittle lithosphere [16, 17] and will not be apparent at the surface. At depth, porosity is reduced by pressure and temperature [18]. Where porosity has been reduced to negligible amounts, lithospheric thickening will occur instead, producing only modest topography. (Long-wavelength mullion-like structures on Europa [19,20] may be an expression of such thickening.) The thickened root will reach beneath the brittle-ductile transition, and can relax through viscous flow.

In the ductile lower lithosphere, creep occurs readily in response to compression. A warm ice substrate is very weak, without substantial basal tractions, so the compensating contracting region can be very broad [21]. Because brittle failure strength in compression is significantly greater than in extension, compression creep can proceed at greater differential stresses without inducing brittle failure; thus, the creeping strain rate in contracted regions can be significantly higher

(by 1-2 orders of magnitude) than in extended regions. Combined with the greater areal extent of contracted terrains, ~2 to 3 orders of magnitude greater creep can be accommodated compared to extended regions.

Moreover, compared to the strain rate in extended terrains, strain rate is expected to be less in the broad regions accommodating compression. While extensional strain creates localized deformation (as in Ganymede's grooved terrain), compression can be distributed across a surrounding region that is perhaps an order of magnitude greater in lateral extent; thus, compressional strain rate would be an order of magnitude less than in extension. This means that the brittle lithosphere is slightly thinner and weaker in contracted regions than might otherwise be expected, and a slightly thicker region of ductile lithosphere exists below such a region. The detailed implications of contractional creep require consideration of the grain-size sensitive creep of ice [22].

Conclusions: Sources of compressional stress sufficient for reverse faulting probably do not exist on most icy satellites. Instead, compression may result in porosity compaction within the upper brittle lithosphere, and thickening and creep in deeper, warmer regions. Contracted areas can be much broader than extended areas, so can experience greater creeping strain rates and accommodate significantly more creep. Geologically active small satellites are most likely to experience reverse faulting, as stress levels required to initiate compressional failure are relatively small. This is consistent with the inferred presence of thrust blocks on Dione and Enceladus, but not on Ganymede.
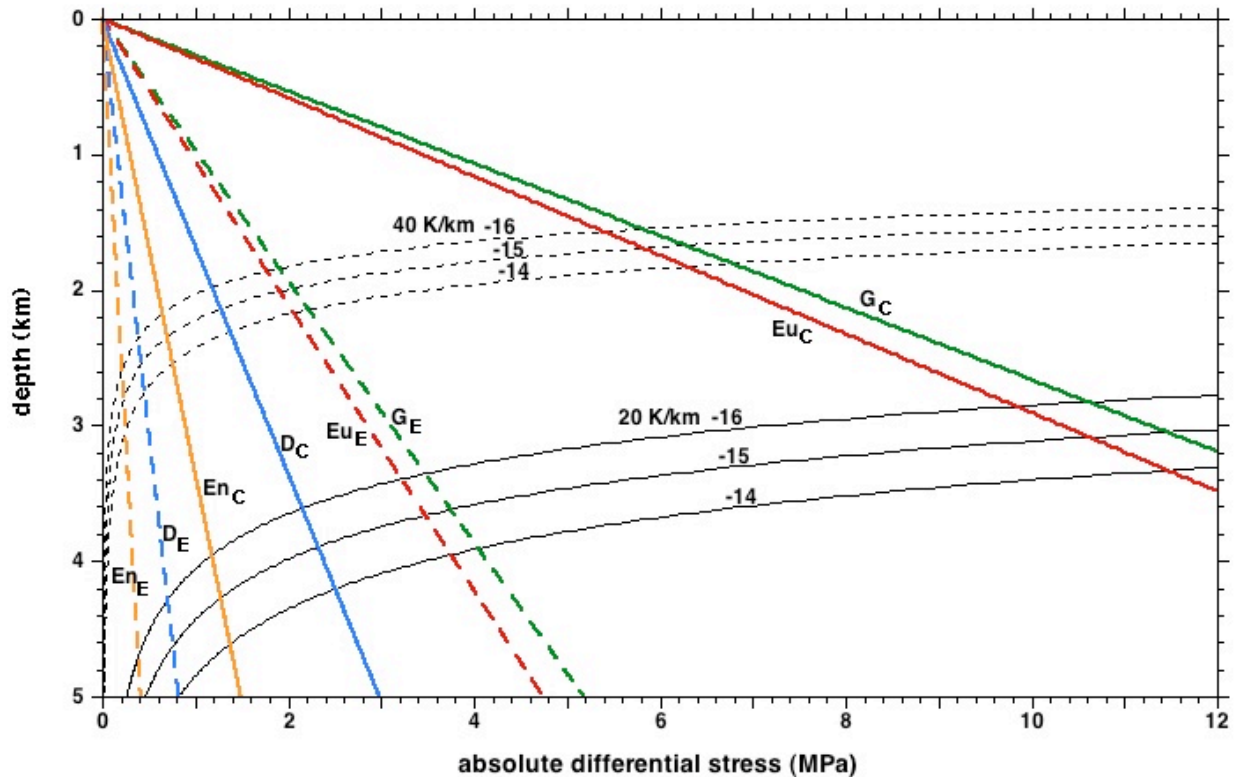
Figure 1. Icy satellite lithospheric strength in the brittle and ductile regimes, for representative satellite gravities, strain rates, and thermal gradients. G = Ganymede (green, $g = 1.43$ m s^{-2}); Eu = Europa (red, $g = 1.31$ m s^{-2}); D = Dione (blue, $g = 0.227$ m s^{-2}); and En = Enceladus (gold, $g = 0.113$ m s^{-2}). For the brittle failure lines, subscript C implies compression (solid straight lines), and subscript E implies extension (dashed straight lines). Ductile strength curves for ice use the ductile B regime of [12], a surface temperature of 70 K, and thermal gradients of 20 K km^{-1} (solid curves) and 40 K km^{-1} (dashed curves), as labeled with the log of strain rate (10^{-16}, 10^{-15}, and 10^{-14} s^{-1}).

References: [1] Squyres & Croft (1986), in *Satellites*, pp. 293-341. [2] Croft & Soderblom (1991), in *Uranus*, pp. 561-628. [3] Hillier & Squyres (1991), *JGR*, *96*, 15665-15674. [4] Pappalardo et al. (1997), *JGR, 102*, 13369-13379. [5] Pappalardo et al. (1998), *Icarus, 135, 276-302*. [6] Prockter et al. (2002), *JGR*, *107*, 10.1029/2000JE001458. [7] Pappalardo & Collins (2005), *J. Struct. Geol.*, *27*, 827-838. [8] Davis et al. (1983), *JGR*, *88*, 1153-1172. [9] Moore (1984), *Icarus*, *59*, 205-220. [10] Helfenstein et al. (2006), *LPSC XXXVII*, #2182. [11] Beeman et al. (1988), *JGR*, *93*, 7625-7633. [12] Durham et al. (1992), *JGR*, *97*, 20883-20897. [14] Nimmo (2004), *JGR*, *109*, doi:10.1029/2003 JE002168. [13] Dombard & McKinnon (2001), *Icarus*, *154*, 321-336. [15] Mueller & McKinnon (1998), *Icarus*, *76*, 437-464. [15] Clifford (1993), *JGR*, *98*, 10973-11016. [16] Binder & Gunga, *Icarus*, *63*, 421-441. [17] Pritchard & Stevenson (2000), in *Origin of the Earth and Moon*, pp. 179-196. [18] Nimmo et al. (2003), *Icarus*, *166*, 21-32. [19] Prockter & Pappalardo (2000), *Science*, *289*, 941-943. [20] Dombard & McKinnon (2006), *J. Struct. Geol.*, *28*, 2259-2269. [21] Davis & Engelder (1985), *Tectonophys*, *119*, 67-88. [22] Goldsby & Kohlstedt (2001), *JGR*, *106*, 11017-11030.

KINEMATIC ANALYSIS OF TRIPLE JUNCTIONS ON EUROPA. G. W. Patterson and J. W. Head,
Department of Geological Sciences, Brown University, Providence, RI 02912 (Gerald_Patterson@brown.edu)

Introduction: Reconstructions of preexisting linear features offset by the formation and evolution of ridges and bands on Europa suggests that its surface is locally fractured into rigid plates that have rotated with respect to each other [1-3]. One consequence of this process should be the formation of triple junctions.

A triple junction represents the intersection of three plate boundaries. In a rigid-plate environment, the motions of the plates involved in a triple junction depend on each other. There are 25 possible types of triple junctions [4], but most are unstable and cannot persist through finite rotations of the plates involved [4-6]. If the poles of rotation for each plate in a junction remain fixed over some finite interval of time, however, that junction can be described as stable.

Here, we use instantaneous velocity diagrams to analyze what appear to be three triple junctions on Europa. Two of the junctions are associated with a set of bands in the south-polar region of Europa and the third is associated with a near-equatorial band we have tentatively named Phaidra Linea. Each of these junctions represents the intersection of three extensional bands. The band-band-band configuration is ideal for analysis because the finite motions of each boundary are clearly recorded on the surface. This helps to constrain the kinematics of each junction and allows us to explicitly utilize the assumptions of plate-rigidity and fixed poles of rotation to explore their behavior.

Triple Junctions in Velocity Space: In analyzing the triple junctions we observe on Europa, we utilize the method developed by [5] of examining junctions diagrammatically in instantaneous relative velocity space. The analysis of triple junctions in velocity space has two components. The first component is a velocity circuit consisting of the relative velocity vectors for each boundary associated with the triple junction. For a three-plate system in a rigid environment, the addition of these vectors must form a closed loop. The second component is a constant frame of reference line for each velocity vector that indicates all possible solutions for the velocity of the plate boundary associated with the vector. The orientation of the reference line with respect to the vector it is associated with is dependent on the mode of deformation that vector describes (i.e., extension, compression, or strike-slip). If these reference lines intersect at a point, the triple junction can be stable over a finite time interval.

To constrain the magnitude and direction of the relative velocity vectors for each of the bands associated with a junction, we use the widths of the bands involved and the direction of offset. These components of the vector are determined by the locations of preexisting offset linear features or the intersections of the bounding ridges of a band with the other two bands in the junction. Potential errors in determining the direction and magnitude of the relative velocity vectors are represented by confidence regions surrounding the tips of the vectors. In this study, the radii of these regions are equivalent to the apparent widths of the bounding ridges of each band, since they can obscure the contact between preexisting offset features and the band and it is often not clear whether they are part of the extension process or are remnants of preexisting, strike-slip boundaries.

South Polar Region: The two junctions in this region each represent the intersection of three bands (fig. 1). Cross-cutting relationships of prominent structural features that pre- and post-date the bands that form these junctions suggest they formed coevally. This implies their formation divided the region into four plates (A, B, C, and D in fig. 2) that subsequently rotated with respect to each other.

Within the confidence regions we have established, the relative velocity vectors associated with the junction that consists of bands 1, 2, and 3 form a closed loop in velocity space (Fig. 2a). This implies that, as the bands formed, plates A, B, and C behaved rigidly in the vicinity of the junction. If we use the endmember reference line for the relative velocity vector of band 3 that represents the trend of its axial trough closest to junction, the reference lines of the vectors for bands 1, 2, and 3 intersect at a point. This indicates that the junction could have been stable for a finite time interval. The point at which the lines intersect falls outside of the relative velocity circuit. Such a configuration results in one of the bands receding with respect to the other two [6]. In this case, it would suggest band 1 is receding.

The relative velocity vectors associated with the junction that consists of bands 3, 4, and 5 also form a closed loop in velocity space (fig. 2b). This implies that, as the bands formed, plates B, C, and D behaved rigidly in the vicinity of the junction. The reference lines for the relative velocity vectors of the bands do not intersect at a point for this junction. This indicates that the current configuration of the junction is not stable.

Phaidra Linea. As with the junctions in the south polar region of Europa, this junction represents the intersection of three bands (fig. 3). The cross-cutting relationships with respect to the bands of features that pre- and post-date them suggest that they formed contemporaneously. This implies that the formation of bands 6, 7, and 8 divided the region into three plates that subsequently rotated with respect to each other (E, F, and G in fig. 4).

Within the confidence regions we have established, the relative velocity vectors of the junction that consists of bands 6, 7, and 8 form a closed loop in velocity space (fig. 4). This implies that, as the bands formed, plates E, F, and G behaved rigidly in the vicinity of the junction. The reference lines for the relative velocity vectors of the bands intersect at a point for this junction. This indicates that the junction could have been stable for a finite time interval.

Conclusions: Given the existence of numerous features on the surface of Europa that share morphological characteristics with terrestrial tectonic features [7-9], it is reasonable to assume that many of the techniques used to understand the tectonic history of Earth could be applied to Europa. We have examined three regions on Europa that, based on morphology and cross-cutting relationships, appear to represent the intersection of three tectonic plates. Two of the junctions are associated with a set of bands in the south-polar region of the satellite and the third is associated with the near-equatorial band Phaidra Linea. Each of these junctions represents the intersection of three extensional bands. Analysis of these junctions using instantaneous relative velocity diagrams suggests that rigid-plate behavior for the plates involved is applicable in the vicinity of the junctions.
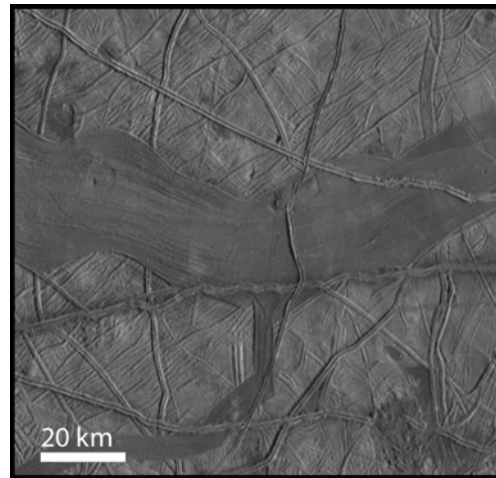
Fig. 3. Galileo image s0420619252 (7°S, 233°) obtained during the E11 encounter of the mission at 220 m/pixel.

Fig. 1. Galileo image s0466670713 (78°S, 121°) obtained during the E17 encounter of the mission at 500 m/pixel.
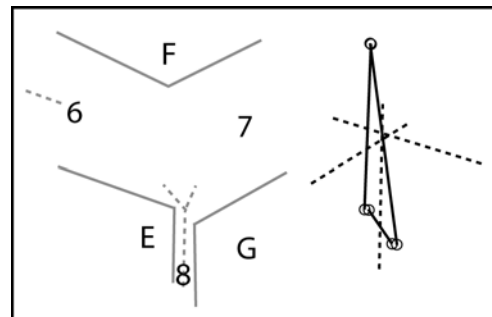
Fig. 4. Idealized representations of the current configuration of the Phaidra junction. Bands are labeled 6-8 and plate E-G. Instantaneous relative velocity diagram is shown with relative velocity vectors as solid black lines and reference lines as dashed black lines. Confidence regions (black circles) are also shown and represent random errors in the determination of the magnitude and direction of each relative velocity vector.

Fig. 2. Idealized representations of the junctions found in the south polar region. Bands are labeled 1-5 and plates A-D in accordance with figure 1b. Relative velocity vectors are shown as solid black lines and reference lines as dashed black lines. Confidence regions (black circles) are also shown and represent random errors in the determination of the magnitude and direction of each relative velocity vector.

References: [1] Schenk and McKinnon, Icarus 79, 75-100, 1989; [2] Sullivan et al., Nature 391, 371-373, 1998; [3] Tufts et al., Icarus 141, 53-64, 1999; [4] Cronin, Tectonophysics 207, 287-301, 1992; [5] McKenzie and Parker, Nature 224, 125-133, 1969; [6] Patriat and Courtillot, Tectonics 3, 317-332, 1984; [7] Hoppa et al., Icarus 141, 287-298, 1999; [8] Head, LPSC XXX, #1286, 2000; [9] Prockter et al., JGR 107, 10.1029/2000JE001458, 2002.

CASSINI ISS OBSERVATIONS OF TITAN'S TRAILING HEMISPHERE. J. E. Perry[1], E. P. Turtle[2], A. S. McEwen[1], D. D. Dawson[1], and C. C. Porco[3]   [1]Lunar and Planetary Lab., Univ. of Arizona, 1541 E. University Blvd., Tucson, AZ, 85721, [2]John Hopkins Univ. Applied Physics Lab., 11100 John Hopkins Rd., Laurel, MD, 20723, [3]CICLOPS, Space Science Institute, 4750 Walnut St., Boulder, CO, 80301. perry@pirl.lpl.arizona.edu

Introduction: Cassini's early 2007 flybys of Titan have provided an opportunity to image the trailing hemisphere of this fascinating satellite. Until February 2007, the trailing hemisphere had been poorly resolved, with the best images having pixel scales greater than 35 km, taken in June 2004. Starting with flyby "T25" (February 22, 2007) and running through T32 (June 13, 2007), Cassini's Imaging Science Subsystem (ISS) and Visual and Infrared Spectrometer (VIMS) observed the trailing hemisphere in daylight, filling in a gap in imaging coverage between 210° and 300° West. The sub-spacecraft latitude during these encounters from 2.3° to 51.6° North, while the sub-spacecraft longitude ranged from 215° to 237° West. The sub-spacecraft point for the ISS observations shifted to south and east with each successive encounter during this sequence.

Imaging Strategy and Processing: To acquire images of Titan's surface, a narrowband filter centered at 938 nm (CB3), in the middle of a methane absorption band, was used in conjunction with a filter centered at 619 nm (MT1), outside of a methane window [1,2]. By either ratioing or subtracting all or a portion of the MT1 image from a sum of the corresponding CB3 frames, a final product with greater contrast than the original CB3 frames can be achieved. These narrow-angle camera observations provide images with pixel scales ranging from 500 m to 2 km, although the actual resolution is likely several times coarser due to atmospheric scattering. A more complete discussion of the processes used is given in [3].

Observations: The region observed (Fig. 1a) covers three major albedo terrains: the 1700-km bright region known as Adiri (Fig. 1b and bottom center in Fig. 1a), equatorial dark terrain (Belet and Shangri-la), and northern and southern mid-latitude bright terrain. Cassini's RADAR captured a SAR (synthetic aperture radar) swath over Adiri and Belet during T8 (October 28, 2005), showing that the very dark terrain in these regions is filled with longitudinal dunes, akin to those seen in many deserts on Earth [4]. The bright terrain in Adiri consists of bright plains and linear mountain chains [5]. The mountains chains are only delineated in ISS images where they are surrounded by the small, dark patches of longitudinal dunes in the center of Adiri. The dark regions Belet and Shangri-la are dotted with numerous bright features known as faculae (discussed below). The mid-latitude bright regions have very low albedo contrasts with only a few albedo

structures visible, such as the dark lineaments seen in the northern mid-latitudes (discussed below) and a chaotic mix of bright and intermediate albedo features near 23° North, 205° West (Fig. 1c).

Dark lineaments. A series of parallel, NW-SE trending, dark lineaments in Titan's northern mid-latitude bright terrain was first observed during the T25 encounter (Fig. 1d). These lineaments range in length from 160 km to 540 km and average approximately 25 km in width. While the northern termini of these features don't have any unique morphology, the southern ends of these features often appear to branch or widen in width. In one case, in a lineament centered at 41° North, 246° West, the lineament appears to bifurcate leaving a small, 26-km long, 18-km wide bright "island" in the middle. The morphology of these features suggests that they were created through fluvial processes, but it is not known if liquid still flows within these features, or whether the flow is from the north or south. However, their parallel nature suggests that these features maybe tectonic structures, graben partially filled with organic sediment. Co-analysis with RADAR observations of these structures may help improve our understanding of how these strange structures formed.

Circular Features. Previous ISS observations of Titan have revealed several circular structures that may be impact features [1]. Several of these have been revealed by RADAR to be impact structures, including the multi-ring basin Menrva and the 80-km-diameter crater Sinlap [6]. However, due to the lack of topographic shading in ISS Titan data, we can not conclusively say that the other circular features are impact structures. However, as more of these features are observed by both RADAR and ISS, we can better get a handle of how to recognize impact structures in the ISS data and tell them apart from possible cryovolcanic features.

In ISS observations of the trailing hemisphere, two Suspiciously Circular Features (SCFs) have been observed. The first is a 95-km-diameter structure located at 7.2° North, 198.8° West, within the dark terrain north of Adiri (Fig. 1e). This feature bears a striking resemblance to Sinlap, with a dark interior, an intermediate albedo ring surrounding the dark material, and a bright, irregular structure surrounding that. Extrapolating from Sinlap, the dark material likely represents the organic sediment-covered crater floor, the intermediate albedo ring represents the crater wall and

rougher terrain along the periphery of the crater floor, and the bright irregular structure repr esents the raised rim and ejecta blanket of the crater.

The second SCF is a 75-km structure located at 39.6° North, 214.6° West (Fig. 1f), within the northern mid-latitude bright terrain. This feature consists of a dark ring surrounding a bright spot 20 km wide. If this feature is an impact crater, then the bright spot may represent the crater's central peak while the dark ring represents the sediment-covered crater floor.

Faculae. Numerous bright features, or faculae, are visible within the Belet and Shangri-la dark terrain regions. These faculae likely represent positive relief features poking up above the surrounding dunes. In several places, the faculae appear elongated with pre-ferred orientation, such as those south of Adiri shown in Fig. 1g. These faculae act as preferred wind direc-tion indicators, as longitudinal dunes wrap around the faculae [4]. In those south of Adiri, this would suggest wind flowing from northwest to southeast, as if Titan's

winds are diverting south around Adiri. Several facu-lae lined up in chains north of Adiri also warrant fur-ther investigation.

Conclusion: Cassini's observations of Titan's trailing hemisphere have revealed a number of in-triguing features. Some of these are variants of terrain types observed in other regions; others are quite unique (like the dark lineaments. Additional observations planned for two upcoming encounters in May and June 2007 may provide additional insights into the southern mid-latitudes that have only been imaged at high emis-sion angles thus far.

References: [1] Porco C. C. et al. (2005) *Nature, 434,* 159-168. [2] Porco, C.C. et al. (2004) *Space Sci. Rev. 115*, 363-497. [3] Perry, J. E. et al. (2005) *LPS XXXVI,* Abstract #2312. [4] Lorenz, R. D. et al. (2006) *Science, 312*, 724-727. [5] Radebaugh, J. et al. (2006) LPS XXXVII, Abstract #1007. [6] Lorenz, R. D. et al. (2007) *GRL 34,* doi:10.1029/2006GL028971..
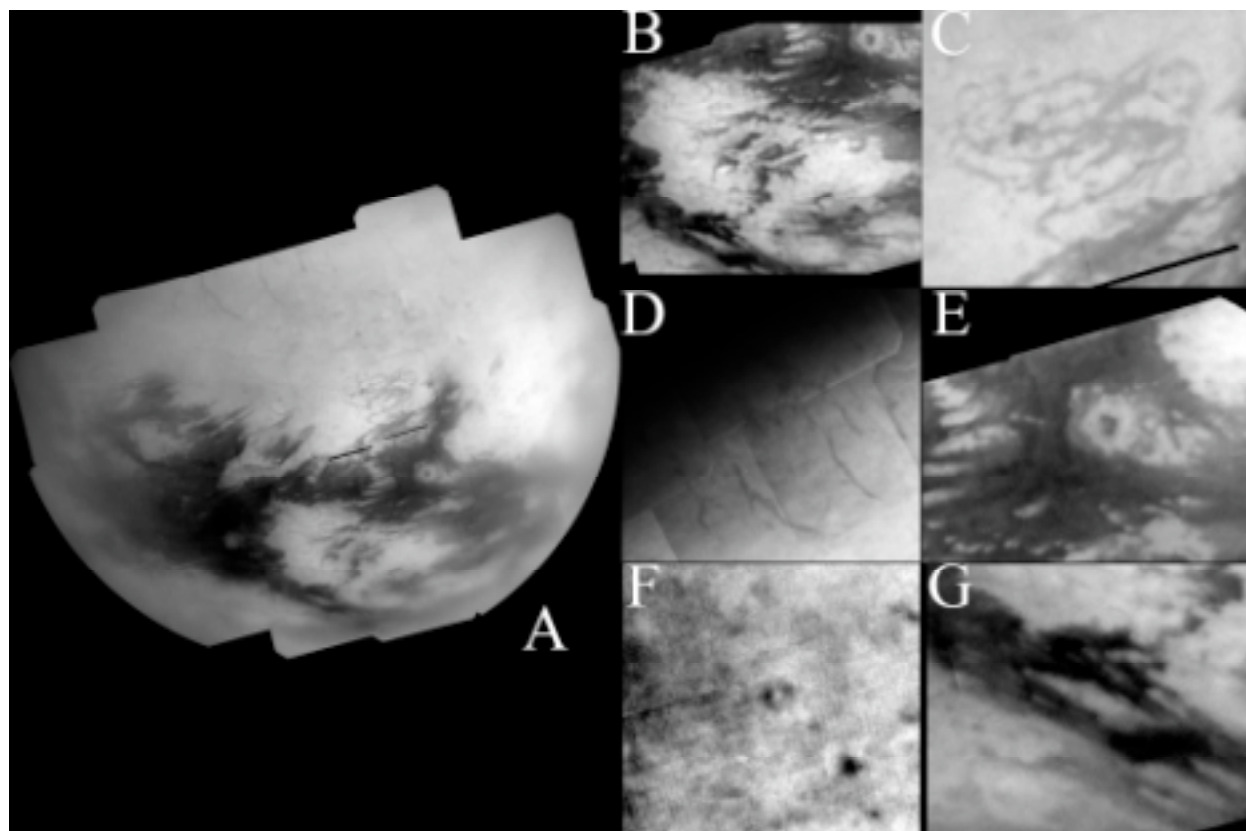
Figure 1: A summary of observations from Cassini's early 2007 encounters with Titan. Inset A shows a 25-image mosaic from the T28 encounter (April 10, 2007) covering much of the region observed during these encounters. Insets B-G highlight specific features observed during these encounters and are discussed in the text.

LONGITUDINAL DUNES ON TITAN AS INDICATORS OF GLOBAL CLIMATE. J. Radebaugh[1], R. Lorenz[2], J. Lunine[3], S. Wall[4], G. Boubin[3], E. Reffet[5], R. Kirk[6], R. Lopes[4], E. Stofan[7], L. Soderblom[6], M. Allison[8], P. Callahan[4] and the Cassini Radar Team,[1]Brigham Young University, Department of Geological Sciences, Provo, UT 84602 *jani.radebaugh@byu.edu* [2]Johns Hopkins University Applied Physics Lab, Laurel, MD [3]Lunar and Planetary Laboratory, Univ. of Arizona, Tucson, AZ 85721. [4]Jet Propulsion Laboratory, 4800 Oak Grove Dr., Pasadena, CA 91109 [5]LESIA-Paris Observatory, Meudon, 92195 France [6]US Geol. Survey Astrobiology Institute, Flagstaff, AZ [7]Proxemy Research Inc., Laystonsville, MD [8]Goddard Institute for Space Studies, New York, NY.

Introduction: The Cassini Titan Radar Mapper has uncovered thousands of longitudinal dunes on Titan's surface [1,2,3]. These features are themselves an indication of unique geologic conditions necessary for their formation and persistence. Additionally, dunes on Titan can be used to help us ascertain global wind patterns and Titan's climate, as we do on Earth and even Mars. Titan's unique possession, among the outer planet satellites, of a dense atmosphere makes it possible for Titan to have the dune-forming process in common with other atmosphere-bound solid bodies. We describe observations thus far of the dunes on Titan and their implications for wind directions and global climate.

Longitudinal dunes on Titan: Dunes on Titan, of the dominant form longitudinal or linar, are dark to both radar and optical instruments, such as VIMS and ISS [4,5], are 1-2 km wide, 1-3 km apart, ~100 m high, and 10 - >100 km in length [2-3, 5-8]. In this respect, they are similar in size to longitudinal (linear) dunes in the African Namib and Saharan deserts [9-11]. They are likely comprised of particulates of hydrocarbons and/or water ice and are found mostly near equatorial regions [2,3,5,12]. They show variations in lengths and spacings due to relative sand supply; more sand appears to be found in vast "sand seas" near the equator than at higher latitudes (Fig. 1). Titan's dunes also show evidence of diversion around topographic highs (Fig. 1) [2,3].
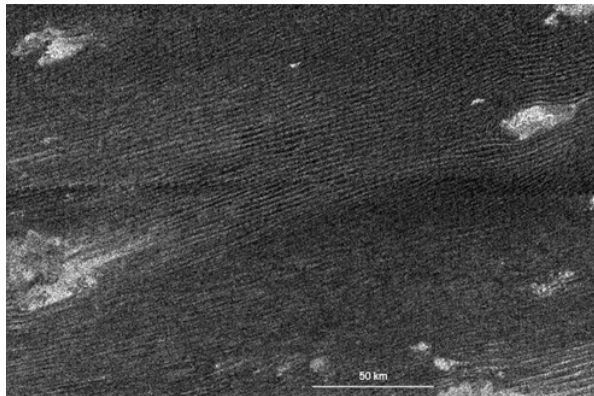
Fig. 1. A portion of the Belet sand sea, which extends nearly 2000 km. Dunes densely cover the underlying basement here, yet still divert around topographic highs. Image obtained during T8 (10/05), ~ 5° S, 250° W, ~175 m px⁻¹, radar illumination from the top (N).

Dune Orientations and Wind Direction: Longitudinal dunes form in Earth's deserts when winds are steady along a single direction parallel to the long axis of the dunes, with minor off-axis wind components that act to "shepherd" the dune particles [11,13-14]. Orientations of dune long axes thus correlate with local, surface wind directions. Orientations obtained for nearly 10,000 dunes on Titan have a mean azimuth (measured clockwise from N) of nearly 90° (Fig. 2), with slight variations by region, likely due to topographic interferences with wind directions. With the exception of these local variations, the generally 90° dune orientations and indicators from topographic interactions are likely direct reflections of the long-term mean wind direction of generally eastwards, extending from at least 30° N to 30° S latitudes.
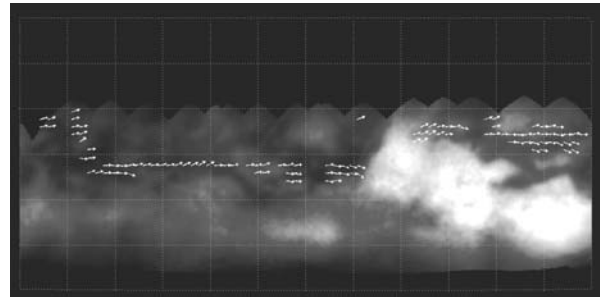
Fig. 2. Mean dune orientation vectors in 5°x5° boxes for all dunes seen on Titan through T19 (10/06). Dunes indicate a general W-E wind direction, but also show evidence of diverging around topographic features.

Titan's Global Climate: We seek to understand how the dunes on Titan can inform our understanding of Titan's climate. Dunes typically form on Earth in deserts, defined by their lack of a threshold yearly precipitation level. Thus, it is tempting to relate the presence of dunes on Titan to conditions of low precipitation. Direct measurements obtained at the Huygens landing site, however, which was near the equator and was in view of some dunes, revealed ambient methane humidity levels of 50% [15,16] and the GCMS measured evaporation of methane and ethane liquids [17]. This seeming paradox of dunes present in conditions of moderate humidity is considered in the context of terrestrial desert distributions and cyclical processes. Deserts on Earth are usually found near 30° N or S,

due to the intersection of the dry, downwelling branch of the Hadley cell with the Earth's surface. On Titan, however, an asymmetric circulation regime has been modeled, in which there is upwelling at the summer pole and downwelling elsewhere [18]. Thus, low latitudes are generally dry, except when seasons change and polar summer shifts, bringing a temporary symmetric circulation regime and rainfall to the equator. A more recent zonally-averaged model of Titan's climate [19] explicitly shows that sporadic rainfall can occur at low latitudes, yet the ground there generally becomes dessicated. The frequency of rainfall and the latitude band that becomes dessicated depends on the total methane inventory in the climate system.

Evidence of the viability of this model of generally dry conditions at the equator exists in the myriad dry riverbeds populating Titan's equatorial regions [17], similar to river basins in the US desert southwest that are generally dry except during brief summer storms. In addition, recent general circulation models [20] predict low humidities at low latitudes and damp conditions near the poles. This is consistent with recent observations of lakes at Titan's north polar regions [21,22].

The importance of relative humidity is overshadowed by the dominant factors in dune formation: sufficient wind and adequate sediment supply. Given that some lakes at Titan's polar regions appear to be fed by channels [21,22], we assume that fluids also carry sediments in channels to be deposited into lake basins. In contrast, generally dry regions near the equator are free of sediment-trapping lakes. Instead, it appears that broad, perhaps locally low-elevation regions near the equator collect sediments that are subsequently reworked into dunes.

Thus, the major factors of generally low humidity, adequate sediment supply, sufficient winds, and absence of sediment trapping (in the form of rivers washing away sediments, or basins containing fluids) must be considered together to explain the presence or absence of dunes on Titan. Based on observations of dunes at Titan's equatorial regions and lakes at the north pole, a global picture of Titan's climate is beginning to emerge. It appears that methane rainfall occurs at Titan's winter pole [21], while generally dry conditions prevail at the equator. Local variations on this theme, such as the humidity observations at the Huygens landing site and some dry lakebeds at the north polar regions [22], highlight the Earth-like complexity of Titan's surface and atmospheric processes.

References: [1] Elachi, C. et al., 2006, *Nature* 441, 709-713. [2] Lorenz, R. D. et al., 2006, *Science* 312, 724-727. [3] Radebaugh, J. et al., *Icarus* submitted. [4] Porco, C. et al., 2005, *Science* 434, 159-168. [5] Soderblom et al., 2007, *PSS*. [6] Kirk, R. D. et al., 2005, *LPSC XXXVI*, Abst #2227. [7] Boubin, G. M. et al., 2005, *AAS DPS 37*, Abst #46.04. [8] Callahan, P., et al., 2006, *AGU FM* Abst #P13A-0165. [9] Spencer, C. et al., this conference. [10] McKee, E. D., 1982, USGS Spec. Pap. 188. [11] Lancaster, N., 1981, *Sedimentology* 1,1-8. [12] Radebaugh, J., et al., 2006, *AGU FM* Abst #P12A-03. [13] Fryberger, S. G. and G. Dean, 1979, *USGS Spec. Pap.* 1052. [14] Lancaster, N., 1995. [15] Tomasko, M. G., e.a., 2005, *Nature* 438, 765-778. [16] Niemann, H. B., et al., 2005, *Nature* 438, 779-784. [17] Lorenz, R. D., et al., 2007, *PSS*, in rev. [18] Hourdin, et al., 1995, *Icarus* 117, 358-374. [19] Mitchell, J. L. and R. D. Lorenz, EGU Conference, April 2007. [20] Rannou, P., et al., 2006, *Science* 311, 201-205. [21] Stofan, E. R., et al., 2007, *Nature* 445, 61-64. [22] Mitchell et al. in prep.

GROUNDBASED OBSERVATIONS OF IO IN SUPPORT OF THE NEW HORIZONS FLYBY. J. A. Rathbun[1] and J. R. Spencer[2], [1]University of Redlands (1200 East Colton Ave., Redlands CA 92373, USA *jullie_rathbun@redlands.edu*), [2]Southwest Research Institute (1050 Walnut St., Suite 400, Boulder, CO 80302, USA).

Introduction: Io is the most volcanically active body in the solar system with dozens of volcanoes erupting at any time. Recently, the volcanoes were extensively studied by the remote sensing instruments on the Galileo spacecraft. But, they have been observed from ground-based telescopes for more than two decades (Rathbun et al., 2002). The frequency of these observations and the number of telescopes used increased dramatically during the Galileo era in order to compliment the data being returned by that spacecraft.

The New Horizons spacecraft flew by Jupiter on February 28, 2007 and made observations of Io on its way through the system. Three of New Horizons' remote sensing instruments were trained on Io: the Multispectral Visible Imaging Camera (MVIC) which is sensitive to the visible range in the spectrum; the Long Range Reconnaissance Imager (LORRI) which is sensitive to the near infrared (0.4 – 1.0 μm); and the Linear Etalon Imaging Spectral Array (LEISA) which is sensitive to slightly longer infrared wavelengths (1.2 – 2.5 μm).

As during the Galileo era, we observed Io from the Infrared Telescope Facility (IRTF) in Hawaii in order to compliment the data being taken by New Horizons. Our observations were at longer wavelengths than New Horizons with some overlap (2.2, 3.5, and 4.8 μm). We were also able to observe Io over a longer period of time which can put the New Horizons data into the proper temporal context. We began observing in August 2006 and our last observation will be in June 2007. Because of solar conjunction, we were unable to observe Io from October through December 2006. The highest concentration of observations took place near the flyby.

Observations: We were awarded 28 partial nights total at the IRTF, all but two of which have passed at the time of this writing (table 1). The observations can be categorized into two broad types. In one type, observations are scheduled during Jupiter eclipses, when Io is in Jupiter's shadow and the volcanoes are seen without interference by reflected sunlight. During the associated occultation events, we can obtain one-dimensional spatial resolution across Io by plotting Io's total brightness as a function of time as it passed behind Jupiter. From this, we can determine the brightnesses of individual volcanoes on the Jupiter facing hemisphere of Io. Nineteen of the awarded partial nights were during Jupiter eclipses, included the

two remaining dates. During twelve of these nights we were able to successfully observe Io.

The other type of observation takes place while Io is in sunlight. This enables us to observe a variety of longitudes and to look for major eruptions over the entire moon. During these observations Io's brightness is mostly due to reflected sunlight. In 1999, an eruption at Tvashtar (figure 1) was

Figure 1: IRTF 3.8 micron image of Io during the November 1999 Tvashtar eruption.

observed by the IRTF before the Galileo spacecraft obtained a higher resolution view (Howell et al., 2001), demonstrating that major eruptions can be seen from the IRTF. Nine of the observations were of this type and seven of those nights were successful for observing. They are spaced in time in order to obtain good coverage of Io at all longitudes.

Table 1: Dates of successful and upcoming IRTF observations in 2006 and 2007. Occultation observations are of the in-eclipse occultation and also include eclipse observations.

Date	Observation type
Aug. 15	Occultation reappearance
Aug. 22	Occultation reappearance
Jan. 3	Occultation disappearance
Jan. 18	Sunlit
Jan. 19	Occultation disappearance
Jan. 23	Sunlit
Jan. 24	Sunlit
Jan. 26	Occultation disappearance
Jan. 27	Sunlit
Jan. 29	Sunlit
Feb. 18	Occultation disappearance
Feb. 20	Occultation disappearance
Feb. 25	Occultation disappearance
Feb. 28	Sunlit
Mar. 2	Sunlit
Mar. 15	Occultation disappearance
Mar. 31	Occultation disappearance
Apr. 22	Occultation disappearance
May 7	Occultation disappearance
May 16	Occultation disappearance
Jun. 24	Occultation disappearance

Results: During all eclipse observations in 2006-2007, Io appears much fainter than observed during earlier periods. The seeing is not often good enough to make out individual volcanoes, but on
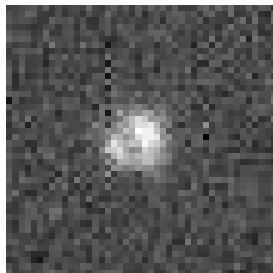
Figure 2: IRTF 3.5 micron image of Io in eclipse on March 6, 2007.

March 6th, 2007 the eclipse was observed in darkness and at a low airmass, allowing us to see three distinct bright spots at 3.5 μm (figure 2). The upper right spot appears to be Loki, the most powerful volcano on Io. The lower left spot may be either Kanehekili or Janus or some combination of both, and the dim lower right spot is still unidentified.

When the eclipsed Io is occulted by Jupiter, we can derive hotspot brightnesses from the observed light-curves. So far, we have been able to reduce light curves for four nights (August 15, January 3 and 26, and February 20). Only one hotspot had a measurable brightness during these events, Loki. It was measured to have a 3.5 micron brightness below 20 GW/micron/str on all four nights. Typical measurements of Loki's flux during eruption are closer to 50 GW/micron/str, indicating that it was, unfortunately, not actively erupting during the New Horizons flyby. Furthermore, none of the sunlit observations reveal an obvious eruption similar to the Tvashtar eruption in 1999. In conclusion, we observed no major outbursts during our 2006-2007 IRTF observations.

Comparison with New Horizons: Early images from New Horizons show a giant plume at the location of Tvashtar along with smaller plumes at other locations (figure 3). Although no major eruptions were observed at IRTF, several of our observations did include the Tvashtar area (table 2). We will thoroughly analyze all the images to see if Tvashtar can be detected at some lower level. If it can, we will use our multiwavelength measurements to constrain the eruption temperature. If it is not observed, we can put an upper limit on Tvashtar's output at the wavelengths with which we observed. If we are able to observe Tvashtar is some images and not in others, we can constrain the date the eruption began.

We will analyze the eclipse images as a function of date in order to see which volcanoes on the Jupiter-facing hemisphere are erupting and compare this to the eruptions observed by New Horizons and determine how long the eruptions have been occurring. We will further use our multiwavelength data to estimate surface temperatures of the observed eruptions.
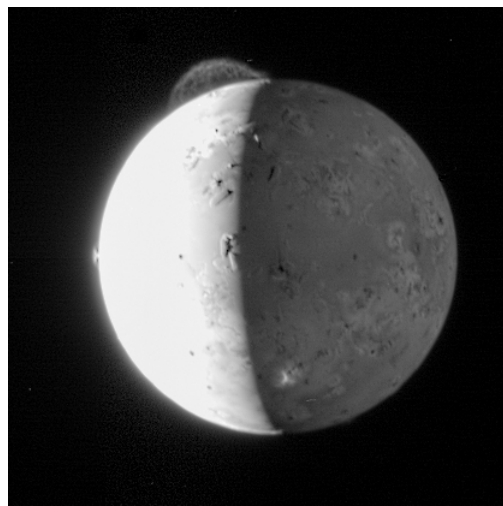
Figure 3: New Horizons image showing Tvashtar's giant plume near the top of the image and several smaller plumes across the disk.

References:

Howell, R. R., et al., Ground-based observations of volcanism on Io in 1999 and early 2000, *J. Geophys. Res.*, **106**, 33,129-22,139, 2001.

Rathbun, J. A., J. R. Spencer, A. G. Davies, R. R. Howell, and L. Wilson, Loki, Io: A periodic volcano, *Geophys. Res. Lett.*, **29**, 10.1029/2002GL014747, 2002.

Table 2: Sunlit observations and the orientation of Io and location of Tvashtar during each.

Date	Central lon.	Location of Tvashtar
Jan 18	130	Near Center
Jan 23	66	On limb
Jan 24	260	Other side
Jan 27	160	Near Center
Jan 29	206	Extreme limb
Feb 28	188	On limb
Mar 2	234	Other side

LONG-TERM STABILITY OF A SUBSURFACE OCEAN ON ENCELADUS. James H. Roberts, Francis Nimmo, *Department of Earth and Planetary Science, University of California at Santa Cruz, Santa Cruz CA 95064-1077, USA, (jhr@ucsc.edu).*

Introduction The discovery of the thermal anomaly in the south polar region of Enceladus [1], has launched a great deal of interest in potential activity in the ice shell. It is assumed that the observed thermal anomaly is an expression of ongoing internal heating due to tidal dissipation. Under reasonable rheologic conditions it is not possible to generate significant tidal dissipation in the silicate core. Substantial tidal heating may be produced in the ice shell if it is decoupled from the core by a subsurface ocean. Thus, such an ocean is believed to exist in order to explain the observed activity.

However, because the core heat production is so small, we find that convective and even conductive heat transport is sufficient to cool the interior, such that a liquid ocean cannot be in long-term thermal equilibrium.

Tidal Heating We computed the tidal heating in an Enceladus model with three primary layers, a silicate core of radius 160 km, and a water ocean and icy mantle with total thickness 90 km, and allowed the ice-water interface to vary between models. Using the general approach of [2], and a propagator matrix method similar to [3], we solved for the heating in a uniform viscosity (η) ice shell and silicate core [4]. A thinner shell is more easily deformable and has a greater tidal heating rate. However, a thin shell also has a smaller volume, limiting the total heat production within it. These two competing effects result in a critical shell thickness, d_c at which the maximum heat flow occurs. d_c is viscosity-dependent but is less than 5 km for all the models considered here. However, the length scales of surface features are inconsistent with a very thin ice shell, so the actual heating rate is unlikely to be near the maximum.

The tidal heating in the silicate core is very small for any reasonable core viscosity ($\eta \geq 10^{13}$ Pa s) , about three orders of magnitude less than the radiogenic heating assuming a chondritic core. We therefore assume that tidal heating is not significant in the core of Enceladus and that the heat flux out of the core, F_c is entirely due to radiogenic heating, resulting in $F_c = 1.9$ mW m^{-2}. For the ocean to be in thermal equilibrium, F_c must equal the heat flux across the base of the ice shell F_b (modified by an appropriate geometric factor). The problem then becomes one of determining what ice shell thickness, d, is consistent with this F_b for a given ice viscosity structure.

Convection We address this question by modeling convection in the ice shell. The bottom boundary is at the melting point of water, and the surface temperature is about 80 K, but varies with latitude [5]. We modeled the convection using the 2D-axisymmetric version of Citcom [6] modified to include the tidal heating from our earlier models. We assume a Newtonian temperature-dependent viscosity, with activation energy $E_a = 60$ kJ/mol [7]. The heating models assume that the material properties within a given layer are constant. We therefore modify the tidal heating at each point based on the local η, according to [5,8].

For the convection modeling, we only considered ice shells

at least 40 km thick. Thinner ice shells are conductive. For each of the tidal heating models in this regime, we ran a corresponding convection model to statistical steady state and examined F_b. For a model to be in thermal equilibrium, F_b must match F_c. Fig. 1 shows F_b for each model. In virtually every case, the heat flux determined from the convection modeling is many times greater than that produced by a chondritic silicate core. Thus we conclude that a stable liquid ocean on Enceladus is inconsistent with a convecting ice shell. Only the low viscosity ($\eta = 10^{13}$ Pa s) series produces heat fluxes that intersect the chondritic core value (marked by the solid line). However, these cases are tidally heated to such an extent that convection cannot cool them, and the lower part of the ice shell melts. The ice shell thins and becomes conductive.

Our results suggest that no combination of η and d allows thermal equilibrium to be established for convective shell, subsurface ocean and chondritic core. In most cases, convection is able to remove the tidal heating as well as cooling the interior. This cooling would cause the ocean to freeze onto the base of the ice shell. Once the ocean freezes completely, the ice shell is no longer decoupled from the silicate core, and tidal heating is greatly reduced. Convection most likely ceases in this case.

Conduction We have also investigated the possiblity that an ocean may exist beneath a conductive ice shell. To determine d that is consistent with the previously established low value for F_c, we make an initial guess as to the thickness and viscosity structure of the ice shell, and find the tidal heating using the same procedure as before. We then compute the
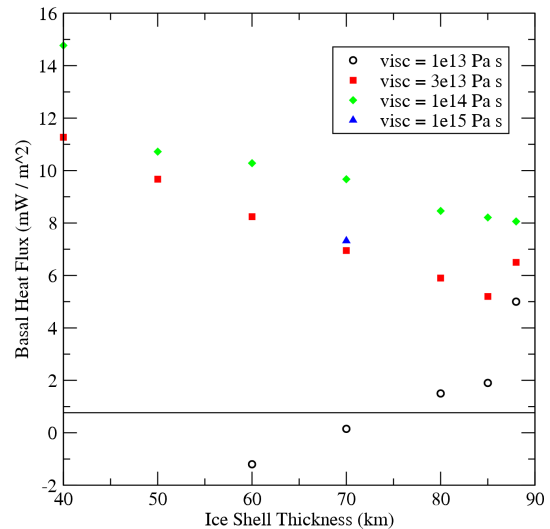

Figure 1: F_b as a function of d from convection models. Blue line denotes that expected from a chondritic core. Values have been normalized to the surface area of the planet. "visc" refers to the viscosity at the base of the ice shell.

conductive temperature, and resulting $\eta(T)$ consistent with this heating, subject to the same temperature boundary conditions used in the convective model, adjusting d as needed in order to match F_b (the computed heat flux at the base of the ice shell) to F_c. We iterate between the heating and temperature models until we have a self-consistent solution.

We find however, that there is no possible d that results in a sufficiently low F_b to match F_c. The heat flux generally scales with the inverse of d. However, even a 90 km (the maximum possible thickness) ice shell (assuming a $\eta_0 = 3 \times 10^{13}$ Pa s), has $F_b \sim 8$ mW m^{-2}, or about 4 times F_c. Fig. 2 shows the dependence of the F_b on η_0.

The physical explanation for this is as follows. Although the conductive heat flux is less than the convective heat flux, the reduction in the case of Enceladus is not that great. Heat flux tends to scale with the thickness of the stagnant lid. For the convection models in this study, the stagnant lid is nearly half of d. Thus, the conductive heat flux is only a factor of ~ 2 lower than the convective flux. A strongly heated ice shell may result in a low temperature difference across the bottom boundary, and thus a low heat flux (e.g. Fig. 1, circles). However, the larger viscosity variations in the conductive cases result in stiffer outer layers. This restricts the deformation of the warmer, lower layers, and reduces the tidal heating everywhere. Although tidal dissipation deep in the ice shell is still the dominant heating mechanism in a conductive ice shell, it is insufficient to reduce F_b to match F_c. This will result in the freezing of any subsurface ocean, and the reduction of the interior temperature. A 40 km thick ocean will freeze in ~ 30 Ma, a similar timescale to that of the orbital evolution.

Discussion In order to maintain a steady-state subsurface ocean on Enceladus, at least one of the following conditions must be met:

1. The silicate core is more strongly heated, raising F_c and relaxing the severe restriction on F_b. The radiogenic heating is unlikely to deviate significantly from chondritic value assumed here. Under no plausible Maxwellian rheology can the core experience siginificant tidal dissipation. Thus, in order for this condition to be satisfied, the core must behave in some non-Maxwellian manner that is more dissipative.
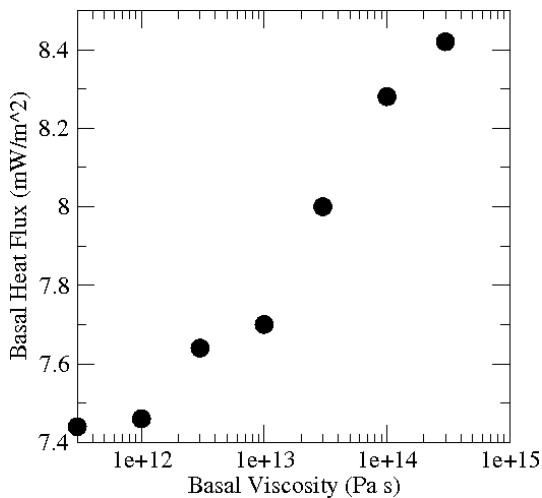
2. The ice shell is more strongly heated, reducing ΔT across the base, and likewise F_b. One way is to reduce the overall viscosity in the ice shell. However, no value of η_0 reduces F_b by enough in the conductive case. A convective shell with $\eta_0 \leq 10^{13}$ Pa s, may have sufficiently low F_b (Fig. 1), but will melt and evolve to a conductive state in which the heating is reduced. Dissipation in the ice shell may also be increased if the orbital eccentricity, e was higher in the past [9]. Increasing e by a factor of 3 from the present-day value is sufficient to sustain an ocean.

3. The ocean may not be pure water. If the ocean contains substantial amounts of other volatiles (e.g. ammonia), the melting point may be severely depressed. However, even at the H_2O - NH_3 peritectic temperature of 175 K [10], $F_b \sim 4$ mW m^{-2}. Furthermore, there is no observational evidence for so vast an amount of NH_3.

We do not find any of these alternatives particularly attractive. An increased e in the past is plausible [9], but implies an ocean would be transient. We also point out that our models fail to reproduce the observed surface heat flux (F_s) of 100 mW m^{-2} in the south polar region [1], a result also found by [10]. F_s for the convection models was ≤ 35 W m^{-2} for all cases.

We suggest therefore that the south polar thermal anomaly may be the result of a regional and possibly transient effect rather than global convection and heating. Shear heating resulting from slip along the "tiger stripes" [11] may produce sufficient heating in the near surface to explain the observation and may also affect the interior dynamics [12]. The regional shear heating can explain the existence of exactly one thermal anomaly, despite the tendency of the degree 2 tidal heating to produce two plumes, one at each pole.

Our results suggest that a subsurface ocean on Enceladus cannot exist in the steady-state. Independent dynamical arguments [9] suggest that the observed heat anomaly [1] cannot be sustained given Enceladus' current orbit. This does not preclude a transient or periodic ocean. A low-viscosity convecting shell may undergo melting and thinning until it becomes conductive. The heating in the conductive shell would drop and the shell may thicken until convection set in again. Alternately, periodic eccentricity variations may cause an ocean to grow and shrink on that timescale, provided it never freezes completely. These remain intriguing problems for future study.

References [1] Spencer et al. (2006) *Science* 311, 1401. [2] Tobie et al. (2005) *Icarus* 177, 534. [3] Sabadini and Vermeerson (2004) *Global Dynamics of the Earth*. [4] Roberts and Nimmo (2007), LPSC XXXVIII, 1429. [5] Ojakangas and Stevenson (1989) *Icarus* 81, 220. [6] Roberts and Zhong (2004) *JGR* 109, E03009. [7] Goldsby and Kohlstedt (2001) *JGR* 106, 11,017. [8] Sotin et al. (2002), *GRL* 29, 1233. [9] Meyer and Wisdom (2007) *Icarus*, in press. [10] Barr and McKinnon (2007), *GRL* 34, L09202. [11] Nimmo et al. (2007), *Nature* 447, 289. [12] Nimmo et al. (2007), this volume.

Figure 2: Minimum F_b for a 90 km conductive ice shell

GLOBAL SCALE SMALL CIRCLE DEPRESSIONS AND POLAR WANDER ON EUROPA.

EUROPA. P. Schenk[1], I. Matsuyama[2], and F. Nimmo[3], [1]Lunar and Planetary Institute, Houston, TX 77058 (schenk@lpi.usra.edu); [2]Carnegie Institute of Washington, Washington DC 20015 (matsuyama@dtm.ciw.edu); [3]Univ. of Calif. Santa Cruz, Santa Cruz, CA 95064 (fnimmo@es.ucsc.edu).

Combined Voyager, Galileo and New Horisons imaging data reveal a series of broad arcuate low-relief small-circle depressions and troughs (SCD's) on Europa, forming two organized antipodal sets of circular concentric lineaments about 45° in radius. These features do not disrupt, and are not disrupted by, other geologic features, and do not fit any known global diurnal tidal stress fields in their current position. A possible mechanism involves formation of extensional troughs primarily due to stressses caused by an episode of ~90° polar wander, followed by ~30° non-synchronous rotation and 30° of rotation about the center of the circles to place the circles in their currently observed positions. The extraordinary depths of some of these depression (>1 km) are inconsistent with a very thin ice shell on Europa.

THE IMPACT OF CRATERING IN THE OUTER SOLAR SYSTEM

P.M. Schenk, Lunar and Planetary Institute, 3600 Bay Area Blvd., Houston, TX 77058 (schenk@lpi.usra.edu), [2]

Introduction: Working on impact cratering related problems may seem tedious beyond description, but the importance of craters cannot be overstated. The peculiar thermal and mechanical properties of water (and other) ice allow impact craters to record processes and materials that would not otherwise not occur or be so obvious on silicate-rich targets. Craters act as natural drill probes into icy lithospheres. They act as recorders of global stratigraphy and global dynamics (including rotational history). They record the flux of incoming projectiles into planetary systems. They record the thermal history of icy satellites. There is little that impact craters cannot do!

Drill Probes: The dynamics of impact cratering disrupt and dislocate vast amounts of material vertically that would otherwise remain hidden from view [1]. On Ganymede and Callisto, central dome craters expose deeper ice-rich ductile material in the central uplift [2]. Dark halo craters have been interpreted to be ejecta contaminated by dark terrain material buried at shallow depths of 1-1.5 km [3].
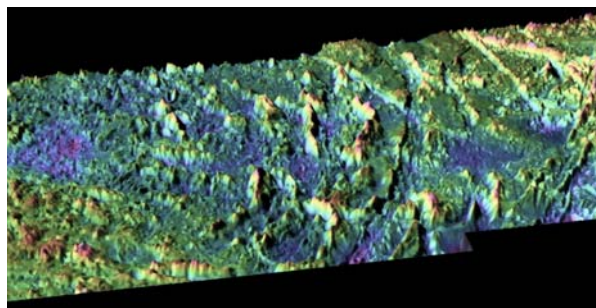

Figure 1. Perspective view of part of the rugged topography (color-coded) of Callanish. This 30-km wide multitiring crater is thought to have penetrated near the base of Europa's floating ice shell, fracturing it. Crater center is near left-hand edge of the scene.

Europa is an extreme case. The comparison with Ganymede is especially telling since craters should be very similar on both satellites. Instead of central peaks, we see deformed craters in the 20-25 km diameter range, and multi-ring structures where we should be seeing central pit craters (Fig. 1) [4,5]. Further, the d/D curve for Europa rolls over at 8-10 km (rather than continuing to increase as on Ganymede; Fig. 2) [6]. These anomalies are clearly linked with Europa's "thin" ice shell and subsurface ocean. Recent numerical modeling [e.g., 7, 8] and even the most simplistic conceptual model of impact crater collapse at these transitions [6] all point to ice shells in the 10-20 km range. The Europan crater story refuses to support a thin (<5 km thick) ice shell

model for Europa, no matter how deperately one might want it to.

The cratering record on Titan is sparse [9] but those few craters are most similar in appearance to Ganymede craters: Titan has no *near-surface* internal ocean.

An extreme example of planetary drilling is satellite disruption. Clearly, any projectile large enough to form 600-km-wide basins on Iapetus and Rhea would effectively shatter any of the small ring moons orbiting Saturn [e.g., 10]. That so many of them still exist is a continuing puzzle.

Recording Impactors: The more important manifestation is the size-frequency distribution of impactor populations. In the absence of an icy satellite sample return program, this has obvious implications for surface ages. 25 years of effort have not yet converged on a definitive answer to how old these surface are. Despite this, we do know that comets dominate the current flux in the outer solar system [10]. Extrapolating the current observed flux allows us to estimate surface ages to within a few factors (tho with less confident as age increases). Europa's surface is young (<100 my), but Ganymede's bright terrain may be 2 Gyr or more old, depending on the breaks). The various ridged terrains on Enceladus probably have ages of 0 to 1-2 Gyr, depending on flux model [11]. Mapping also shows that resurfacing moved from the (current) equator to the south pole. Triton's surface age may be younger than Europa [12].

The simple story above is marred by the likelihood of intersatellite debris [13], euphamistically referred to as sesquinary cratering. Zahnle and collegues have shown that significant amounts of ejecta can be launched into orbit about the primary planet. Some debris will migrate to other satellites, adding a projectile population not accounted for by comet models (a.k.a. Population II [14]). Indeed, fragmental ejecta from Io may be contaminating Europa [15].

Recording Dynamics: Icy satellites live in peculiar dynamical regimes. They are typically synchronous (although they can be jostled out of this state in the right circumstances [16]), and are subject to various tidal and rotational forces due to proximity to other satellites. Predicted global asymmetries in crater distribution of 30x or more have not materiallized, except on Ganymede where the difference is only a factor of 4 [17]. One interpretation is that Ganymede spent considerable time out of snychronicity, blurring the impact distribution globally. Another outrageous exception is the case of Triton, where all the observed craters are on the leading hemisphere [12]. This is explained by impact of prograde nonheliocentric debris on a retrograde orbiting

satellite. The debris could have been blasted off one of Neptune's inner or outer satellites.

Icy satellites have even recorded the impact of tidally disrupted comets [18]. Prominent split comet crater chains are known on Ganymede and Callisto, but none have been found on the other satellites systems.
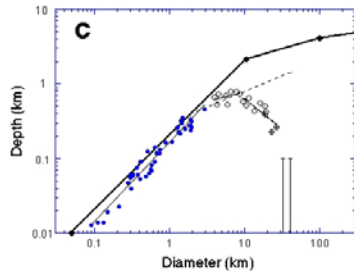

Figure 2. Depth diameter curve for craters on Europa (bottom). The rollover at 8-10 km correlates with impact crater detection of the base of the icy shell. Data from []. Open symbols represent complex craters. Dashed line is the Ganymede curve, which Europa deviated from.

Thermal Probes: The rheology of water ice is strongly sensative to temperature [19]. Larger icy satellites are inherently warmer and more sensative to thermal history than smaller satellites, although some, such as Enceladus and Dione, have not escaped the torch. Ganymede craters record a history of widespread viscous relaxation, mostly on ancient dark terrain. Recent mapping of relaxed crater distribution shows that the period of high heat flows associated with relaxed craters is directly linked to bright terrain formation and that Ganymede cooled considerably afterwards, arresting relaxation. Relaxation has been very important locally on Enceladus and Dione, suggesting that heat flow has been high there but not uniformly so [20].

Another manifestation of thermal history has been the changing morphology of large (D>60 km) impact basins on Ganymede (and Callisto) [5]. Detailed mapping reveals that basin morphology changed from multiring through palimpsest, penepalimpsest (coincident with bright terrain formation), penedome crater, to modern day central dome crater (Fig. 3).
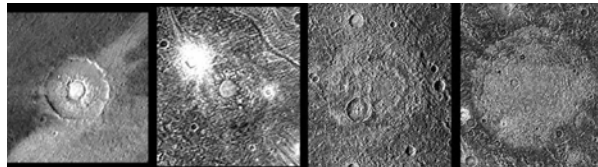
Figure 3. Changing morphology of Ganymede craters over time. From left to right (with increasing age): central dome crater, penedome crater, peneplaimpsest, palimpsest. Craters scaled to appear similar in size.

The most ancient large impacts on the Jovian satellites are characterized by numerous concentric ridges and graben and an absence of large-scale topography [21]. These multiring structures occur nowhere else and are probably a manifestation of very high heat flow and thin lithospheres. Graben spacing can be used to estimate thermal gradients.

Conclusions: Impact craters are key to understanding interior stratigraphy and properties, thermal histories, and a host of other issues in the outer solar system. Much work remains, however. We eagerly await the first results from Pluto encounter in 2015. Continued mapping of impact crater sizes, shapes and statistics is required, especially in the Saturn system. Advances in numerical modeling hold hope of translating observed morphologies and transitions into real properties, such as lithospheric thicknesses, ocean depths, or thermal profiles, glimpsed only darkly at present.   Continued research focus on the mechanics and dynamic of impact cratering process (especially as it differs in icy regoliths) will be critical for understandign what craters are telling us. Finally, a return to Jupiter to complete Galileo's failed global mapping objectives is critical for understanding how these unusual impact craters form, are modified, and are distributed. These craters offer some of our best opportunities to map out the stratigraphy and thermal histories of these satellites .

References: [1] Melosh, H.J., Impact cratering,Oxford, 1989. [2] Schenk, P., JGR, 98, 7475, 1993. [3] Schenk, P., and W. McKinnon, JGR, 90, C775, 1985. [4] Moore, J., and others, Icarus, 151, 93, 2001. [5] Schenk, P., et al., in *Jupiter*, Cambridge Press, 2004. [6] Schenk, P., Nature, 417, 419, 2002. [7] Turtle, E., and E. Pierazzo, Science, 294, 1326, 2002. [8] Bray, V., et al., Lunar Planet. Sci. 37, abstr. 1175, 2006. [9] Elachi, C et al., Nature, 441, 709, 2006. [10] Zahnle, K., et al., Icarus 163, 263, 2003. [11] Kirchoff, M., et al., Lunar Planet Sci. 38, 2007. [12] Schenk,P., and K. Zahnle, Icarus, in press, 2007. [13] Alvarellos, J., et al., Icarus, 178, 104, 2005. [14] Smith et al., Science, 215, 504, 1982. [15] Zahnle, K, et al., Lunar Planet Sci. 38, 2007. [16] Showman, A. et al., Icarus 129, 367, 1997. [17] Zahnle, K., et al., Icarus 153, 111, 2001. [18] Melosh, H.J. and P. Schenk, Nature, 365, 731, 1993. [19] Durham, W., and L. Stern, *Annu. Rev. Earth Planet. Sci.* 29, 295, 2001. [20] Schenk, P., Lunar Planet. Sci 38, 2007. [21] McKinnon, W., and H.J., Melosh, Icarus, 44, 454, 1980; Schenk, P. et al., *Lunar Planet. Sci. 28*, 1249, 1997.

CONSTRAINTS ON THE SALINITY OF ENCELADUS' PLUMES

N. M. Schneider, M. E. Burger, R. E. Johnson, J. S. Kargel, E. L. Schaller, and M. E. Brown

We report on a search for sodium emission from the vicinity of Enceladus as a strong constraint on the potential salinity of the plumes. While the dominant plume constituent is H_2O, the presence or absence of trace constituents may help decide between models of the plume origin. Sodium is an important first test since it is readily detectable and cosmically abundant. Salts may also be enhanced if Enceladus has subsurface liquid water in contact with rocky material. We will present the results of recent high-resolution spectroscopic observations using the Keck and Anglo-Australian Telescopes. We will also discuss two critical theoretical considerations: the efficiency with which trace elements are incorporated in the plumes, and the efficiency with which sodium is later liberated in atomic (and therefore observable) form. Taken together, the observations and theory will place useful limits on plume composition, and potentially their origin.

THE CONVECTIVE DYNAMICS OF ICY SATELLITES AND IMPLICATIONS FOR SURFACE EVOLUTION. Adam Showman, Lunar and Planetary Laboratory, University of Arizona, 1629 E. University Blvd., Tucson AZ 85721.

Europa, Ganymede, Callisto, Titan, and several smaller icy satellites have probably experienced ice-shell convection during their histories, and in several cases, convection or diapirism may have played a crucial role in causing surface tectonics.

I will review the current status and future directions in research on convection in the ice shells of icy satellites, with a particular emphasis on whether and how convection can influence the surface geology. My discussion will connect the latest theoretical ideas to surface observations of Europa, Enceladus, Titan, and other moons.

Tectonic Resurfacing Processes on Ganymede, Insights From Physical Models. D. W. Sims[1], D.Y. Wyrick[1], and R. T. Pappalardo[2], [1]Dept. of Earth, Material, and Planetary Sciences, Southwest Research Institute®, 6220 Culebra Rd., San Antonio, TX, 78238, dsims@swri.org, [2]Jet Propulsion Laboratory, Pasadena, CA 91109.

Introduction: Grooved terrain on Ganymede generally occurs as individual lanes and polygonal cross-cutting swaths of bright terrain. Internally, grooved terrain swaths consist of parallel to sub-parallel ridges and troughs at a variety of scales; the ridges and troughs generally show similar morphology, size, and orientation. Grooved terrain on Ganymede has been interpreted by most authors as the product of fault-accommodated, distributed crustal extension, possibly accompanied by cryovolcanism [1-5]. It is generally assumed that Ganymede's lithosphere is a thin (~2 km), brittle, upper crust of predominantly water ice above an icy ductile horizon. Fault scarps are clearly observable in images of Ganymede's surface, indicating that the uppermost crust deforms as brittle material.

Fault spacing on Ganymede has been interpreted as proportional to lithospheric thickness [4]. Dombard and McKinnon [6] modeled multiple wavelength instabilities of magnitudes similar those interpreted to occur on Ganymede. The results of their models are consistent with their assumption [after 5] that the lithosphere is fractured on a scale smaller than ridge-and-trough system wavelengths. Our physical models show faulting and fracturing on a scale smaller than the relatively large displacement faults that bound ridge and trough systems [7]. Studies of fracture (joint) spacing in layered rock on Earth show a range of both linear and non-linear proportional relationships between joint spacing and layer thickness [8,9,10]. These studies, most often confined to rock layer thickness of less than two meters, suggest that spacing is influenced by layer thickness, structural position, and mechanical properties of the rock [11]. These fractures are often confined to strong layers and do not pass through weaker, less cohesive layers. Terrestrial fracture data show that the relationship between bed thickness and fracture spacing varies widely with structural position, even within the same geologic formation [9].

Methodology: We use physical analog models to simulate the formation of grooved terrain by normal faulting in response to distributed extension in a brittle layer over a horizontal detachment surface [11]. The brittle lithosphere is represented by a 1 to 2.5 cm constant-thickness claycake that deforms by faulting and behaves as a time-independent material at the strain rates interpreted for crustal processes. Extension is distributed across the claycake by a rubber sheet at its base.

Results: Fault dip and fault spacing are important variables for estimating extension. Fault dip and spacing exhibit strong control on surface morphology and topography, including ridge and trough symmetry, slope angles of both the fault scarp and the upper free surface of half-graben fault block, and the magnitude of topographic relief [5]. Our physical models show that initial fault dips of 60-80° result in surface morphology that closely mimics the ridge and trough systems observed on Ganymede (Fig. 1). Topographic relief resulting from fault displacement increases proportional to the horizontal component of fault displacement (heave) and to the magnitude of fault dip. For a given heave, steep or high angle faults produce more topographic relief than do low angle faults, which may result in an overestimation of extension where topographic relief is the only metric for fault displacement.
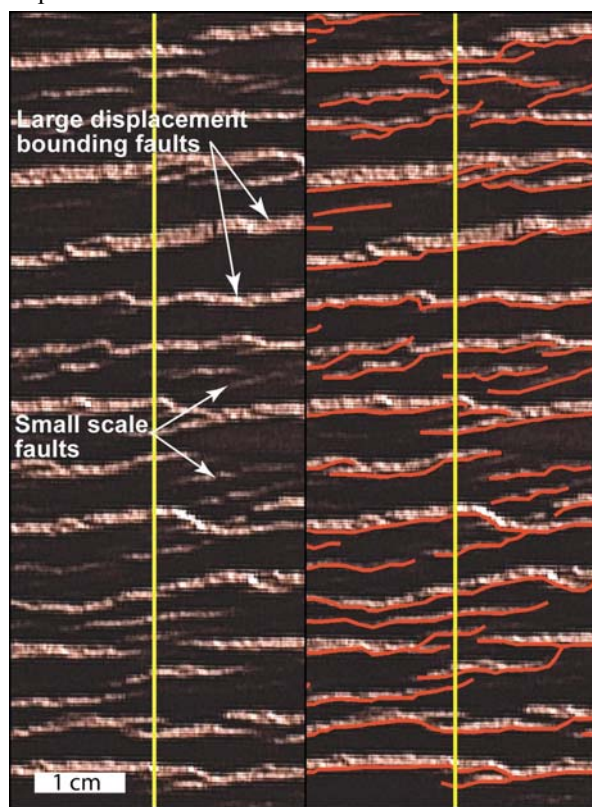

Figure 1. Model fault development showing both large displacement bounding faults and small scale faults.

Red lines are interpreted footwall traces. Yellow scanline is parallel to extension direction.

Further, where crustal thinning or necking is accommodated by brittle faulting, steep faults are more efficient because small horizontal displacements translate to large vertical displacements.

Rotated block faulting, such as is interpreted to occur on Ganymede, requires a relatively weak zone at some depth to accommodate fault-block rotation. In our models, this weak zone is represented by the rubber sheet at the base of the model layer. On Ganymede, the simplest case would be that the weak zone or detachment is the lower boundary of the lithosphere. Our models represent this simple case of a single weak layer at the base of the rotated fault blocks. However, we do not infer that faulting on Ganymede must necessarily be rooted at the base of the lithosphere.

Fault spacing on Ganymede is mappable to the limit of image resolution. The thickness of Ganymede's lithosphere is generally accepted to be less than ten kilometers, and often interpreted to be on the order of a few kilometers [4]. Our models are scaled to represent layer thickness of a few kilometers or less. The claycake in the pre-deformation state may be considered homogeneous and isotropic, and experimental results are reproducible. This provides assurance that the effects resulting from change of a single variable, such as layer thickness, can be isolated, thus giving insight into thickness and fault-spacing relationships on Ganymede.

Preliminary model results suggest a relationship between layer thickness and fault spacing. Figure 2 shows results from 1, 2, and 2.5 cm thick claycake models. Each model represents a distributed-extension (25%) half-graben system. Spacing is measured parallel to extension direction (Fig. 1), and only large-scale faults that bound ridge and trough systems are considered. The number of samples for each model ranges from 24 to 40. Figure 2 suggest a relationship between layer thickness and fault spacing. Although these data are too few to draw firm conclusions, they strongly support a relationship between fault spacing and lithospheric thickness. A regression line is plotted for illustrative purposes only.

Conclusions: Results from physical modeling of tectonic resurfacing give insight to the control of geometric features such as fault dip and spacing upon the processes and results of rotated half-graben faulting. Compared with shallowly dipping faults, steep faults require less extension to produce appreciable topographic relief .

Preliminary results that test the effect of layer thickness upon fault spacing in physical models suggest a positive correlation between model thickness and the spacing of relatively large-displacement faults that bound ridge and trough systems.
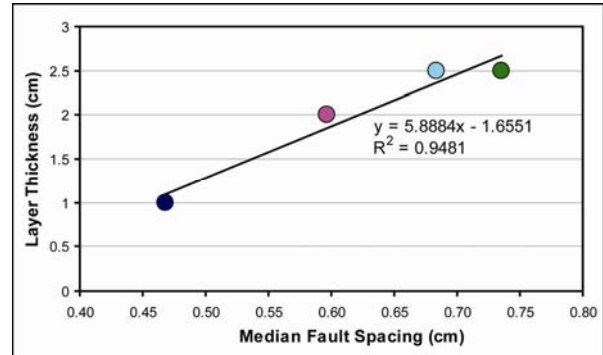
Figure 2. Chart plotting layer thickness versus fault spacing..

References: [1] Shoemaker, E.M. et al. (1982), In *Satellites of Jupiter*, Morrison, D., ed., University of Arizona Press, Tucson, 435–520. [2] Squyres, S.W. and Croft, S.K. (1986) In *Satellites*, Burns, J. and Matthews, M., eds., University of Arizona Press, Tucson, 293–341. [3] Pappalardo, R.T. et al. (1998) *Icarus 135*, 276–302. [4] Pappalardo, R.T. et al. (2004) In *Jupiter: The Planet, Satellites & Magneto-sphere*, F. Bagenal et al., eds., Cambridge University Press, Cambridge, 363-396. [5] Collins, G.C. et al. (1998) *GRL 25*(3), 233-236. [6] Dombard, A.J. and McKinnon, W.B. (2001) *Icarus 154*, 321-336. [7] Sims, D.W. et al. (2006) LPSC XXXVII, #1774. [8] Lerche, I., and Narr, W. (1986) *Soc. Petrol. Eng. Formation Evaluation*, 249-258. [9] Narr, W. (1991) *AAPG Bull. 75*(8), 1300-1323. [10] Narr, W. and Suppe, J. (1991) *J. of Structural Geology 13*(9), 1037-1048. [11] McQuillan, H. (1973) *AAPG Bull. 57*(12), 2367-2385.

STUDIES OF VISCOUS RELAXATION OF CRATERS ON ENCELADUS. D. E. Smith[1], V. J. Bray[2], E. P. Turtle[3], H. J. Melosh[1], and J. E. Perry[1], [1]Department of Planetary Sciences, University of Arizona, 1629 E. University Blvd, Tucson, Arizona 85721-0092 (dsmith@lpl.arizona.edu), [2]Imperial College London, Exhibition Road, London, SW7 2AZ, United Kingdom, [3]Johns Hopkins University Applied Physics Laboratory, 11100 Johns Hopkins Road, Laurel, Maryland 20723-6099.

Introduction: Enceladus' icy surface displays evidence of a wide range of diverse terrains and geologic processes including fractures, ridges, active plumes, and variable crater density [e.g., 1, 2]. Considering Enceladus' lack of radiogenic heating (~500 km in diameter) and low availability of tidal heating [1], this amount of geologic activity is somewhat mysterious. There are heavily cratered areas and others almost devoid of craters, and the craters display a range of morphologies including both relaxed and unrelaxed forms. In some areas both relaxed and unrelaxed craters are present together. Such a heterogeneous surface raises many questions into the nature of Enceladus' subsurface and rheology. By studying craters that have undergone different degrees of viscous relaxation and the distribution thereof, we can constrain Enceladus' subsurface rheologic and thermal properties.

Observations: The Imaging Science Subsystem (ISS) aboard the Cassini spacecraft has observed Enceladus many times during encounters with the satellite. These images have revealed diverse terrains of ridges, fractures, and both relaxed and unrelaxed craters on Enceladus' surface. It has also been observed that there is an active plume erupting from an obvious heat source at the South Pole [2]. The observed plume activity gives evidence that the South Pole is a currently geologically active region. This is supported by the general lack of craters in the South Polar Terrain (SPT), which indicates that the surface is relatively young. Such a strong heat source may have a profound effect on the relaxation of geologic features, and we indeed observe a lack of craters in the southern latitudes. Figure 1 shows a good demonstration of a group of unrelaxed craters around 42°N, 344°W. In contrast, Figure 2 illustrates an example of an impact crater that has undergone a large degree of relaxation.

Crater morphology over time is known to respond to local heatflow. Therefore, the study of the impact craters on Enceladus can reveal variations of heatflow based on the change in relaxation state with latitude (Figure 3). Figure 3 demonstrates how these relaxed craters are distributed over most of the surface of Enceladus. We observe that the number and extent of relaxed craters is higher in the southern latitudes as well as a general increasing trend in the relaxation state moving toward the south [3, 4].

Modeling: For a material that obeys a Newtonian rheology, viscosity is independent of the state of stress and its behavior can be represented analytically [5]. Analytic solutions can be derived by decomposition of the crater topography into J_0 Bessel functions to illustrate basic first-order evolution of crater topography as a result of viscous relaxation [4]. However, the nature of ice is non-Newtonian [e.g., 6], which means that the viscosity is actually stress dependent. Analytical modeling, although good to first order, fails in this regime [4]. To more accurately model Enceladus' icy lithosphere, it is necessary to explore numerical modeling of our problem. For this, we will use finite-element analysis to explore crater relaxation on Enceladus using Tekton, a finite-element analysis tool [7].

References: [1] Brown, R.H. et al. (2006) *Science*, 311, 1425–1428. [2] Porco, C.C. et al. (2006) *Science*, 311, 1393–1401. [3] Bray, V.J. et al. (2007) *LPSC XXXVIII,* Abstract #1873. [4] Smith, D.E. et al. (2007) *LPSC XXXVIII,* Abstract #2237. [5] Melosh, H.J. (1989) Impact Cratering: A geologic process, Oxford University Press. [6] Durham, W.B. et al. (1997) *JGR*, 102, 16, pp. 293-302. [7] Melosh J. and Raefsky (1980), *Geophys. J.R. Astr. Soc.*, 60, 333.
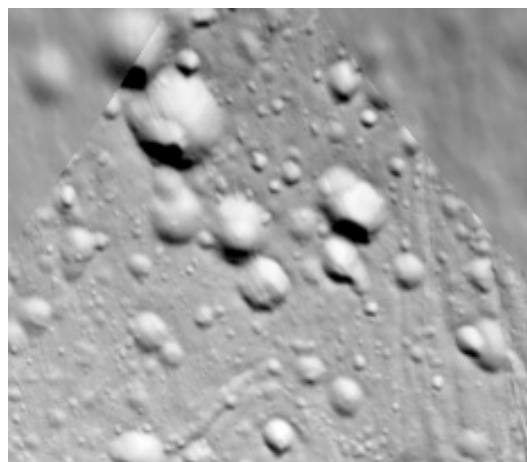
Figure 1. Group of unrelaxed craters in the northern latitudes centered at about 42°N, 344°W. The largest crater in this image is ~10 km in diameter. Relaxed craters are also present in the northern hemisphere, which is expected for old craters in ice that is warm enough to be mobile. These relaxed craters in the North represent somewhat larger and older craters when compared to craters in the South.

Relaxation States of Craters and their location
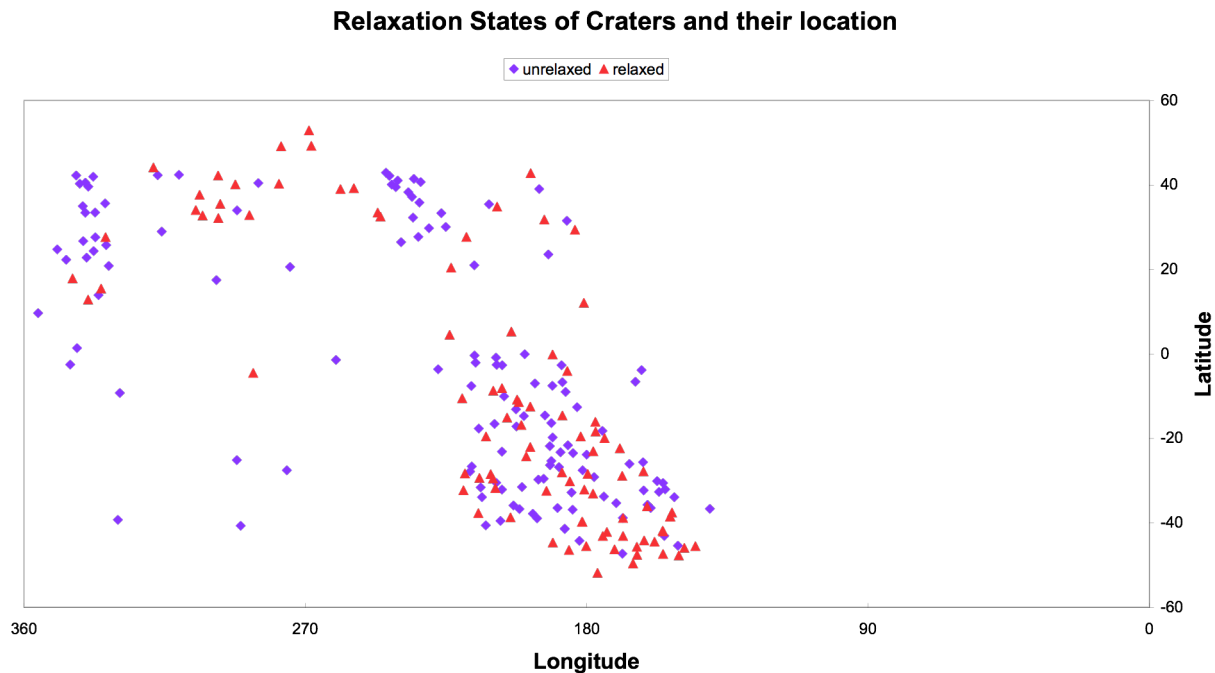
Figure 3. Crater relaxation as a function of latitude on Enceladus. The region between 0° and ~140°W has only been imaged at low resolution (~1 km/pixel) and was not included in this survey. This region or parts of it may be observed at higher resolution during the Cassini extended mission. Although the number of relaxed craters in the southern latitudes may not be statistically greater than those in the northern latitudes, the degree of relaxation exhibited by southern craters is, indeed, greater than for those observed in the north.
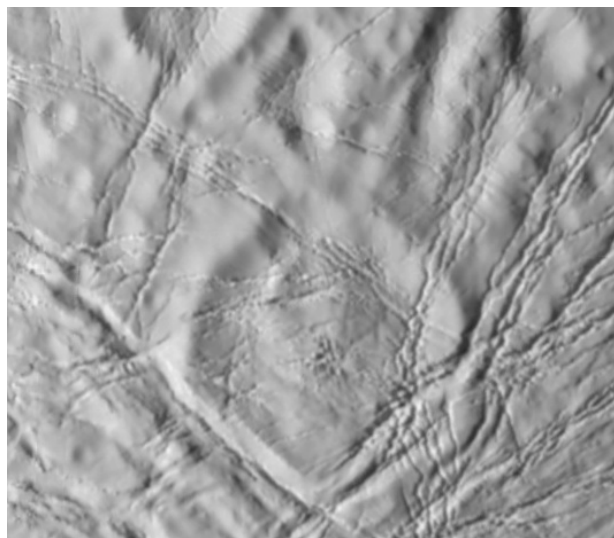
Figure 2. Example of a relaxed crater centered at approximately 52°S, 177°W. Note the upbowed floor and the persistent rim that is characteristic of crater relaxation. The rim-to-rim diameter of this crater was measured to be approximately 22 km.

TIDALLY DRIVEN FAULT DEFORMATION AND STRESS ACCUMULATION AT ENCELADUS'S TIGER STRIPES.
Bridget R. Smith-Konter[1] (Bridget.R.Konter@jpl.nasa.gov), Zane Crawford[1,2], and Robert T. Pappalardo[1], [1]Jet Propulsion Laboratory, California Institute of Technology, [2]Laboratory for Atmospheric and Space Physics, University of Colorado, Boulder.

Introduction: Cassini observations of the south polar region of Enceladus revealed four large linear fractures associated with anomalous temperature gradients and active plumes [1, 2]. These features, referred to as "tiger stripes", are now thought to be the source of tectonic strike-slip and/or oblique open-close motions [3,4], similar to those of the faulting regimes inferred for Jupiter's moon Europa [5]. These motions are likely a result of tidally induced stresses that are exerted on a satellite during its daily orbital (diurnal) cycle around its parent body.

In this study, we investigate tidally driven strike-slip and fault-normal deformation of Enceladus's tiger stripes and their resulting failure stress behavior over a complete Enceladus tidal cycle. We simulate 3D surface deformation and stress changes at depth by specifying tidally induced stresses across inferred tiger stripe fault planes. Our approach can be summarized in three primary steps: (1) calculate tidal stresses that will act as the driving forces for shearing and normal motions; (2) integrate these stresses into a 3D time-dependent fault dislocation model to evaluate tidally induced displacements and stress changes at depth; (3) calculate resulting fault-to-fault stress interactions and failure conditions as a function of position within the orbital cycle.

While previous studies have followed a similar approach to investigate individual modes of failure (shear vs. normal) of the tiger stripes [3, 4], this work differs in that (1) contributions of both shear and normal stress are considered and (2) a sophisticated 3D viscoelastic dislocation model is used to kinematically drive displacements and inspect resulting stress changes of the tiger stripe fault system. Here we present preliminary results demonstrating the role of aseismic secular displacements at depth, which impart stress changes onto each tiger stripe fault plane within the shallow brittle layer. As an example of this method, we demonstrate this behavior for tidally induced left-lateral strike-slip motions for the first half of Enceladus's orbit. Future applications of this approach are valid for deformation studies of Europa and other icy moons of the outer solar system where diurnal stress variations are important.

Stress Modeling:
Tidal Stress Model. We assume that diurnal tidal stresses provide sufficient driving forces for shear and normal fault motions to occur along the tiger stripe fractures. To extract the tidal diurnal stress components, we utilize the computer program SatStress [6], a numerical modeling code that calculates the 2D tidal stress tensor at any point on the surface of an icy satellite for diurnal and/or non-synchronous rotation stresses. We adopt model parameters appropriate for an Enceladean ice shell of thickness 24 km underlain by a global subsurface ocean [3]: Love numbers h_2 = 0.2 and l_2 = 0.04, shear modulus μ = 3.5 GPa, Poisson ratio ν = 0.33, gravity g = 0.11 m/s^2, radius r = 252 km, and eccentricity e = 0.0047. For Enceladus, we also assume that satellite obliquity is zero and we neglect any non-synchronous rotation. Using these parameters, we calculate tidal diurnal stresses in the region of the tiger stripe fractures, which approach peak absolute amplitudes of ~70 kPa throughout the tidal cycle. To provide shear and normal driving stresses for the dislocation model, we resolve shear (τ_s) and normal (σ_n) stresses onto discrete tiger stripe fault elements of specified orientation [3, 4, 7].
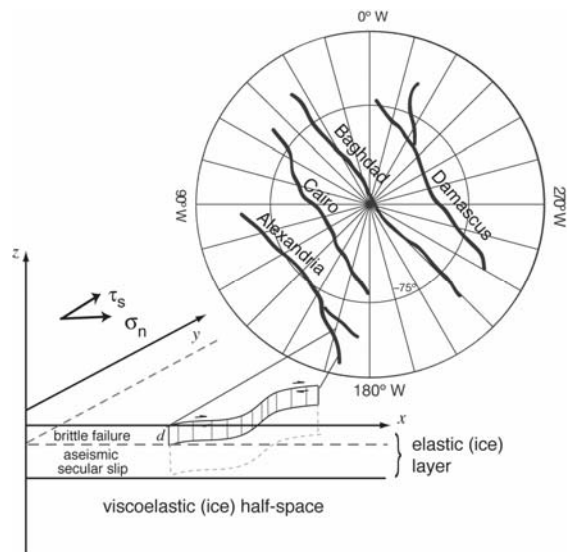
Fig 1. Polar stereographic projection of Enceladus tiger stripes and 3D sketch of viscoelastic dislocation model. Deformation is kinematically driven by prescribed diurnal tidal stresses at each tiger stripe location throughout the tidal cycle. Discrete vertical fault planes are embedded in an elastic ice layer that responds to both shallow brittle failure and deep secular slip. Both near-field (shallow, coseismic) and far-field (deep, aseismic) displacements can be prescribed along each fault plane.

Viscoelastic Dislocation Model. Using the tidal stresses derived above, we simulate strike-slip (shear) and open-close (normal) surface deformation on a set vertical fault planes embedded in an elastic layer overlying a viscoelastic half-space (Fig. 1). We use a 3D semi-analytic dislocation model [8, 9], originally developed for terrestrial applications, which calculates displacement, stress, and strain caused by horizontal shear, vertical shear, or fault-normal displacement as a

function of depth. The model assesses displacements and stresses at variable temporal scales. Analogous to a fractured terrestrial tectonic plate, shallow brittle failure drives both an elastic and time-dependent vis-coelastic response at depth due to a redistribution of stress imparted by the breaking of a fault. Secular (or long-term, time-invariant) slip beneath the fault assumes a purely elastic model and captures the aseismic response of the moving fault system. The model is sensitive to fault locking (or brittle-layer thickness) depth d, total elastic ice layer thickness (which includes zones of both aseismic and brittle failure), viscosity η, and the restoring force of gravity, g. Here we assume $d = 4$ km, $\eta = 10^{15}$ Pa s, and other model parameters identical to those used to derive the tidal stresses.

The tiger stripe dislocations are projected about an effective pole of deformation and placed into a model-space Cartesian coordinate system (Fig. 2). We apply a depth-integrated stress [10] that drives slip at depth, which then generates stress changes within the shallow brittle (locked) layer. Both shear and normal stresses are applied along the vertical fault patches as a function of orbital position. The applied shear stresses mainly drive fault-parallel strike-slip displacements, while normal stresses control the opening and closing displacements of the fracture system.

To investigate the role of stress change within the brittle layer as a function of orbital position, we also calculate Coulomb stress change, σ_f [7]. According to the Coulomb failure criterion ($\sigma_f = \tau_s - \mu_f \sigma_n$), frictional sliding will occur on optimally oriented fault segments when the resolved shear stress exceeds the frictional resistance on the fault, which is a function of the normal stress and the effective coefficient of friction ($\mu_f = 0.3-0.7$). We compute Coulomb stress change to identify regions of the fault system that are more or less likely to fail throughout the tidal cycle for a given set of applied conditions. We also use Coulomb calculations to investigate the implications of stress triggering (enhanced failure conditions on a fault segment due to an imparted coseismic stress change on neighboring fault segments), and any temporal variations in stress due to viscoelastic relaxation.

Preliminary Results: Using tidally driven stresses, which are resolved onto the tiger stripe fault planes as a function of orbital cycle, we simulate shear aseismic displacements and generate maximum shear deformation at periapse (left-lateral) and apoapse (right-lateral). These deformations range from +/- 20 mm in the horizontal (fault parallel and perpendicular) directions and +/- 2 mm of vertical uplift and subsidence. Likewise, maximum Coulomb stress change for the entire fault system (Fig. 2) is inferred at periapse (left-

lateral shear) and weakens as Enceladus advances in orbital location, reaching a minimum at periapse + 120°. Subsequent orbital positions yield an increased Coulomb stress change, although in a right-lateral sense, as the satellite approaches apoapse. This behavior is repeated, although in the opposite sense, as the second half of the orbital cycle is completed. Using the Coulomb failure criterion, it is feasible to predict failure direction, frequency, and location along each tiger stripe throughout the orbital cycle. We are presently compiling a suite of time-dependent models that simulate these stress behaviors, in addition to those of tidally forced dislocations due to the opening/closing of a fault, to investigate possible failure scenarios and stress triggering interactions of the tiger stripe fault system.
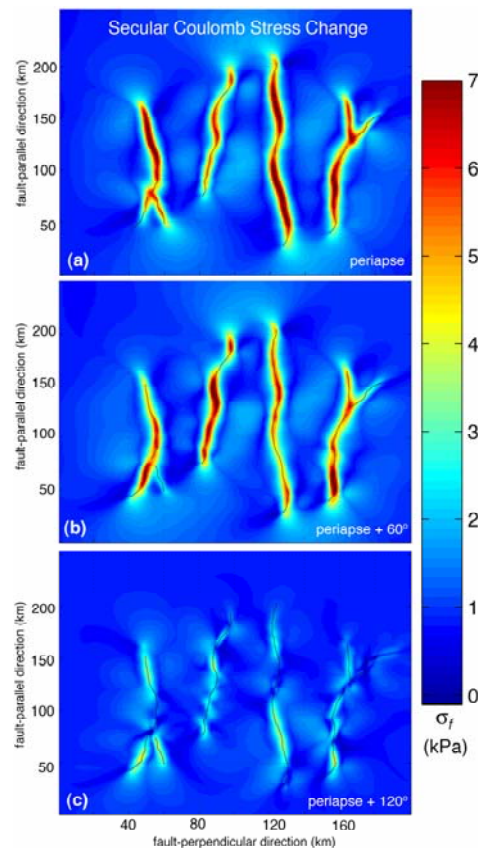
Fig. 2. Snapshots of secular Coulomb stress change, σ_f (kPa), due to tidally induced left-lateral displacements within the deep aseismic layer, observed at (a) periapse, (b) periapse + 60°, and (c) periapse + 120°. Stresses are observed at a depth of 2 km within the brittle layer. Large, positive stresses are indicative of fault segments that are brought closer to failure within the brittle layer.

References: [1] Porco, C.C. et al. (2006), *Science*, 311, 1393-1401. [2] Spencer, J.R. et al. (2006), *Science*, 311, 1401-1405. [3] Nimmo, F. et al. (2007), *Nature*, 447, 289-291. [4] Hurford, T.A. et al. (2007), *Nature*, 447, 292-294. [5] Hoppa, G.V. et al. (1999), *Icarus,* 141, 287-298. [6] Wahr, J. et al., in preparation. [7] King.G.C.P. et al. (1994) *BSSA*, 84, 935-953. [8] Smith, B., and D.T. Sandwell (2003), *JGR.*, 108, doi:10.1029/2002JB002136. [9] Smith, B., and D.T. Sandwell (2004), *JGR*, doi:10.1029/2004JB003185. [10] Sandwell D.T. et al. (2004), *JGR,* 109, doi:10.1029/2004JE002276.

Processes Shaping Galilean Satellite Atmospheres from the Surface to the Magnetosphere.

W. H. Smyth[1] and M. L. Marconi[2], [1]Atmospheric and Environmental Research, Inc. (131 Hartwell Avenue, Lexington, MA 02421, wsmyth@aer.com), [2]Prisma Basic Research (1625 Buffalo Avenue, Niagara Falls, NY 14303).

Introduction: The atomic and molecular species in the atmospheres of the Galilean satellites provide a direct link to surface processes and interior composition. The structure and abundance of gases in the atmospheres are established by the flow of gases (or supply rates) between the satellite surface, the bound atmosphere, and the extended neutral clouds of gravitationally escaping gases that form asymmetric gas tori about Jupiter, where the gas densities in the vicinity of the satellite orbit are peaked about the satellite's location. The distribution and loss of these gases are also shaped by their interactions with the planetary magnetosphere, and these gases consequently supply ions to and alter the properties of the planetary magnetosphere. In turn, alterations in the magnetosphere can affect the surfaces and atmospheres of the Galilean satellites. This overall complex flow of gases from the satellites has been best studied for Io, less well studied for Europa, even less well studied for Ganymede, and virtually unstudied for Callisto.

Io has a bound atmosphere dominated by SO_2, which is supplied by active volcanoes and sublimation of surface frost. The interaction and the relative source rates of the day-to-night supersonic flow of the sublimation atmosphere and the volcanic plume atmospheres as well as the global nature of Io's atmosphere during eclipse in Jupiter's shadow are topics of great interest. The electrodynamic interaction of the corotating plasma torus with the satellite [1] drives atmospheric chemistry [2] and gas escape [3, 4, 5] and creates neutral emissions [6, 7] in (1) a "limb glow" all around the satellite, (2) equatorial aurorae near the sub-Jupiter and anti-Jupiter points, and (3) a near portion of the Io plasma wake. The SO_2 family (SO_2, SO, O_2, O, S) of species as well as minor gas species (Na, K, S_2, NaCl) in the atmosphere have substantial escape rates that create circumplanetary gas tori which, through electron impact ionization and charge exchange reactions together with direct ion escape from the satellite, supply the primary source of the heavy-ions (O^+, O^{++}, S^+, S^{++}, S^{+++}) for the Io plasma torus and the larger planetary magnetosphere [8, 9]. A significant fraction (~60%) of neutrals originally lost from Io are lost from the Jupiter system as fast neutrals through charge exchange reactions, and the remaining are transported outward as plasma and ultimately lost down the magnetotail. Some of these ions, initially derived from materials on Io's surface and interior, also contribute to the energetic particles

and thermal plasma that process the surfaces of Europa and Ganymede and create their atmospheres.

Europa has a bound atmosphere dominated by O_2 at lower altitudes and by H_2 at higher altitudes [10], both noncondensable chemical products arising from the H_2O family (H_2O, OH, H_2, O_2, O, H) of species supplied from the water ice surface by ion sputtering and more complex sub-surface processes [11]. Hubble Space Telescope observations [12, 13] of O (1304 Å, 1356 Å) emissions, produced by magnetospheric electron impact dissociative excitation of O_2, have confirmed a tenuous but collisional atmosphere. Ground-based observations of Europa [14, 15] have also detected the minor atmospheric species Na and K likely liberated from surface salts supplied by underlying ocean brines [16]. The escape of these atmospheric species creates gas tori, whose size and density for the dissociative products O and H are determined by exothermic reaction energies and plasma interactions as well as by dissociation and dissociative recombination reactions of molecular ions like H_2^+ in the magnetosphere. H due to its light mass will be created with high velocities and therefore will be distributed at low density throughout the entire planetary system. The dominant H_2 gas torus, characterized primarily by thermal escape and consequently much more localized about the satellite orbit, has a circumplanetary gas population that is even larger than that for the O and S gas tori for Io [10]. The Europa gas tori thereby establish within the magnetosphere a second prominent circumplanetary maximum both in the radial neutral-density profile and in its corresponding instantaneous ion production-rate profile. These substantial circumplanetary neutral distributions can alter the thermal plasma in ways yet to be determined and are known to alter the population and pitch angle distribution of inward-moving energetic particles through charge exchange reactions, creating copious quantities of energetic neutral atoms [17] that rapidly escape the Jupiter system.

Ganymede, which has a substantial intrinsic magnetic field that includes both closed and open field line regions, is thought to have a more complex two-part atmospheric structure [18]. H_2O is predicted to be the primary bound atmospheric species in the closed field line region near the subsolar point, where the dominant gas source is H_2O sublimation. O_2 and H_2 are predicted to be the primary bound atmospheric

species near the poles in the open field line regions, where magnetospheric ion sputtering is the dominant gas source, and are also predicted to be the primary bound atmospheric species within the nightside atmosphere. Hubble Space Telescope observations of O (1304 Å, 1356 Å) emissions [13, 19] have been interpreted as being produced by magnetospheric electron impact dissociation of O_2 in a collisional but tenuous atmosphere.   H, which is expected to be produced mainly from electron impact dissociation of H_2, has also been detected with the Hubble Space Telescope [19] and the Galileo UV spectrometer [20] in an extended distribution from near the surface to several Ganymede radii via its scattering of solar Lyman-α photons.   Pickup ions formed in the atmosphere can accumulate in the closed field line regions and escape more readily in the open field line regions, affecting the charge exchange loss of neutrals from the atmosphere and the detection of near-satellite ions, as is the case for Europa, through pickup ion signatures [21] and ion-cyclotron waves [22].   In addition, substantial gas escape rates are expected from dissociative products, mainly O and H, with exothermic reaction energies forming even more distant gas tori about the planet. The primary escaping species and also dominant species at higher altitudes is, however, H_2. Like the H_2 from Europa, the H_2 from Ganymede escapes thermally and is also expected to form a torus but one that is more dispersed due to its larger distance from Jupiter.

In   summary,   neutrals,   ions,   and   their emissions along the flow of gases from the satellite surface, to the bound atmosphere, to the extended neutral clouds, and to the magnetosphere contain vital information that, through measurements and modeling, provides a powerful approach to connect and illuminate the physical processes that occur along this chain of events.

References: [1] Saur J. et al. (1999) *JGR, 104*, 25105-25126. [2] Smyth W. H. and Wong M. C. (2004) *Icarus, 171*, 171-182. [3] Smyth W. H. and Combi M. R. (1997) *Icarus, 126*, 58-77. [4] Smyth W. H. and Marconi M. L. (2000) *JGR, 105*, 7783-7792. [5] Wilson J. et al. (2002) *Icarus, 157*, 476-498. [6] Roesler F. L. et al. (1999) *Science, 283*, 353-357. [7] Retherford K. D. et al. (2000) *JGR, 105*, 27157-27165. [8] Smyth W. H. and Marconi M. L. (2003) *Icarus, 166*, 85-106. [9] Smyth W. H. and Marconi M. L. (2005) *Icarus, 176*, 138-154. [10] Smyth W. H. and Marconi M. L. (2006) *Icarus, 181*, 510-526. [11] Johnson R. E. and Quickenden T. I. (1997) *JGR, 102*, 10985-10996. [12] Hall D. T. et al. (1995) *Nature, 373*, 677-679. [13] Hall D. T. et al. (1998) *Ap.J., 499*, 475-481. [14] Brown M.E. and Hill R.E. (1996) *Nature, 380*, 229-231. [15] Brown M. E. (2000) *Icarus, 151*, 190-195. [16] Leblanc F. et al. (2002) *Icarus, 159*, 132-144. [17] Mauk B. H. et al. (2003) *Nature, 421*, 920-922. [18] Marconi M. L. (2007) *Icarus*, in press. [19] Feldman P. D. et al. (2000) *Ap. J., 535*, 1085-1090. [20] Barth C. A. et al. (1997) *GRL, 24*, 2147-2150. [21] Paterson W. R. et al. (1999) *JGR, 104*, 22779-22792. [22] Volwerk M. et al. (2001) *JGR, 106*, 26033-26048.

3-D MULTI-FLUID MODEL OF THE PLASMA INTERACTION AT TITAN HIGHLIGHTING THE IMPORTANCE OF ION GYRORADUS EFFECTS.

D. Snowden[1] and R. Winglee [1]University of Washington, Box 351310 , Seattle WA 98195-1310, dsnowden@u.washington.edu

Abstract: Using a 3D multi-fluid simulation we show that finite ion gyroradius effects are important in characterizing the plasma interaction at Titan. The plasma interaction is similar to that at Venus and Mars in that the incoming flow is deflected around Titan through an interaction with Titan's ionosphere. This interaction forms an induced magnetosphere that consists of a cavity region around Titan and a wake of outflowing plasma. However, the plasma interaction at Titan is significantly different from Venus and Mars because the incident ions have gyroradii on the order of Titan's diameter. The multi-fluid method is ideal for studying Titan's plasma interaction with Saturn's magnetosphere because it incorporates ion cyclotron and multi-ion species effects similar to hybrid codes but the fluid treatment enables grid refinement down to as small as 26 km.

The results from our three dimensional multi-fluid simulation demonstrates that ion gyroradius and heavy ion effects cannot be neglected when characterizing the plasma interaction near Titan. Ion gyroradius and heavy ion effects drastically change the mass loading and magnetic field draping around Titan. The asymmetric pick-up of ions from Titan's ionosphere leads to a very asymmetric mass loaded region. We find that the large ion gyroradius of picked-up ionospheric species results in an extension of the ionosphere and, therefore, the mass loading and magnetic pile-up on the anti-Saturn side of Titan. Also, the additional thermal pressure provided by heavy ion cyclotron motion in the near Titan causes the shielding currents to form at higher altitudes. The flow of energetic ions into Titan's ionosphere is also greatly affected by the inclusion of ion gyroradius effects. Ions on the anti-Saturn side of Titan's magnetosphere are accelerated away from Titan's into Saturn's magnetosphere however ions on the Saturn facing side of Titan's are accelerated towards Titan and back into the ionosphere. Therefore, the Saturn facing side of Titan's ionosphere experiences both less shielding from incident Kronian plasma and additional heating due to the acceleration of heavy ions in the ionosphere.

Finally, ion gyroradius effects also very important to the dynamics of ion outflow into the Kronian magnetosphere. We find that well confined heavy ion beams form on the anti-Saturn side of Titan's magnetosphere and extends more than three Titan radii from Titan's main ion tail before rejoining the ion tail about six Titan radii downstream. The location of this ion beam is dependent on the Kronian field orientation and we find that during the TA, TB, and T3 encounters the bulk of the ion beam was located below Titan's equatorial plane. We also find good agreement with Cassini magnetometer data from the TA, TB, and T3 encounters and the ion loss rate measured by Cassini during the TA encounter for a single set of incident conditions.

These results demonstrate that heavy ion and ion cyclotron effects change the size of the induced magnetosphere around Titan, the distribution of plasma within the induced magnetosphere, and the localized deposition of energy into Titan's upper atmosphere by pick up ions. The multi-fluid simulations also verify the formation of heavy ion beams that extend several Titan radii in to the Kronian magnetosphere.

COMPARATIVE ANALYSIS OF LONGITUDINAL DUNES ON SATURN'S MOON TITAN AND THE NAMIB DESERT, NAMIBIA.
C. Spencer[1], J. Radebaugh[1], R. Lorenz[2], S. Wall[3], J. Lunine[4], and the Cassini Radar Team, [1]Brigham Young University, Department of Geological Sciences, Provo, UT 84602 *spenchristoph@gmail.com*, [2]Johns Hopkins University Applied Physics Lab, Laurel, MD, [3]Jet Propulsion Laboratory, 4800 Oak Grove Dr., Pasadena, CA 91109, [4]Lunar and Planetary Laboratory, Univ. of Arizona, Tucson, AZ 85721.

Sand Seas on Titan: Beginning in 2005, the Cassini Titan Radar Mapper has discovered sand seas made of thousands of longitudinal dunes in the equatorial regions of Saturn's Moon Titan [1,2,3]. The dune forms observed by Cassini are similar in morphology and scale to longitudinal dune fields found on Earth [2,4,5,6]. These dunes are concentrated in the low latitudes and appear to cover as much as 40% of these terrains and 20% of Titan's total surface [4,5,6]. The longitudinal dunes of Titan have heights of roughly 100 meters, widths of 1-2 kilometers and lengths from <5 to nearly 150 kilometers [2,3,4,5].

In order to better understand the formation of these landforms and the implications for wind strength and direction on Titan, we analyze similar features found in the Namib Desert on Earth.

Namib Desert Geography and Climate: The Namib Desert is located on the southwest coast of Namibia in southwest Africa. For the most part the desert is composed of a massive sand sea covering over 34,000 km^2 [7]. The sand sea is made up of mostly longitudinal or linear dunes with minor transverse, barchan, and star dunes [7]. Precipitation in the Namib Desert ranges from 15mm/yr to the south, 14mm/yr to the north, and 23mm/yr in the interior. The Namib has a general wind direction from south-southwest to southwest along the coast and swings around inland southwest to west southwest for the greater part of the year (January to March and October to December); however, during April to September periodic winds blow from the north-northeast to east-southeast [8].

Longitudinal Dunes of the Namib Desert:

The longitudinal (linear) dunes of the Namib Desert range in size between 100-150 meters high [9] and between 1-3 kilometers apart (measured from Landsat photographs and [7]). These dunes are extremely large in comparison to other longitudinal dunes around the world, which reach only 15-35 meters high [7]. In comparison to the dunes on Titan the dunes in Namibia come closest in comparison considering their size and morphology. Where sand supply is less and/or topography creates an obstacle, barchan, transverse, and star dunes are also present with parabolic (blowout) dunes near the shoreline south of Walvis Bay.

Dune Interaction with Topography: Within the sand seas on Titan we see how the dunes interact with the surrounding topography; diverging and converging around highlands and narrowing together between two
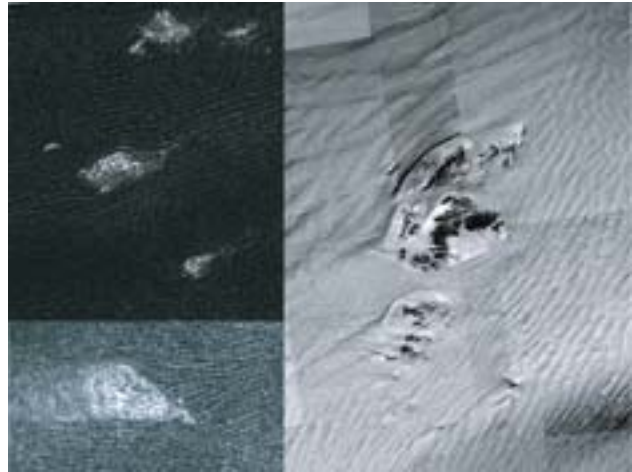
Fig. 1. Dune/topography interaction on Titan (left) and Earth (Namib) (right).

near-by highlands [5] (Fig. 1). Similar features are seen in the Namib Desert. Where sand supply is low and/or topographic obstacles are present, longitudinal dunes dominate, with only minor transverse dunes [2,5].

Dynamics of Longitudinal Dunes: It has been widely accepted that two principal wind directions perpendicular to one another are responsible for the formation of the longitudinal dunes; however, much controversy has surrounded the formation of these dunes [7,10,11]. Unidirectional wind hypotheses were proposed in earlier years, but have since been discredited [7,11].

The term longitudinal or linear dune was subdivided by [11] into lee dunes (small dunes that form behind an obstacle), vegetated linear dunes (covered by vegetation with a rounded profile), and seif dunes (forms from bidirectional winds). Because in the Namib Desert and on Titan we have neither dunes covered with vegetation nor small dunes forming behind obstacles, the most compelling hypothesis for the formation of these longitudinal dunes is the bidirectional wind hypothesis. From the formation of longitudinal seif dunes, it is affected by wind blowing obliquely from both sides of its slopes, meeting the dune at an acute angle and separated over the crestline. Each wind is diverted at the lee slope to blow parallel to the crest in a down-dune direction [11]. Evidence for this hypothesis comes from many different longitudinal dune fields around the Earth, including Australia [13], Namibia [7], and the Sahara [14].

Comparative Analysis of Dune Forms on Earth and Titan: Similarities in the presumably ongoing behavior of dunes around topography on Titan and in the Namib can be seen in Fig. 1. We also seek to understand the evolution of Titan's dunes to their current state.   Some have claimed [11,12] some longitudinal dunes are the products of the evolution of barchan and transverse dunes seen in many parts of the world's deserts [15,16,17] including Namibia [8] and the Rub al-Khali (Fig. 2). Due to the lack of barchan and transverse dunes on Titan the analog might fall short. However, because waves and/or fluvial processes eventually destroy the longitudinal dunes on Earth, we are unable to see these dunes in an advanced, evolved state. Conversely, if the dunes on Titan originally began as barchonoid and transverse dunes only to evolve into longitudinal dunes, and with no wave and minor fluvial processes to speak of in the region of the dunes, these dunes will have continued to migrate around the equatorial regions of the planet developing into what can be considered highly evolved and mature dune forms that we see now. This is not the only way in which linear dunes develop [7,10], but due to the apparent lack of other dune types on Titan, this method may be most applicable.

Because the dunes forms seen in the Namib Desert are so similar to those on Titan, a detailed macro- and microanalysis of these dunes on Earth will enable a more concise model for the genesis, evolution, and morphology of the dunes found on Titan.

References: [1] Elachi e.a. 2005. LPSC XXXVI, Abst #2294. [2] Lorenz R. e.a. 2006. Science, 312:724-27. [3] Boubin, e.a. 2005. Am. Astr. Society, DPS meeting 37:723. [4] Radebaugh, J. e.a., 2006. Am. Astr. Society, DPS mtg 38, Abst. 52.07. [5] Radebaugh, J. e.a., submitted. Icarus, in revision. [6] Lorenz R. e.a. 2007. European Geophys. Union Mtng. Abst., Vol. 9:04604. [7] McKee, E.D. 1982. USGS Spec. Pap. 188. [8] Lancaster, N. 1980. Z. f. Geomorph., 24:2:160-67. .[9] Lancaster, N. 1981. Sedimentology, 1:1-8. [10] Mainguet, M. 1984. in El-Baz, F. (ed.), Deserts and arid lands. Martinus Nijhoff Publishers, pp. 31-58. [11] Tsoar, H., 1989. Prog. in Phys. Geog., 13:4:507-28. [12] Bagnold, R. 1942. NY, W. Morrow. [13] Mabbutt, J.A. Sullivan, M.E., 1968. Austrl. Geog., 10:483-87. [14] Price, A.W., 1950. Geogr. Rev., 40:462-65. [15] Kerr, R. e.a., 1952. AAPG 36:1541-1573. [16] Tsoar, H., 1974. Z. f. Geomorph., 12:200-20. [17] Tsoar, H., 1984. Z. f. Geomorph., 28:99-103.
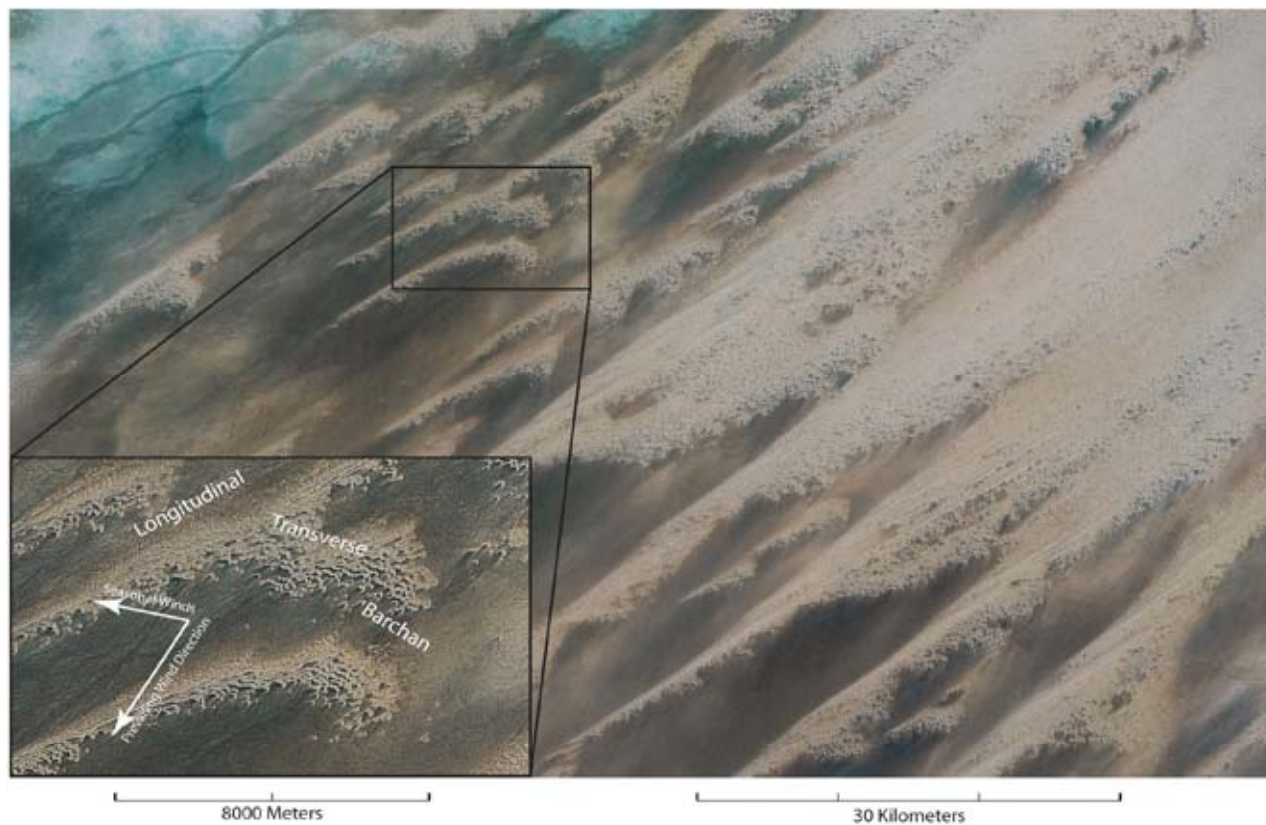

Fig. 3.: Satellite Image of the Rub al Khali, Saudi Arabia. Note the evolution of longitudinal dunes from barchan and transverse dunes. Wind directions obtained from: Dabbagh e.a. 1997. JPL Unpub: http://southport.jpl.nasa.gov/reports/finrpt/Dabbagh/dabbagh.htm.

NEW HORIZONS OBSERVATIONS OF IO'S VOLCANISM. J. R. Spencer[1], S. A. Stern[2], J. Moore[3], R. M. C. Lopes[4], K. Retherford[5], O. Abramov[5], M. Showalter[6], A. F. Cheng[2], H. A. Weaver[7], D. C. Reuter[8], A. Lunsford[8], C. Olkin[5], H. Throop[5], K. L. Jessup[5], [1]Southwest Research Institute, 1050 Walnut St., Suite 300, Boulder, CO (spencer@boulder.swri.edu), [2]NASA Headquarters, [3]NASA Ames Research Center, [4]Jet Propulsion Laboratory, [5]Southwest Research Institute, [6]SETI Institute, [7]Applied Physics Laboratory, [8]NASA Goddard Spaceflight Center.

Introduction: The New Horizons spacecraft flew past Jupiter on February 28th 2007 en route to its primary destination, the Pluto system. In addition to obtaining a gravity assist from Jupiter and taking calibration data, the spacecraft was able to conduct an extensive series of observations of the Jupiter system. Because New Horizons' closest approach distance to Jupiter, 2.3 million km, was about four times closer that that of Cassini, its data rate was much greater than that of Galileo, and it carried a suite of instruments with unique capabilities, the spacecraft was able to provide much new information about the Jupiter system.

A prime target for New Horizons was Io, which was observed with multiple instruments in 39 separate sets of observations. The observations were designed to inventory changes in Io's surface and plume activity since the last Galileo images in 2001, measure high-temperature thermal emission from Io's hot spots to constrain surface temperatures, and to study Io's auroral emissions in sunlight and Jupiter eclipse.
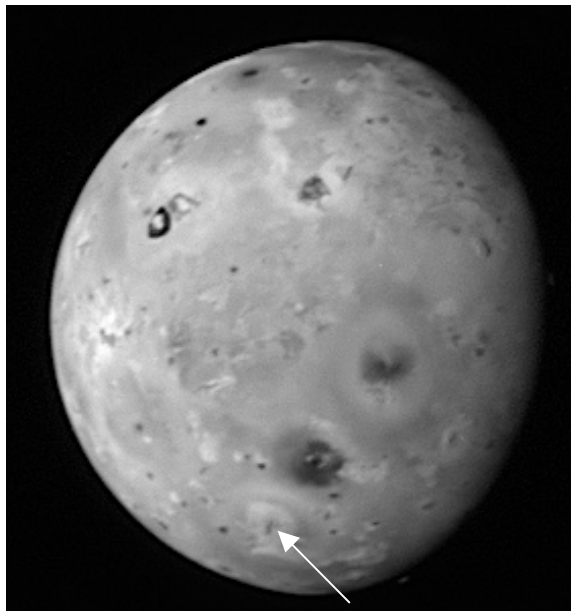
Figure 1 *LORRI image of the Jupiter-facing hemisphere of Io showing pyroclastic deposts from a new eruption at Lerna Regio (arrowed). Image taken on February 27th 2007.*

Surface Changes: New Horizons imaged all of Io's surface using its panchromatic Long-Range Reconnaisance Imager (LORRI) [1] with a resolution between 12 and 20 km/pixel, and also imaged the night side in four colors with the Multicolor Visible Imaging Camera (MVIC) [2] at a resolution of about 50 km/pixel. Many local surface changes were apparent in the more than five years since the last Galileo observations [3]. The most striking was a new 400-km diameter ring of pyroclastic deposits (Fig. 1) from a previously unknown volcanic center at Lerna Regio, near 60 S, 280 W. The 1300 km diameter pyroclastic ring from the Tvashtar volcano, centered near 60 N, 130 W, which formed towards the end of the Galileo mission, was still present.
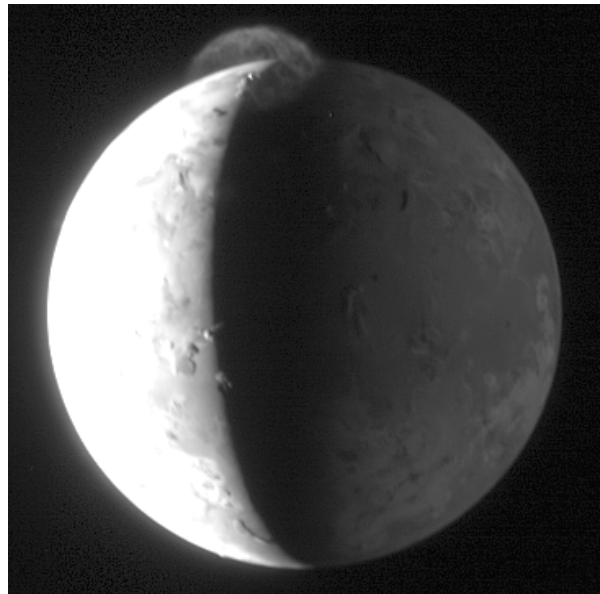
Figure 2 *The Tvashtar plume and central hot spot (near the terminator), observed by LORRI on February 28 2007. The night side of Io is illuminated by Jupiter.*

Plumes: New Horizons observed many active volcanic plumes on Io. Some, such as Prometheus and Masubi, have been active since the 1979 Voyager fly-bys, but several new plumes were also detected, including one from the Lerna Regio eruption. By far the most striking plume was from the Tvashtar volcano. A large, Pele-type [4] plume was seen by the Cassini spacecraft in 2000, at low spatial resolution at ultravio-

let wavelengths, but Galileo saw only the plume deposits, not the plume itself, due to its limited temporal coverage of Io. The New Horizons-era plume was first imaged by the Hubble Space Telescope on February 14th 2007, and was then seen in almost all New Horizons observations between February 24th and March 3rd 2007. The plume height (about 330 km) was roughly constant through the encounter. The plume showed complex filamentary structure (Fig. 2) similar to that first seen by Voyager 1 in the Pele plume, which had similar size and shape, though the structure was seen much more clearly in the New Horizons images. This structure varied dramatically on short timescales, revealing the motion of the plume particles in images taken a few minutes apart.

Hot Spots: Thermal emission from numerous volcanic hot spots was seen on Io's night side and during Jupiter eclipse, using LORRI, MVIC, and New Horizons' 1.2 – 2.5 micron Linear Etalon Imaging Spectral Array (LEISA) [2]. The Tvashtar hot spot was by far the brightest and could be seen even in daylight near the terminator by LORRI (Fig. 2). Combined thermal emission measurements of Tvashtar from 0.6 to 2.5 microns will provide valuable constraints on eruption temperatures. Another bright hot spot, near 20 N, 230 W, is from a previously-unknown volcano and showed no surface changes since Galileo observations in daytime images, possibly indicating that this is a relatively recent eruption.

Implications for Future Exploration: The New Horizons observations of Io, particularly those of the Tvashtar eruption which was unlike anything observed by Galileo during six years in Jupiter orbit, highlight the importance of good temporal coverage - something that Galileo was unable to provide - in exploring the full range of phenomena that Io can exhibit. It is likely that even more dramatic phenomena occur occasionally and have been missed by all spacecraft observations so far. Future Jupiter missions which place a high priority on good temporal coverage of Io (even at moderate spatial resolution) will generate major discoveries that will greatly increase our understanding of this remarkable world.

References: [1] Cheng, A., et al. (2007) *Space Science Reviews,* in press. [2] Reuter, D. C. et al. (2007) *Space Science Reviews,* in press. [3] Geissler, P. E. et al. (2004) *Icarus, 169,* 29-641. [4] McEwen, A. S. and L. Soderblom (1983) *Icarus, 55,* 191-217.

THE JETS OF ENCELADUS ERUPT FROM THE WARMEST REGIONS ON ITS SOUTH POLAR FRACTURES.

J. N. Spitale[1] and C. C. Porco[1], [1] CICLOPS, Space Science Institute, 4750 Walnut St., Boulder, CO 80301

Introduction: Cassini ISS images of Enceladus have revealed about a dozen jets of fine icy particles emerging from the south polar terrain (SPT) of Enceladus and feeding a giant plume that extends thousands of kilometers into space[1]. Cassini CIRS infrared observations have also shown the SPT to be anomalously warm[2], and the comparison of high resolution images of the SPT with the highest resolution thermal measurements has shown a coincidence between the hottest measured temperatures in the SPT and the "tiger stripe" fractures, which straddle the region[1,2].

Preliminary triangulation measurements of the plumes seen in a series of 11 images over 36 minutes and spanning only 7.5° of total separation, suggested that the tiger stripes are the source regions of the jets[1]. Here we use Cassini ISS images taken from a large range of viewing directions and spanning over 2 years time to determine by triangulation the precise source locations for the most obvious jets, and compare these with the CIRS hot spot locations. We also compare our results with the recently proposed localized heating mechanism[3] that predicts a daily cycle of jet activity as a result of tidally induced shearing within the tiger stripes.

Approach: Positional measurements of the jets were taken from Cassini Narrow Angle Camera images[4] obtained from a variety of look directions with respect to the surface of Enceladus and distributed in phase angle from 148° to 178°. The highest resolution image acquired at high phase angle, in which tiny particles become more visible due to the process of diffraction, clearly shows about a dozen prominent jets emanating from the south polar region of the satellite. It was taken looking perpendicular to the south polar fractures[1]. Comparable images at different geometries but somewhat poorer resolution had to be digitally enhanced to distinguish individual jets. The lowest resolution image used in this study has a spatial scale of about 14 km/pixel. Because of the tenuous nature of the jets and the (inferred) predominance of tiny, micron-sized particles, jets have been seen only in images obtained at high phase geometries – i.e., phase angles greater than about 150° – where tiny particles are bright due to diffraction scattering of light. (The ISS does not sense vapor in these images.) For most images, the sub-spacecraft latitude was within a few degrees of Enceladus' equator, putting the south pole close to the satellite's limb. In one image, the sub-spacecraft latitude was ~ 15° N.

A plume's position and direction in the two-dimensional plane of an image were measured by selecting two points: one at the base of the visible plume as seen from the spacecraft, and another at higher altitude. Each of the two points defines a geometric ray extending from the camera, and the two rays in space define a plane coincident with the plume. The sources of all of the jets contributing to the measured plume must lie somewhere on the ground track formed by the intersection of that plane with the surface of the satellite.

Results: The figure shows the locations of our jet source solutions (yellow roman numerals) as well as the locations of the hot spots (green capital letters) identified by the CIRS experiment[2]. The red regions show the CIRS footprints for each hot spot that they identified and the white circles show the scatter in our source solutions, which were observed to be comparable to the uncertainties estimated in a rigorous, but time-consuming Monte Carlo approach in which the measurement was repeated several times and the camera pointing was varied by one pixel in each direction. We see a strong correspondence between our source locations and the hottest CIRS locales: of the six sources that occur in areas covered by the CIRS observations, three overlap CIRS hot spots, and a further two are within less than one CIRS footprint of hot spots. As the latter two CIRS observations were not accompanied by simultaneous ISS imaging, the imperfect correspondence may be explained by errors in `pointing', i.e., locating the CIRS footprint on the surface. The source associated with the largest number of unambiguous sightings, source I, was not observed at high resolution by CIRS; however, their low-resolution brightness temperature map[2] does suggest elevated temperatures along the 30° W meridian in that vicinity.

Our solution accounts for the most obvious jets in our image set and associates each of them with one of the four tiger stripes. The fainter plumes observed during the two closest encounters would probably not have been visible in the other image sets and are thus impossble to triangulate. The strongest sources are on Baghdad and Damascus. For each tiger stripe, although individual jets may emerge at oblique angles, all of the jets appear to lie in nearly the same plane, which in all 4 cases is within 2° of being perpendicular to the surface. The plumes from each of the 4 fractures appear to be well collimated, with most of the visible material from the Baghdad plume confined to about ± 10° of the mean plane.

Our source locations are largely consistent with the CIRS hot spot locations[2], but disagree with the prediction of the shear-heating model[3] in that we observe Baghdad to be the most active fissure while the model predicts it to be the least active. We predict that several additional hot spots will be discovered in future Cassini thermal observations.

References: [1] Porco, C.C. *et al.* (2006) *Science* **311**, 1393. [2] Spencer, J. R. *et al.* (2006) *Science* **311**, 1401. [3] Nimmo F. *et al.* (2007) *Nature* **447**, 289. [4] Porco, C. C. *et al.* (2004) *Space Sci. Rev.* **115**, 363.
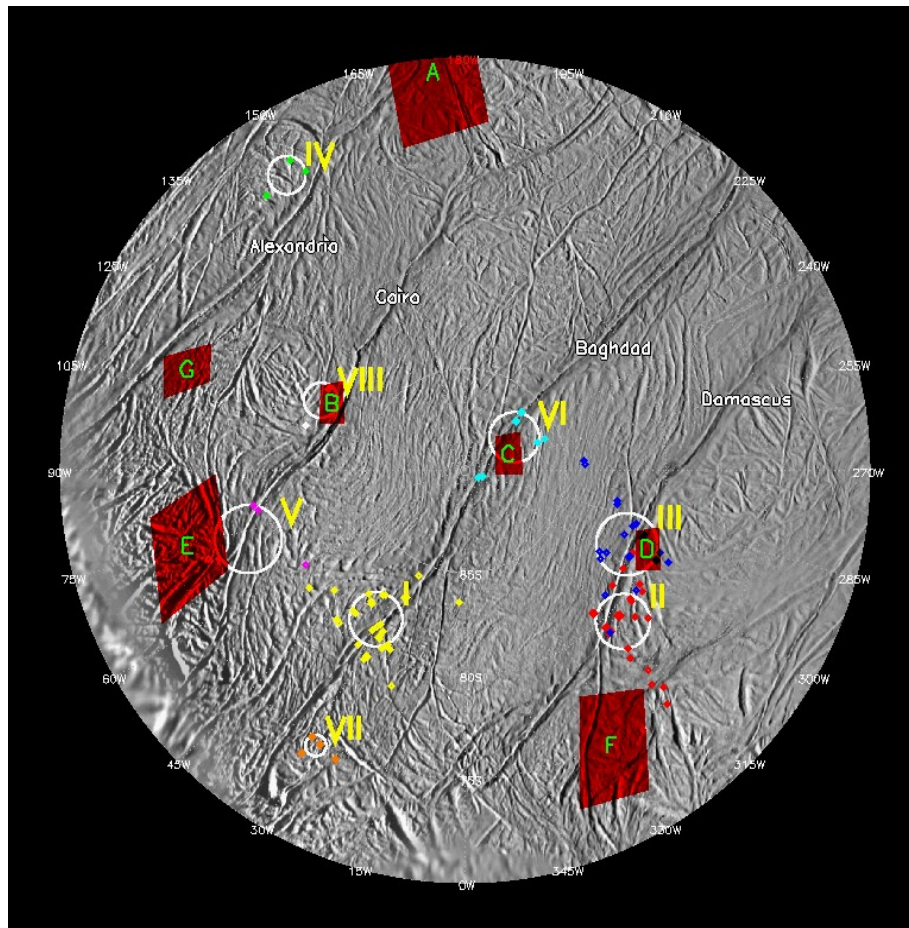
Trajectory Design for Europa Explorer

N.J. Strange, R.P. Russell, B.B. Buffington, and J.A. Sims

This poster will describe the trajectory design of the proposed Europa Explorer mission. The Europa Explorer mission is a NASA flagship-class mission will perform a low-radiation tour of the Jovian system prior to entering its final science orbit at Europa. This poster will describe the observational opportunities during the Jovian tour phase of the mission as well as the final science orbit. Orbit stability of the final science orbits will also be discussed.

Trajectory Design for Jupiter System Observer

N.J. Strange, R.P. Russell, D.F. Landau, C.L. Yen, and J.A. Sims

This poster will describe the trajectory of the proposed Jupiter System Observer mission. The Jupiter System Observer is a NASA flagship-class mission that will perform a science tour of the Jovian System and then enter into a science orbit of Ganymede.   This poster will describe the trajectory and the observational geometries during the tour and the science orbits of Ganymede.   Orbit stability of the final science orbits will also be discussed.

CASSINI IMAGING SCIENCE SUBSYSTEM OBSERVATIONS OF TITAN'S HIGH-LATITUDE LAKES.

E. P. Turtle[1], J. E. Perry[2], A. S. McEwen[2], R. A. West[3], D. D. Dawson[2], C. C. Porco[4] and S. Fussner[2], [1]Johns Hopkins Univ. Applied Physics Lab., 11100 Johns Hopkins Rd., Laurel, MD 20723, Elizabeth.Turtle@jhuapl.edu; [2]Lunar and Planetary Lab., Univ. of Arizona, 1541 E. University Blvd., Tucson, AZ 85721; [3]Jet Propulsion Lab., 4800 Oak Grove Dr., Pasadena, CA 91109; [4]CICLOPS, Space Science Inst., 4750 Walnut St., Boulder, CO 80301.

Introduction: Cassini's Imaging Science Subsystem (ISS) has been observing Titan for three years, beginning during final approach to the Saturnian system in Spring 2004 [1] and continuing through the 30 targeted Titan encounters that Cassini has performed through 12 May 2007. Titan's atmosphere obscures its surface quite effectively at visible wavelengths, so the ISS narrow- and wide-angle cameras include narrow bandpass filters at 938 nm and IR polarizer filters [2] to take advantage of a window in methane's absorption spectrum in the near-IR where the optical depth of Titan's complex organic atmospheric haze is lower and the fact that the haze is highly polarized near phase angle 90º [3]. However, even with these filters, scattering by haze particles limits the best resolution that can be achieved to ~1 km [2]. Despite the challenges presented by Titan's atmosphere, to date Cassini has imaged almost all of Titan's illuminated surface at resolutions of tens of kilometers and a substantial fraction of the surface at significantly better resolution, down to the limit imposed by atmospheric scattering. These observations have been combined to produce an albedo map of the surface (Fig. 1; see also Perry et al. [4] for even more recent observations).

Observations and Interpretations: The brightness variations revealed by ISS are due to the presence of surface materials with different albedos rather than topographic shading. Even high-phase-angle images are likely to reveal only albedo markings: (1) an icy satellite of this size is not expected to have topographic relief high enough that shadows would be detectable at kilometer scales [5]; and (2) atmospheric scattering severely reduces the contrast between slopes facing towards and away from the Sun. Observations repeated with different illumination angles have not revealed changes consistent with topographic shading.

The compositions of the materials responsible for the observed albedo variations are still not well understood; however, morphologic interpretations of ISS images as well as observations by Cassini's RADAR and Visual and Infrared Mapping Spectrometer (VIMS) and by Huygens' Descent Imaging Spectral Radiometer (DISR), appear to have confirmed hypotheses that darker regions are generally lower elevations where liquid and solid hydrocarbons, which are expected to have precipitated from the atmosphere in substantial quantities over Titan's history [e.g., 6], have accumulated, while brighter regions represent higher-standing exposures of less-contaminated water-ice bedrock or brighter organic material [e.g., 1, 7-11].

The morphologies of the albedo patterns observed on Titan's surface appear to represent a wide variety of geological features (Fig. 1; see also [1, 4]): linear boundaries likely indicate faulting and tectonic control; bright, roughly east-west, streamlined shapes suggest aeolian processes, consistent with RADAR observations of expanses of dunes covering the dark equatorial regions [12]; narrow, curvilinear, dark lines that wind across the surface appear to be fluvial channels; Ontario Lacus, a dark feature near the South Pole that is a few hundred kilometers long with a smooth margin is suggestive of a lake (Fig. 2; [13]); the relatively uncommon circular albedo features have often been confirmed to be impact structures [14], further evidence for a geologically young surface; and other, more complex, patterns still defy easy interpretation. To date we have not observed any evidence of changes in surface albedo patterns.

Lakes and Seas: Although ISS has observed the specular point at numerous locations at low latitudes on Titan's surface, detailed analysis has detected no enhancement, indicating no substantial coverage of the surface by liquid in these areas. However, illumination geometry and atmospheric scattering prevent useful observations of the specular point at high latitudes where there is more compelling evidence for the presence of surface liquids. In addition to Ontario Lacus, ISS has observed numerous smaller, dark surface features around the South Pole (Fig. 2). Furthermore, large convective cloud systems were commonly observed at high southern latitudes through 2004 [1, 15-16], evoking the interpretation of these features as lakes filled by recent methane rain [13]. The subsequent identification of lakes at high northern latitudes by Cassini RADAR [17], further supports this hypothesis. More recent observations by Cassini ISS of northern latitudes as the approaching equinox brings improved illumination have revealed an extensive low-albedo surface feature with a complex boundary. The structure is more than 1000 kilometers long and at its northernmost extent coincides with a large liquid-filled region identified in an overlapping RADAR SAR swath. If the entire dark region revealed in the ISS observation is currently filled with liquid, it would represent a sea with an area of 340,000 km^2. Thus, the liquid reservoirs required to replenish the hydrocarbon-

bons in Titan's atmosphere currently appear to exist in the form of surface lakes and seas at high latitudes.

Upcoming observations: Cassini has completed 30 of the 44 targeted Titan encounters planned during its nominal mission (4 more are scheduled to occur from May through July 2007) and much still remains to be seen, especially as Titan's high northern latitudes emerge from darkness as equinox approaches in August 2009. Further observations by Cassini's suite of instruments and coanalysis thereof will help to further improve our understanding of Titan's surface and the processes at work thereupon.
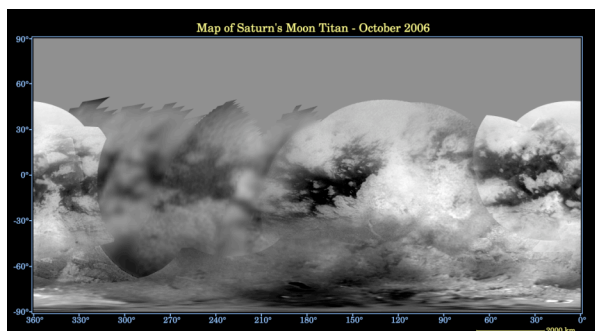

Figure 1: Albedo map of Titan compiled from ISS 938-nm observations (Apr. 2004 through Oct. 2006; http://photojournal.jpl.nasa.gov/catalog/PIA08346). Resolution varies according to available viewing opportunities. It is currently late winter in the northern hemisphere, so high northern latitudes are still poorly illuminated. For improved views of the trailing hemisphere and high northern latitudes acquired more recently see Perry et al. [4].
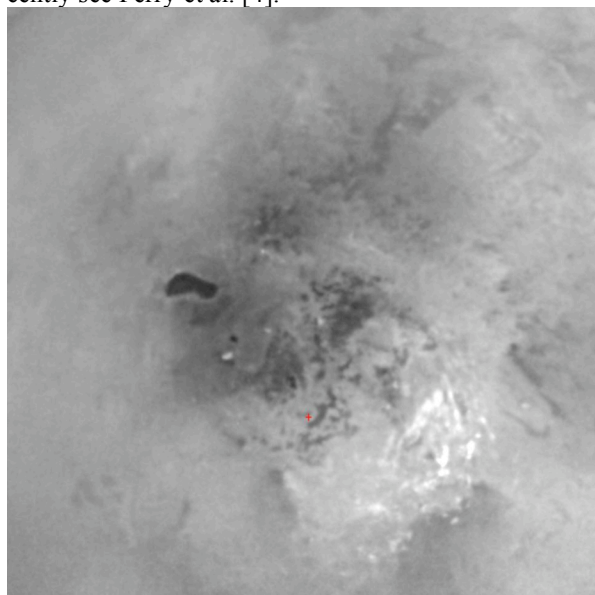
Figure 2: ISS image of Titan's South Pole (marked by the red cross just below center). Ontario Lacus is the relatively large, dark feature to the left of center.

Smaller dark features in this region may also be, or have been, liquid-filled lakes similar to those seen at high northern latitudes [17]. The very bright features to the right of the South Pole are tropospheric clouds (cf. a movie of this region illustrating cloud motions at: http://photojournal.jpl.nasa.gov/catalog/PIA06241.)
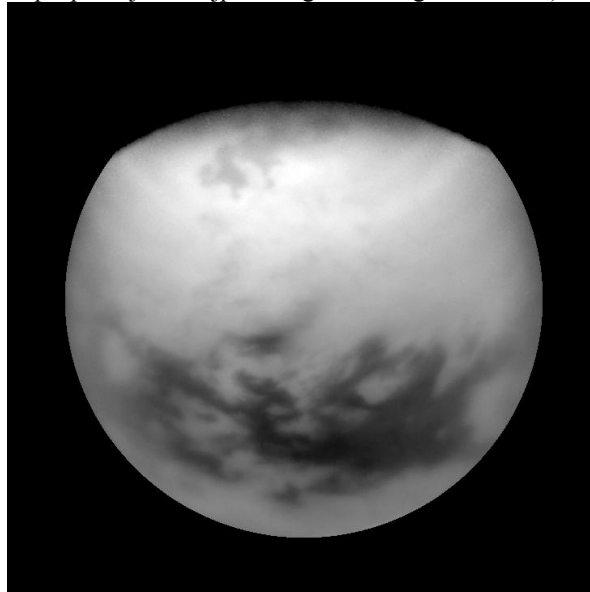
Figure 3: ISS image of Titan's trailing hemisphere at high northern latitudes. The complex dark feature just below the terminator at the top of the disk appears to be the full extent of one of the northern lakes identified by Cassini's RADAR (cf. ISS and RADAR observations combined to illustrate the overlapping coverage: http://photojournal.jpl.nasa.gov/catalog/PIA08365). In contrast, the dark expanses seen toward the bottom of the disk are the equatorial regions of Senkyo (to the west) and Belet (center and east), which have been shown to consist of dark longitudinal dunes [12].

References: [1] Porco, C.C. et al. (2005) *Nature 434*, 159-168. [2] Porco, C.C. et al. (2004) *Space Sci. Rev. 115*, 363-497. [3] Griffith, C.A. et al. (1991) *Icarus 93*, 362-378. [4] Perry, J. (2007) et al., this volume. [5] Perron, J.T. and de Pater, I. (2004) *GRL 31*, L17S04. [6] Lorenz, R.D. and Lunine, J.I. (2005) *PSS 53*, 557-576. [7] Elachi, C. et al. (2005) *Science 308*, 970-974. [8] Elachi, C. et al. (2006) *Nature 441*, 709-713. [9] Soderblom, L.A. et al. (2006) *B.A.A.S. 38*, #52.08. [10] Barnes, J.W. et al. (2007) *Icarus 186*, 242-258. [11] Tomasko, M.G. et al. (2005) *Nature 438*, 765-778. [12] Lorenz, R.D. et al. (2006) *Science 312*, 724-727. [13] McEwen, A.S. et al. (2005) *B.A.A.S. 37*, #53.04. [14] Lorenz, R.D. et al. (2007) *GRL 34*, doi:10.1029/2006GL028971. [15] Schaller E.L. et al. (2006) *Icarus 182*, 224-229. [16] Schaller E.L. et al. (2006) *Icarus 184*, 517-523. [17] Stofan, E.R. et al. (2007) *Nature 445*, 61-64.

SOLID NITROGEN AND SIMPLE HYDROCARBONS ON CHARON. A. J. Verbiscer [1], D. E. Peterson[1], M. F. Skrutskie[1], M. Cushing[1], M. J. Nelson[1], J. D. Smith[2], and J. C. Wilson[1] [1]University of Virginia, P.O. Box 400325, Charlottesville VA 22904 (verbiscer@virginia.edu), [2]Steward Observatory, University of Arizona, Tucson AZ 87512.

Introduction: A near-infrared spectrum 0.8 – 2.5 μm of Pluto's satellite Charon (Fig. 1) suggests the presence of solid N2 ice on its surface. The spectrum was obtained with the CorMASS [1] spectrometer while it was a visiting instrument at the 6.5-m Magellan telescope at Las Campanas, Chile in May 2005. Normally a difficult observation without adaptive optics, Pluto and Charon were spatially resolved in the CorMASS slit because they were near maximum elongation in their orbit (0.7") and Magellan had excellent seeing (0.4") at the time of data acquisition. The phase angle at the time of these observations was 1.3° and the sub-Earth point was in the southern trailing hemisphere at latitude -36° longitude 303°. The resolution ($R = \lambda/\Delta\lambda$) of these spectra ($R \sim 300$) exceeds that of previously obtained spectra of the same region on Charon [2-3], although higher resolution spectra ($R \sim 600$ have been obtained of the sub-Pluto and anti-Pluto hemispheres [4]. The wavelength range covers the rarely observed region 0.8 – 1.3 μm.

The spectrum is dominated by the features of crystalline H_2O ice I_h with prominent absorptions at 1.5, 1.65, and 2.0 μm. In addition, an absorption band at 2.21 μm clearly shows the presence of ammonia hydrate $NH_3 \cdot H_2O$ on the trailing hemisphere of Charon. As it has been observed on the sub and anti-Pluto hemispheres [4] as well as the leading hemisphere [5], ammonia hydrate $NH_3 \cdot H_2O$ appears on all sides of Pluto's satellite.

A narrow feature at 2.14 μm suggests the presence of solid N_2 ice on the surface. Solid nitrogen ice undergoes a phase change from cubic α nitrogen to hexagonal β nitrogen at 35.6 K [6]. This feature in our Charon spectrum is too narrow to be fit by by βN_2 suggesting that regions must be below 35 K, possibly on a south polar cap. We model the spectrum of Charon using a Hapke model [7] with an areal mixture in which 20% of the surface is covered by solid N_2 3mm thick, 30% by a dark neutral abosorber, and the remaining 50% by an intimate mixture of crystalline

H_2O ice particles 25 μm in diameter and ammonia hydrate (3% $NH_3.H_2O$) particles 100 μm in diameter. Additionally, we are investigating the incorporation of simple hydrocarbons such as C_2H_4 and C_2H_6 diluted in solid N_2 at 21 K [8] to explain absorption features longward of 2.2 μm that are present in this CorMASS spectrum of Charon.
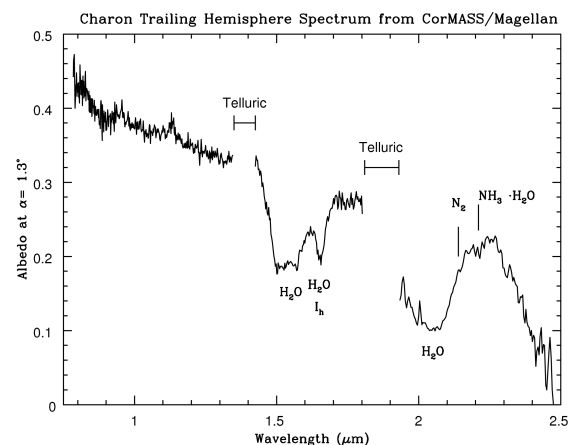
References: [1] Wilson, J. C. et al. (2001) *PASP* 113, 227-239. [2] Buie, M. W. & Grundy, W. M. (2000) Icarus 148, 324-339. [3] Brown, M.E. & Calvin, W. J. (2000) Science 287, 107-109. [4] Cook, J. C. et al. (2007) ApJ, in press. [5] Dumas, C. et al. (2001) *AJ 121*, 1163-1170. [6] Scott, T. A. (1976) Phys. Rep. 27, 87-157. [7] Hapke, B. (1993) *Theory of Reflectance and Emittance Spectroscopy*. Cambridge Univ. Press. New York. [8] Quirico, E. and Schmitt, B. (1997) *Icarus* 127, 354-378.

VEHICLE FOR ICY TERRAIN LOCOMOTION: A ROVER PROTOTYPE FOR EUROPA BY A UNIVERSITY OF COLORADO AEROSPACE ENGINEERING SENIOR PROJECTS TEAM. V. Vertucci[1], K. Rash[2], R. Hickman, C. Homolac, J. Krupp, H. Love, K. Ligon, A. Paulson, [1]University of Colorado Aerospace Engineering Sciences Veronica.Vertucci@colorado.edu, [2]University of Colorado Aerospace Engineering Sciences Kathryn.Rash@colorado.edu.

Introduction: The Senior Design Praticum is a year long senior level class in the Aerospace Engineering Department at the University of Colorado in which students design, fabricate, test, and verify projects in the Aerospace Engineering field.

The primary objective of the Vehicle for Icy Terrain Locomotion (VITL) team is to design and build a prototype for the locomotion system of a vehicle exploring a Europa-like surface capable of traversing 1 km of icy terrain in 7 days with characteristic obstacles. This objective was built off of past work done by JPL scientists on a future Europa mission [2].

Objectives for a Theoretical Europa Mission (TEM) include environmental temperatures around 100K, ice with a Brinell hardness of about 170 as well as a very harsh radiation environment with a dose of about 1 MRad in seven days making shielding absolutely necessary. The materials and moving parts used in the rover need to account for these effects of the harsh environmental elements. Similarly, the mass of the vehicle needs to be minimized in order to make its launch with landing gear feasible.

Power issues are also a major constraint for a Europa mission as solar power is not feasible and the use of an RTG could contaminate the pristine Europa environment.

Europa, in addition to the aforementioned environmental complications, has a gravity of near that to the Moon, about 1/6 Earth's gravity. This lowers the normal force that can be achieved with ice-traction methods and makes the wheel system much more difficult to design. Europa is also without a substantial atmosphere so surface conditions are near vacuum ambient pressures (10^{-6} Pa). Standard low-pressure design procedures must be included in engineering the vehicle in a TEM.

Science payloads will absolutely be included in a TEM. These science packages would be designed to go on board and must be allowed to operate unhindered by the normal operations of the TEM vehicle.

The specialized materials and power sources needed for this mission were not available to the VITL team due to budget and schedule constraints; thus considerations were made in the design to incorporate these necessary changes. The overall objective of building a vehicle that can maneuver on Europa's ice is not affected and the current design accomplished this.

Europa's ice, as previously mentioned, has a Brinell hardness of about 170, similar to that of mild steel or concrete. Europa's ice also has a coefficient of friction of about 0.55, ice to ice. There are also theoretical characteristic ruts and bumps that cover the ice which have been estimated by high resolution photos from spacecraft, shown below in Figure 1.. These are roughly one inch high by three feet long bumps and ruts as well as slopes up to 20°. Other obstacles include walls and cliffs that the rover must avoid upon encountering.
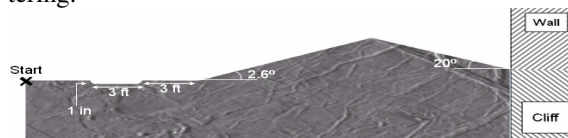
Figure 1: Europa terrain characteristics [1].

The objectives of the simplified Senior Projects Engineering Design and Manufactured Unit (EDMU) are similar in many ways to a TEM. The ice and surface characteristics will be the same but there are many environmental simplifications. For example, the temperature that the vehicle will be designed for is increased from 100K to 0ºC. This simplification allows for a cold temperature design requirement and testing, but is feasible for the team to accomplish compared to the 100K requirement.

The power issues and science payloads involved in creating a TEM are accounted for in the design by accommodating the mass and volume of a required power supply and a theoretical payload, but the development of such a supply or instrument lies outside the scope of this project. The pressure and radiation effects were likewise not implemented as these lie outside the scope.

Design Requirements: The major requirements of the prototype are outlined below. These requirements drove the design of the overall system and subsystems for the vehicle.

Geometry: The vehicle shall fit within a 1 cubic meter volume. This size restriction exists in order to satisfy the payload faring constraints of a typical long-range launch vehicle which would house the spacecraft caring the vehicle in addition to any landing gear.

Payload: A 10 kg dummy payload was used to simulate the mass and volume of a potential TEM science package.

Obstacle Detection: Sense impassable obstacles specified in the Introduction (above) and stop.

Mission Life: All systems shall be capable of operation at least 7 days (3.5 days of commanded operation), to simulate the radiation limiting factor.

Terrain Crossing and Inclination: Cross terrain specified in the Introduction including up to 20º slopes on Europa which translates to 2.62º on Earth by equating toques.

Direction Change: The vehicle shall be able to change the direction of motion on a slope to avoid impassable obstacles.

Temperature: Although the 100K environment of Europa cannot be simulated the system shall be capable of operation at 0ºC.

Range: During the 7 day mission, the vehicle and its components shall be capable of traveling up to 1 km in total distance.

Efficiency/Accuracy: After traveling 100 m on a flat surface in a straight line, the vehicle shall be within one body length of its expected position.

Final Design Architecture: The final system architecture can be seen in the following figure. The vehicle system consists of six wheels: four "slip" wheels and two powered spike wheels. Each of the spiked wheels consists of four rows of spikes. The vehicle will use the two powered spiked wheels to gain enough traction to pull itself up 20° slopes (2.62° slope for gravity equivalence on Earth), and over several obstacles outlined in the Introduction. The increase in slope is so that all geometry requirements of the suspension can be met while testing the vehicle up a slope.
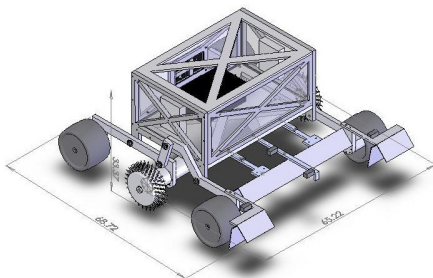

Figure 2: Final system architecture

The iso-grid structure of the rover is made from solid aluminum plates although for a future mission other materials with more desirable performance at cryogenic temperature can be utilized. The structure supports the rest of the subsystems and is the attachment point to the Rocker-Bogey suspension system. The rover is well under the one cubic meter requirement.

The current design illustrates the obstacle detection system which uses IR sensors to detect deflection of the mechanical bumper when an obstacle is encoun-

tered. Similarly the center beam includes an IR sensor which detects an approaching cliff. The only other additional sensor is an accelerometer mounted on the PCB inside the component box which determines when the vehicle encounters a slope of greater than 20 degrees.
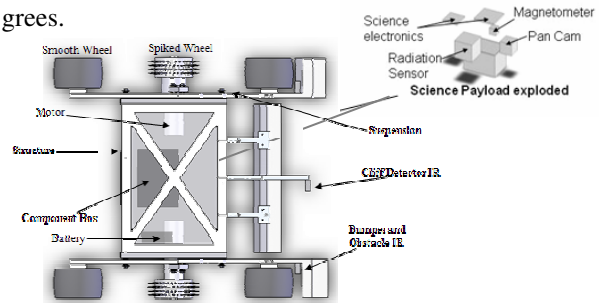
Figure 3: View of obstacle detection sensors, internal layout, and science payload.

Figure 3 shows the internal layout of the vehicle, the potential postion of the science payload, and the arial view of all other components. Although only one battery is illustrated for testing purposes, this number would need to be brought up to 36 batteries to power a 7 day TEM, which adds an additional 22.5 kg to the rover mass. Currently, the motors and structure are designed to accommodate this additional mass as well as up to 10 kg of payload mass. VITL used two interchangeable, rechargeable batteries to demonstrate successful completion of the requirements. The vehicle turns by skid steering, rotating the two powered, spiked wheels in opposite directions that create a moment about the center of the rover. The accuracy of the vehicle can be measured through the motor encoders, but this was not completed due to time constraints.

Conclusions: In short, the completed VITL rover, shown below, satisfied all of the project's requirements that were within scope. It also provides a preliminary design for a future terrestrial exploration vehicle on Europa.
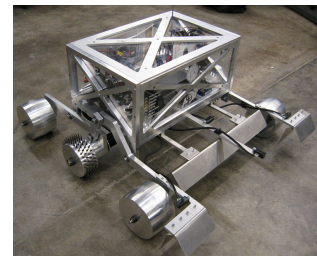
Figure 4: Completed VITL rover.

References:

[1] Murray, Norman. Universiy of Toronto. http://www.cita.utoronto.ca/~murray/GLG130/Pictures/Jupiter/Europa_flow.jpg [2] Balint, Tibor S. "Europa Surface Science Package Feasibility Assessment" JPL, Pasadena, CA 2004.

THE GLOBAL GEOLOGIC MAP OF IO: APPROACH AND MAPPING STATUS. David A. Williams[1], Laszlo P. Keszthelyi[2], Paul E. Geissler[2], Windy L. Jaeger[2], Tammy L. Becker[2], David A. Crown[3], Paul M. Schenk[4], and Julie A. Rathbun[5]; [1]School of Earth and Space Exploration, Arizona State University, Box 871404, Tempe, Arizona, 85287 (David.Williams@asu.edu); [2]Astrogeology Team, U.S. Geological Survey, Flagstaff, Arizona; [3]Planetary Science Institute, Tucson, Arizona; [4]Lunar and Planetary Institute, Houston, Texas; [5]University of Redlands, Redlands, California.

Introduction: Jupiter's volcanic moon Io is a challenging place to study using typical planetary mapping techniques, because of 1) rapid (in geologic terms) resurfacing from volcanic activity and 2) non-uniform coverage from multiple spacecraft flybys, resulting in a wide range of image resolutions and photometric properties. Nevertheless, because Io's level of volcanic activity makes it unique in our Solar System, it is desirable to map its surface in order to complete a global reconnaissance of its surface features and material units and to understand better its geologic evolution. In this abstract we discuss our approach and progress in producing a global geologic map of Io. For production of our map, we are using a set of combined *Galileo-Voyager* global mosaics and ArcGIS software. We are also creating a GIS database to contain all compatible *Galileo*, *Voyager*, and other Io data sets to show surface changes and aid in geologic interpretations.

Background: Io, the innermost Galilean satellite of Jupiter, is the most volcanically active body in the Solar System. Tidal heating produces magma that feeds ~300 active volcanic centers [1-3]. The 1979 *Voyager* flybys observed ~25% of Io's surface at resolutions of <2 km/pixel (the rest at 2-20 km/pixel: [4]), covering mostly the subjovian hemisphere. The *Galileo* mission (1996-2003) included five close flybys of Io, focused mostly on the antijovian hemisphere [5-7], with resolutions between ~10 m/pixel to 20 km/pixel. Previous geologic mapping of Io includes a series of four regional *Voyager*-based maps [8], a *Voyager*-based global map [9], and four *Galileo*-based regional maps [10].

The complementary coverage of Io by *Voyager* and *Galileo* has enabled the production of a series of high quality grayscale and color global mosaics. Our goal is to complement the new mosaics with a corresponding global compilation of geologic understanding at the end of the *Galileo* era. Geologic mapping is a tool that enables the definition and characterization of surface features into process-related material units and structures and places them within their stratigraphic context, allowing recognition of the geologic evolution of an area, region, or planet.

Global Io Mosaics: The USGS Io global mosaics (1 km/pixel nominal resolution) are now the definitive global compilation of image products for Io. They consist of four distinct products: 1) a global mosaic of *Galileo* color images (756nm-green-violet as R-G-B, 4˚ phase angle); 2) a global mosaic of the best resolution *Galileo* monochrome images; 3) a global mosaic

of the best resolution *Voyager* and *Galileo* monochrome images; and 4) a merged product combining *Galileo* color information with the higher resolution monochrome images. Each of these four products is available as an ISIS cube in Sinusoidal, Mercator and Polar Stereographic projections (both north and south pole). An extensive set of ancillary data was developed for all of these mosaics to help users understand the various combinations of data from different sensors, filters, dates, and illumination and viewing geometries. These include footprint plots showing the identity of each of the component images and diagrams that show the incidence, emission, and phase angles, along with the spatial resolutions of the individual frames used.

Strategies for Global Mapping: After analysis of all previous geologic maps and study of the new global mosaics, we developed the following strategy for global mapping. All mapping is done using ArcMap software, part of the ArcGIS package by ESRI:

1) *Map diffuse deposits using Galileo global color data.* This is done because of the wide variety of diffuse deposits on Io (black, yellow, white, red, green), which are thought to represent distinct compositions (silicates, sulfurous materials, SO_2-dominated materials, short-chain sulfur allotropes, products of silicate/sulfur interaction, respectively).

2) *Map mountains, surrounding plateaus, and structural features using various mosaics.* Various image products are used to identify mountains, layered plateaus, and other materials delineated by scarps and other structural features, because they have nearly the same color and texture as background plains and cannot be identified except in images taken during low solar incidence angles.

3) *Map vents and paterae using various mosaics.*

4) *Map lava flow fields using various mosaics.* We first map the outermost boundaries of each flow field around a vent, followed by the addition of more detail (individual lobate flow margins, fresher interior flows) as the available resolution permits. Active or recently active flows are identified by the following criteria: 1) observed surface changes in images obtained at different times; 2) thermal anomalies detected in NIMS data; and/or 3) an observed plume source at or near the flow margins.

5) *Map plains.* The bright plains include everything not mapped in the previous categories, and are thought to consist of silicate crust mantled by various S-bearing materials [10]. The primary interpatera Plains Material has three subunits based on color (Yellow, White, and Red-Brown); Layered Plains are composed

of plateaus separated from surrounding plains by scarps and are thought to be produced by degradational processes [11].

Mapping Progress: We have mapped the polar regions of Io (±57.5°-90°) as of May 2007. The following summarizes our results:

In general, Io displays five primary types of morphological units: plains, patera floors, flows, mountains, and diffuse deposits. Plains materials cover ~86% of Io's surface in the polar regions. The greatest percentage (79%) consists of radiation-altered Red-Brown Plains, with lesser amounts of White Plains (SO_2-dominated, 3%) and Bright (yellow) Plains (sulfur-dominated, 2%). Eroded plateaus, or Layered Plains, make up ~3% of the polar regions.

Patera floors have a range of albedos and colors in the polar regions, and are mapped as Bright (presumably sulfur-covered, 0.3%), Dark (presumably silicate-covered, 0.3%), and Undivided (0.8%). There are suggestions of additional paterae in the polar regions, based on albedo and color differences in the mosaics, but confirmation must await more high-resolution coverage. Patera floors range from bright white to yellow-orange to dark black in *Galileo* images, in which the colors suggest various compositions, including mixes of silicates, sulfurous compounds, and relatively pure sulfur dioxide in some cases [12]. Heno Patera (57.1°S, 311.5°W), a 71.1 km diameter patera, has dark floor and dark flows that surround a circular feature approximately centered on the patera floor. We speculate that this may be a site of an impact that is experiencing modification by volcanism.

There are significant expanses of Bright Lava Flow materials in the polar regions (3% of all mapped polar units), thought to be indicative of sulfur volcanism. The area of the Bright Flows is twice that of the Dark Flows (silicate-dominated, ~1%), although Undivided Flows (units with intermediate albedos and colors) make up another 6% of polar materials. These mapping results suggest that lava flows outside paterae may have a greater role in resurfacing Io than previously thought. Many polar bright flow fields are not directly adjacent to dark flows, perhaps indicative of a significant component of primary sulfur volcanism. Lithologically, Patera Floor materials and Lava Flow materials are probably identical in composition. However, their distinctive geologic settings justifies separating them on the global map.

In the polar regions, Lineated Mountain materials make up about ~2% of the surface. By number there are more mountains identified in the south polar region, due to the better *Voyager* imaging {i.e., need right illumination & resolution}. Mottled and Undivided Mountain materials each make up <1% of the polar areas. Lineated Mountain materials are topographically-distinct massifs (relative to layered plains) containing ridges, grooves, scarps, and lineaments on

positive-relief edifices. This unit is interpreted as tectonically-disrupted sections of crust containing planar structural features, possibly faults involved in uplift and/or collapse during mountain formation [2]. Massifs with no visible patterns are classified as Undivided. Mottled Mountain materials have smoother surfaces lacking lineations and indicative of mass wasting processes. No volcanic mountains (Tholus, Cone, or Shield materials) were recognized in the polar regions.

The polar regions contain extensive diffuse deposits, which cover 16.5% of the surfaces of other units. White Diffuse deposits are thought to be dominated by SO_2-rich frosts, and make up 64% of all diffuse deposits at the poles. They usually occur at the margins of lava flows or around paterae, but also make up extensive halos around some mountains. Yellow Diffuse deposits are likely composed of some combination of sulfur-rich materials and SO_2, albeit less SO_2 than White deposits. Only 10% of diffuse deposits at the poles are yellow, and these are less extensive than in equatorial regions. Red Diffuse deposits occur as ephemeral mantles around active vents, and make up ~10% of polar diffuse deposits. There are the remnants of two faint red rings in the north polar region, one surrounding Dazhbog Patera (which erupted during the *Galileo* I31 flyby) and one around an unnamed patera at 70°N, 55°W. They have been interpreted as pyroclastic deposits rich in metastable, S_3 and S_4 allotropes, which are red when quenched from magmatic S_2 gas [13], possibly also containing Cl-bearing materials at some vents [14]. Dark Diffuse deposits are interpreted as pyroclastic deposits derived from silicate lavas [15], and cover ~16% of the area of polar units.

A wide range of structural features can be identified in the polar regions of Io, including scarps, ridges, lineaments, and circular depressions (pits and patera rims). The additional low-sun observations and higher resolution of the *Galileo* camera has enabled recognition of these and other structural features over a wider part of Io's surface than was previously possible.

References: [1] *Radebaugh et al.*, 2001, *JGR 106*, 33,005-33,020; [2] *Schenk et al.*, 2001, *JGR 106*, 33,201-33,222; [3] *Lopes et al.*, 2004, *Icarus 169/1*, 140-174; [4] *Smith et al.*, 1979a,b, *Science 204*, 951-972, & *Science 206*, 927-950; [5] *McEwen et al.*, 2000, *Science 288*, 1193-1198; [6] *Keszthelyi et al.*, 2001, *JGR 106*, 33,025-33,052; [7] *Turtle et al.*, 2004, *Icarus, 169/1*, 3-28; [8] *Moore, H.J.*, 1987, *USGS Map I-1851*, 1:1,003,000; *Greeley, R., et al.*, 1988, *USGS Map I-1949*, 1:2,000,000; *Schaber, G.G., et al.*, 1989, *USGS Map I-1980*, 1:5,000,000; *Whitford-Stark, J.L., et al.*, 1991, *USGS Map I-2055*, 1:5,000,000; [9] *Crown, D.A., et al.*, 1992, *USGS Map I-2209*, 1:15,000,000; [10] *Williams, D.A., et al.*, 2002, *JGR 107*, 5068, doi:10.1029/2001JE001821; *Williams, D.A., et al.*, 2004, *Icarus 169*, 80-97; *Williams, D.A., et al.*, 2005, *Icarus 177*, 69-88; *Williams, D.A., et al.*, 2007, *Icarus, 186*, 204-217; [11] *Moore et al.*, 2001, *JGR 106*, 33,223-33,240; [12] *Carlson, R.W., et al.*, 1997, *GRL 24*, 2479-2482; [13] *Spencer et al.*, 2000, *Science 288*, 1208-1210; [14] *Schmidt & Rodriguez*, 2003, *JGR 108*, 5104, doi: 10.1029/2002JE001988; [15] *Geissler et al.*, 1999, *Icarus 140*, 265-282.

XANADU – DISAGGREGATION OF TITAN'S BRIGHT TERRAINS. C. A. Wood[1], E.R. Stofan[2], R.D. Lorenz[3], R.L. Kirk[4], R.M. Lopes[5], P. Callahan[5], B.W. Stiles[5]. [1]Wheeling Jesuit University, Wheeling, WV26003; chuckwood@cet.edu, [2]Proxemy Research, Bowie, MD 20715; [3]Johns Hopkins Applied Physics Lab., Laurel, MD 20723; [4]US Geol. Survey, 2255 N. Gemini Dr., Flagstaff, AZ 86001; JPL, [5]Cal Tech, Pasadena, CA 94305.

Introduction: A landform inventory of the satellites of the outer solar system is largely limited to craters, cracks and flows. Only Titan has a diversity of features far beyond those common planetary landforms. Some of Titan's landforms are a consequence of atmospheric processes (dunes, lakes and rain-fed river systems) but many appear to result from internal processes that produced volcanism, mountains and other terrains that are harder to interpret. Here we describe Xanadu, the largest known feature on Titan, and discuss evidence it provides of the geologic processes and history of this excellent world.

Discovery: Xanadu is one of the rare outer solar system satellite landforms discovered from Earth. In 1996 infrared images from the Hubble Space Telescope revealed albedo variations including the detection of a continent-size bright spot subsequently named Xanadu [1]. Although it is large (~4000 X 2000 km) and bright, Xanadu is unique in being dimmer at 5 micrometers than other bright areas [2]. From the telescopic and Cassini spectral information there is little detailed evidence of the nature of Xanadu.

Radar Evidence: The geology of part of Xanadu has been revealed by Cassini radar swath T13, which crosses Xanadu from east to west, and T3 which nips its northern-most extent. Xanadu is radar bright and has complex patterns of surface texture.

The Shangri-la Shore. The western edge of Xanadu has a sharply defined boundary with its irregular bright edge abutting east-west trending dark dunes. A number of bright "islands" appear to be highlands that are surrounded by dunes. These suggest that Xanadu previously extended further west. In some places dunes stop at the western edge of Xanadu and in other areas they lap up onto it. The western edge of Xanadu is thus higher than the adjacent dunes. This is consistent with a general relation on Titan – bright areas are observed to be local highs that dunes diverge around [3].

Mottled Riverland: From the west end of Xanadu inland about 650 km is a distinctive terrain. It is slightly bright, relatively flat and includes dozens of roughly circular dark units typically a few tens of kilometers wide. This area is completely transected by four major dendritic river systems. These rivers start near the northern and western edges of Xanadu and all flow to the south. The two major drainages are the centers of darker and rougher terrain.

Knobby Terrain: The largest portion of Xanadu (about 2000 km width) is characterized by small bright interconnected ridges. A few river segments cut through flat spaces between ridges and occasionally through the ridges. Although most of these ridge bits are interconnected they do not form what would be called mountain ranges. They are more like a pervasive ground cover.

Dark, flat and elongated embayments become more common toward the eastern section of the Knobby Terrain. They create a linear mountain and flat plain look reminiscent of Basin and Range terrain in the Western US on Earth.
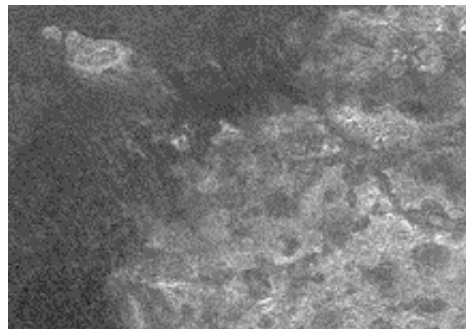
Mottled Riverland (right) and Shangri-la Shore (left). All look directions from top; incidence angle (IA) 21°, 190 x 310 km.
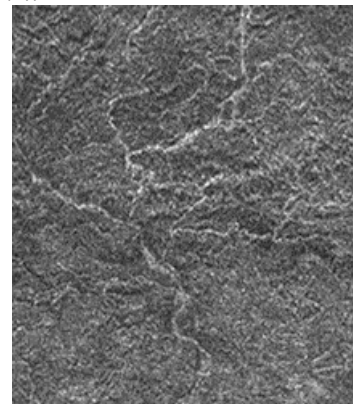
River system. IA = 15°, 130 x 120 km.

Knobby terrain. IA=26°, 70x60 km.

Subdued Cratered Terrain: The easternmost 1200 km of the T13 radar swath of Xanadu has yet another surface texture. It has a subdued mountainous look, lacks the individual ridge peaks, and appears flatter than Knobby Terrain. It is extensively cut by straight-sided, lower and smoother dark material that is the same as that bor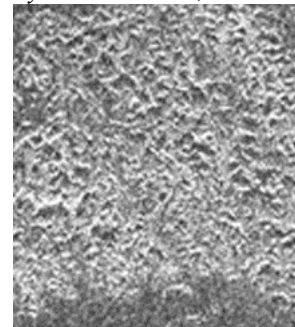dering the eastern end of Xanadu. Both the dark and bright material are cut by rivers, but they do not form an integrated drainage pattern as in the Mottled Riverland. The Subdued Cratered Terrain contains eight possible impact craters in various erosional states. No other impact craters are visible in the rest of Xanadu, although two possible ones occur on the islands to the west.
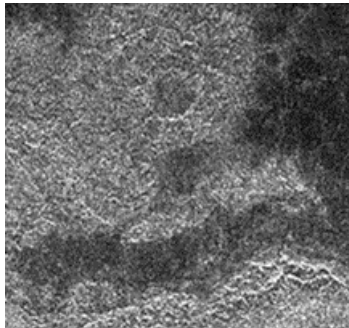

Subdued Cratered Terrain. IA=17°, 110x110 km.

The Eastern Shore: At its eastern edge some of the dark troughs that cut bright Xanadu open up to smooth dark terrain. Irregular patches of bright Subdued Crater Terrain are completely surround by the dark unit, and it is cut by a number of bright rivers.

Interpretations: Xanadu is not a homogenous terrain, as is generally true for such large areas on Earth and other worlds. Xanadu's brightness at radar wavelength is due to its many peaks and hills, but there is little evidence that the topographic relief is very great. The overall impression is that the different terrains of Xanadu are relict from an earlier time. The fact that the subdued cratered terrain contains numerous likely eroded impact craters suggests that it is older than other observed surfaces on Titan.

Both the eastern and western ends of Xanadu are broken and replaced by lower dark terrains. On the Shangri-la side the dark material is dunes, and on the eastern end it is simply a smooth surface. The disaggregation appears to have reduced the extent of Xanadu, as evidenced by the bright islands at each end. At the eastern and northeastern edges the radar-bright highland mass is sundered by dark troughs that appear caught in the act of transforming the surface. This disaggregation may be an ongoing process, and appears to be happening elsewhere on Titan where optically bright terrains are bordered by dark ones with nearby white islands. A characteristic of the replacement of bright with dark terrains is that often the created boundaries are linear, suggesting a tectonic influence.

The mechanism of transformation from bright hilly terrain to smooth dark terrain is not certain, but one clue is that the transformations are most pervasive near the edges of Xanadu. Also, the linear boundaries of the dark areas implies that the process is more deeply seated than simple surficial erosion.

Another possible clue to a mechanism for transforming bright hilly terrain to dark smooth material is the occurrence of roughly circular dark blobs in western Xanadu. One is teardrop shaped, suggesting viscous flow. These may be diapirs of lower density material that were heated at depth and moved upward. The dark blobs do not occur elsewhere on Xanadu and are different from the linear dark troughs in the east. Perhaps there are multiple processes for transforming bright material.
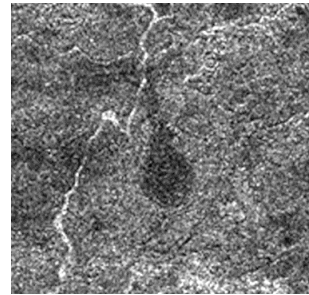
Teardrop dark blob surrounded by collar of modified country rock. IA=21°, 80x80 km.

Global Speculations: Broad scale coverage by ISS and VIMS shows that Titan has surfaces of various reflectivity and hue, but a zero order division exists of bright and dark terrains. The larger dark terrains (e.g. Senkyo, Belet, Shangri-la, Fensal) are interconnected by narrower linear ones (Aaru, Ching-tu, Aztlan), and nearly all are within 30° of the equator. All the adjacent bright areas (Tsegihi, Adiri, Dilmun, Xanadu) appear to be being broken up and disaggregated.

This leads to a speculation that Titan may have been initially surfaced by bright hilly terrain such as Xanadu and that within the equatorial zone it is being destroyed and replaced by lower elevation dark material. This may be a planetwide process with Xanadu being the largest relatively intact older terrain in the equatorial region. The existence of eight possible old impact craters in eastern Xanadu supports its interpretation as older material. Indeed, all three of the accepted impact structures (Menrva, Sinlap and Krs) occur on patches of bright terrain. A proposed working relationship for Titan is bright equals old and high, dark equals young and low. Now we need more radar coverage to test it!

References:
[1] Smith, P.H. et al, 1996, Icarus 119, 336-349. [2] Barnes, J. et al, 2007, *Icarus*, in press. [3] Radebaugh, J. et al, 2007, *Icarus*, in press.

3D Modeling of Landscape-Modifying Processes on the Galilean Satellites

Stephen Wood, Jeff Moore, Paul Schenk, Alan Howard, and John Spencer

We evaluate the sequence and extent of volatile redistribution and erosional processes that have shaped the topography of the Galilean satellites by applying a physics-based 3-D landform evolution model to Galilean satellite erosional landforms. Model simulations of icy satellite landform erosion and volatile redistribution are guided and constrained by iteratively comparing model results with the general statistics of erosional landform classes derived from DEMs. In some cases, DEMs of pristine landforms (e.g. fresh craters, fault blocks) are used as the "initial conditions" in model runs. The model includes the following coupled processes: (a) sublimation and re-condensation of surface volatiles; (b) subsurface heat conduction; (c) direct solar heating and radiative cooling; (d) indirect solar and thermal radiation from other surfaces (reflected and emitted); (e) shadowing by topography; (f) subsurface sublimation/condensation and vapor diffusion; (g) development of a "sublimation lag" of non-volatile material; and (h) disaggregation and downward sloughing of surficial material.

In comparison to previous topographic thermal models for airless icy bodies [Spencer, 1987; Colwell *et al*., 1990; Vasavada *et al*. 1999], our model includes several important additions and improvements:

(a) <u>Dynamic topography</u> - We model the changes in landform predicted to result from sublimation/condensation and gravitational mass wasting. Previous studies have speculated about scenarios for how the surface might evolve as a result of these processes, but given the many potential feedbacks between topography, temperature, albedo, the amount of ice present, and the stability of slopes, it is very difficult to predict without using a model that can track the time evolution of these variables in a self-consistent way.

(b) <u>Shadowing and radiative scattering/emission for asymmetric surfaces with non-zero thermal inertia</u> - Previous models that included these effects were restricted to symmetric geometries such as idealized craters and trenches, and assumed surface temperatures were always in radiative equilibrium. Our modeling uses realistic topography that includes exposures of high thermal inertia material, which can respond differently to being shadowed during the morning versus the afternoon.

(c) <u>Treatment of temperature-dependent thermal properties</u> - The thermal conductivity of particulate minerals in vacuum has the functional form $k = A + BT^3$ [Cremers and Birkebak, 1971], while the conductivity of solid water ice is $k_{ice} = 567/T$ [Squyres *et al.*, 1985], and for both materials the heat capacity increases linearly with temperature over the range found on the Galilean satellites (80-160K). These dependencies can cause significant diurnal variations in the efficiency of subsurface heat conduction.
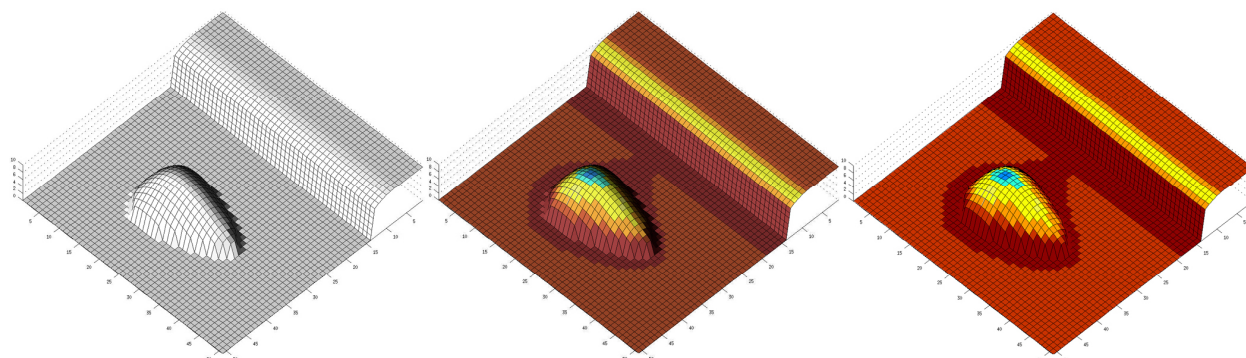
Model Components and Implementation

Sublimation: This component is based on a new 3-D finite-element sublimation model developed to study the long-term evolution of ice deposits on Mars. The sublimation rate of an ice surface is determined almost entirely by its temperature, and on planetary bodies with little or no atmosphere, the surface temperature is largely controlled by the topography (e.g. slope, azimuth, and shadowing). But the temperature varies on a much more rapid timescale than the topography, so one of the key modeling considerations is how to link the calculations of z(t) and T(t). In order to accurately capture the variations in surface temperatures we need to use a time step less than 1/10 of a diurnal cycle, whereas the timescale for significant topographic changes is likely to be on the order of $10^{5\text{-}7}$ years. For the case of the Galilean satellites, we can take advantage of the fact that they do not experience significant seasonal variations in their insolation patterns (obliquity < 1 deg.), so that one day is pretty much like any other. That means that we can simply multiply the results obtained for one day by the number of days required to exceed some criteria of minimum change in the topography (or surface albedo).

The model surface is a rectangular grid of points with fixed horizontal spacing ($\Delta x = \Delta y$) and variable height (z). At each time step, the vertical displacement of each grid point due to sublimation is given by

$$\Delta z_{sub} = \Delta t * (q_{sub} / \cos\theta) * (1/\rho_{ice})$$

where q_{sub} is the sublimation rate, θ is the average local slope, and ρ_{ice} is the ice density. The factor of ($1/\cos\theta$) accounts for the fact that sublimation occurs perpendicular to the surface slope. For numerical stability, we have implemented this finite difference equation using the Lax method which has the additional advantage of being robust to the slope discontinuities that tend to develop.

Subsurface Heat Conduction: Our model includes one-dimensional (vertical) heat conduction below each surface grid point. Rather than prescribing the thickness of each layer, we prescribe the depth of the interface(s) between regions with different thermal properties, and use a fixed number of layers within each region. We then use a semi-implicit finite-difference scheme, which is unconditionally stable and accurate to second-order, to solve the diffusion equation within each region and match the heat flux across each interface. This model makes it much easier to account for changes in layer thickness or composition, and allows us to use the largest possible time steps without sacrificing vertical resolution.

Subsurface Sublimation and Lag Deposits: Thin layers of non-volatile material on the surface can increase sublimation by lowering the albedo, but thicker layers can dramatically reduce sublimation: by damping the subsurface thermal wave and by physically impeding the vapor flux. The thermal effects of the lag are easily simulated by adjusting the thermal properties of the upper model layers. The vapor diffusion effects are modeled by replacing the surface ice sublimation term with an expression for subsurface sublimation: $q_{sub} = F_v = D_k (\varepsilon/\tau) N_{ice}/z_{ice}$, where N_{ice} is the equilibrium vapor density at the depth of the ice (z_{ice}), D_K is the Knudsen diffusion coefficient, ε is porosity, τ is the tortuosity of the diffusive path (e.g., Moore *et al.* [1996]).

References
Colwell, J. E., Jakosky, B. M., Sandor, B. J., and Stern, S. A. ,1990. *Icarus* 85, 205-215.
Cremers, C. J. and Birkebak, R. C., 1971. Proc. 2nd Lunar Sci. Conf., Vol. 3, 2311.
Howard, A.D., 2004. *Lunar and Planetary Sci. Conf*. XXXV, Abstract 1054.
Moore, J.M., Mellon, M.T., and Zent, A.P., 1996. *Icarus* 122, 63-78.
Spencer, J.R. 1987. *Icarus* 69, 297-313.
Squyres, S. W., MacKay, C. P., and Reynolds, R. T., 1985. *J. Geophys. Res*. 90, B14, 12381-12392.
Vasavada, A. R., Paige, D.A., and Wood, S.E., 1999. *Icarus* 141, 179-193.

COMPOSITION OF TITAN'S SURFACE FEATURES CONSTRAINED THROUGH BACKSCATTER MODELING.

L. C. Wye[1], H. A. Zebker[1], M. A. Janssen[2], R. D. Lorenz[3], R. D. West[2], and the Cassini RADAR Team, [1]Stanford University, Department of Electical Engineering, 350 Serra Mall, Stanford, CA 94305, lcwye@stanford.edu, [2]Jet Propulsion Laboratory, California Institute of Technology, 4800 Oak Grove Drive, Pasadena, CA 91109, [3]Space Department, Johns Hopkins University Applied Physics Laboratory, Laurel, MD 20723.

Introduction: The Cassini RADAR is a multifunctional instrument, shifting between four modes as it swings by Titan on a given orbit. Starting at a distance of 100,000 km, it begins in radiometer mode, passively listening to the microwave emission radiating from the surface's disk. Flying closer (9000-25000 km), the scatterometer mode takes over, actively scanning the 4-m high-gain antenna beam over the surface in a raster pattern to cover large areas as well as sample the regional backscatter response. Closer yet, the altimeter mode steers the beam towards nadir and records elevation profiles beneath the spacecraft. And around closest approach, the SAR mode images swaths with resolutions as high as 350 m. Each RADAR mode is primed for a specific science objective and sets up a particular observing geometry to achieve it. Here, we utilize this geometry diversity to create a more complete set of surface backscatter functions for a collection of features than is possible with the scatterometry data alone.

By modeling the backscatter response for individual features rather than the average response over regional areas, we can constrain the composition and structure of specific units on Titan's heterogeneous surface. This will further constrain the processes responsible for the feature's formation and evolution.

The specific features that we model include the dune fields, crater ejecta (Sinlap), bright albedo regions (Tsegihi, Quivira, and Adiri), dark albedo regions (Senkyo, Shangri-la), and bright spots called facula (Shikoku), among others.

Combining Data Sets: The scatterometer uses the 0.37° central antenna beam at 13.78 GHz (2.17 cm) in a real-aperture mode to produce regional-scale backscatter images across large areas of the surface. Observing from distances between 9000 and 25000 km, the typical resolution cell is 90-km by 150-km, as determined by the beam footprint and the pulse length. Raster scanning achieves large angular coverage of the surface to properly sample the average backscatter function over the region. Yet, multi-angle coverage of a particular area, or feature, is lacking unless we have multiple scans overlapping. The 17 scatterometry scans acquired to-date (TAi, TAo, T3, T4, T8i, T8o, T13, T16, T19, T21, T23i, T23o, T25, T28, T29, T30i, T30o) overlap only over eight distinct areas, and just two of these have overlap from more than 2 scans. It

is clear that, for a particular feature or area, scatterometer-data alone does not provide adequate backscatter-function sampling.

By applying the real-aperture processing techniques of the scatterometer to the other active radar modes, we can combine datasets to achieve greater angular sampling of a feature's backscatter response. The altimetry data provides the very low angle response (less than 1°), while the SAR data gives the mid-range response (10° to 40°).

Because the scatterometry has already observed close to 80% of the surface (Figure 1), a large portion of altimetry and SAR coverage is coincident with scatterometry. The 15 SAR swaths collected to-date (TA, T3, T7, T8, T13, T16, T17, T18, T21, T23, T25, T27, T28, T29, T30) cover roughly 20% of the surface. The 19 altimeter tracks collected (TAo, T3i, T3o, T8i, T8o, T13, T16, T19i, T19o, T21, T23i, T23o, T25i, T28i, T28o, T29i, T29o, T30i, T30o) cover less than 1%. Together, the multi-angle radar reflectivity coverage is more complete (Figure 2).
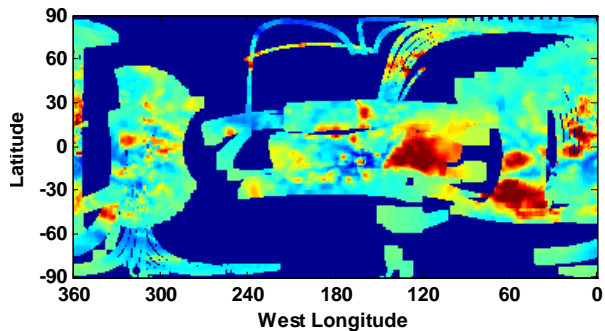

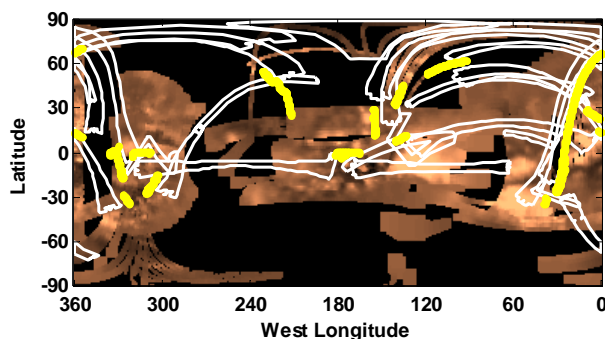*Fig. 1: Global scatterometry map as of May, 2007.*

Fig. 2: Coincident radar coverage: SAR (white), altimetry (yellow), scatterometry (pink).

Calibration. The challenge in combining the active mode datasets is verifying that all modes are calibrated to the same scale. Calibration, or conversion from quantized data numbers to watts, is performed by computing the noise power from an equivalent system noise temperature and comparing to the measured noise variance of the data. For two reasons, this is more complex than expected. First, each mode uses a different receiver filter and bandwidth and thus has a different system noise temperature. Engineering tests show that the smaller the receiver bandwidth, the higher the noise temperature, suggesting a narrow-band back-end noise contaminant [1]. Second, each mode cycles through a different set of attenuation factors to account for their different viewing geometries and echo power levels. Typically, the equivalent system temperature is dominated by the front-end gain of the receiver, which is ideally large enough to dampen the effects of gains and losses further down the receiver chain. Yet, the Cassini radar receiver has a noise temperature that is strongly dependent on the leading attenuator value. Thus, in addition to measuring noise temperatures for each mode's bandwidth, we must also cycle through the various attenuation levels to see how the equivalent temperature changes.

Backscatter Modeling: A backscatter function over a wide range of angles reveals much about the dielectric composition, surface and subsurface scattering properties. We separate the backscatter response into two different regimes: surface scatter dominates at low angles and volume scattering dominates at the larger angles. The surface component yields the tightest constraints on dielectric constant and surface slopes, while the volume component is most descriptive of scattering centers such as cracks or inclusions within the near-surface material.

We use traditional facet scattering models to describe the quasi-specular scatter of the surface term, such as Hagfors' or Gaussian laws. We then consider two different approaches to incorporate the volume term. The first approach is to use an empirical cosine-law to model the diffuse volume scatter [2]. This is used solely to measure and eliminate the contribution of the diffuse scatter to the low-angle backscatter, so that the quasi-specular model can be applied more accurately. The cosine-law parameters reveal nothing physical about the sub-surface scattering. An example of this composite model fit to the scatterometry and altimetry points of Shangri-la is shown in Figure 3. Our second approach is to consider a volume scattering model that incorporates the emission measurements collected by the radiometer. While the active modes await receipt of their echoes, the radiometer listens to the natural microwave emission, yielding

coincident emission and reflectivity measurements. By assuming the system to be in thermal equilibrium, so that absorption equals emission, and using Kirchhoff's law for thermal radiation (where the sum of reflected plus absorbed energy equals unity), we have derived a model that incorporates both data types under a single set of physical parameters including the surface dielectric constant, wavelength-scale surface roughness, and the size distribution of scattering centers within the near-surface material [3]. The results of both models applied to each feature's backscatter curve are presented.
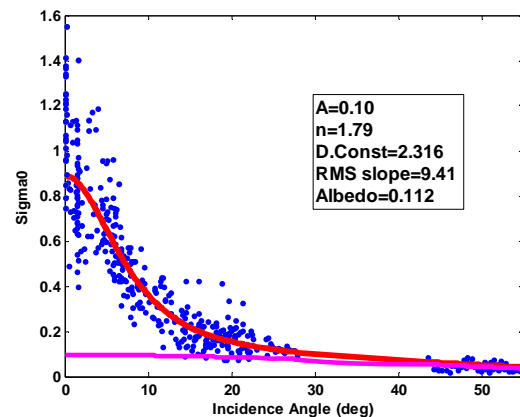

Fig. 3: The results of a composite Hagfors fit (red) using the diffuse cosine law (pink) to the scatterometry + altimetry points over Shangri-la (blue) suggest a dielectric constant around 2.3 and surface slopes on the order of 9°. Dielectric constants between 2 and 2.4 are thought to represent solid hydrocarbons [4].

Identifying Surface Features: We examine the high-resolution SAR and the ISS and VIMS infrared images to identify specific features and feature types from all available Titan passes, and use the locations derived from this catalog to extract the measurements corresponding to each feature type. In this way features that we cannot readily identify in the lower resolution modes of the radar can be extracted reliably. We find sufficient numbers of features at various incidence angles across all of the available Cassini passes, to infer the properties of specific feature types, and determine for instance whether the dune features scatter differently from the mountain or plains features. Determining the dielectric properties of each feature type will also constrain theories about feature formation.

References: [1] West R. et al. (2007), in prep. [2] Wye L. C. et al. (2007) *Icarus, 188,* 367-385. [3] Zebker H. A. et al. (2007) *Icarus,* (submitted). [4] Thompson W. R. and Squyres S. W. (1990) *Icarus, 86,* 336-354.

PRIMARY, SECONDARY, AND SESQUINARY CRATERS ON EUROPA. K. Zahnle[1], J. Alvarellos[2], A. Dobrovolskis[3], P. Hamill[4], [1]NASA Ames Research Center (kzahnle@mail.arc.nasa.gov), [2]Loral Space Systems, [2]University California Santa Cruz, [4]San Jose State University.

Introduction: Small impact craters are abundant on Europa [1-3]. Few of these craters represent primary impacts by errant comets [2,3]; rather, most are secondary craters or sesquinary[1] craters made by ejecta from impacts by relatively large comets. Here we report on a concise model of secondary and sesquinary cratering that takes into account primary comet impacts both on Europa and also on the neighboring Galilean satellites [6]. We focus is on impact ejecta from Io, because (i) these ejecta provide rock to Europa's ice and (ii) being made of rock they are likely to be relatively big compared to ice ejecta and thus better suited to making big sesquinary craters.

We first discuss primary impact cratering on Io and Europa. Taking volcanic resurfacing into account we find that, for our nominal comet impact rate, there should be 1.3 impact craters on Io. Io's impact crater is equally likely to be of any diameter between 100 m or 20 km. The parallel model for impact craters on Europa predicts an average global surface age between 60 and 100 Ma.

We next address the mass of material transferred from Io to Europa by impact and celestial mechanics. Test particle simulations indicate that 8% of the impact ejecta reaching orbit about Jupiter following a comet impact on Io hits Europa [6]. The amount of Ionian basalt that reaches Europa is considerable. Most of it crosses over in a relatively small number of brief events. We use a Monte Carlo model to quantify the probability distribution of events.

As an example consider a million time window. In such a short interval the amount of material transferred to Europa is usually modest, because the biggest comet to hit Io in a typical million year window is usually not very big. The median is 4e14 g of basalt transferred. Half the trials give between 8e13 and 2e15 g. Thus, in a typical million year time window, basalt ships to Europa at a rate of 2.5-60 g/s. The median of 13 g/s is

somewhat smaller than the estimated 45 g/s micrometeoroid flux [7]. By contrast the mean—4e16g, or 1300 g/s—is very big, much bigger than the micrometeoroid flux. The mean is dominated by impacts that have only a small chance of actually taking place during the life of the solar system at current impact rates. On longer time scales the mass of basalt transferred from Io to Europa exceeds the micrometeoroid flux. The median over any 10 Myr window is 90 g/s, and over 100 Myr the median rises to 250 g/s.

We then develop a general description of secondary and sesquinary craters based on theoretical ideas proposed by Melosh [8]. Melosh split impact ejecta into two kinds: "Grady-Kipp fragments" to describe rocks from below the surface that are associated with the main excavation flow, and "spalls" that originate where the excavation flow breaches the surface. Our model predicts the number and sizes of ejecta in each category. At this level of description the model has no free parameters. However, there is an ambiguity in the size of spalls that relates to their originating as thin plates of rock. Vickery [9] found that the bigger secondary craters were made by flocks of boulders that had originated as a single spall plate but had not had time enough to separate. Spall plates are expected to break up into fragments of a scale comparable to the thickness of the plates. We found it necessary to introduce a free parameter to describe the partitioning between "tabular" spalls and "equant" spalls.

Discussion: Our model's chief successes are that it correctly predicts the size of the largest secondary crater, it correctly predicts the steep size-number distribution of small craters on Europa, and it predicts the right number of small secondary craters. The model also predicts the size of the crater where the size-frequency distribution of secondary craters changes slope, but this prediction has bnot been tested.

Our model's successes indicate that Melosh's overall picture—of an excavation flow made up of Grady-Kipp fragments, topped by a thin spall layer that gives rise to the biggest and fastest ejecta—has, at minimum, the merit of being quantitatively useful.

Our model's failures are interesting as well. Our model predicts that many if not most of the 0.1-1 km diameter craters on Europa have their origin in spalls ejected from Io. Put another way, the model predicts that the number of sesquinary and secondary craters on

---

[1] "Sesquinary" stems from the latin root ``sesqui-'' meaning one-and-a-half; its most familiar use in English is in ``sesquicentennial." We use sesquinary to describe craters by impact ejecta that went into orbit about the central planet. In previous papers [4,5] we used "poltorary," which has a slavic root, for the same concept. Sesquinary craters have a character intermediate between primary craters and conventional secondary craters.

Europa should be comparable (Figure 1). This is not what is seen. Bierhaus et al. [2] conclude that no more than 5% of the 0.2-1 km diameter craters on Europa belong to a uniform random background population. Our model predicts that the background population should be rich in sesquinary craters made by spalls from Io. The implication is that our model overpredicts the number of these big iogenic sesquinaries by a factor of several.
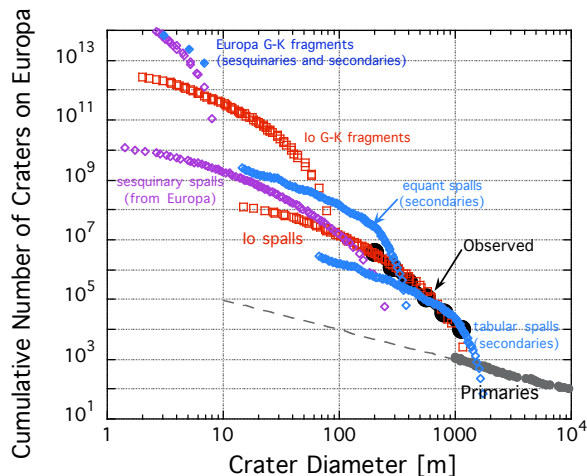

Figure 1. Predicted and observed size-number distributions of small impact craters on Europa, produced by comet impacts on Io and Europa in a typical 60 Ma period. The slight waviness seen in the secondary crater distributions is an artifact of binning. The craters are sorted according to the different categories discussed in the text. In this example 10% of the mass of spalls is in tabular spalls and the balance in equant spalls.

To first approximation Bierhaus et al. [2] sorted craters between secondaries (clustered or with variable steep size-number distributions) and primaries (not clustered and with a shallow size-number distribution). They did not explicitly consider sesquinary craters (not clustered but with variable steep size-number distributions). Thus there may be room in their analysis for a 10-20% contribution from sesquinaries. But there is little doubt that most of the craters they map are clustered and therefore are conventional secondaries. Thus we conclude that a large fraction of the equant spalls from the biggest impacts on Io must themselves break up into fragments that are small compared to the thickness of the spall plate.

There is no inconsistency here with Melosh's arguments—Melosh [8] warned against using his spall-size equation for very high velocity spalls—yet it is something of a disappointment nonetheless. Presumably the actual sizes of these ejecta will range from the

spall plate thickness down to the Grady-Kipp fragment size, at least those generated by the 50-100 km crater on Io, and additional information is needed to describe their size-distribution usefully.

Our estimates of the total mass of basalt transferred from Io are relatively robust, as they depend on two independent estimates of the total ejecta mass launched at velocities exceeding Io's escape velocity, and on celestial mechanics. We find that Ionian basalts are probably the leading source of rocky matter to Europa's ice shell, although the lead over other published sources (e.g. micrometeoroids) isn't great. Io's basalts are plausibly the major source of incompatible lithophile elements (e.g. Na and K) to Europa's ice, but they are less likely to be the major source of sulfur (which is abundant in cosmic matter), carbon, or siderophiles.

Ionian basalts could make fine stratigraphic horizons on Europa, given that most of the basalts come in a few very brief events each corresponding to a single significant impact on Io. The scattered basalts might then provide tracers of a former surface. They'd be pushed about by the flow of the ice, perhaps to accumulate where ice converges or to be cleaned away where ice is fresh.

Impact velocities on Europa are generally high enough (the distribution ranges from 1.6 to 9 km/s [6]) that we would expect most basaltic projectiles to disintegrate on impact into gravel, sand, or dust, but there might also be some intact boulders, especially where impacts are oblique or at relatively low velocity. To first approximation the best chances for seeing intact boulders from Io would be on Europa's trailing hemisphere, where impact velocities are lower, but not too near the antapical pole where nothing from Io falls.

Another thing that basalts from Io will make possible is accurate radiometric dating of Europa's surface. The dates would be obtained from the basalts by standard methods. To a good approximation the age of a basalt will equal the length of time it has been on Europa, because no basalt grows old on Io.

References: [1] Bierhaus E. B. et al. (2001) *Icarus 153,* 264-276. [2] Bierhaus E. B. et al. (2005) *Nature 437,* 1125-1127. [3] McEwen A.S. and Bierhaus E. B. (2006) *Ann. Rev. Earth Planet. Sci. 34,* 535-567. [4] Alvarellos J. L. et al. (2002) *Icarus 160,* 108-123. [5] Alvarellos J. L. et al. (2005) *Icarus 178,* 104-123. [6] Alvarellos J. L. et al. (2007) submitted to *Icarus.* [7] Cooper J. F. et al. (2001) *Icarus 149,* 133-159. [8] Melosh H. J. (1989). *Impact Cratering: A Geological Process.* [9] Vickery A. M. (1986) *Icarus 67,* 224-236. [10] Zahnle K. J. et al. (2007) submitted to *Icarus.*

CHEMICAL EVOLUTION OF AN EARLY OCEAN ON EUROPA: A KINETIC-THERMODYNAMIC MODELING. M. Yu. Zolotov[1] and M. V. Mironenko[2], [1]School of Earth and Space Exploration, Arizona State University, Tempe, Arizona 85287-1404, e-mail: zolotov@asu.edu. [2]Vernadsky Institute of Geochemistry and Analytical Chemistry, Russian Academy of Sciences, 19 Kosygin Str., Moscow 119991, e-mail: mironenko@geokhi.ru.

Introduction: A release of heat from radioactive decay and tidal dissipation on Jupiter's moon Europa could have maintained an existence of a water ocean throughout history [1]. Although the oceanic composition remains unknown, it could be evaluated by modeling of origin and evolution of water-rock interactions in the satellite's interior [3-6]. Here, we evaluated the timing of water-mineral chemical reactions that drove an early evolution of a primordial ocean.

Formation of chemical composition of an early ocean (the concept): Europa was accreted as a mixture of water ice, a polycyclic aromatic polymer, and a reduced anhydrous material of solar composition. Melting of ice in the outer part of the satellite could have occurred at late stages of accretion [7]. Inside the body, release of radioactive heat also caused melting of ice and accumulation of liquid water in an ocean. The ocean was likely to be covered by an icy shell, which was often disrupted by impacts. The composition of oceanic water was controlled by dissolution and precipitation of minerals in a layer of permeable rock beneath the ocean [6,8]. Water-rock reactions led to hydration and oxidation of primary rocks. H_2 production in oxidation reactions was followed by its upward migration, separation into the gas phase, and escape [5,6,8]. An accumulation of H_2 gas beneath the icy shell and its escape drove oxidation beneath the oceanic floor.

Coupled kinetic-thermodynamic models: Aqueous alteration of a rocky suboceanic material was investigated through numerical modeling. The model includes dissolution kinetics of primary and secondary solids, the oxidation rate of Fe-rich metal by H_2O, as well as chemical equilibration among solutes, precipitates, and dissolved gases. In the model, secondary phases form through dissolution of primary minerals, all species in aqueous solution are in equilibrium, and secondary precipitation is controlled by solubilities of minerals. A thermodynamic block of the model is based on the GEOCHEQ code [9], which uses the Gibbs free energy minimization method to calculate equilibria.

Alteration was modeled for 0°C and 2 kbar in the system H-O-Fe-Mg-Ca-Al-Si-Na-K-S-Cl-C that was either closed or open with respect to H_2 gas. Closed system models represent conditions when H_2 is not allowed to leave the system (e.g., alteration beneath impermeable icy shells or rock layers). Open system calculations are used to model H_2 removal. For the open system, fugacity (f) of H_2 was 127 bar, which corresponds to the conditions of gas separation at the bottom of ~10 km thick icy shell. The rock composition was assumed to be solar and the original mineralogy was represented by Fe-metal, forsterite, enstatite, diopside, feldspars, and troilite. Pyrene ($C_{16}H_{10}$) was used as a proxy for polyaromatic compounds. In nominal models, primary and secondary mineral grains (1 μm in diameter) were entirely exposed to the solution. The calculations were performed for the water/rock mass ratio of unity, which corresponds to interaction of a 100 km thick ocean with the underling rock layer of ~30-40 km thick. Freshly melted water was represented by 0.044 molal (mol per kg H_2O) HCl solution [c.f. 10]. The solution also contained CO (10^{-5} molal) added to represent water-soluble carbon compounds. Formation of CH_4 and other light hydrocarbons was suppressed because of the inhibition of their formation at low temperatures.

Results and discussion: The closed system modeling shows an increase in fH_2 through oxidation of Fe-metal, which quickly leads to equilibration between metal and magnetite at $\log fH_2 = 3.9$,

$$3Fe^o + 4H_2O(liq.) = Fe_3O_4 + 4H_2(aqueous/gas) \quad (1).$$
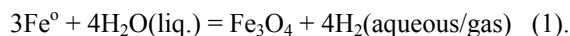
Further oxidation does not occur unless H_2 is allowed to leave the system. Alteration of silicates leads to Mg-rich phyllosilicates. The closed system scenario is not consistent with sulfate-bearing composition of the ocean [11]. In addition, a low thickness of the icy shell in geologic history (3-70 km [1]) should have not prevented H_2 escape.

Open system models demonstrate rapid oxidation of Fe^o metal according to reaction (1). Fe-rich metal, pyroxenes, and feldspars are completely altered during first ~10^3 yr. Forsterite dissolves by ~2×10^4 yr, and abundances of troilite and pyrene do not change much during at least 10^4 yr (Fig. 1a). At early stages of alteration, magnetite and greenalite (Fe-serpentine) are major secondary phases (Fig 1b). At later stages, significantly altered rocks consist of Mg-Fe-serpentine, Fe-chlorite, brucite, portlandite, calcite, Ca-K-saponite, magnetite, and mostly unaltered troilite and polyaromatic compound(s). Each time, rock mineralogy consists of secondary minerals equilibrated with solution, previously precipitated unstable phases, and unaltered primary phases. Total volume of solids increases in time, while the amount of solution decreases because of hydration and H_2 removal (Fig. 1c).

Rapid neutralization of the original acidic fluid led to an alkaline solution with pH ~12-13.5. The solution
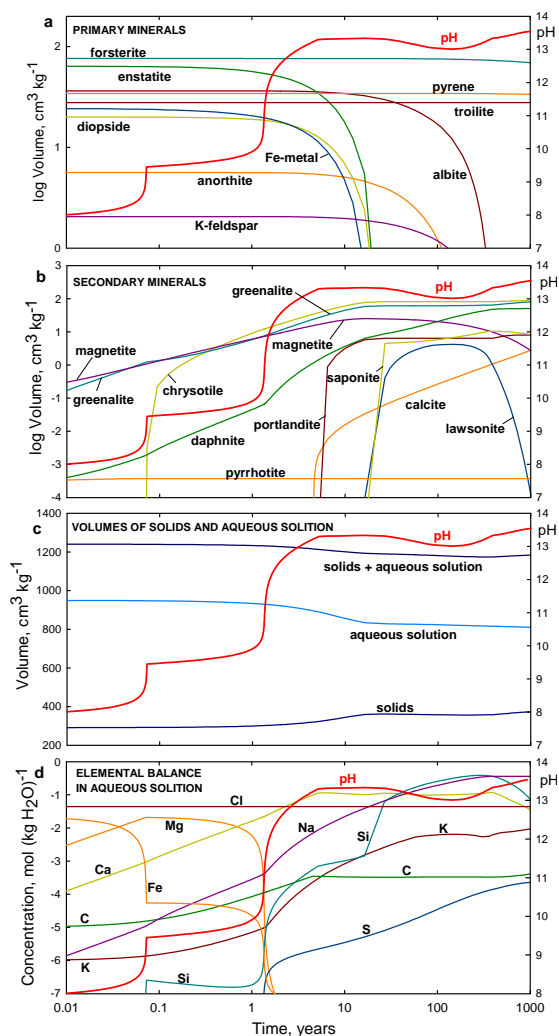
Figure 1. Temporal changes in mineralogy and aqueous chemistry during early evolution of Europa's ocean at 0°C and 2 kbar total pressure. The system is open with respect to H_2 (fH_2 = 127 bar). Water-rock mass ratio = 1.

The timescales shown in Fig. 1 represent a fast evolution scenario. Alteration could have occurred several orders of magnitude slower due to large grain sizes and low permeability of rocky materials. Note that the change in rock volume during hydration (Fig. 1c) could have decreased effective surface area and rock permeability.

Summary: The composition of an early ocean on Europa evolved dramatically during the first 10^4-10^5 yr after ice melting. Rapid oxidation of Fe-metal, H_2 escape, and pervasive alteration of micron-size mineral particles led to extremely alkaline oceanic water that slowly approached equilibrium with underlying altered rocks. Note that slow dissolution of troilite and polyaromatic compounds favored their survival among secondary minerals.

References: [1] Haussmann H. and Spohn T. (2004) *Icarus*, *171*, 391-410. [2] Kargel J. S. et al. (2000) *Icarus*, *148*, 226-265. [3] Zolotov M. Yu. and Shock E. L. (2001) *J. Geophys. Res.*, *106*, 32,815-32,827. [4] McKinnon W. B. and Zolensky M. E. (2003) *Astrobiology*, *3*, 879-897. [5] Zolotov M. Y. and Shock E. L. (2004) *J. Geophys. Res.*, *109*, E06003. [6] Zolotov M. Yu. et al. (2006) *Lunar Planet. Sci. XXXVII*, abstract 1435. [7] Stevenson D. J. et al. (1986) in *Satellites*, Univ. Ariz. Press, 39-88. [8] Zolotov M. Yu. et al. (2007) this issue. [9] Mironenko M. V. et al. (2000) *DGGGMS RAS*, *5*(15), 96-97. [10] Zolotov M. Yu. and Mironenko M. V. (2007) *Lunar and Planet. Sci. XXXVIII*, abstract 2340. [11] McCord T. B. et al. (1999) *J. Geophys. Res.*, *104*, 11827-11851.

becomes more saline in time and the ionic strength reaches ~0.7 by 10^4 yr. Variations in pH and solution composition were affected by precipitation of secondary phases (Figs. 1b and 1d). At very early low-pH stages, Cl^-, Fe^{2+}, Mg^{2+}, and Ca^{2+} were the dominant solutes. At advanced alkaline stages, Na^+, Ca^{2+}, K^+, Cl^-, OH^-, and H_2 dominate (Table 1). Carbon species are mostly presented by methanol, CO_3^{2-}, and formate. Note that abundance and speciation of aqueous C species are limited by inefficient dissolution of primary organics and by low rates of redox reactions. Sulfur is in sulfide form ($HS^- + S^{2-}$) and its concentration increases with pH. Sulfate species are not present.

THE FORMATION AND NATURE OF EARLY OCEANS ON ICY SATELLITES: GEOCHEMICAL

CONSTRAINTS. M. Yu. Zolotov[1], M. V. Mironenko[3], C. R. Glein[1], and E. L. Shock[1,2], [1]School of Earth and Space Exploration, [2]Department of Chemistry and Biochemistry, Arizona State University, Tempe, Arizona 85287, [3]Vernadsky Institute of Geochemistry and Analytical Chemistry, Russian Academy of Sciences, 19 Kosygin Str., Moscow 119991, E-mail: zolotov@asu.edu.

Introduction: The incorporation of abundant water ice and rocky materials containing radioactive elements on non-planetary bodies in the outer solar system could have led to the formation of water oceans. Early oceans could have existed on the Galilean satellites of Jupiter, certain satellites of Saturn and Uranus, Triton, and multiple trans-Neptunian objects. Water-rock interactions on these bodies would have resulted in the dissolution of solids, precipitation of secondary phases, and formation and escape of gases. These processes would have affected oceanic compositions, which could be reflected by the present-day compositions of surfaces, atmospheres, and geysers on ice-rock bodies. Here, we discuss the geochemistry of ocean-forming processes using insights from aqueously altered chondrites, observations of icy satellites, and physical-chemical modeling of rock-water-gas interactions (see Appendix).

Insights from aqueous processes in asteroids: Despite the different sizes of asteroids (i.e., parent bodies of chondrites) and icy satellites, the early stages of their evolution could have been similar. Some asteroids (e.g., Ceres [1]) could represent the silicate cores of earlier water-covered bodies. Fortunately, the formation and evolution of aqueous solutions on asteroids can be revealed by studying the mineralogy and isotopic composition of chondrites [2,3], and can be quantified using physical and chemical models [e.g., 4-7].

Asteroids accreted a mixture of reduced and anhydrous solids (e.g., Fe-Ni metal, Mg-silicates, Ca-Al-oxides, FeS, presolar grains), amorphous and organic materials, and water ice. The decay of short-lived radionuclides (e.g., ^{26}Al) melted ice [4], and the chemistry of aqueous solutions was controlled by the dissolution of primary minerals, precipitation of secondary minerals, inorganic-organic reactions, and production and escape of gases. As alteration progressed, water was consumed by hydration and oxidation reactions. The oxidation of Fe, Ni, S, P, C, and Si led to the formation of ferrous and ferric minerals (e.g., magnetite), Ni-rich alloys and sulfides, pyrrhotite, phosphates, carbonates, sulfates, and oxygenated organic compounds. H_2 was produced by oxidation reactions, and the oxidation of Fe-rich metal was a major source of H_2. The separation and escape of H_2 as well as elevated temperatures (T) favored oxidation. The formation of sulfates occurred in water-rich, porous bodies, such as the parent bodies of CI/CM chondrites, where the production and escape of H_2 was highly efficient. Impermeable rocks and ice sealants would have restricted H_2 escape, which would have inhibited oxidation and caused reduction in H_2-rich localities. Although restricted fluid convection in small bodies (< ~80 km [8]) led to isochemical alteration, the closing of pores during the formation of hydrated minerals could have squeezed fluids toward the surface of asteroids. Despite the transfer of water toward the surface, low gravity and limited water content prevented the formation of oceans on typical (i.e., small) asteroids. Aqueous alteration on asteroids ceased after ~10-15 My [3].

Initial composition of icy satellites: Satellites of giant planets may have formed from a mixture of water ice and rocky materials that slowly accumulated from the surrounding solar accretion disk [9,10]. In contrast to asteroids, these rocky materials would not have been processed in the accretion disk and would have consisted of dust particles (< ~1 μm in diameter) without chondrules. The bulk composition of the building blocks of icy satellites was most likely solar. The accretion of solids as dust implies that minerals would not have been aqueously altered prior to accretion. Thus, icy satellites might have accreted similar materials as asteroids did (i.e., reduced and anhydrous solids), together with amorphous and organic compounds, and possibly NH_3. The initial composition of icy satellites probably graded between that of asteroids and comets with increasing heliocentric distance.

Chemistry of ocean-forming processes: Compared to water-bearing asteroids, aqueous processes on icy satellites were characterized by higher water/rock ratios and migration of fluids and rocks in stronger gravity fields. In addition, the higher volume/surface area ratio of icy satellites and generation of tidal heat in some cases supported the prolonged existence of oceans on some bodies (e.g., Galilean satellites, Titan, Triton).

The melting of water ice led to the outward migration of liquid water and its accumulation in peripheral parts of icy satellites. The chemistry of primordial oceans was a result of low-T (~0°C) aqueous alteration, often in the presence of partially melted ice. The composition of ocean-forming fluids and early oceans was controlled by the kinetics and thermodynamics [11] of water-rock interactions in the uppermost layers of rocky cores. The dissolution and oxidation of primary minerals and precipitation of secondary minerals (e.g., Mg-Fe-phyllosilicates, magnetite, phosphates) produced very reduced (H_2-rich) and alkaline (pH > 11) primordial oceans. Our models [e.g., 11] indicate that early oceans were dilute NaCl solutions depleted in Mg and sulfide species. Sulfates would not have formed in the reduced oceans.

Geochemical modeling reveals that the exsolution of H_2-rich gas from aqueous solutions occurred in low-pressure (P) peripheral zones of the bodies. The accumulation of H_2-rich gas beneath ice shells eventually led to its escape owing to impact/tectonic disruptions of ice and diffusion through ice. Despite H_2 escape, aqueous systems would not have re-equilibrated under more oxidizing conditions because redox reactions would have been kinetically inhibited at low T [11]. Our calculations indicate that oxidation was faster in H_2-poor systems (e.g., $Fe^o \rightarrow Fe_3O_4$), and H_2 removal was necessary to insure Fe-rich metal oxidation even at relatively low P (e.g., ~1-2 kbar below Europa's ocean [12]). After Fe-rich metal was exhausted, the rate of H_2 production decreased, and the depth of gas separation decreased as well. Further H_2 escape and oxidation were limited by the permeability of ice shells.

On large bodies (e.g., Ganymede, Titan, Triton), thick ice shells suppressed H_2 separation at high P, retarded H_2 diffusion, and caused extremely reducing conditions in oceans (i.e., high activities of dissolved H_2). In addition, strong gravity slowed H_2 escape from primordial atmospheres, and the formation of a layer of high-pressure ices above cores upon cooling terminated oxidation reactions involving water. High fugacities (f) of highly non-ideal H_2 ($fH_2 \gg P_{total}$ at high P_{total}) and low T limited the oxidation of Fe-rich metal and favored the formation of secondary Fe-Ni alloys (as in Earth's serpentinites [13]). The alloys could have catalyzed the high-P hydrogenation of carbon species, forming CH_4 and other light hydrocarbons. This mechanism is consistent with observations of CH_4 on Titan [14,15]. On Europa, the lack of CH_4 could be explained by significant H_2 escape caused by periodic melting and disruptions of the ice shell, low gravity, elevated surface T, and Fe^o-FeS core formation.

Hydrothermal processes. Heat production in rocky cores induced dehydration of early-formed hydrated minerals (e.g., phyllosilicates, tochilinite) and upward migration of hydrothermal fluids, which affected the mass and composition of oceans. Again, the composition of ocean-forming fluids was chiefly controlled by interactions in the uppermost rock layers. During and after core dehydration, hydrothermal processes took place as oceanic water circulated through permeable rocks below the ocean-rock boundary. The release of tidal heat and/or magmatic activity in subjacent rocks enhanced the circulation.

Our models show that hydrothermal circulation altered the mineralogy of permeable rocks and promoted oxidation (e.g., Fe-silicates and Fe-Ni alloy to magnetite and pentlandite) and H_2 generation. High-T fluids were rich in sulfide species (e.g., H_2S), and the mixing of hydrothermal fluids with oceanic water led to the precipitation of metal sulfides at ocean-rock interfaces. The upward transport (bubbling, diffusion, convection) and escape of H_2 oxidized icy satellites. High-T and low-fH_2 conditions increased the carbonate ($CO_2 + HCO_3^- + CO_3^{2-}$) and sulfate ($HSO_4^- + SO_4^{2-}$) concentrations of hydrothermal fluids [c.f. 17]. The oxidation of sulfides favored the partial dissolution of Mg-silicates, which led to the formation of Mg-sulfates in severely oxidized satellites, such as Europa. Presumably, the slow escape of H_2 allowed mineral assemblages to control the oxidation state (fH_2) of hydrothermal systems. On early Enceladus, sluggish hydrothermal circulation might have led to CH_4-CO_2 and NH_3-N_2 equilibria at ~250-300°C in a buffered environment [16,18]. Our calculations suggest that H_2 escape drove the oxidation state of hydrothermal systems on early Enceladus to the pyrrhotite-pyrite-magnetite (PPM) buffer. Reactions in the C-N-O-H system could have been catalyzed by magnetite and/or sulfide minerals.

The high-T transformation of accreted aromatic polymers with aliphatic, N-, and O-bearing side chains led to the partial oxidation and release of O- and N-bearing species (e.g., carbonate species, methanol, carboxylic and amino acids) into buoyant fluids. NH_3 (if present) might have been oxidized to N_2 [19,16], except in reduced oceans such as Titan's. The accumulation of soluble oxidized C (i.e., carbonate species, organic acids) in oceans, precipitation of carbon-

ates at ocean-rock boundaries, and escape of relatively insoluble CH_4 (if formed) contributed to satellite oxidation.

Summary: The composition of early oceans on ice-rock bodies was a consequence of low-T (~0°C) dissolution, hydration, and oxidation reactions between minerals and liquid water during ice melting and gravitational separation of water and rocks. Subsequent heating of rocky cores affected oceanic chemistry by contributing water from dehydration reactions in cores and promoting hydrothermal circulation of water through permeable rock layers. The escape of H_2 led to the oxidation of minerals, hydrothermal fluids, and oceans. Thus, H_2 escape drove the redox evolution of icy satellites. Restricted H_2 escape favored the mineral-catalyzed hydrogenation of carbon species and formation of CH_4.

References: [1] McCord T. B. and Sotin C. (2005) *J. Geophys. Res.*, *110*, E05009. [2] Brearley A. J. and Jones R. H. (1998) in *Planetary Materials*, *Rev. in Mineralogy*, *36*, 1-398, Mineral. Soc. Am. [3] Krot A. N. et al. (2006) In *Meteorites and the Early Solar System*, ed. by D. S. Lauretta and H. Y. McSween, Univ. of Ariz. Press, 525-554. [4] Grimm R. E. and McSween H. Y. Jr. (1989) *Icarus*, *82*, 244-280. [5] Zolensky M. E. et al. (1989) *Icarus*, *78*, 411-425. [6] Young E. D. et al. (1999) *Science*, *286*, 1331-1335. [7] Zolotov M. Yu. et al. (2006) *Meteor. Planet. Sci.*, *41*, 1775-1796. [8] Travis B. J. and Schubert G. (2005) *Earth. Planet. Sci. Lett.*, *240*, 234-250. [9] Canup R. M. and Ward W. R. (2002) *Astron. J.*, *124*, 3404-3423. [10] Schubert G. et al. (2004) In *Jupiter – The Planet, Satellites, and Magnetosphere*, ed. by F. Bagenal et al., Cambridge Univ. Press, 281-306. [11] Zolotov M. Yu. et al. (2006) *XXXVII Lunar and Planet. Sci.* [CD-ROM], Abstr. 1435. [12] Zolotov M. Yu. and Mironenko M. V., this issue. [13] Frost B. R. (1985) *J. Petrol.*, *26*, 31-63. [14] Zolotov M. Yu. et al. (2005) *Eos Trans. AGU*, 86(52), Fall Meet. Suppl., Abstr. P43B-O4. [15] Owen T. et al. (2006) *Faraday Discuss.*, *133*, 387-391. [16] Glein C. R. et al. (2007) in prep. [17] Zolotov M. Yu. and Shock E. L. (2003) *J. Geophys. Res.*, *108*, E4, 5022. [18] Glein C. R. et al. (2007) *XXXVIII Lunar and Planet. Sci.* [CD-ROM], Abstr. 1251. [19] Matson D. L. (2007) *Icarus*, *187*, 569-573. [20] Mironenko M. V. et al. (2000) *Herald DGGGMS RAS*, *5*(15), 96–97. [21] Mironenko M. V. and Zolotov M. Yu. (2005) *XXXVI Lunar and Planet. Sci.* [CD-ROM], Abstr. 2207. [22] Zolotov M. Yu. and Mironenko M. V. (2007) *J. Geophys. Res.*, *112*, in press.

Appendix: We use the modified GEOCHEQ code [20,21] to calculate chemical equilibrium in gas-water-solid multicomponent systems at T = 0-400°C and P < 5 kbar. Input data include the thermodynamic properties of one-component crystalline solids and non-ideal solid, gas, and aqueous species. Isobaric and isochoric conditions can be explored. Sophisticated models account for rates of mineral dissolution and oxidation. We use these codes to quantify aqueous geochemistry on early asteroids, Europa, Enceladus, and Mars [7,11,12,18,22].

NOTES

NOTES